The Breakup Reactions of 90MeV ^{9}Be

Thesis

Submitted by

Euan Walter Macdonald, B.Sc.

for the degree of

Doctor of Philosophy

Department of Physics

University of Edinburgh

May 1988

I would like to dedicate this thesis to my parents, my brother and to Pamela.

Abstract

The breakup of 90MeV ^{9}Be has been studied for the reactions $^{9}Be+^{12}C$ and $^{9}Be+^{120}Sn$. Kinematically complete $\alpha+\alpha+n$ triple coincidence data have been obtained for both of these reactions. To enable the collection of data of high statistical quality, a new type of ^{8}Be-detector has been developed which has a very large effective solid angle.

The sequential breakup process $^{12}C,^{120}Sn(^{9}Be,^{9}Be^{*}_{2.43}\rightarrow^{5}He_{gs}+\alpha \rightarrow\alpha+\alpha+n)$ has been identified. Strong evidence for the direct breakup of ^{9}Be in the $^{120}Sn(^{9}Be,^{8}Be_{gs}+n)^{120}Sn_{gs}$ reaction has also been obtained. A Coulomb excitation calculation for this reaction is presented.

Declaration

The data presented in this thesis was obtained by myself and other members of the Edinburgh University Nuclear Physics Group. The data interpretation and analysis are entirely my own work. This thesis has been composed by myself.

Acknowledgements

I would like to thank:

- My supervisors, Dr Alan Shotter and Dr Derek Branford for their help, suggestions and encouragement.
- All of the members of the Edinburgh University Nuclear Physics group, past and present, for considerable help and friendship.
- I would especially like to thank Dr Javad Rahighi for his expert advice and work on the design and construction of the neutron detectors.
- Professors Wallace and Cowley for the use of the facilities of the Edinburgh University Physics Department.
- The staff and crew of the Nuclear Structure Facility.
- The S.E.R.C. for the research studentship.
- My parents, for reasons too numerous to mention.
- Pamela, for keeping me sane over the last few months.

Table of Contents

CHAPTER 1
INTRODUCTION

1.1 General Introduction

The work discussed in this thesis comprises an experimental investigation of ^{9}Be induced breakup reactions at a beam energy of 10MeV/A.

A considerable amount of experimental and theoretical effort has gone into the study of the breakup reactions of light-ions ($A \leq 4$) and light heavy-ions ($6 \leq A \leq 20$) at projectile energies which are $\geq$10MeV/A. Perhaps the earliest motivation for studying these breakup reactions came from the discovery of beam-velocity bumps in the inclusive energy spectra produced by the scattering of these ion species. As early as 1947, Helmholtz et al [HELM47] reported the existence of a high yield of fast, forward-focused neutrons in 190MeV deuteron induced reactions. Since then, numerous projectile+target systems have been investigated. In ^{3}He and ^{4}He induced reactions, beam-velocity bumps of p,d,t and ^{3}He fragments [MEIJ85] are seen. For reactions involving light heavy-ions, such as ^{6}Li, ^{7}Li and ^{12}C [DAVI87, SIWE79] beam velocity bumps of p,d,t, ^{3}He, ^{4}He, and ^{8}Be nuclei are all produced. The origin of the beam-velocity groups has been associated with projectile breakup and related processes.

A typical inclusive spectrum is shown in figure 1.1. This particular spectrum was obtained for the reaction 90MeV ^{9}Be+^{120}Sn. Its features however, are qualitatively similar to those which are observed with a wide range of projectile+target systems. At energies close to the beam energy, direct transitions dominate. At lower energies, a broad bell-shaped continuum is the strongest feature. This continuum corresponds to beam-velocity α-particles; a considerable fraction of which are produced by the breakup of the ^{9}Be projectile. The remainder of the α-particles are due to transfer-breakup and partial-fusion reactions. A slight enhancement in the inclusive energy spectrum at $\sim$80MeV is due to beam-velocity ^{8}Be nuclei. These are produced by ^{9}Be breakup and neutron transfer reactions. (Since ^{8}Be is α-particle unstable, the ^{8}Be events correspond to two coincident α-particles entering the counter). Lying underneath the continuum bump is a contribution due to compound-nucleus evaporative emission and to pre-equilibrium emission. Figure 1.1 demonstrates that breakup represents a significant

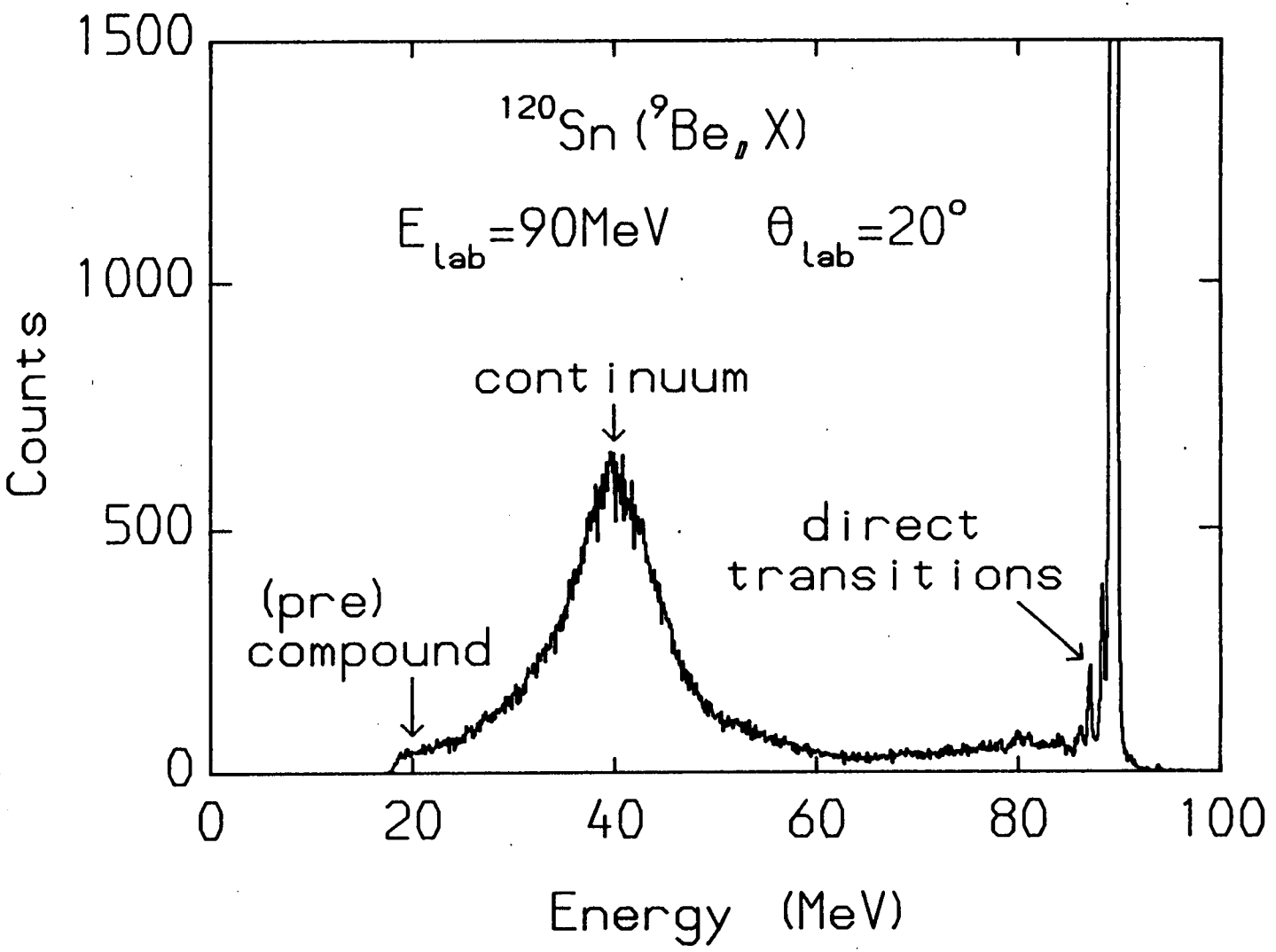

Figure 1.1: Inclusive energy spectrum for the reaction 90MeV ^{9}Be+^{120}Sn.

fraction of the total reaction cross-section. This strength of the breakup channel is, in itself, a motivation for the study of breakup reactions.

The influence of breakup on other reaction channels, such as elastic scattering, can be considerable. For example, in CDCC calculations (§1.4.5) for the elastic scattering of loosely-bound projectiles, such as ^{6}Li and ^{12}C, it is found that it is necessary to explicitly include resonant and non-resonant breakup states to achieve a good fit to the data [SAKU86].

Further interest in breakup reactions arises out of the possibility of extracting information on low-energy fusion reactions from breakup data. This can only be achieved for the case of pure Coulomb breakup. In a Coulomb breakup reaction, the projectile absorbs a virtual photon from the projectile+target Coulomb field, and then decays into two or more fragments. This reaction is the inverse of the fusion reaction in which the breakup fragments fuse together by the emission of a real-photon. So long as the nuclear field of the target is not involved, the reciprocity theorem can be applied and fusion cross-sections can be determined from the breakup data. The principal advantage of this technique is that it permits the investigation of low-energy fusion reactions. Such reactions correspond to Coulomb breakup processes in which a small amount of energy is absorbed by the projectile. The breakup fragments, however, have high laboratory energies (typically beam-velocity energies) and are forward focused, so their detection is straightforward compared to the identification of fusion events.

Of course, breakup reactions and their related processes, such as partial-fusion, are of interest in their own right. Furthermore, this category of reactions provides a significant challenge to nuclear reaction theories.

1.2 Breakup Nomenclature

A study of the literature shows that no standard nomenclature exists for the description of breakup processes. Various different terminologies have been adopted by different authors. Indeed, in some cases, the same name has been used for quite different reactions. The following list outlines the intended meaning of the terms used in this thesis. It is not claimed that this terminology is by any means the most appropriate.

Breakup - a reaction leading to a final state of three or more particles, regardless of the mechanism.

Elastic breakup - a reaction in which all of the final state fragments are in their ground states.

Inelastic breakup - a reaction in which one of the fragments is excited in the final state, usually this will be the residual nucleus.

Coulomb breakup - breakup reaction due to the Coulomb interaction between the projectile and the target.

Sequential breakup - a reaction in which the ejectile is excited to an unbound resonance state which subsequently decays over a time scale that is greater than the transit (or interaction) time of $\sim 5 \times 10^{-22}$s.

Direct breakup - a reaction in which fragmentation of the projectile occurs over a time-scale comparable to the transit time.

Partial-fusion - a reaction in which a constituent of the projectile fuses with the target nucleus. The remainder of the ejectile is emitted at, essentially, the beam velocity. The hot compound system decays by α,n and γ-ray emission or by fission.

Final state interactions - These are interactions between the the breakup fragments and the residual nucleus. In general, this term also applies to interactions between the breakup fragments themselves. However, in the present work, such interactions are only rarely considered.

1.3 Survey of Existing Breakup Data

In this section, a brief overview of the existing experimental data on breakup reactions is presented. In particular, attention will be focused on beam energies above the Coulomb barrier and on the identification of several different types of breakup reaction.

1.3.1 Light-ion Breakup Data

Most of the research into breakup reactions has concentrated on the breakup processes of light-ions. The earliest theoretical and experimental investigations, dating back to 1935 [OPPE35a, OPPE35b, LAWR35], looked at the breakup of the deuteron. At beam energies well below the Coulomb barrier, the d→p+n reaction has been carefully studied by Jarczyk and Lang [JARC73] by

means of a kinematically complete p+n coincidence experiment. The general features of this data are reasonably well reproduced by pure-Coulomb calculations. If the final state interaction between the neutron and the target is included (as was done in the post-form DWBA analysis of Baur and Trautmann [BAUR76]) then an excellent fit to the sub-barrier d→p+n data is achieved. This indicates that the Coulomb interaction dominates the breakup in this energy region.

At higher deuteron beam energies, direct nuclear stripping reactions become increasingly important. These reactions were first observed by Helmholtz et al [HELM47]. A simple geometrical model was developed by Serber [SERB47] to explain them.

Both ^{3}He and ^{4}He induced reactions have also been studied extensively. Due to the greater complexity of these nuclei, a much wider range of breakup processes has been identified for them than for the deuteron. These processes include sequential and direct breakup, partial-fusion, transfer breakup, pick-up breakup and inelastic breakup. Recently, a comprehensive review article by de Meijer and Kamermans [MEIJ85] has discussed in detail the breakup phenomena of ^{3}He and ^{4}He projectiles. Since the breakup reactions of the Helium isotopes comprise an excellent example of breakup reactions in general, some of the material covered by de Meijer will now be reviewed briefly. (For data and references see MEIJ85).

Firstly, we consider sequential breakup. The production of unbound ejectiles occurs in a variety of different ^{3}He and ^{4}He induced reactions. The simplest of these involves the excitation of the projectile to a particle unstable state; as in the reaction ($\alpha,\alpha^{*}\rightarrow t+p$), in which the α-particle is excited to its 20.1MeV 0^{+} state. In pick-up and transfer reactions, sequential breakup is also evident. For example, the following sequential reactions have all been observed:

- (^{3}He,^{2}He→p+p)
- (^{3}He,d*→p+n)
- (α,^{5}Li→α+p)
- (α,^{2}He→p+p)
- (α,^{7}Li*→α+t)

With direct reactions, a similar variety of processes is observed. These

include the simple fragmentation of the projectile, as in the (^{3}He,d+p) reaction, as well as more complicated reactions in which mass is transferred to (or from) the target nucleus e.g. (α,p+d) and (^{3}He,p+p).

Other ^{3}He and ^{4}He induced direct reactions include partial fusion. This has been identified via the detection of beam velocity fragments in coincidence with evaporative particles. Two excellent examples of reactions in which partial fusion is seen are ^{28}Si(α,p+d) and ^{28}Si(^{3}He,p+p). In both of these reactions, beam velocity bumps and evaporative tails are clearly visible in the energy spectra of the breakup fragments. The partial fusion data for reactions with ^{3}He and ^{4}He projectiles are qualitatively in agreement with the spectator participator model of nuclear reactions.

A subject of considerable interest in ^{3}He and ^{4}He induced reactions has been the explanation of the inclusive energy spectra. Since a large number of reactions contribute to the inclusive spectra (direct and sequential breakup, partial fusion, inelastic breakup etc), comprehensive datasets must be obtained on all of these reactions in order to fully understand the inclusive spectra. A beautiful example of the decomposition of an inclusive spectrum is discussed by de Mejier [MEIJ85] for the reaction ^{28}Si(^{3}He,d).

1.3.2 Light Heavy-ion Breakup Data

In recent years, a considerable effort has gone into studying the breakup reactions of the light heavy-ions ($6 \leq A \leq 20$). In particular, the nuclei ^{6}Li and ^{7}Li have been well studied. For these loosely bound nuclei, breakup is a strong reaction channel.

At beam energies above the Coulomb barrier, ^{6}Li breakup has been comprehensively studied by Castaneda et al [CAST80]. In this work, particle+particle and particle+γ-ray correlation techniques were employed to investigate the processes contributing to the high flux of beam velocity fragments produced in the 75MeV ^{6}Li+^{197}Au reaction. Partial fusion reactions such as:

- ^{197}Au(^{6}Li,αxnγ)$^{199-x}$Hg
- ^{197}Au(^{6}Li,dxnγ)$^{201-x}$Tl

were identified from coincidences between prompt γ-rays and beam velocity α-particles or deuterons. The reaction channel was cleanly defined by

selecting γ-rays from discrete transitions of the residual nuclei.

The particle+particle coincidence data showed the existence of sequential breakup of ^{6}Li, via its 2.18MeV 3^{+} state, into the α+d channel. A coulomb excitation calculation for the reaction $^{197}Au(^{6}Li,^{6}Li^{*}_{2.18}\rightarrow\alpha+d)$ was found to be moderately successful at forward scattering angles but to be seriously in error at more backward angles. This indicates the, perhaps obvious, importance of nuclear processes in breakup reactions above the Coulomb barrier. Sequential breakup, via the reaction $^{197}Au(^{6}Li,^{5}Li_{gs}\rightarrow\alpha+p)$, was also thought to be the mechanism responsible for the α+p coincidence yield.

The observation of large angle α+d coincidence events was taken as evidence of the direct nuclear breakup reactions $^{197}Au(^{6}Li,\alpha+d)$.

The breakup phenomena of ^{7}Li projectiles are similar to those which are observed in ^{6}Li induced reactions. Shotter et al [SHOT81] have reported on the sequential breakup of 70MeV ^{7}Li in the reactions $^{12}C,^{208}Pb(^{7}Li,^{7}Li^{*}_{4.63}\rightarrow\alpha+t)$. This sequential reaction has been observed with many other target nuclei [DAVI87]. For heavy targets, elastic breakup dominates. For light targets however, such as ^{12}C, inelastic reactions are important.

In ^{7}Li induced reactions, sequential breakup is also observed in pick-up and transfer reactions. For example the reactions $(^{7}Li,^{6}Li^{*}_{2.18}\rightarrow\alpha+d)$ and $(^{7}Li,^{8}Be^{*}_{gs,3.04}\rightarrow\alpha+\alpha)$ have been identified for many targets [DAVI87].

Of particular interest to the present work, was the discovery by Shotter et al of a small-angle direct breakup mechanism for ^{7}Li projectiles at forward scattering angles. This mechanism was initially observed in the reaction $^{208}Pb(^{7}Li,\alpha+t)^{208}Pb_{gs}$ at a beam energy of 70MeV [SHOT81]. Subsequent work identified the direct breakup mechanism with ^{120}Sn, ^{96}Zr and ^{56}Ni targets [SHOT84, DAVI87]. For lighter targets, such as ^{12}C, no evidence for the direct mechanism exists. This is presumably due to the greater influence of FSIs on the separation angle of the breakup fragments at scattering angles beyond the grazing angle; all of the existing light target data has been collected at such angles.

The direct breakup mechanism for ^{7}Li was clearly identified by the fact that broad distributions existed in the coincident α-particle and triton energy spectra which did not correspond to energies accessible via sequential breakup.

The production of such distributions is however possible within the constraints of direct 3-body kinematics.

The amount of energy absorbed by the ^{7}Li projectiles, during direct breakup events, was small, typically 3.5MeV, and elastic breakup was the dominant reaction channel. These observations suggest that the Coulomb interaction is responsible for the direct breakup mechanism.

The ^{7}Li→α+t direct breakup reaction has been investigated theoretically via a Coulomb excitation calculation and by means of an adiabatic model nuclear breakup calculation. For ^{120}Sn [SHOT84] and ^{96}Zr [SHOT88b] targets, the Coulomb calculation was found to produce a remarkable fit to the shape and magnitude of the experimental data in the forward scattering region. For the ^{208}Pb target [SHOT88a], the cross-section was under-predicted at forward angles. This is possibly due to an enhanced nuclear breakup contribution for this target. At more backward angles, Coulomb excitation seriously over predicts the breakup cross-section for all of the targets. The adiabatic model calculation, which assumes only a nuclear interaction, has been performed for the case of a ^{208}Pb target [THOM83]. At forward angles, this calculation under predicts the direct breakup cross-section. At backward angles, it well reproduces the shape and magnitude of the angular distribution. An interesting point that arises from the adiabatic model calculation [SHOT88a], is that there exists an appreciable nuclear breakup cross-section at forward angles. Indeed, at very forward scattering angles ($<8^{o}$), nuclear breakup dominates. Consequently, the extraction of fusion cross-sections from the breakup data will be impossible without a detailed knowledge of the nuclear breakup process.

The results of these two theoretical approaches are in accord with a simple picture of breakup reactions in which Coulomb breakup dominates inside the grazing angle, whilst nuclear processes dominate at angles beyond grazing.

In ^{7}Li induced reactions, partial fusion has been identified as being a strong reaction channel. This process was investigated by Davinson et al [DAVI87] via the particle+γ-ray correlation method. For ^{120}Sn and ^{208}Pb targets, the partial fusion channels (^{7}Li,αxnγ), (^{7}Li,txnγ) and (^{7}Li,dxnγ) were identified. By examination of the contributions to the inclusive yields from the sequential, small-angle direct and partial fusion reactions, it was established that a large

fraction of the inclusive yields was unaccounted for (≈50%). It was suggested that the missing yield was contained in wide angle breakup reactions. Recently, Yorkston et al [YORK88] have measured high yields of wide angle α+t coincidences in the reactions $^{12}C,^{120}Sn(^{7}Li,\alpha+t)$. Initial analysis suggests that both direct and sequential processes are contributing to this breakup yield.

For nuclei heavier than ^{7}Li, breakup processes become increasingly complicated and tend to involve greater multiplicities of breakup fragments. This behaviour simply reflects the more complicated nature of the heavier projectile nuclei. Even for sequential processes, four-body final states are common. Two good examples of such sequential processes are seen in the breakup reactions of ^{9}Be and ^{12}C. The study of ^{9}Be breakup comprises the subject of this thesis, so it will be discussed in detail later. At present, it suffices to say that four-body final states are accessible via reactions like:

- $(^{9}Be,^{9}Be^{*}_{2.43}\rightarrow^{8}Be_{gs}+n\rightarrow\alpha+\alpha+n)$
- $(^{9}Be,^{9}Be^{*}_{2.43}\rightarrow^{5}He_{gs}+\alpha\rightarrow\alpha+\alpha+n)$

For the case of a ^{12}C projectile, breakup into the $^{8}Be_{gs}+\alpha$ channel has been studied by Bice et al [BICE82] at bombarding energies of 132, 187 and 230MeV. This is a difficult reaction to observe, since the two α-particles from the $^{8}Be_{gs}$ decay have an angular separation of only a few degrees. Nevertheless, high quality data were obtained on several reactions, including the sequential breakup reactions $^{208}Pb(^{12}C,^{12}C^{*}_{7.6,9.6}\rightarrow^{8}Be_{gs}+\alpha\rightarrow\alpha+\alpha+\alpha)$. By comparison of this data with the partial fusion data of Siwek-Wilczynska et al [SIWE79] and the inclusive α-yields, the existence of a direct $^{12}C\rightarrow^{8}Be+\alpha$ reaction was inferred. At the highest beam energy, the data also indicated the presence of a direct $^{12}C\rightarrow\alpha+\alpha+\alpha$ reaction. Since this last reaction leads immediately to a four body final state, it would be necessary to collect triple coincidence data to study it properly.

With even heavier projectile nuclei, attention has focused on heavy-ion+α-particle coincidence measurements. For example, a large amount of data now exists on the $(^{14}N,HI+\alpha)$ reaction [BHOW80, BHOW82, DRIE80]. These data have demonstrated that the wide-angle portion of the double differential cross-section can be factorised in the following manner:

$$d^{2}\sigma/d\Omega_{HI}d\Omega_{\alpha}=K\ d\sigma/d\Omega_{HI}\ d\sigma/d\Omega_{\alpha} \qquad (1.1)$$

Where $d\sigma/d\Omega_{HI}$ and $d\sigma/d\Omega_{\alpha}$ are the inclusive heavy-ion and α-particle cross-sections respectively. The remarkable feature of this equation is that 'K' is approximately constant for a considerable range of targets, beam energies and values of θ_{HI} and θ_{α}. The successful factorisation of the HI+α yield, combined with the observation that the HI+α coincidence energy spectra are very similar in shape to the inclusive spectra [BHOW81], indicates that the correlation between the fragments has been destroyed during the breakup interaction. Consequently, the breakup process presumably consists of a rapid disintegration of the projectile in the nuclear field of the target, followed by strong final state interactions between the breakup fragments and the target. This picture is in accord with the fact that the uncorrelated HI+α events are predominately inelastic. In addition to this form of direct breakup, numerous sequential decay channels have also been observed in close-geometry data [DRIE80]. These include:

- $(^{14}N,^{14}N^{*}\rightarrow^{10}B+\alpha)$
- $(^{14}N,^{15}N^{*}\rightarrow^{11}B+\alpha)$
- $(^{14}N,^{10}B^{*}\rightarrow^{6}Li+\alpha)$
- $(^{14}N,^{11}B^{*}\rightarrow^{7}Li+\alpha)$

The emission of the heavier ejectiles, $^{14}N^{*}$ and $^{15}N^{*}$, tends to occur in elastic reactions, whereas the production mechanism of the lighter ejectiles, $^{7}Li^{*}$ and $^{6}Li^{*}$, is predominately inelastic. This is probably a consequence of the greater mass transfer involved in the latter case, since this implies that deeper collisions are involved. Of course, the inferred inelasticity of the reaction could be due to the production of a four fragment final state. Such a possibility leads to uncertainties in the interpretation of the data. Clearly, one would wish to obtain triple coincidence data either in the form of particle + particle + particle events or particle + particle + γ-ray events. In the latter case, the ejectile, and its excited state, could be identified from the particle + particle data and the residual nucleus from the γ-ray energy. The collection of such data however, represents a considerable experimental challenge. It is interesting to note that the original motivation for obtaining double coincidence data was to answer questions regarding inclusive data. As seen here, the double coincidence data have led to further, if more precise, questions. Undoubtedly, more complete data will create more questions than answers.

The data for ^{16}O projectiles display similar features to those observed with

^{14}N. Both inelastic direct reactions [BINI80] and quasi-elastic sequential reactions [RAE81] have been identified.

The preceding paragraphs comprise a very brief review of the types of breakup reactions which are observed with light-ion and light heavy-ion projectiles. It is seen that the range and complexity of the reactions increase as the projectile mass increases. However, common features exist in that, for most projectile+targets systems, it is possible to identify sequential breakup, direct breakup, partial fusion and inelastic processes. Furthermore the types of particle+particle coincidences which are observed reflect the structure of the projectile nuclei.

The work which has been discussed here was mainly motivated by a wish to understand the mechanisms of breakup reactions. In many cases however, breakup reactions, and the experimental techniques which have been developed to study them, have been applied in nuclear structure research and other more exotic areas of nuclear physics. An excellent example of the former, is the work of Fulton and Rae on *molecular* states in ^{24}Mg at high excitation energies, $E_x \sim 20$MeV [FULT86]. These states have been investigated via sequential breakup reactions such as $^{12}C(^{24}Mg,^{24}Mg^{*}\rightarrow^{12}C+^{12}C)$ and $^{12}C(^{24}Mg,^{24}Mg^{*}\rightarrow^{16}O+^{8}Be)$. An interesting example of a more unusual application of breakup techniques is found in the work of J.Pochodzalla et al [POCH87], who measured two-particle correlations for ^{40}Ar induced reactions on ^{197}Au at a bombarding energy of 2,400MeV. In this work, the sequential decay of a vast number of ejectiles was identified e.g. $^{4}He^{*}\rightarrow t+p$, $^{4}Li_{gs}\rightarrow ^{3}He+p$, $^{5}He^{*}\rightarrow t+d$, $^{5}Li_{gs}\rightarrow \alpha+p$, $^{5}Li^{*}\rightarrow ^{3}He+d$, $^{6}Li^{*}\rightarrow \alpha+d$, $^{7}Li^{*}\rightarrow \alpha+t$, $^{7}Be^{*}\rightarrow \alpha+^{3}He$, $^{8}Be^{*}\rightarrow \alpha+\alpha$, $^{8}Be^{*}\rightarrow ^{7}Li+p$ etc. These data were used to extract information on the highly complex nuclear systems which are formed in the collisions of very heavy ions at high energies.

1.4 Theoretical Approaches to Breakup

In this section, some of the theoretical approaches to breakup reactions will be discussed. For most of these approaches only a brief outline is given, but since a semi-classical Coulomb excitation calculation is considered in Chapter 6, this type of calculation will be discussed in more detail. We start with one of the earliest breakup theories.

1.4.1 The Serber Model

The Serber model [SERB47] was developed to explain the beam velocity neutron bumps in the (d,n) data of Helmholtz et al [HELM47]. It is assumed that the proton is stripped off the deuteron in an instantaneous interaction. The neutron is not 'disturbed' by the stripping process, so its energy spectrum is determined by its momentum distribution in the deuteron and the momentum of the centre of mass of the deuteron at the instant of stripping. The cross-section is determined by simple geometrical considerations and by assuming that the target is opaque. The Serber model offers an intuitive picture of stripping reactions and, despite its simplicity, it successfully reproduces the shape of the beam velocity bumps in light-ion breakup reactions. Recently, an extended version of the Serber model [UTSU85] has been applied, with a moderate degree of success, to heavy-ion reactions such as 280MeV $^{14}N+^{165}Ho$ and 218MeV $^{16}O+^{208}Pb$.

1.4.2 Coulomb Excitation

The subject of Coulomb excitation has received considerable theoretical attention [ALDE56]. In part, this is due to the fact that the Coulomb force is well understood, hence accurate theories can be constructed. Furthermore, Coulomb excitation processes are commonly observed phenomena. Coulomb excitation theory is most often applied in the context of target excitation by energetic projectiles. The nomenclature of the theories tend to reflect this. Of course, there is no intrinsic difference between projectile excitation and target excitation, so the theories can equally well be applied to the excitation and decay of projectile states. The only complication in looking at breakup data, as opposed to inelastic scattering data, is that the efficiency for detection of the unbound ejectile must be known. One interesting advantage that arises from detecting the decay of excited projectiles is that it is possible to study the excitation of very light nuclei (i.e. the projectile) by very heavy nuclei (the target). The reversed reaction is inaccessible to experimental study because of the extreme forward focusing.

The simplest approach to Coulomb excitation is to use a semi-classical model. Such a model is applicable if the Sommerfield parameter, η, is considerably greater than unity, as it is for most heavy-ion collisions at energies $>$10MeV/A. The Sommerfield parameter, in natural units, is given by:

$$\eta=0.15\ Z_T\ Z_P/(E_P/M_P)^{1/2} \qquad (1.2)$$

where E_P and M_P are the laboratory energy (in MeV) and mass (in amu) of the projectile, respectively. For $\eta>10$, quantal effects are very small.

In this thesis, the reactions 90MeV $^{9}Be+^{12}C$ and 90MeV $^{9}Be+^{120}Sn$ are studied. For the ^{12}C target $\eta=1.1$, for the ^{120}Sn target $\eta=9.5$. Therefore, the application of semi-classical theory to the 90MeV $^{9}Be+^{120}Sn$ reaction is justifiable. The data on this reaction is compared with a semi-classical Coulomb excitation calculation in Chapter 6.

In the semi-classical model, the projectile is assumed to follow a Rutherford trajectory. The effect of the Coulomb field on the projectile nucleus, minus the mono-pole term which is responsible for the scattering, can then be treated by time dependent perturbation theory. Since the projectile velocities considered here are small compared to the speed of light ($v/c\sim10\%$), it is possible to neglect magnetic excitations. The electric excitation cross-section, for excitations in the range E_x to E_x+dE_x, can be written as a sum over the contributions from each electric multipole moment *viz*,

$$d\sigma_E=\sum d\sigma_{E\lambda} \qquad (1.3)$$

The cross-section for a multipole moment of order λ is given by,

$$d\sigma_{E\lambda}=(Z_T e/\hbar V_P)^2\ a^{-2\lambda+2}\ B(E\lambda)df_{E\lambda}(\theta,E_x)dE_x \qquad (1.4)$$

where

$$a=Z_P Z_T e^2/(\mu V_P^2) \qquad \mu=M_P M_T/(M_P+M_T) \qquad (1.5)$$

The reduced transition probability, $B(E\lambda)$, contains the nuclear structure information, whilst the dependency of the cross-section on the orbit is determined by $df_{E\lambda}(\theta,E_x)$, which is the standard Coulomb orbital function [ALDE56]. The contribution to the cross-section from successive multipole moments falls off rapidly. In practice therefore, it is normally sufficient to consider only the lowest multipole moment.

A parameter which is useful when considering Coulomb excitation is the dimensionless quantity ξ, defined by,

$$\xi = aE_x/(\hbar V_P) \qquad (1.6)$$

For values of $\xi < 1$, excitation is strong, for values of $\xi >> 1$, $df_{E\lambda}(\theta, E_x)$ decreases exponentially with ξ. Consequently, Coulomb excitation is most probable for low values of E_x and high beam energies.

Most theoretical and experimental studies of Coulomb excitation have involved the excitation of resonance states. Recently, Shotter et al [SHOT84] have applied Coulomb excitation theory to the case of the direct breakup of ^{7}Li into the α+t continuum. The motivation for this calculation came from the discovery of a direct breakup mode for ^{7}Li in the reactions ^{96}Zr,^{120}Sn,^{208}Pb(^{7}Li,α+t) (see §1.3.2 and SHOT81, SHOT84, SHOT88b). One of the interesting features of these reactions is that the breakup fragments have very low relative energies. Since small relative energies correspond to small values of E_x, it was thought that Coulomb excitation was a probable reaction mechanism. For the ^{96}Zr and ^{120}Sn targets, the experimental cross-section was well reproduced, at forward scattering angles, by the Coulomb excitation calculation. A remarkable fit to the shape of the fragment energy spectra was also achieved. The calculation under-predicted the direct breakup yield for the ^{208}Pb target. As noted earlier (§1.3), this is probably due to the presence of larger nuclear breakup component with this target. (Nuclear breakup is essentially a peripheral process, since partial waves inside the grazing impact parameter will be absorbed. Therefore, one would expect the nuclear breakup cross-section to go as $A_T^{1/3}$). For the forward angle data, the Coulomb calculation also reproduces the energy dependence of the direct breakup cross-section, over the energy range 50MeV$<E_{^7Li}<$70MeV [SHOT88b].

These results provide ample evidence that the mechanism of the direct breakup process for ^{7}Li in the forward direction is predominately Coulomb in origin.

1.4.3 DWBA Breakup Calculations

In the formalism of the Distorted Wave Born Approximation (DWBA), the influence of the nuclear and Coulomb fields of the target on the wave-functions of the projectile and breakup fragments, are explicitly included by the use of distorted elastic scattering wave-functions. These wave functions are obtained from the optical model potentials for the various target+fragment and fragment+fragment systems.

DWBA calculations can be divided into two types:

- Prior-form DWBA
- Post-form DWBA

The only difference between the two forms of DWBA is that in the prior-form, approximate wave-functions are used for the final channel, whereas in the post-form, approximate wave-functions are used for the initial channel. Clearly, the choice of formulation depends on the nature of the reaction being studied.

An example which is quite informative, and simple, is that of the sub-barrier Coulomb breakup of the deuteron [BAUR72]. This reaction is also an interesting test of the DWBA method, since the breakup fragments (i.e. the proton and the neutron) have no internal structure and the nuclear field of the target can be ignored to first order. For this reaction, a choice of post-form DWBA leads to a reduction in the computational task since the T-matrix element contains only the short range n-p potential. The initial channel wave-function is simplified by using the product of a deuteron elastic scattering wave-function with a deuteron ground state wave-function. With this approximation, the polarising effect of the Coulomb field on the deuteron has been neglected.

In the prior-form DWBA, the product of a neutron plane-wave and a proton elastic scattering wave-function is used for the final channel wave-function. With this approach, the n-p interaction is ignored, which may be a good approximation due to the short range nature of the p-n potential. The deuteron polarisation potential however, is fully included.

A considerable simplification to the post-form DWBA is achieved by use of the zero-range approximation. In the example discussed above, this is

equivalent to replacing a realistic n-p potential with a delta function. Such a procedure introduces serious errors for heavy ions. Even for the deuteron, finite range effects can be important. In Baur and Trautmann's [BAUR72, BAUR76] post-form DWBA treatment of the d→p+n reaction, a Hulthen form is used for the p-n potential. It was shown that if the n-target interaction in the final channel is included, the post-form DWBA well reproduces the experimental data. The break-down of the zero-range approximation is evident from the failure of a DWBA analysis to reproduce ^{6}Li induced breakup reactions [BAUR84].

To simplify the calculation of the DWBA T-matrix elements, a semi-classical method has been developed [BAUR74] which is applicable to heavy-ion breakup. This method has been successfully applied to the sub-barrier breakup of ^{9}Be [BAUR79]. The importance of recoil corrections, in the analysis of heavy-ion reactions, was demonstrated.

One of the advantages of the prior-form DWBA, is the explicit inclusion of the target+fragment potentials in the breakup T-matrix. The final state interactions between the fragments and the target are therefore properly accounted for. This is particularly important in the case of nuclear direct breakup reactions. Thompson and Nagarajan [THOM83] have applied the prior-form DWBA to the direct breakup of 70MeV ^{7}Li in the reaction ^{208}Pb(^{7}Li,α+t). It was found that this approach led to an over-prediction of the breakup yield by a factor of 30. To explain this over-prediction, it was suggested that the ^{7}Li projectile must to a large extent recover from the forces acting to break it up. Therefore, a large fraction of the calculated breakup yield actually corresponded to virtual breakup. It was concluded that a calculation with greater coupling between the breakup and elastic channels was necessary.

1.4.4 High Energy Adiabatic Model

The high energy adiabatic approximation was first suggested by Johnson and Soper [JOHN70]. In this model, the total wave-function of the system, $\Psi(\underline{R},\underline{r})$, is expressed as a product of a projectile internal wave-function, $\phi(\underline{r})$, and a projectile target wave-function, $\chi(\underline{R},\underline{r})$, i.e.

$$\Psi(\underline{R},\underline{r})=\phi(\underline{r})\chi(\underline{R},\underline{r}) \qquad (1.7)$$

Where $\underline{R}$ is the position vector of the centre of mass of the projectile relative to the target, and $\underline{r}$ is the relative vector of the clusters in the projectile. The choice of this form of the total wave-function results in the replacement of the intrinsic Hamiltonian of the projectile (in the decomposition of the total Hamiltonian) with a constant, equal to the binding energy of the projectile. For this to be a good approximation the excitation of the projectile must be very much less than its kinetic energy. Therefore, the high energy adiabatic approximation is applicable in situations where the beam energy is high and the projectile excitation is low. Such a situation is found in the case of the direct breakup of 70MeV ^{7}Li on ^{208}Pb, which prompted Thompson and Nagarajan [THOM83] to apply the high energy adiabatic approximation to this reaction. They found that the data could be well fitted if a pure nuclear calculation was performed. However, a Coulomb+nuclear analysis over-predicted the data by a factor of 3. The adiabatic approximation is equivalent to assuming that the nuclear volume of the projectile remains constant over the interaction. For the long range Coulomb polarizing force this is not true, and in part this explains the failure of the Nuclear+Coulomb calculation.

It has been noted that the double folding model fails to describe the real part of the optical model potentials for loosely bound projectiles, such as ^{6}Li and ^{9}Be [SATC78, SATC79]. The difference between the folded potentials and the experimentally derived potentials is thought to arise from the high breakup yields for these projectiles. In an attempt to account for the effect of the breakup channel in the elastic scattering of 156MeV ^{6}Li off ^{12}C, ^{40}Ca and ^{208}Pb targets, Thompson and Nagarajan [THOM81] have made use of the high energy adiabatic approximation, with an α+d cluster model for the ground and excited states of ^{6}Li. They found that the inclusion of the breakup channels resulted in a considerable improvement in the agreement between the data and the theory. A similar approach was adopted by Nagarajan et al [NAGA82] to explain the elastic scattering of 89MeV ^{7}Li off ^{40}Ca and ^{48}Ca targets. It was found that the data could not be explained if only the first and second excited states of ^{7}Li were coupled to the elastic channel. By including the direct breakup channel however, a good fit was achieved.

1.4.5 Coupled Channels Breakup Calculations

In the coupled channel method, the total wave-function of the system, Ψ, is written as a sum over the internal states of the projectile, ψ_i, the internal states of the target, ϕ_j, and states of relative motion of the projectile target system, $\chi(\underline{R})_{i,j}$ i.e.

$$\Psi=\sum\psi_i\phi_j\chi(\underline{R})_{i,j} \qquad (1.8)$$

To treat breakup properly, it is necessary to include bound-states, unbound resonance states and continuum breakup states (i.e. states resulting from direct breakup). The latter two types of states are dealt with by the Coupled Discretized Continuum Channels method (CDCC). In this approach, the continuum is divided into a series of 'bins'. Each 'bin' is then treated as an ordinary state. By the insertion of equation 1.8 into the Schrodinger equation, a set of coupled channels equations are derived. The potentials used in these equations are obtained by folding an effective nucleon-nucleon interaction over the internal wave-functions of the projectile and target. The problems involved in solving the coupled equations are considerable. Their solution requires a large amount of computing time on fast machines (e.g. CRAY super-computers). Some simplification of the equations is achieved, if the effect of target excitations is included in the imaginary part of the potentials.

CDCC calculations, of the nature described above, have been successfully used to explain the elastic scattering of a number of projectiles (e.g. ^{6}Li, ^{7}Li) where the breakup channel is strong [SAKU86]. The elastic breakup of ^{7}Li into the α+t channel has also been analysed by the CDCC approach. For sequential breakup via the 4.63MeV state of ^{7}Li, good fits to the experimental angular distributions have been achieved for ^{12}C and ^{120}Sn targets, by including only the nuclear potential. The direct breakup component of the ^{7}Li$\rightarrow\alpha$+t reaction is well reproduced for the ^{120}Sn target, again by using a pure nuclear potential. However, for the ^{12}C target, a significant ^{7}Li direct breakup yield is predicted by the CDCC calculation, whereas there is no experimental evidence of such a process. This disagreement between the data and theory is an outstanding problem.

When the Coulomb potentials are included in the calculations, and coupling to the direct breakup channel is omitted (for computational simplicity), it is

found that the shape of the angular distributions for the $^{120}Sn,^{208}Pb(^{7}Li,^{7}Li^{*}_{4.63}\rightarrow\alpha+t)$ sequential breakup reactions is very well reproduced. However, the magnitude is over-predicted by about factor a of $\sim$3. It is believed that this may be due to the omission of the direct breakup channel. Work is currently in progress to determine whether this is the case.

Calculations within the CDCC frame-work have achieved a high degree of success in explaining breakup phenomena. This success, at an early stage in the development of the technique, indicates that the CDCC method will be an important theoretical tool in the understanding of breakup reactions.

1.5 Motivation and Choice of Thesis Research

In the preceding sections, many breakup phenomena have been discussed. Of special interest though, is the recently discovered direct breakup mechanism for ^{7}Li [SHOT81].

This mechanism is intriguing for several reasons. First of all, it is highly unusual for a direct breakup process to produce a strong small-angle correlation; the bulk of direct reaction cross-sections are in wide angle breakup, partial fusion and inelastic processes. The extent to which a simple Coulomb calculation reproduces the shape and magnitude of the breakup data is also remarkable. It would be of interest to see if a Coulomb direct breakup process exists for nuclei other than ^{7}Li, and if so, whether a Coulomb excitation calculation can reproduce the features of the breakup of these nuclei.

There are only certain nuclei for which a direct Coulomb process is probable. To see this, it is constructive to consider the Coulomb interaction Hamiltonian, H_{int}. For disintegration into two clusters (Z_1,M_2) and (Z_2,M_2), the $E\lambda$ multipole term of H_{int} is proportional to,

$$H_{int}\sim r^{\lambda}\ Y_{\gamma\mu}\ (Z_1/M_1{}^{\lambda}+(-1)^{\lambda}Z_2/M_2{}^{\lambda}) \qquad (1.9)$$

Since the E1 multipole contains most of the excitation strength, it is natural to concentrate on nuclei with high E1 predicted yields. For λ=1, equation 1.9 reduces to,

$$H_{int}\sim rY_{1\mu}\ (Z_1/M_1-Z_2/M_2) \qquad (1.10)$$

It is interesting to note that the quantity $(Z_1/M_1-Z_2/M_2)$, which is sometimes referred to as the E1 effective charge, determines the differential acceleration of the clusters in the Coulomb field of the target. This observation leads to an intuitive picture for the direct breakup process, in which the projectile is dis-associated in the field of the target nucleus by the differential acceleration exerted on the clusters.

The two important factors which determine the size of the E1 yield are,

1. The magnitude of the quantity $(Z_1/M_1-Z_2/M_2)$
2. The Q-value for particle breakup. (A high Q-value means that a high excitation energy is required to breakup the projectile. As previously noted, the Coulomb excitation cross-section falls off with E_x).

The importance of the quantity $(Z_1/M_1-Z_2/M_2)$ is demonstrated by the existing close geometry breakup data. Such data have been obtained for several reactions, e.g. $^{6}Li \rightarrow \alpha+d$, $^{12}C \rightarrow ^{8}Be_{gs}+\alpha$, $^{16}O \rightarrow ^{12}C+\alpha$ and of course $^{7}Li \rightarrow \alpha+t$. The $^{7}Li \rightarrow \alpha+t$ reaction is the only one with a finite value of $Z_1/M_1-Z_2/M_2$, and is therefore the only one with a finite E1 interaction strength. Apart from $^{7}Li \rightarrow \alpha+t$, none of these reactions reveal a direct forward-angle breakup component.

Therefore, to maximise the E1 yield, one would choose a nucleus whose dominant clustering structure is highly asymmetric in Z/M and which is weakly bound against breakup into this cluster configuration. Obvious reactions to consider are the breakup of the neutron rich nuclei ^{9}Be, ^{13}C and ^{17}O into the neutron channel. In particular, the $^{9}Be \rightarrow ^{8}Be_{gs}+n$ reaction is of interest, since it has a Q-value of only 1.66MeV. In the table below, the $^{9}Be \rightarrow ^{8}Be_{gs}+n$ and $^{7}Li \rightarrow \alpha+t$ reactions are compared.

Reaction	Q-value(MeV)	$Z_1/M_1-Z_2/M_2$
$^{7}Li \rightarrow \alpha+t$	2.47	0.17
$^{9}Be \rightarrow ^{8}Be_{gs}+n$	1.66	0.5

It is seen that the $^{9}Be \rightarrow ^{8}Be_{gs}+n$ reaction has a higher E1 effective charge and a lower Q-value than the $^{7}Li \rightarrow \alpha+t$ reaction. So, on the basis of the simple arguments presented here, ^{9}Be should have a high Coulomb breakup yield. A study of the breakup reactions of ^{9}Be would therefore represent an excellent test of whether the ^{7}Li Coulomb breakup mechanism is specific to ^{7}Li or is a generally occurring mechanism. Due to the fact that $^{8}Be_{gs}$ decays into two

α-particles with a half-life of $\curvearrowleft 10^{-16}$s, the study of the breakup of ^{9}Be involves a triple coincidence α+α+n measurement. Therefore, such a study would also be experimentally challenging.

The choice of ^{9}Be as a projectile nucleus only fixes one element of the experiment. It is also important to consider beam energies, targets and the constraints imposed by the capabilities of particle accelerators.

To properly study breakup reactions, coincidence experiments are necessary, hence the use of DC beams is most appropriate. Furthermore, to make accurate measurements, beams of high energy resolution are needed. Therefore, Van de Graaff accelerators are ideally suited for research into breakup reactions, since they produce DC beams of high energy stability.

The choice of beam energy is influenced by its effect on the Coulomb excitation probability. As noted earlier, the predicted Coulomb excitation cross-section increases as the beam energy increases. The data on the ^{7}Li→α+t direct breakup reaction also shows an increase in cross-section with beam energy [SHOT88b]. For a ^{120}Sn target, the breakup yield at 70MeV is a factor of 10 larger than the yield at 50MeV. However, as the beam energy increases, the grazing angle, and therefore the angular region within which Coulomb effects can be expected to dominate, decreases. A ^{9}Be beam energy which is a sensible compromise, and is attainable with modern tandem Van de Graafs, is 90MeV.

Several factors influence the choice of targets. Firstly, it is interesting to investigate a wide range of target masses. Secondly, the use of targets for which ^{7}Li→α+t data already exists, simplifies the comparison between ^{9}Be induced reactions and ^{7}Li induced reactions. A final consideration is that, the use of target nuclei which have well separated ground and first excited states permits a clean selection of the reaction channel. Two targets which satisfy most of these requirements are ^{12}C and ^{120}Sn. The ^{120}Sn target is particularly interesting since, with this target, the Coulomb excitation calculation for the ^{7}Li→α+t reaction reproduced the data well. Unfortunately, the first excited state of ^{120}Sn is at 1.17MeV and the best possible total energy resolution in the ^{9}Be experiment is $\curvearrowleft$1MeV (see §2.2). Therefore, it will not be possible to completely reject breakup events which involve mutual excitation of this state. This however, is not anticipated to be a significant problem, since the 1.17MeV

state can only be excited by E2 Coulomb transitions or by nuclear processes. Hence, in the forward scattering region its excitation should be weak.

1.6 Thesis Objectives and Structure

The principal objectives of the work described in this thesis were:

1. To develop an efficient experimental method of studying the breakup reactions of 90MeV ^{9}Be.
2. To identify the breakup processes of ^{9}Be in the reactions 90MeV ^{9}Be+^{12}C and 90MeV ^{9}Be+^{120}Sn.
3. To determine whether the direct Coulomb breakup model is applicable to the breakup of ^{9}Be.

The bulk of this thesis concerns these objectives. In Chapter 2, the design of the experiment and the crucial effect of the reaction kinematics on the choice of design are discussed. Chapter 3 describes the Monte-Carlo simulation programs which were used in the design of the experiment and in the interpretation of the data. The kinematically complete ^{9}Be→α+α+n data is presented in Chapter 5 and in Chapter 6 a Coulomb excitation calculation for the ^{120}Sn(^{9}Be,^{8}Be$_{gs}$+n)^{120}Sn$_{gs}$ reaction is given.

During the course of the experimental work discussed here, anomalous peaks were observed in the α+α coincidence data. The data on these peaks is presented in Chapter 4. Several explanations for the anomalous peaks are also considered.

A summary of the conclusions reached in this work is given in Chapter 7. Possible directions for future research will also be discussed.

CHAPTER 2
EXPERIMENTAL EQUIPMENT AND TECHNIQUES

2.1 Kinematics and Event Selection

The principal objective of the experimental work described here was to determine the nature and importance of the breakup processes of ^{9}Be. In order to do this it was necessary to perform a kinematically complete coincidence experiment.

Before discussing the equipment that was used to do this experiment, it is useful to consider the reaction kinematics that are relevant to the breakup of ^{9}Be.

At a beam energy of 90MeV, the majority of the breakup reactions of ^{9}Be result in a four fragment final state ($\alpha+\alpha+n+$target). However, the reactions of most interest proceed in 2 or 3 distinct steps, e.g.

$^{120}Sn(^{9}Be,^{8}Be_{gs}+n)$, $^{8}Be_{gs}\rightarrow\alpha+\alpha$ (direct breakup)

and

$^{120}Sn(^{9}Be,^{9}Be^{*}\rightarrow^{8}Be_{gs}+n)$, $^{8}Be_{gs}\rightarrow\alpha+\alpha$ (sequential breakup)

Such reactions can be described by the application of 3-body kinematics, followed by the use of 2-body theory. In fact, for the case of the sequential breakup of an excited state of ^{9}Be into the ^{8}Be+n channel, the reaction process can be described by three consecutive 2-body reactions.

2.1.1 3-Body Kinematics

Following the notation of de Meijer [MEIJ85], a reaction with two particles in the initial channel and three in the final state, can be described by the equation, $a+A\rightarrow1+2+3$, where the letters 'a' and 'A' refer, respectively, to the projectile and the target and '1,2,3' are the labels of the final state fragments. In a reaction of this nature, there are ten unknown quantities. These are the nine momentum components of the three final state particles plus, the 3-body reaction Q-value, Q_3. Q_3 is defined by, $Q_3=Q_3^{g}-E_x^{tot}$ where Q_3^{g} is the 3-body ground-state to ground-state Q-value ($Q_3^{g}=m_a+m_A-m_1-m_2-m_3$) and E_x^{tot} is the

total excitation energy of the particles in the final state. Conservation of momentum and energy provides four equations, so it is necessary to measure six kinematic parameters for the experiment to be kinematically complete. For the reactions investigated here, it is simplest to detect the projectile-like fragments (i.e. α-particles and neutrons), since they are moving at approximately beam velocity and are forward focused. Therefore, the most convenient set of kinematic parameters to measure are $E_1,\theta_1,\phi_1,E_2,\theta_2,\phi_2$, where θ_1,θ_2 are the polar angles of fragments 1 and 2, relative to the beam direction, and ϕ_1,ϕ_2 are the azimuthal angles. For fixed detection angles, and for a given Q_3, the values of E_1 and E_2 are related via the following (non-relativistic) equation [MEIJ85],

$$\begin{aligned} Q_3+E_a(1-m_a/m_3)=(1/m_3)[&E_1(m_1+m_2) \\ &+ E_2(m_2+m_3)-2(m_a m_1 E_a E_1)^{1/2}\cos\theta_1 \\ &- 2(m_a m_2 E_a E_2)^{1/2}\cos\theta_2 \\ &+ 2(m_1 m_2 E_1 E_2)^{1/2}\cos\theta_{1-2}] \end{aligned} \qquad (2.1)$$

where:

$\cos\theta_{1-2}=\cos\theta_1\cos\theta_2+\sin\theta_1\sin\theta_2\cos(\phi_1-\phi_2)$

The angle θ_{1-2} is equal to the angle between the velocity vectors of particles 1 and 2. Equation 2.1 shows that the possible values of E_1,E_2 lie on a curve on the E_1/E_2 plane. For each value of Q_3, a different curve will be produced. For example, if particles 1 and 2 are emitted in their ground-states, then kinematic loci will be observed on the E_1/E_2 plane corresponding to the states of particle 3 which are excited. By placing 2-dimensional windows on these loci, it is possible to select the events associated with the excitation of particular states of particle number 3. Normally, this particle will be the recoiling target.

2.1.2 Identification of the Breakup Process

In determining whether a breakup event is sequential or direct, the important quantity is the relative-energy of particles 1 and 2, ε_{1-2}. The relative-energy is defined as the total kinetic energy of particles 1 and 2, measured relative to the centre of mass of the 1-2 system. From the velocity vector diagram of figure 2.1, it can easily be shown that ε_{1-2} satisfies the equation:

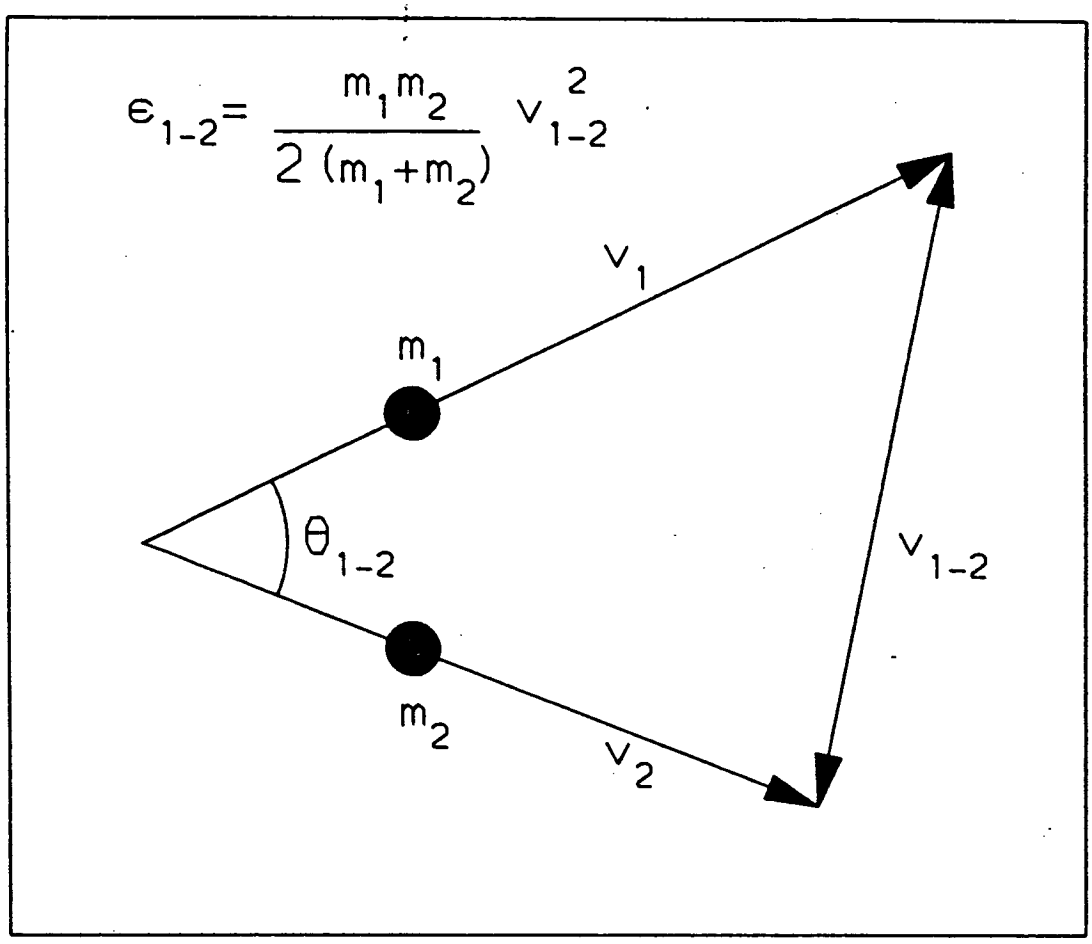

Figure 2.1: Velocity vector diagram showing the relationship between the laboratory energies of two particles (E_1,E_2) and their relative-energy, ϵ_{1-2}.

$$\varepsilon_{1-2}=[m_2E_1+m_1E_2-2(m_1m_2E_1E_2)^{1/2}\cos\theta_{1-2}]/(m_1+m_2) \qquad (2.2)$$

In sequential breakup reactions, particles 1 and 2 are produced by the decay of an intermediate nucleus. Therefore these reactions can be written as, $a+A\rightarrow 12^{*}+3$, $12^{*}\rightarrow 1+2$, where the symbol '12^{*}' has been used to represent the intermediate nucleus. The value of ε_{1-2}, for a sequential reaction, is given by $\varepsilon_{1-2}=E_x^{12}+Q_{12}^{g}$, where E_x^{12} is the excitation energy of 12^{*} and Q_{12}^{g} is the ground-state to ground-state Q-value for the reaction $12^{*}\rightarrow 1+2$. The intermediate nucleus may be the excited projectile, or it may be a particle-unstable ejectile produced by a transfer or pick-up reaction. From equations 2.1 and 2.2, it can be seen that there are two solutions for E_1 and E_2 for given values of ε_{1-2} and Q_3. Therefore, sequential breakup, from a discrete state, will produce events at two points on the E_1/E_2 plane.

In most of the reactions studied here, particles 1 and 2 are produced by the fragmentation of the projectile. For a direct breakup reaction, the value of ε_{1-2} depends on the energy given to particles 1 and 2 by the projectile-target interaction, and also on the final-state interactions between 1 and 2 and the target. All of these interactions can give a range of energies to the particles, so a broad ε_{1-2} distribution is produced. Because a given ε_{1-2} value corresponds to two points on the E_1/E_2 plane, direct reactions will enhance sections of the kinematic loci. In particular, events will be produced on parts of the loci which do not correspond to any state of the intermediate nucleus.

Experimentally, the presence of sequential and direct processes can be established by first identifying particles 1 and 2, and then creating a spectrum of E_1 versus E_2. The details of the processes can be obtained by examining such a spectrum.

In principle, it is possible to create an ε_{1-2} spectrum by using equation 2.2 and the measured values of E_1, E_2 and θ_{1-2}. However, the ε_{1-2} resolution depends on the energy resolution of the detectors, and on the range of θ_{1-2} values over which the detection system integrates. Because there is a conflict between optimizing the ε_{1-2} resolution and the detection efficiency - the former is improved by limiting the solid-angles of the detectors and the latter by increasing them - it is usually difficult to create an accurate ε_{1-2} spectrum. For the present work, in which detection efficiency is very important, it is most

convenient to work with the E_1/E_2 spectra. The effect of the energy and angular resolutions of the detectors on these spectra is easily taken into account, by using Monte-Carlo simulation techniques (see Chapter 3).

2.1.3 Kinematics of ^{9}Be Breakup

Most of the important features of the kinematics of ^{9}Be breakup are made clear by considering the reaction,

$$^{12}C(^9Be,^8Be_{gs}+n)^{12}C^*,\ ^8Be_{gs}\rightarrow\alpha+\alpha$$

In this reaction, each state of the residual $^{12}C^*$ nucleus corresponds to a definite value of Q_3. For the values of Q_3 corresponding to the 0.0, 4.44 and 7.65MeV states of $^{12}C^*$, the solutions to equation 2.1 are plotted in figure 2.2. In calculating these loci, detection angles of $\theta_{8Be}=\theta_n=16^\circ$ were used. These angles are characteristic of the close-geometry detection arrangement described in §2.8 . When the reaction proceeds sequentially, i.e. via the breakup of states of ^{9}Be, the kinematics are constrained by equation 2.2. The solutions of this equation, for ^{8}Be-n relative-energies of ε=0.024, 0.76 and 1.38MeV, are plotted on figure 2.2. These relative-energies correspond to breakup from the 1.69, 2.43 and 3.05MeV states of ^{9}Be.

At the points of inter-section of the Q_3 loci with the sequential breakup curves, one would expect to see events due to sequential reactions. In principle, direct breakup reactions can populate the full length of each Q_3 locus. However, due to the $\theta_{8Be}=\theta_n$ geometry, the detection efficiency decreases rapidly as the relative-energy increases (see §2.8). Therefore, most of the detected events, whether they are due to sequential or direct processes, will lie within the lines defined by ε=1.38MeV.

2.1.4 Identification of ^{8}Be Events from $\alpha+\alpha$ Data

Before the experimental version of figure 2.2 can be created, the $^8Be_{gs}+n$ events must be identified. Due to the fact that $^8Be_{gs}$ decays into two α-particles, the first step in doing this is to select $\alpha+\alpha+n$ triple coincidence events. The detection and identification of the α-particles and the neutron are dealt with in §2.6 and §2.7 respectively. Once an $\alpha+\alpha+n$ event has been identified, it is then necessary to determine whether the α-particles were produced by the breakup of $^8Be_{g.s}$ nuclei.

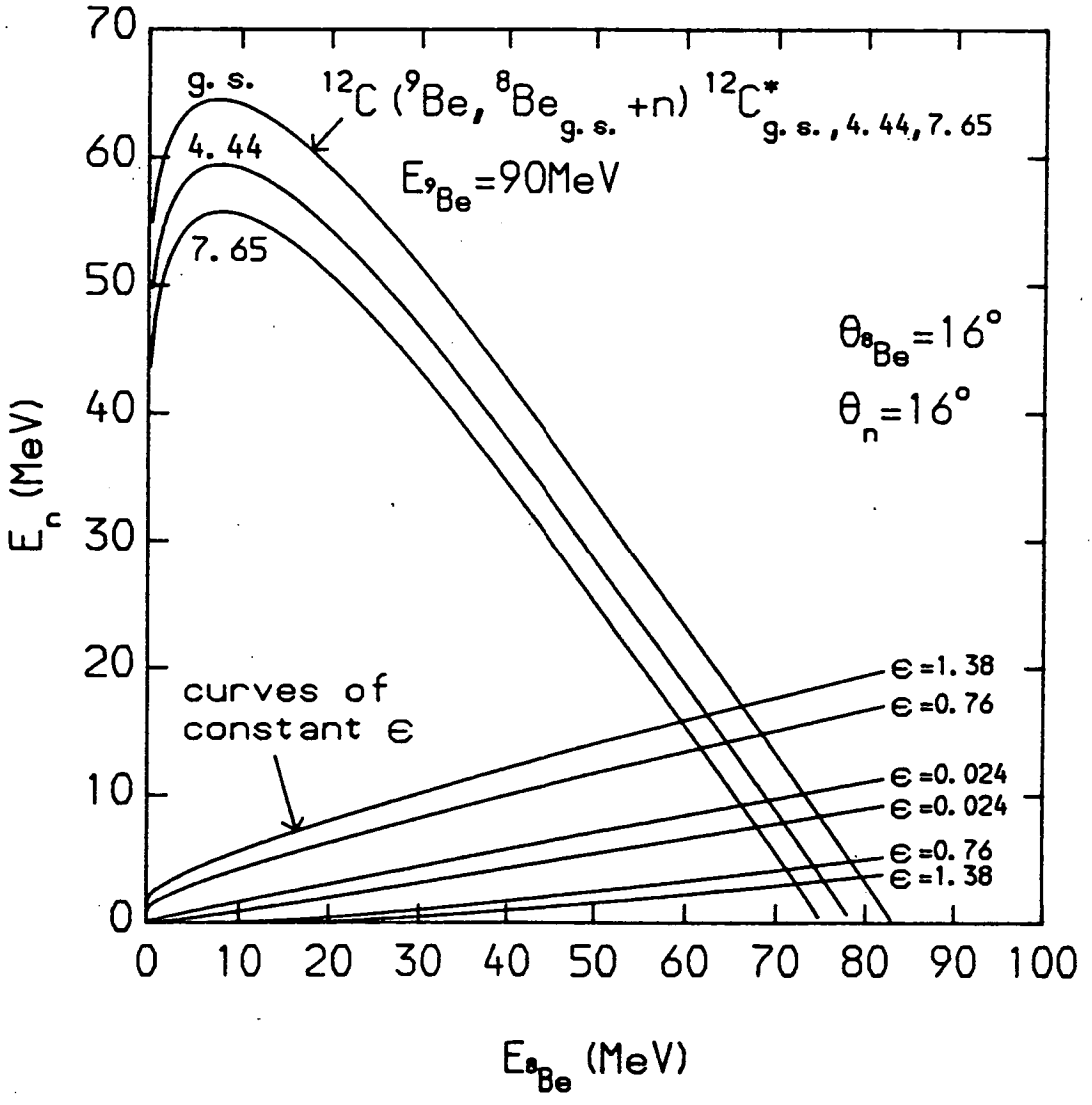

Figure 2.2: Kinematic loci for the reactions $^{12}C(^{9}Be,^{8}Be_{g.s.}+n)^{12}C^{*}_{g.s.,4.4,7.65}$ at $E_{^{9}Be}$=90MeV and relative-energy curves for ^{8}Be-n relative-energies of 0.024, 0.76 and 1.38MeV.

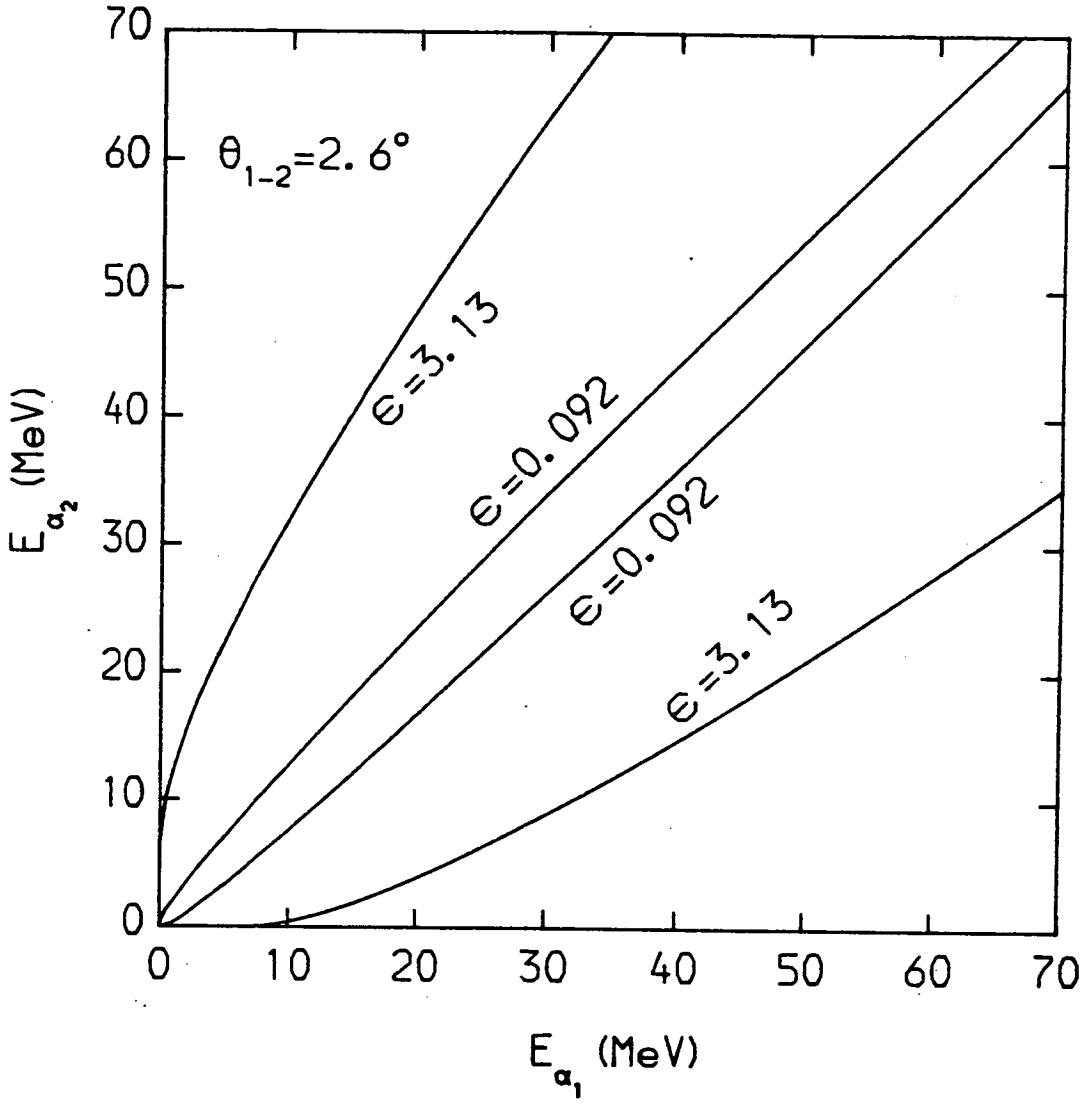

Figure 2.3: α_1–α_2 relative-energy curves for ϵ values of 0.092 and 3.13MeV. These values of ϵ correspond to break-up from the ground and first excited states of ^{8}Be.

Figure 2.3 shows the kinematic loci for the breakup of the ground and first excited states of ^{8}Be (E_x=0.0, 3.04MeV). These two states correspond to α_1-α_2 relative-energies of 0.092 and 3.13MeV respectively. The loci were calculated using equation 2.2. θ_{1-2} was set equal to the average separation angle of neighbouring sections of the ^{8}Be-telescope shown in figure 2.12. There is a clear separation between the loci produced by the decay of the ground-state of ^{8}Be and those produced by the decay of the first excited state. Hence it is possible to select $^{8}Be_{gs}$ events by placing a window on an $E_{\alpha 1}$ versus $E_{\alpha 2}$ spectrum. Events due to the decay of the first excited state of ^{8}Be can be selected just as easily.

2.2 Requirements of the Detection System

The detection system that was used in this work had to be capable of measuring the energies and angles of the breakup fragments of ^{9}Be. The precisions with which the energies and angles of the fragments had to be measured, were determined by the need to be able to identify the reaction channel and breakup process. The required experimental resolutions are discussed in this section.

One of the critical experimental quantities is the value of the summed energy of the ^{8}Be and the neutron. Its importance can be seen by considering figure 2.2; this shows the kinematic loci for the reaction:

$$^{12}C(^{9}Be,^{8}Be_{gs}+n)^{12}C^{*},\ ^{8}Be_{gs}\rightarrow\alpha+\alpha$$

Only small sections of the loci are of experimental interest. These are the low relative-energy portions (i.e. $\varepsilon<2.0$MeV), and they are well represented by straight lines of the form $E_{8Be}+E_n$=constant$-E^{ex}_{tar}$, where E^{ex}_{tar} is the excitation of the target nucleus. Therefore, for each state of the target that is excited in the breakup reactions, there will be a corresponding peak in the ^{8}Be+n summed energy spectrum. To resolve the target states, the ^{8}Be+n energy resolution must be less than the minimum separation between the states of interest.

The two nuclei selected as targets for the ^{9}Be experiment were ^{12}C and ^{120}Sn (see §1.5). Since the main experimental interest was in looking at elastic breakup (most of the cross-section was thought to be in this channel) it was important to try and resolve the ground-states of these nuclei from the first

excited states. The first excited state of ^{12}C is at 4.44MeV. For ^{120}Sn, the first excited state is at 1.17MeV.

The ^{8}Be+n energy resolution is determined by the intrinsic resolutions of the detectors and the kinematic broadening caused by the detector opening angles. Most of the kinematic broadening is associated with the ^{8}Be. It is therefore necessary to measure the scattering angle of the ^{8}Be quite accurately, to about 2°. This restricts the effect of kinematic broadening to about 1.5MeV for the ^{12}C target and to about 100keV for the ^{120}Sn target.

It is fairly simple to design a ^{8}Be detector with an intrinsic energy resolution of about 100keV, but it is difficult to measure the energy of the neutrons with anything like this resolution. A neutron energy resolution of about 1MeV, for 10MeV neutrons, is about the best than can be achieved without reducing the detection efficiency to an unacceptably low value. (This will be discussed more fully in §2.7).

It is therefore possible to achieve a ^{8}Be+n energy resolution, for a ^{12}C target, of about 2MeV. This is sufficient to resolve the ground-state from the first excited state. For the ^{120}Sn target, the best ^{8}Be+n energy resolution that can be managed is about 1MeV. With this resolution, it is not possible to completely separate the ground-state events from the first excited state events. It was thought however, that the probability of excitation of the first excited state of ^{120}Sn would be low for breakup events at forward scattering angles (see §1.5). It was decided therefore, not to compromise the experimental efficiency and to accept a ^{8}Be+n energy resolution of $\curvearrowright$1MeV.

In addition to being able to resolve the target state, it was also necessary to be able to determine the nature of the breakup process. As discussed in the last section, the breakup process can be identified from the E_n versus E_{8Be} spectrum. For any detection system, it is possible to calculate what the experimental E_n/E_{8Be} spectrum will look like, by using Monte-Carlo simulation techniques. In this manner, the effect of the sizes of the detector apertures on the E_n/E_{8Be} spectrum can be studied, and the identifying properties of the system investigated. It was found that, if sequential breakup of ^{9}Be is to be distinguished, then the angular separation between the ^{8}Be and the neutron must be measured to about 6°. It has already been established, that the in-plane angular resolution of the ^{8}Be-telescope must be $\curvearrowright$2°. Furthermore, it

will be shown in §2.7 that a neutron angular resolution of $\sim 4^{\circ}$ (for both in-plane and out-of-plane directions) is a natural consequence of the sizes of the commercially available photo-multiplier tubes. Therefore, it is possible to tolerate a ^{8}Be out-of-plane angular resolution of $\sim 6^{\circ}$.

The required dynamic ranges of the detectors were determined from the reaction kinematics. For low relative-energy breakup events ($\varepsilon < 2.0$MeV), the ^{8}Be kinetic energies are in the range 60-85MeV. The neutron energies are in the range 2-20MeV.

In fact, because there was some interest in studying the inclusive ^{8}Be yield, and since it was not difficult to do so, the ^{8}Be detector was designed to have a minimum dynamic range of 40-95MeV.

2.3 Summary of Experimental Method

The purpose of this section is to give a brief overall summary of the experimental methods. The details of the methods are discussed in the following sections.

The ^{9}Be breakup work was carried out on the 20MV tandem Van de Graaff accelerator of the Nuclear Structure Facility (NSF). This accelerator was used to provide a beam of 90MeV $^{9}Be^{4+}$ ions. The beam was focused onto targets, which were positioned at the centre of a conventional scattering-chamber. After passing through the chamber, the ^{9}Be beam was transported several meters to a well shielded Faraday-cup.

A ^{8}Be-telescope was mounted on a rotatable table, within the scattering chamber, and a group of 6 neutron detectors were arranged at a distance of 2m from the target. The ^{8}Be-telescope was constructed from a stack of silicon strip-detectors. Mass and charge identification of the charged-particles was performed by examining their energy loss in successive strip-detectors. The neutron detectors consisted of liquid scintillator cells, coupled to fast, focused photo-multiplier tubes. Pulse-shape discrimination techniques were used to distinguish between γ-ray and neutron induced events. The *time of flight* method was used to measure the neutron energies.

The energy and timing signals from the detectors were processed by a NIM based electronic circuit. This circuit contained an analogue section, which

generated signals that were subsequently fed into ADCs, and a logic section, which produced a trigger pulse for each event of interest. For every event that was accompanied by a valid trigger, the ADC conversions were read-out and written to tape.

The collection of the data was monitored on-line by means of a Data Collection Program (DCP). This program employed the event selection procedures, discussed in §2.1, to sort the event-by-event data into different event-types. For each event-type, energy, particle-identification and *time of flight* spectra were created and were studied on-line.

2.4 Accelerator and Beam-line

2.4.1 Accelerator

The data discussed here were collected at the Nuclear Structure Facility (NSF) of the Science and Engineering Research Council's Daresbury Laboratory. The NSF consists of an electro-static accelerator together with a variety of experimental stations, support laboratories and data acquisition systems. The accelerator is a tandem Van de Graaff high voltage generator, with an operating range of 9 to 20MV. Its structure is illustrated in figure 2.4.

Beam is injected into the accelerator as either molecules or atoms with a single negative charge. At the centre terminal, stripper foils are used to strip the beam particles of electrons; at this stage the molecular beams are also dis-associated. The fully accelerated beam is energy analysed by a 90° bending magnet at the base of the machine.

For the work described here, a 90MeV $^{9}Be^{4+}$ beam was produced by injecting $(^{9}Be^{1}H)^{1-}$ molecules into the accelerator. The Alton ion-source was used to produce the primary $(^{9}Be^{1}H)^{1-}$ molecular beam. To achieve a beam energy of 90MeV, the centre terminal was held accurately at a voltage of about 18.3MV. The stability of the terminal voltage is a few parts in 10^{4}, so an energy stability of better than 50keV was achieved for the 90MeV $^{9}Be^{4+}$ beam. The beam intensity was typically 1 electrical nA.

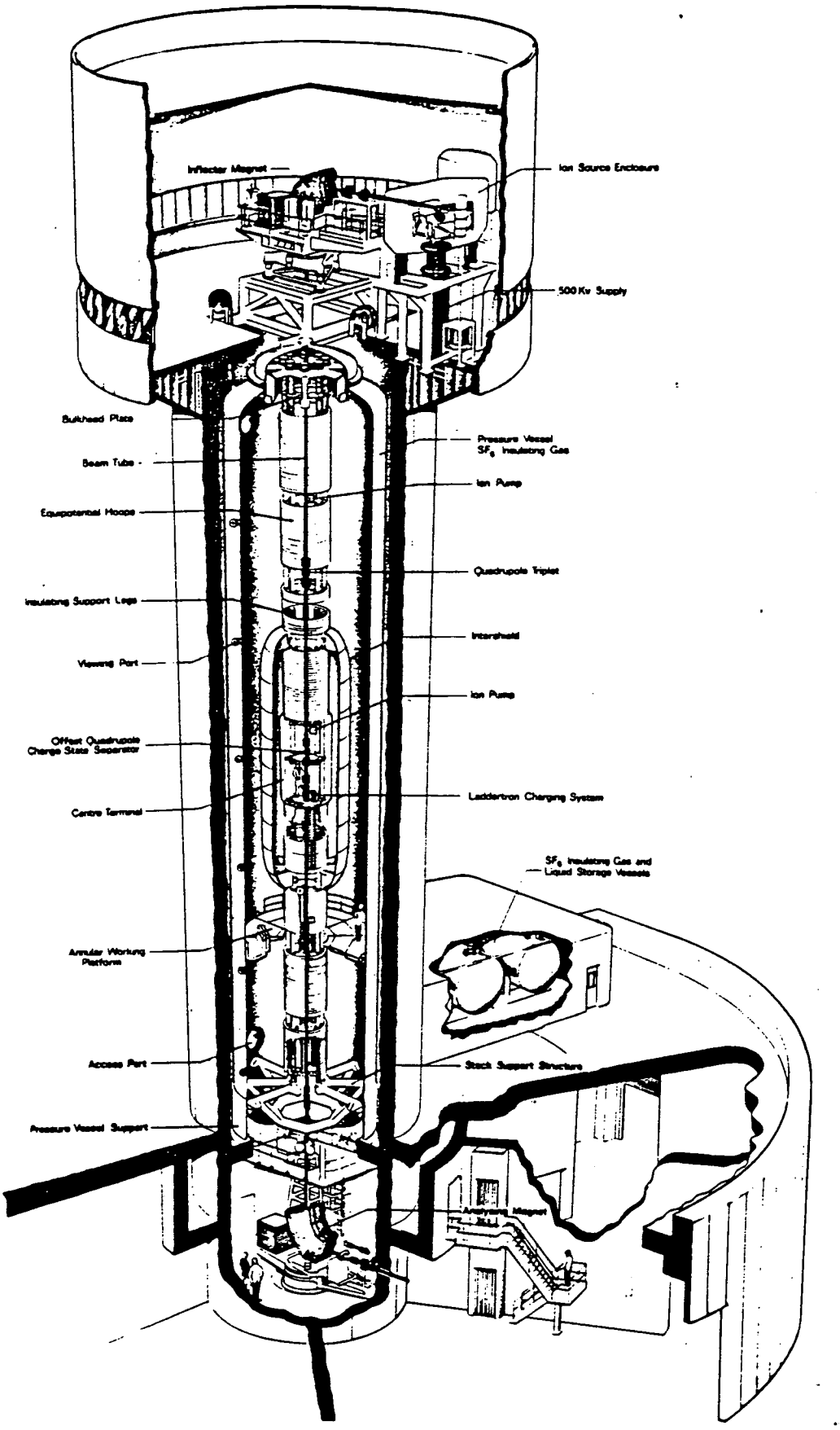

Figure 2.4: Cutaway diagram of the 20MV Tandem Van-de-Graaff accelerator of the NSF, Daresbury.

2.4.2 Beam-line

All of the experimental work was carried out on the 79° beam-line (see figure 2.5). On entrance to the experimental area, the ^{9}Be beam was passed through a 2mm by 2mm defining aperture. A set of quadrupole doublets was used to bring the beam to a focus at the centre of a 33cm diameter, cylindrical scattering-chamber. After passing through the chamber, the beam was re-focused, by means of another set of quadrupole doublets, and directed through the 1m chamber of the 79° beam-line, to a carefully shielded Faraday-cup.

Due to its thin (∿2mm) uniform walls, the 33cm scattering-chamber was ideally suited to the requirements of the ^{9}Be breakup experiment. It was specially installed on the 79° beam-line for the ^{9}Be experiment. By positioning it at 10m from the beam-dump it was hoped that the rate of background γ-ray and neutron events would be considerably reduced.

In general, the transmission and focusing of the beam was good. Approximately 80% of the beam passed through a 2mm ϕ aperture in the scattering chamber. With a target in the chamber, ∿ 90% of the beam, that was incident on the target, reached the Faraday cup.

Throughout the experimental runs, the beam-line and chamber were held at pressures which were better than 10^{-6}mbar, by means of a combination of ion, turbo and diffusion pumps.

2.5 Targets

All of the targets used in the ^{9}Be breakup runs consisted of thin, self-supporting films of either ^{12}C or ^{120}Sn. These films were 10x10mm^2 in area and were glued onto aluminium frames. The targets were manufactured by the Target Preparation Laboratory of the NSF.

The masses of the targets were determined by measuring the amount of energy that was deposited in them by 5.5MeV α-particles. It was estimated that this method gave the target masses to within 10%. For the ^{120}Sn target, a value of (0.69±0.07)mg/cm^2 was obtained, and for the ^{12}C target, a value of (0.42±0.04)mg/cm^2.

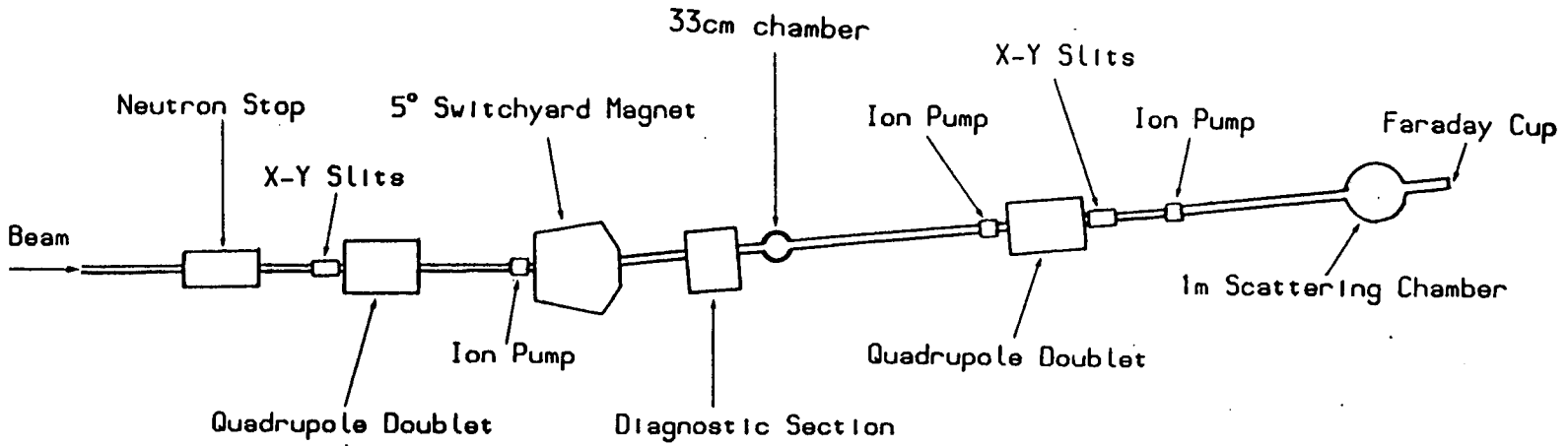

NOT TO SCALE

Figure 2.5: Plan diagram of 79° beamline.

For both targets, the sum of the energies lost by the 90MeV ^{9}Be beam and the breakup α-particles, in passing through the targets, was typically ∿190keV. The variation in the total energy loss was about 70keV, so the target thicknesses did not contribute significantly to the overall α+α+n energy resolution of ∿1MeV.

2.6 The ^{8}Be-telescope

2.6.1 Introduction

The properties that were required of the ^{8}Be-telescope were:

- high detection efficiency for the ground and first excited states of ^{8}Be, over a range of ^{8}Be kinetic energies (40-95MeV)
- angular resolution of ∿2° in the reaction plane
- angular resolution of ∿6° perpendicular to the reaction plane
- large solid-angle (several msr)
- mass resolution capable of separating ^{3}He, ^{4}He and ^{6}He
- ^{8}Be kinetic energy resolution of ∿200keV
- ability to distinguish between the ground and first excited states of ^{8}Be
- fast signal rise-times (<40ns)

The low-lying states of the ^{8}Be nucleus are short lived and decay by α-emission into the two α-particle channel. In particular, the ground-state of ^{8}Be has a half life of ∿10^{-16}s and a Q-value for α-decay of 0.092MeV. Hence, the first step in identifying ^{8}Be is to detect two coincident α-particles.

Of most importance in this work was the detection of high energy ^{8}Be ground-state nuclei ($E_{^{8}Be}$=70-90MeV). When such nuclei decay, the angular separation of the emitted α-particles is small, <4°. It is therefore difficult to detect both of the α-particles in separate counters. For example, if two conventional surface-barrier detectors are used, it is not possible to position the active areas of the detectors to closer than ∿6mm. (This is due to the construction of the detector cases and the way in which the silicon wafers are mounted in the cases). At a separation of 6mm, the detectors have to be positioned at a considerable distance from the target (∿150mm), which results in the detection system having a low solid-angle.

The performance of coincidence detection systems is normally measured in

terms of the 'effective solid-angle' of the system, denoted by Ω_{eff}. For a given type of ejectile, breaking up in a certain manner, the effective solid-angle is equal to the total solid-angle subtended by the counter system, multiplied by the efficiency of detecting all of the fragments of the ejectile. Clearly, the effective solid-angle depends on the masses of the particles involved, on the kinetic energy of the ejectile and on the excitation of the ejectile above its breakup threshold. In principle, it also depends on the angular distribution of the breakup fragments, relative to a co-ordinate system fixed in the ejectile. For most purposes however, this angular distribution is assumed to be isotropic, since little information on the distribution is known beforehand.

By working with Ω_{eff}, it is possible to think of a coincidence detection system as a single counter, of given solid-angle, which *detects* particle-unstable nuclei. This idea is particularly useful when it comes to estimating the experimental count-rate, or in evaluating the performance of different configurations of detectors. It is also useful in converting double differential cross-sections into single differential cross-sections.

A typical arrangement for ^{8}Be detection, which can be achieved using conventional detectors, is shown schematically in figure 2.6. In Figure 2.7, the variation of the effective solid-angle of this system with ^{8}Be kinetic energy and excitation is shown. (The Ω_{eff} curves of figure 2.7 were produced using Monte-Carlo techniques that are described in Chapter 3). The values of the effective solid-angle are very low, typically 0.2msr for $^{8}Be_{gs}$ and 0.035msr for $^{8}Be^{*}_{3.04}$.

The overall experimental efficiency of the ^{9}Be breakup experiment was severely reduced by the need to detect the breakup neutron. Hence it was necessary to use a ^{8}Be detector with a high effective solid-angle (several msr). The effective solid-angle of the conventional ^{8}Be-telescope, discussed above, was far too small to be of any use. It was therefore necessary to develop a new, more effective type of ^{8}Be detector.

Past workers have created some ingenious ^{8}Be identifiers. The simplest of these identifiers have relied on the fact that a ^{8}Be event, in which both of the ^{8}Be α-particles are detected in the same ΔE-E_{res} telescope, identifies as ^{7}Li when a particle-identification algorithm is applied to the ΔE and E_{res} signals. This approach is limited, of course, since genuine ^{7}Li events will corrupt the

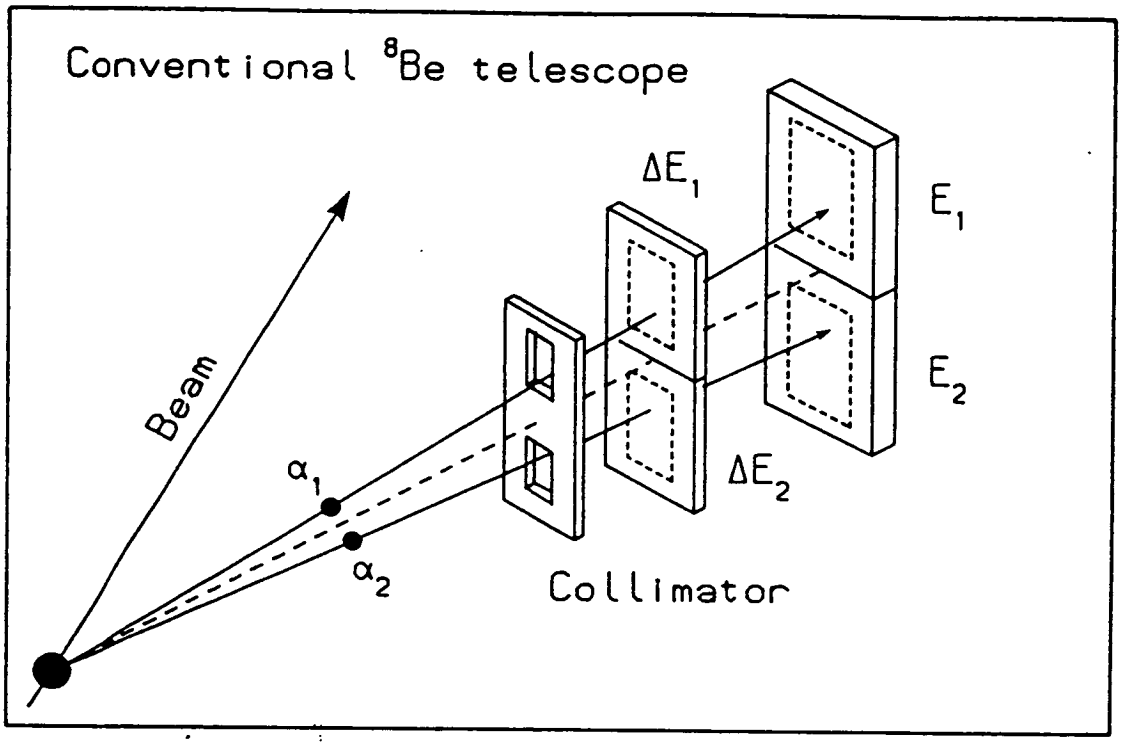

Figure 2.6: Schematic diagram of a conventional ^{8}Be detection system. The collimator apertures are 8mm wide by 10mm high and are separated by 6mm. The collimator is at a distance of 150mm from the target.

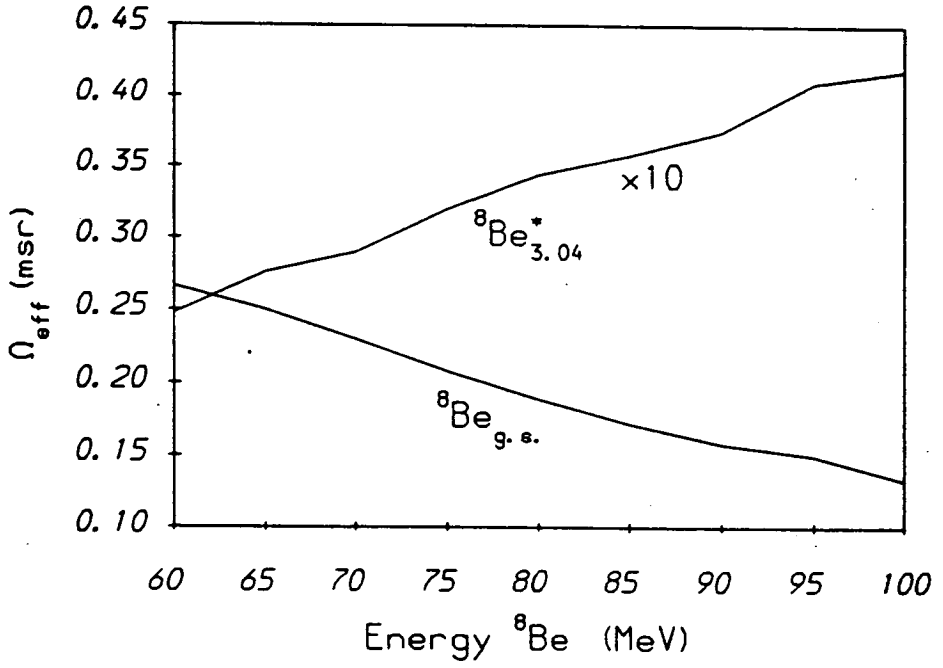

Figure 2.7: Variation of the effective solid-angle of the conventional ^{8}Be-telescope shown in figure 2.6 with ^{8}Be kinetic energy and excitation.

data, and since it is not possible to identify the different states of ^{8}Be. The advantage of this method is that the effective solid-angle can be made very high. A more sophisticated approach is to place a split collimator in front of a position-sensitive detector and to then put a window on events which give a position signal corresponding to the region blanked out by the post of the collimator. In practice, it is necessary to combine both of the above techniques in order to reject random coincidences and to achieve good ^{8}Be selection. This inevitably reduces the effective solid-angle of the identifier.

Of particular interest is the ^{8}Be detection system developed by Wozniak et al [WOZN74, WOZN76]. This consists of two ΔE detectors, diffused side by side onto a single silicon wafer, in front of one position-sensitive back detector. Due to the use of large area detectors (10x20mm^2) and because the ΔE's are separated by an undiffused region of only 1mm, this telescope has a high effective solid-angle ($\Omega_{eff}\sim$1.3msr at $E_{^{8}Be}$=60MeV). ^{8}Be events are selected by several means. Particle-identification is performed as previously described, using the sum of the ΔE signals and the E_{res} signal. In addition, the energies deposited in the ΔE's are compared to see if they are consistent with the passage of two α-particles of almost equal energy through the telescope. Finally, to separate out the states of ^{8}Be, the difference in the *time of flight* of the α-particles is measured. Because the back detector is position-sensitive, the direction of the ^{8}Be ejectile can be determined, and ^{8}Be angular distributions extracted.

Although this is an impressive ^{8}Be identifier, there are some problems with it. Firstly, sub-nanosecond timing is necessary in order to resolve the ground and first excited states of ^{8}Be; this is difficult to achieve in most experimental environments. Secondly, because position sensitive detectors are intrinsically slow devices, the maximum count-rate of the telescope will be limited to a few kcps. A more fundamental objection to the design is the fact that the scope of the detector is restricted because the fragments are not individually identified. In many cases it is of interest to study different particle+particle coincidences simultaneously. For example, in reactions induced by ^{7}Li projectiles, there is a large flux of α+t and α+α coincidence events. It is clearly desirable to collect data on both of these types of events simultaneously.

Nevertheless, the technique of placing two detectors on the one silicon wafer clearly indicates the way in which a high-efficiency ^{8}Be detector can be

constructed.

2.6.2 Strip-detectors

In recent years, new types of detectors have been designed to satisfy the demands of increasingly ambitious experimental programmes. In particular, particle physicists have had to meet the challenge of detecting and tracking the multitude of sub-atomic particles that are produced during high energy collisions. One of the ways that they have tackled this is by using a new generation of detectors, known as silicon strip-detectors (SSDs). These consist of large area silicon wafers (up to 50x50 mm^2) onto which charge-collecting strips have been positioned. Each of these strips acts as an individual detector. The most versatile and precise way of constructing the strips is to use ion-implantation techniques. The shape and number of strips is then determined by the mask that is used in the ion-implantation process. Since it is possible to construct very complex masks, SSDs can be specifically designed to meet the requirements of a particular experiment. It is fair to say that the only restriction on the shape, size and number of strips is the need to read-out and instrument all of the individual elements of the detector. The most expensive part of the manufacture of SSDs is the production of the mask - this can cost several thousand pounds. The typical unit price of the detectors, once the cost of the mask and other setup charges have been met, is a few hundred pounds.

Although SSDs have only recently become available, many different designs have already been used in a variety of experiments. For example, detectors with 1000 50μm wide strips are currently being used as vertex tracking devices in experiments at CERN. Counters with annular strips have also been constructed, as have detectors with position sensitive strips. It is even possible to manufacture pixel devices.

It is clear that, by using silicon strip-detectors, it should be possible to create highly efficient charged-particle detection systems. Strip-detectors certainly provide an ideal solution to the problem of ^8Be detection. This is due to the fact that the width of the inter-strip region can be made as low as a few μm, so fragments emerging with very small separation angles can be observed in coincidence. One restriction on this width is that for very small widths (<30μm) charge-sharing effects become important.

Initial calculations suggested that a strip-detector based ^{8}Be-telescope could have an effective solid-angle of as high as 10msr. This motivated the design of a strip-detector that would meet the requirements of the ^{9}Be breakup experiment.

There were some basic restrictions on the design of the strip-detector:

- the surface area of the silicon wafer had to be less than 50x50mm^2
- the wafer thickness had to be in the range, 200-600μm
- the strips had to be positioned in such a manner that connections could be made from them, via a printed circuit board (PCB), to the electronics

There were also many experimental considerations which influenced the choice of strip geometry and PCB design. These included:

- the effective solid-angle of the detector
- the energy resolution per strip
- the in-plane angular resolution
- the amount of inter-strip cross-talk and the probability of charge-sharing between adjacent strips (these two effects were important since they could cause spurious 'coincidence' events)
- the need to take the detector to forward scattering angles (this limited the size of the PCB)

The final design of the strip-detector had to represent a compromise between flexibility and performance. The flexibility was essential, since the high cost of the mask meant that the detector still had to be suitable even if experimental ideas changed.

After much consultation and discussion with the manufacturers (Micron Semi-Conducter), a final design for the strip-detector was reached. This design is shown in figure 2.8. A photograph of one of the finished detectors is shown in figure 2.9. Each detector consisted of a 24x24mm^2 silicon wafer, with ten parallel, rectangular strips. The strips were 2mm wide by 20mm long and were separated by 0.1mm. Although the number of strips was more than could be individually instrumented, this choice offered considerable freedom in the way in which the detector was used.

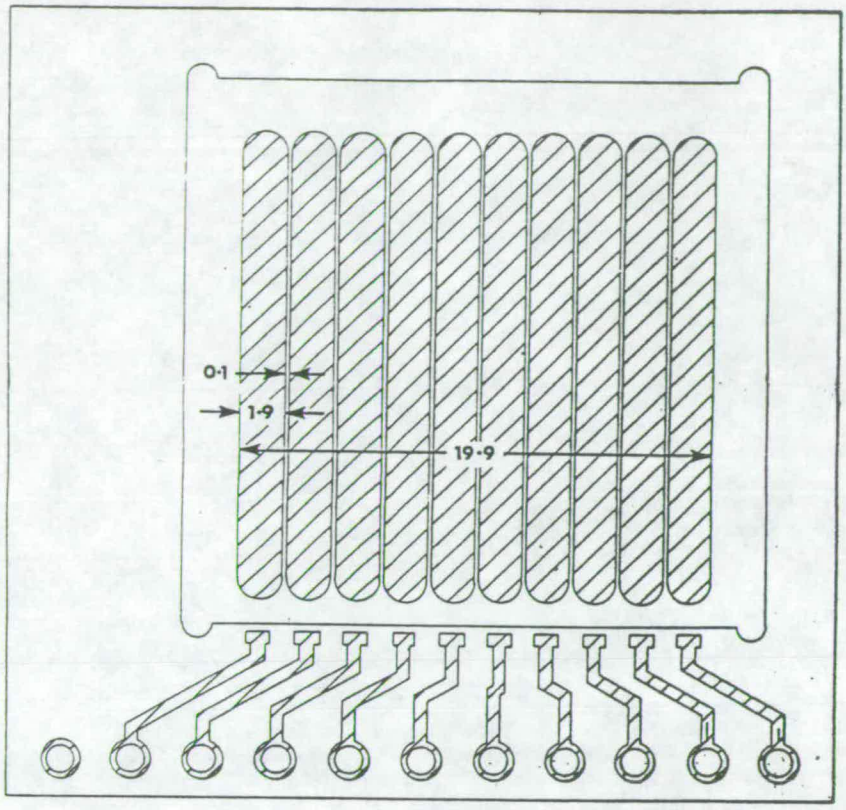

Figure 2.8: Schematic diagram of 10-channel strip-detector. Dimensions are in milli-meters.

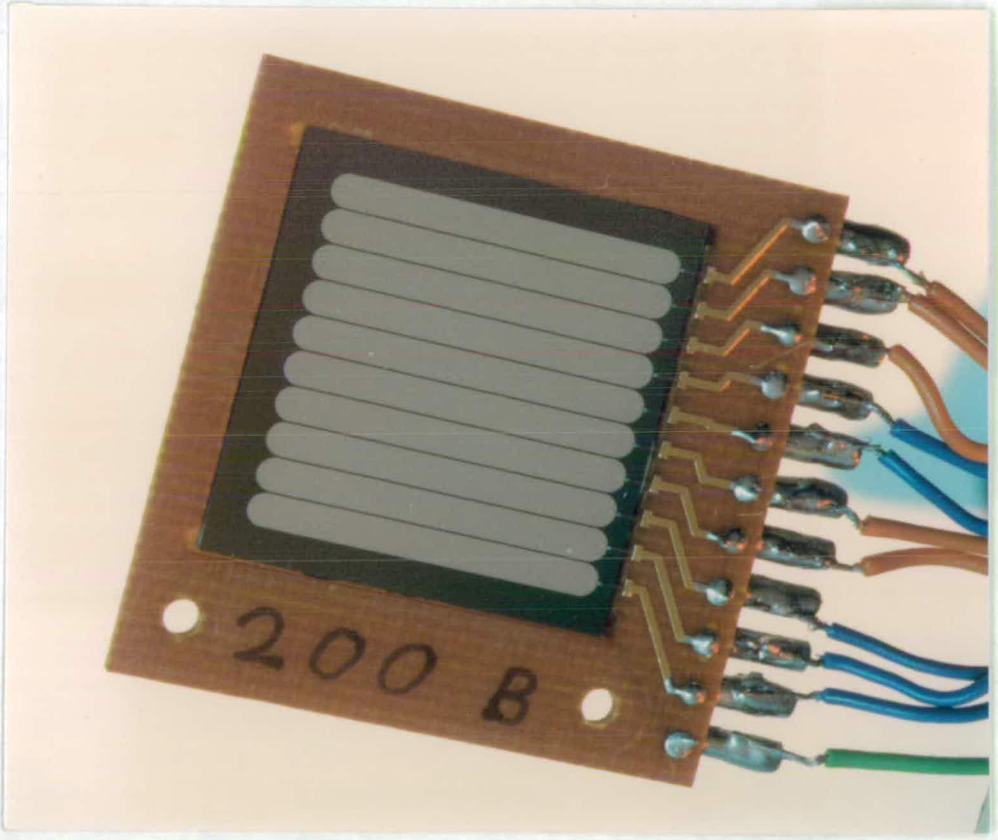

Figure 2.9: Photograph of 10-channel strip-detector.

2.6.3 Basic Properties of the Strip-detectors

Extensive tests were carried out on the strip-detectors to ensure that they would work reliably under beam conditions. These tests indicated that the counters had been very well constructed and that they more than met the design specifications. A summary of their properties is given below:

- energy resolution per strip ∿20keV (for 5.5MeV α-particles)
- average leakage current per strip ∿10-50nA
- full depletion voltages of 20V for 200μm detectors and 100V for 600μm detectors
- signal rise-time of ∿30ns (out of fast pre-amps)

2.6.4 Radiation Damage

The behaviour of the counters was carefully monitored during the experimental runs. Over the course of the runs there was no significant degradation of the energy resolution of the strip-detectors. The leakage currents however, steadily increased with time, from about 100nA per detector to ∿900nA. Because these leakages were so low to start with, the increases resulted in only small changes (∿1V) in the detector bias voltages. Interestingly, the leakage currents returned to their normal values shortly after the beam was switched off, even thought the bias remained on the counters. This indicated that the counters had suffered little radiation damage, despite having being been exposed to a dose of about 16×10^8 particles per cm^2. Significant deterioration is seen in surface-barrier detectors at about 10^8-10^9particles/cm^2 if they are exposed to 5.5MeV α-particles.

2.6.5 Charge-sharing

Previous work on strip-detectors [YORK87] has demonstrated the existence of two different processes that cause charge-sharing between neighbouring strips. Both processes only effect particles entering the inter-strip regions of the detectors. The first consists of the simple division of the deposited charge between two strips, resulting in two pulses of the same polarity. The second effect is more complicated and rather unusual. What is observed in this case is the production of two pulses of opposite polarity, where the sum of the magnitudes of the two signals is proportional to the amount of charge deposited close to the strip-detector surface (i.e. within a few tens of microns of the strips). The anomalous polarity pulses are most noticeable for

highly-ionzing particles, such ^{241}Am α-particles and ^{252}Cf fission fragments. They are not produced by non-penetrating particles incident on the rear of the detectors. These observations indicate that the effect is related to the surface structure of the inter-strip region. It is thought that the anomalous pulses result from the trapping of charge in the inter-strip region, and that the trapped charge induces a pulse of the opposite polarity on one of the strips.

Tests carried out on the strip-detectors designed for the ^{9}Be experiment showed virtually no evidence of positive+positive charge-sharing. For detectors with a inter-strip width of 25μm this process has been observed to be important [EDIN85]. The present detectors have an inter-strip width of 100μm. Since positive+positive charge-sharing events are caused by the expansion of the charge cloud it is reasonable that such events will become less likely for detectors with wider inter-strip regions.

The effect of opposite polarity charge-sharing can be clearly seen in the two-dimensional spectrum of figure 2.10. This spectrum was obtained using the strip-detector telescope which is described later in this section. The spectrum shows the energy deposited in the front detector versus the total energy deposited in the telescope, by ^{9}Be ejectiles produced via the reaction $^{9}Be+^{120}Sn$ at E_{9Be}=90MeV. As indicated on the diagram, the horizontal distribution was produced by events in which charge-sharing occurred in the middle detector. The diagonal line was produced by similar events, in which the charge-sharing occurred in the front detector (the ^{9}Be was stopped before it reached the back counter). The final feature in the figure is the vertical distribution; this was caused by straggling in the front strip-detector.

Charge-sharing events of this type were not a great problem, since they only occurred for about 3% of the particles entering the detector. Those that did occur were thrown out during the particle-identification stage of the analysis, therefore they did not corrupt the data. Furthermore, because these events were not associated with positve+positive pulses, they did not produce a high rate of false coincidence triggers. Finally, the effect of the charge-sharing processes on the detection efficiency was taken into account in the Monte-Carlo program that was used to calculate the efficiency of the detection system.

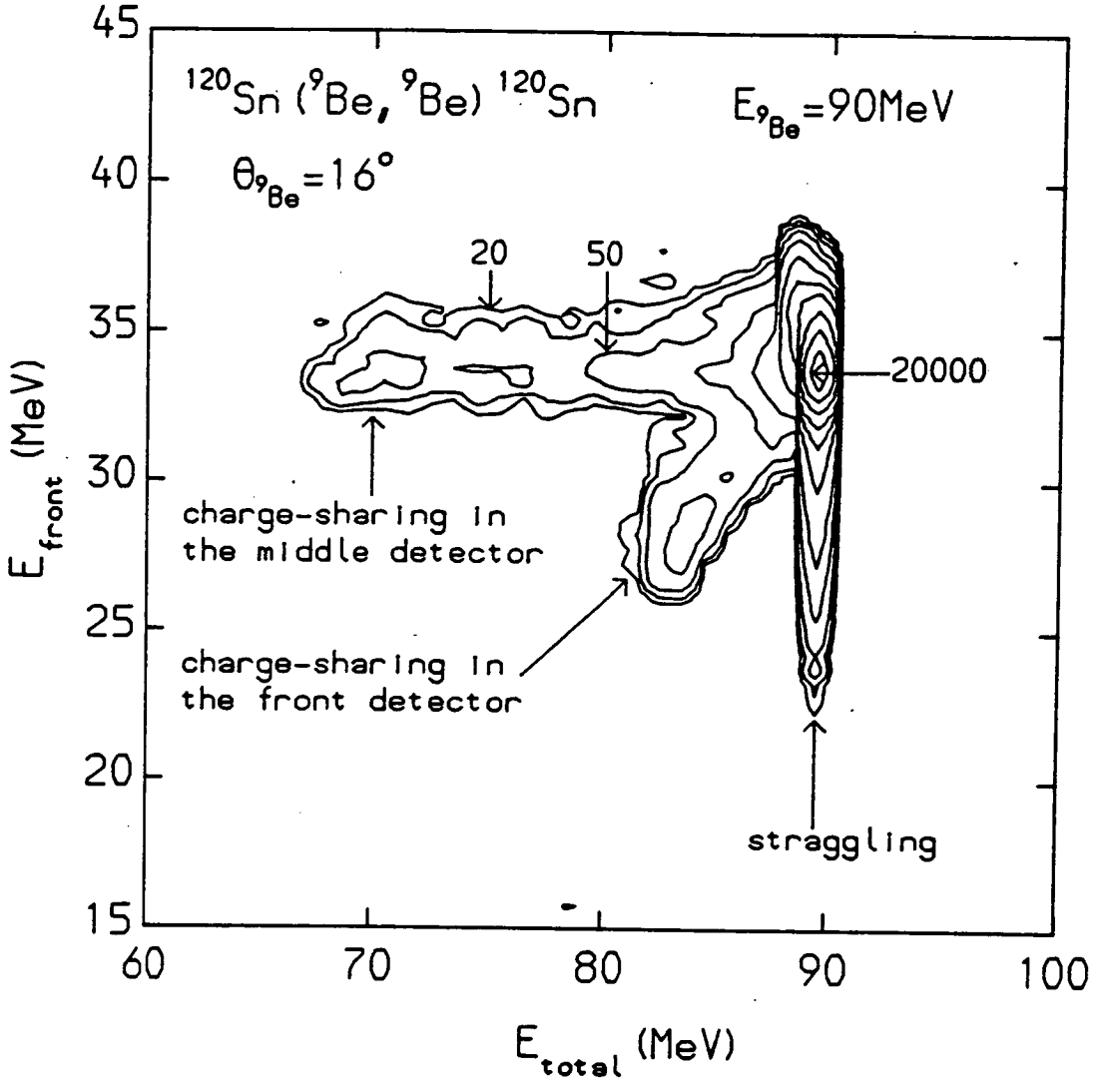

Figure 2.10: Spectrum of the energy deposited in the front strip-detector versus the total energy deposited in the strip-detector telescope by ^{9}Be nuclei produced via the reaction ^{120}Sn(^{9}Be,^{9}Be)^{120}Sn at $E_{^{9}Be}$=90MeV.

2.6.6 Strip Connections

In the ^{9}Be induced reactions of interest, the breakup α-particles had a maximum energy of about 50MeV. At this energy, their range in silicon was about ∿1.1mm. The strip-detectors could only be manufactured with thicknesses in the range 200-600μm, so it was necessary to stack three detectors one behind the other in order to gain a total thickness of greater than 1.1mm. Accordingly, the ^{8}Be-telescope contained 30 individual strips. At the time of the experiment, the data acquisition system of the NSF was limited to 36 ADCs. Since 12 ADCs were necessary for the neutron detector signals, it was clear that all of the strips could not be individually read-out. Therefore, a way had to be found of connecting up the strips which simplified the electronics, but did not significantly compromise the angular resolution or efficiency of the telescope.

It was desirable to position the ^{8}Be detector close to the target, so that it had a large solid-angle. However, it was also necessary to be able to measure breakup events at forward scattering angles (∿13°). With the most forward strips of the telescope positioned at 13°, the detector had to be placed at least 88mm from the target to ensure that the beam did not hit the PCB. At this distance, a 20x20mm^2 strip-detector with 4mm wide strips has a ^{8}Be angular resolution, in the direction perpendicular to the strips, of about 2°, and an effective solid-angle of about 14msr. Such a design of strip-detector, if used with its strips perpendicular to the reaction plane, satisfies the solid-angle and angular resolution requirements outlined at the start of this section. This suggested that a sensible way of simplifying the ^{8}Be-telescope would be to connect the 2mm wide strips of the 10-channel strip-detectors together in groups of two. In the final design of the telescope however, a collimator was included, which covered the first and last strips, hence it was decided to divide each detector into four sections. The first section consisted of 3 strips, the next two sections of 2 strips each, and the final section of 3 strips. This reduced the number of channels from 30 to 12.

All three strip-detectors were oriented with their strips perpendicular to the reaction plane. This configuration was chosen because it had the highest efficiency. The efficiency of a telescope with crossed strip-detectors is lower by about a factor of two. (This difference in efficiency is due to the probability of the two α-particles entering the same section of one of the middle or back

detectors).

Further simplifications to the telescope were made by connecting together alternate sections of the middle and back counters, i.e. sections 1 and 3 were connected together, as were sections 2 and 4. Connecting the sections in this manner resulted in only a small reduction in efficiency. This was due to the fact that most of the α-particles produced by the decay of the ground-state of ^{8}Be entered neighbouring sections of the strip-detectors. The angular resolution was not effected, because all four sections of the front detector were separately read-out.

To prevent events in which particles passed through the front detector, near the perimeter of its active area, but missed either the middle or back detectors, a 2mm thick tantalum collimator was positioned in front of the telescope. The aperture of the collimator was 14x14mm^{2}. The height of this aperture (14mm) was chosen to give an out-of-plane angular resolution of $\sim$6°. (N.B. the out-of-plane angular resolution for ^{8}Be detection is not equal to the out-of-plane angle subtended by the aperture. This is due to the rapid fall-off of the ^{8}Be detection efficiency at $\sim$2mm from the edge of the aperture). A veto counter was placed at the back of the telescope to enable the rejection of events in which particles were not fully stopped.

A schematic diagram of the ^{8}Be-telescope is shown in figure 2.11, and a photograph of the fully assembled detector is given in figure 2.12. For clarity, the diagram shows an *exploded* view of the telescope, which exaggerates the separation of the strip-detectors. The actual separation is 6mm. The four sections of the front strip-detector have been labelled F1A, F2A, F1B and F2B respectively. Sections 1 and 3 of the middle detector, which were connected together, have been labelled jointly as M1. M2 has been used to label sections 2 and 4 of the middle detector, which were also connected together. Similarly, B1 and B2 have been used to describe the sections of the the back counter.

The sections defined by M1 and B1 are positioned directly behind sections F1A and F1B. Taking divergence into account, approximately 93% of the particles that enter either section F1A or F1B have trajectories which pass through the sections of M1 and B1. Similarly, the sections of M2 and B2 are *covered* by sections F2A and F2B. So, the ^{8}Be-telescope can be thought of as consisting of two separate *telescopes* with divided front detectors, *viz*

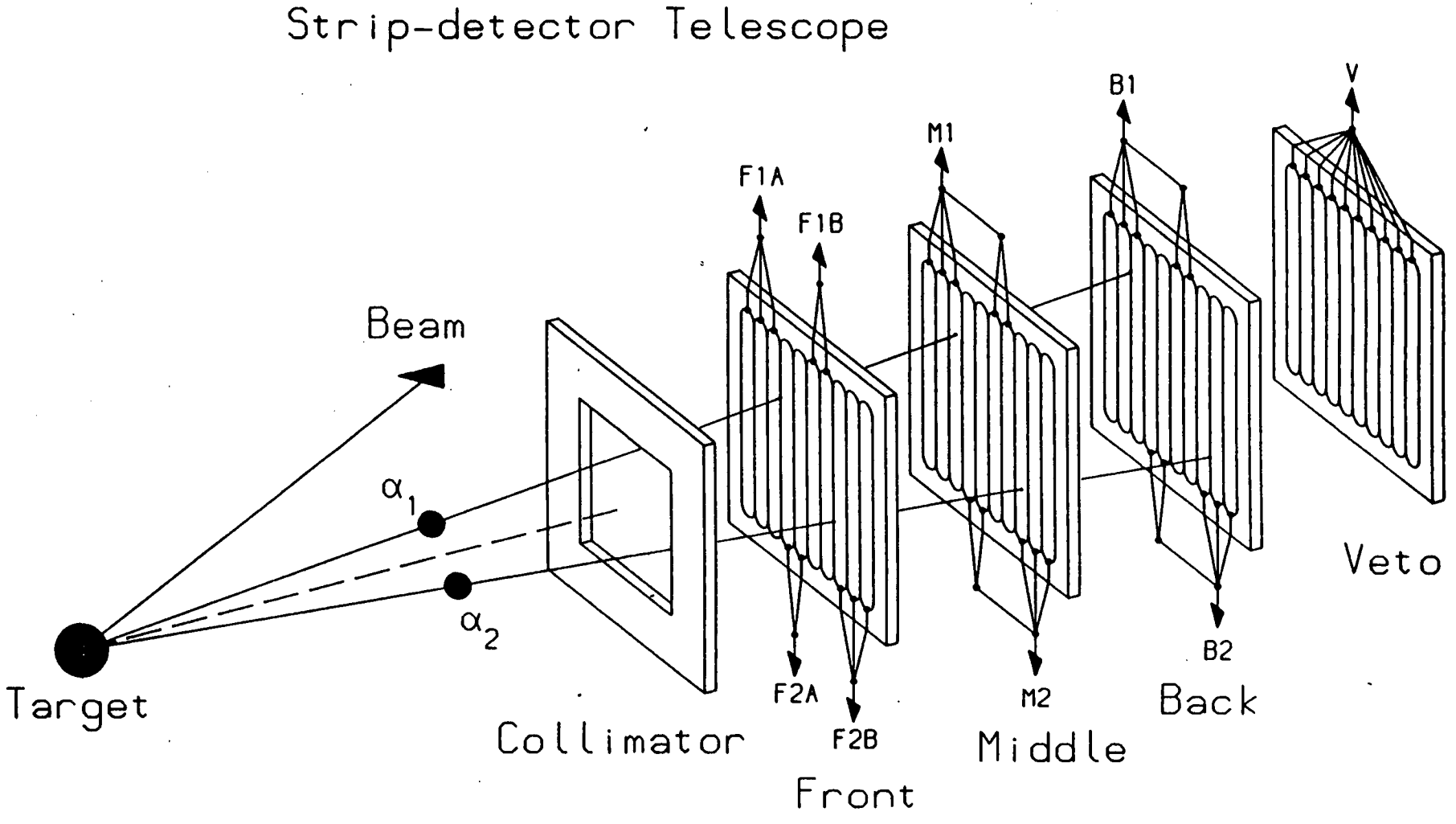

Figure 2.11: *Exploded* view of the strip-detector based ^{8}Be telescope.

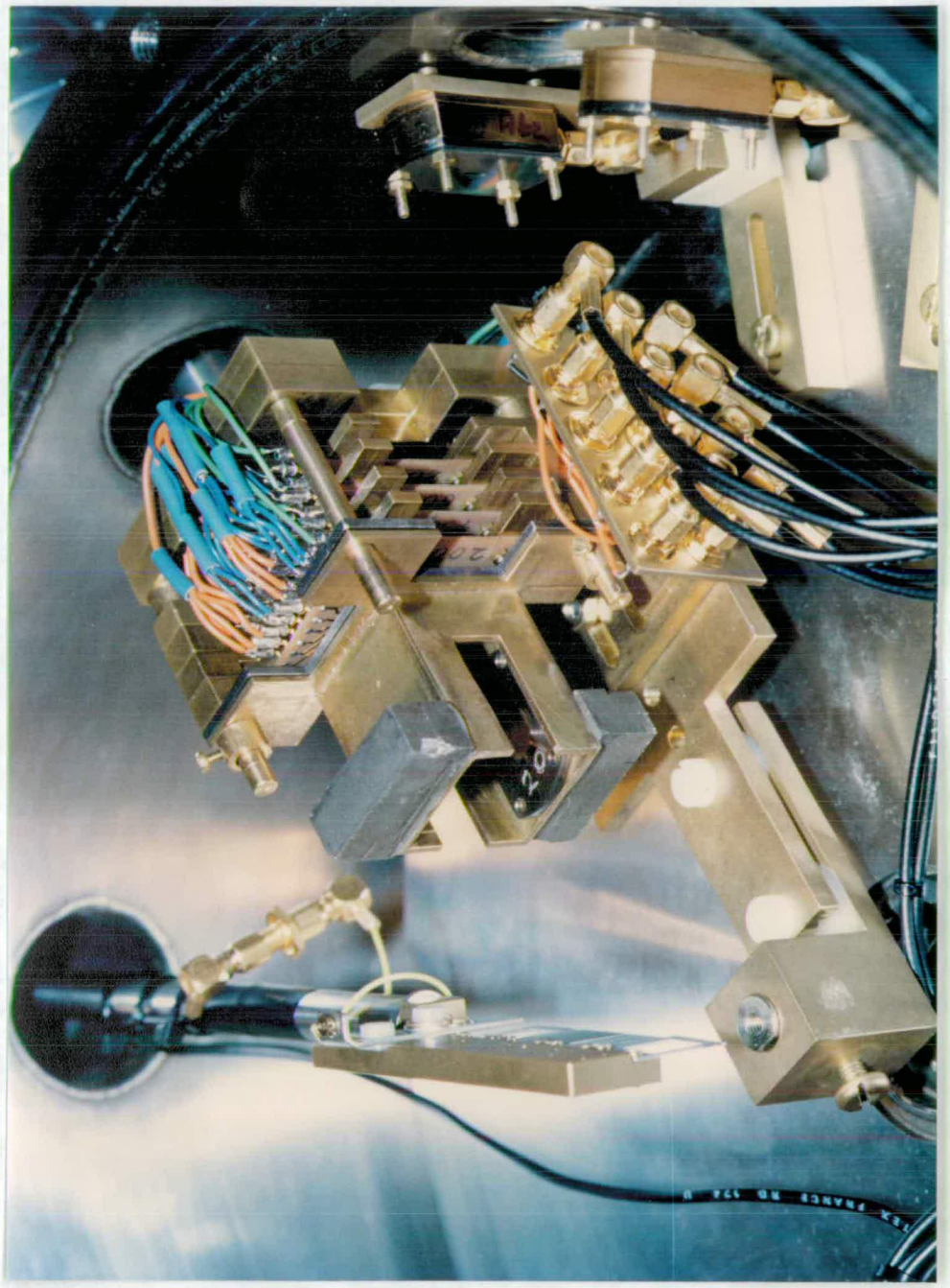

Figure 2.12: Photograph of the strip-detector based ^{8}Be-telescope mounted inside the scattering chamber.

- telescope 1: (F1A and F1B)+M1+B1
- telescope 2: (F2A and F2B)+M2+B2

Therefore, there are four possible types of singles event. Furthermore, there are four possible types of coincidence event i.e. F1A+F2A, F2A+F1B, F1B+F2B and F1A+F2B. (Events in which coincident particles enter sections F1A and F1B, or F2A and F2B, are thrown out during the sorting of the data, since in these events the particles enter connected sections of the middle and back counters and it is therefore impossible to identify the particles).

Events in which particles diverge from one *telescope* into the other are rare. In addition, the vast majority of them will be rejected during the particle-identification stage of the analysis.

One feature of the design which is not apparent from the photograph of figure 2.12 is the presence of ^{241}Am α-sources between the counters. Because of the need to stack the SSD's as close together as possible, these sources had to be very small (18x4x1mm^3). They were specially manufactured at the NSF's radiation laboratory. The α-sources provided an energy calibration point, at 5.5MeV, for each of the detectors. Magnetic suppression of electrons scattered from the target was achieved by positioning a *snout*, which had permanent magnets attached to it, in front of the telescope.

2.6.7 Effective Solid-angle

The effective solid-angle of the ^{8}Be-telescope, as a function of ^{8}Be kinetic energy and excitation, is shown in figure 2.13. This figure demonstrates that the detector has a very high effective solid-angle, typically 9msr for $^8Be_{gs}$ and ∿0.5msr for $^8Be^*_{3.04}$. This represents an improvement of a factor of 45 over what can be achieved with a conventional ^{8}Be-telescope, like the one shown in figure 2.6. When the new telescope is compared to the ^{8}Be identifier developed by Wozniak et al, it is found that its effective solid-angle is approximately 6 times larger.

2.6.8 Identification Properties of the ^{8}Be-telescope

In figure 2.3, the kinematic loci for the reactions $^8Be^*_{gs,\ 3.04}\rightarrow\alpha+\alpha$ are shown. These loci were calculated using the average separation angle of neighbouring sections of the strip-detector telescope. As can be seen, there is a clear separation between the ^{8}Be ground-state loci and the curves for the first

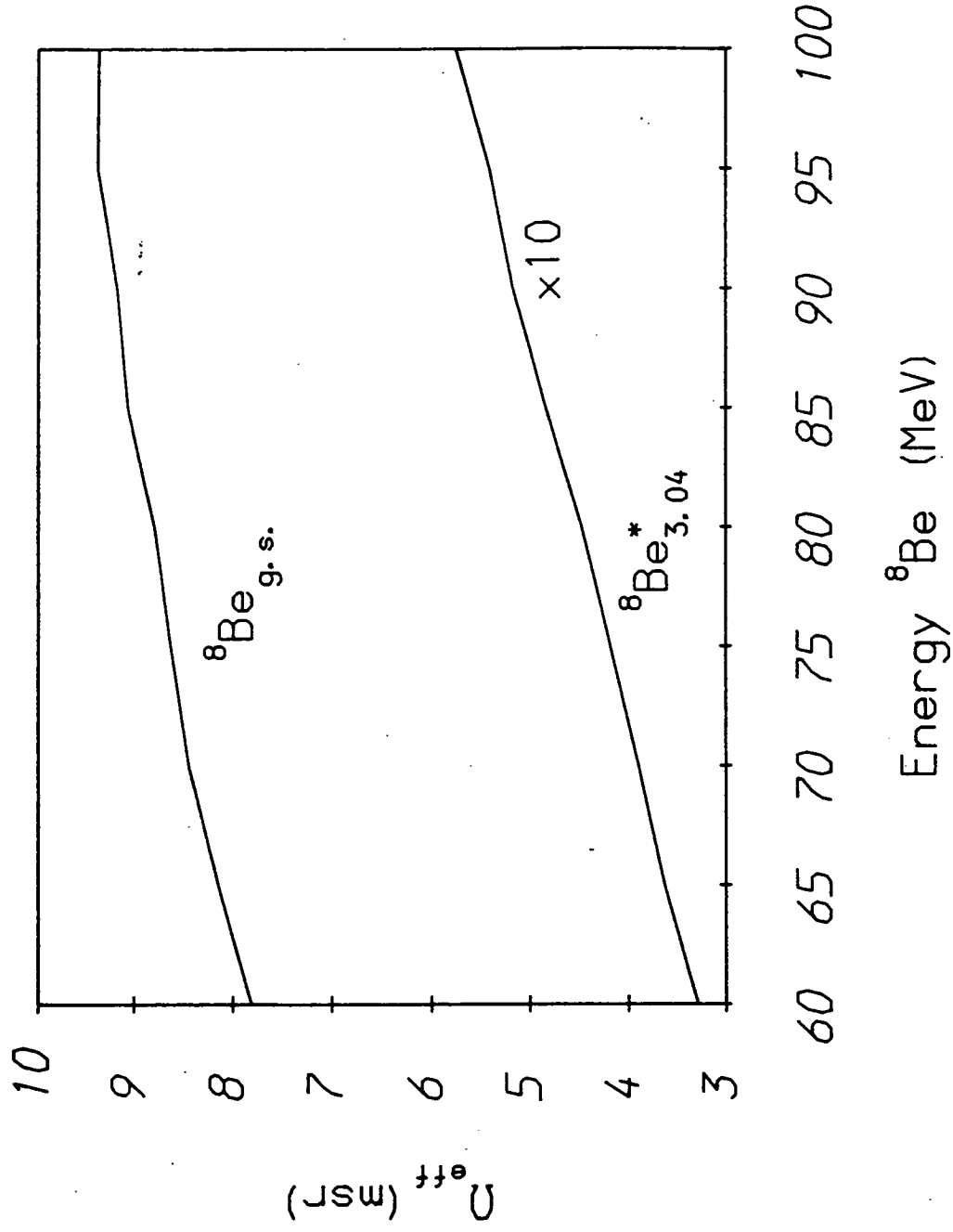

Figure 2.13: Variation of the effective solid-angle of the strip-detector based ^{8}Be-telescope with ^{8}Be kinetic energy and excitation.

excited state of ^{8}Be. In the experimental $E_{\alpha 1}/E_{\alpha 2}$ spectra, the kinematic loci are still well separated, even though they have been broadened by the finite size of the detector apertures and the width of the 3.04MeV state. Examples of the experimental $E_{\alpha 1}/E_{\alpha 2}$ spectra are shown in figures 4.1 and 4.2.

2.6.9 Angular Resolution

The angular resolution of the telescope depends on the variation of the $^{8}Be_{gs}$ detection efficiency across the surface of the strip-detectors. The dramatic nature of the efficiency variation can be seen in the Monte-Carlo spectrum of figure 2.14. This shows the number of $^{8}Be_{gs}$ nuclei which are successfully identified (per unit area of the front detector) as a function of the point of inter-section of the ^{8}Be velocity vector with the plane of the detector. If this two-dimensional spectrum is *squashed* along the direction of the strips, then the spectrum of figure 2.15 is produced. There are three peaks in this spectrum. The positions of the peak centres correspond to the edges of sections of the strip-detectors. The positions of the two troughs in the spectrum correspond to the midpoints of sections of the strip-detectors. This behaviour reflects the fact that the α-particles, produced by the decay of a ^{8}Be nucleus which was originally travelling towards the centre of a section, must enter the same section, or connected sections, of the strip-detectors. The three peaks have been labelled 'F1A+F2A', 'F2A+F1B' and 'F1B+F2B', to indicate that each peak corresponds to coincidences between two particular sections of the strip-detectors e.g. the peak labelled 'F1A+F2A' corresponds to coincidences between sections F1A and F2A. Since the four sections of the front detector are individually read out, it is possible to determine which of the three peaks a particular event belongs to. Therefore, the position resolution of the ^{8}Be-telescope is just the FWHM of the peaks in figure 2.15. The width of the peaks is $\curvearrowright$2.2mm and the front detector is at 88mm, so the in-plane angular resolution of the telescope is $\curvearrowright 1.4^{\circ}$.

2.6.10 Mass Resolution and Dynamic Range

The wafer thicknesses of the front, middle and back detectors were respectively 230, 450 and 600μm. The total thickness of the telescope was therefore 1.28mm, so it was possible to stop α-particles with energies of up to 55MeV. α-particles with energies lower than 20MeV did not penetrate the front detector. Therefore the dynamic range for ^{8}Be detection was

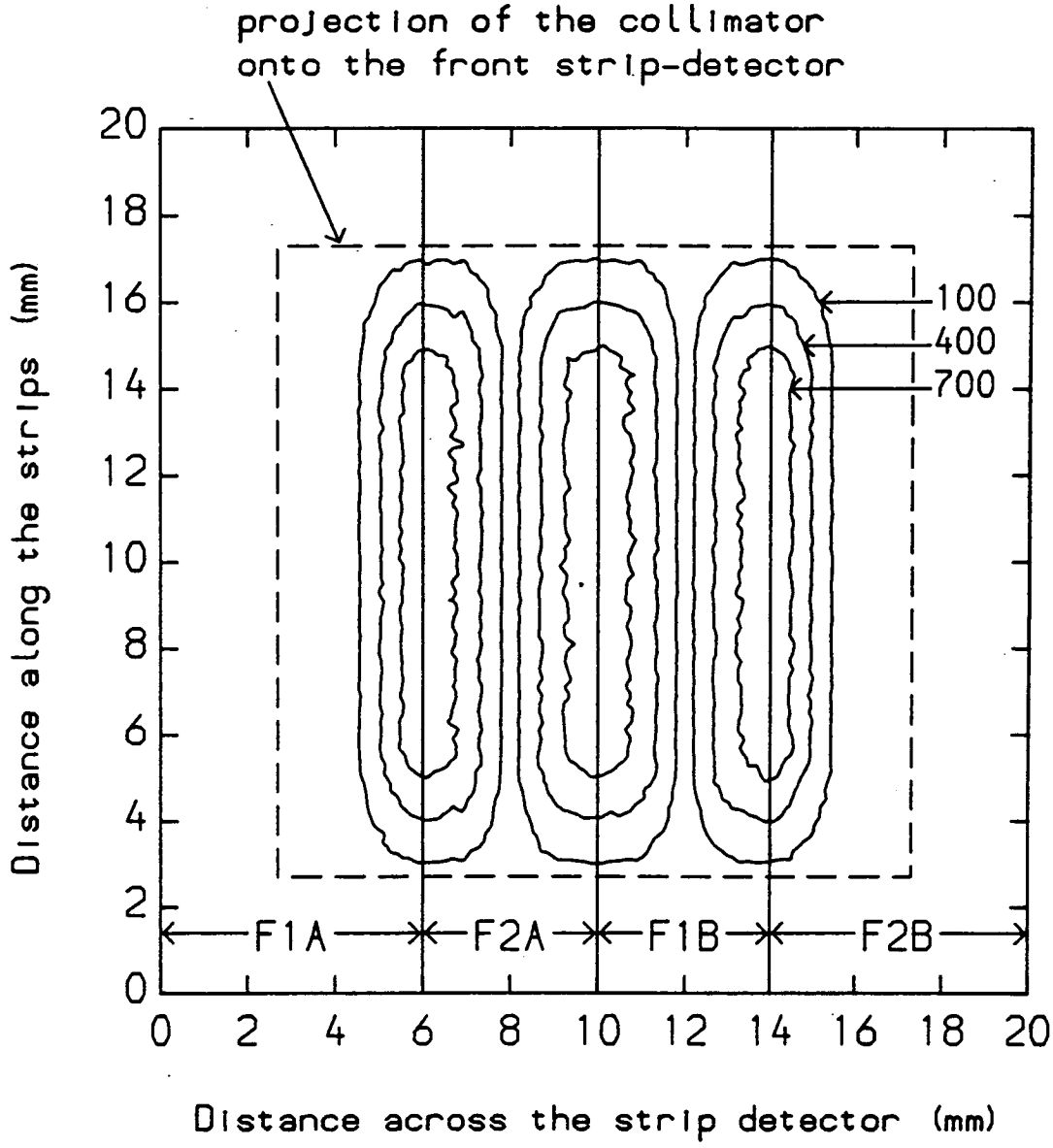

Figure 2.14: Efficiency of the strip-detector based ^{8}Be-telescope as a function of the position of the point of inter-section of the ^{8}Be velocity vector with the surface of the front strip-detector. The contours represent the number of 80MeV $^{8}Be_{g.s.}$ nuclei detected per unit area (the absolute values are arbitrary).

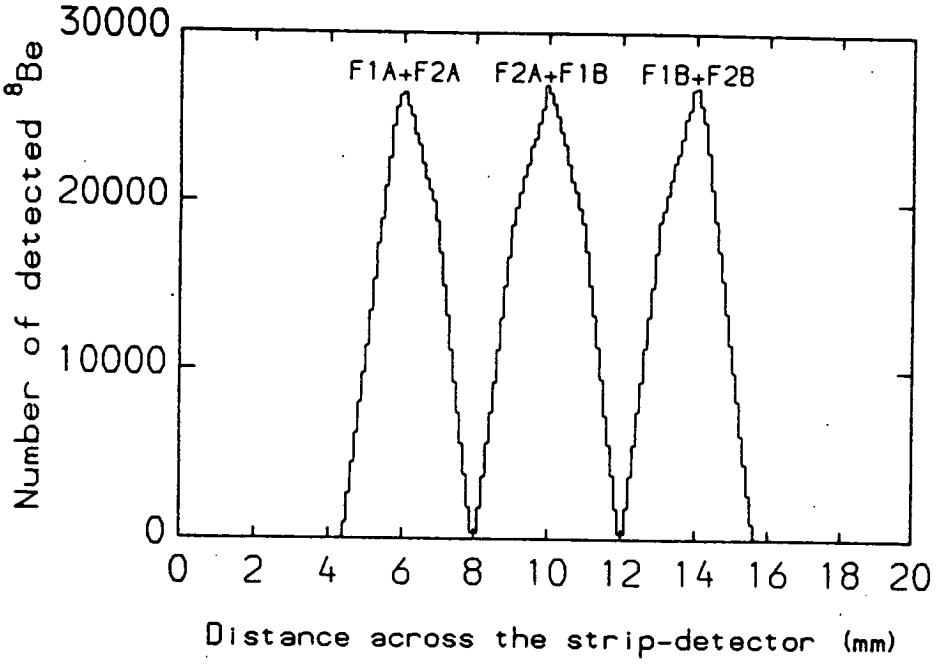

Figure 2.15: Efficiency of the strip-detector based ^{8}Be-telescope as a function of the distance across the the front strip-detector (in arbitrary units).

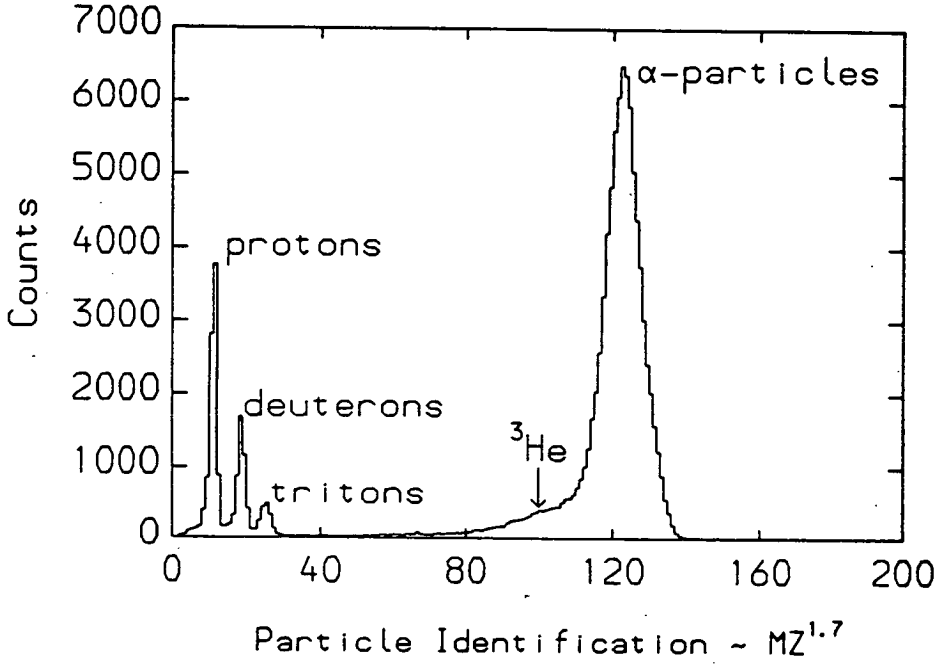

Figure 2.16: Typical particle-identification spectrum obtained with the strip-detector based ^{8}Be-telescope.

$40MeV < E_{8Be} < 110MeV$.

The thickness and uniformity of the front detector determines the particle-identification properties of a telescope. Ideally, a thinner front counter would have been used for the ^{8}Be-telescope, but with the detectors available, a good mass resolution was achieved. A typical particle-identification spectrum is shown in figure 2.16. The mass-resolution of this spectrum is more than adequate to define the events due to the α-particles. Fold-back has been minimized by the use of the veto counter at the back of the telescope.

2.6.11 Summary

A novel ^{8}Be-telescope, constructed from silicon strip-detectors, has been developed. This telescope has a high efficiency and excellent identifying properties. It is particularly suited to the needs of the ^{9}Be breakup experiment.

The detection of ^{8}Be provides a good example of one of the possible uses of strip-detectors in nuclear physics. There is no reason why the telescope described above could not be further developed by the addition of thicker stopping counters (e.g. SiLi's, CsI-crystals+photo-diodes, etc) to permit the measurement of z=1 particle+particle coincidences. For reactions involving higher energies (>10MeV/A), where the forward focusing of the fragments is greater, strip-detectors will also have an important role to play since they are capable of detecting fragments produced with small separation angles.

2.7 Neutron Detectors

The basic properties that were required of the neutron detectors used in the ^{9}Be breakup experiment were:

- energy resolution of better than 1MeV, for 10MeV neutrons
- high count rate capacity (greater than 1kcps)
- good discrimination against background γ-rays
- angular resolution of $\curvearrowright 4^{\circ}$
- reasonable efficiency, >10%

To achieve the $\curvearrowright$1MeV energy resolution, it was decided to measure the neutron energy via the *time of flight* technique (TOF). The *start* signal for the *time of flight* measurement was taken from the ^{8}Be-telescope. Scintillation cells were used to detect the neutron and to provide the *stop* pulse. The

energy resolution obtained with the TOF method depends on the intrinsic timing resolution of the electronics and on the *time of flight* of the neutron across the scintillation cell. There are many contributions to the intrinsic timing resolution. These include:

- response time of scintillator
- spread in the transit-time of the pulses in the dynode chain
- noise of anode signal
- pulse-height dependence of timing circuitry

Typically, if fast, focused linear tubes are combined with *constant fraction discrimination* (CFD) units, it is possible to achieve a timing resolution of ≈1ns. With such a timing-resolution, it is necessary to place the scintillation cells at about 2m from the target to gain an energy resolution of 0.5MeV for 10MeV neutrons. The depth of the cells can then be chosen, such that it does not substantially effect the energy resolution. For cells at 2m from the target, a reasonable depth is about 5cm. The total neutron energy resolution is then about 0.7MeV.

If the use of light-guides is to be avoided, then the diameter of the scintillator cell is limited by the size of the photo-multiplier tube. Since the effective diameter of the cathode of the largest available tube is about 125mm, cells with an inner diameter of 124mm were used. This diameter corresponds to an angular resolution of about 3.5° at 2m.

2.7.1 NE213 Liquid Scintillator

A scintillator suitable for neutron detection must have a high proton density, since the detection process depends on n+p scattering, and a fast response time. A large range of plastic scintillators meet these requirements. Unfortunately, these scintillators are also highly sensitive to γ-radiation, via Compton scattering. It is very difficult to predict what the intensity of the γ-ray flux will be during an experiment. Therefore, it is hard to estimate how large a problem γ-ray induced events will be. Prompt γ-ray events can be rejected by their *time of flight* and random events can be reduced by using lead shielding. However, by using shielding alone, it is not possible to completely exclude random γ-ray events from the *time of flight* spectra. Therefore, to permit the rejection of γ-ray induced events, it was decided to use NE213 liquid-scintillator. This scintillator has excellent particle-identification properties.

The ability to distinguish between different charged-particles, when using a scintillator such as NE213, results from the differences between the shapes of the pulses produced by the particles. This type of particle-identification technique is referred to as pulse-shape-discrimination (PSD). To separate neutron induced events from γ-ray induced events, PSD techniques must be employed on the pulses produced by protons and electrons. In general, any charged particle interacting with a scintillator, such as NE213, will produce a signal which is composed of two exponentially decaying components, one component is fast, with a decay constant of about 4ns, the other is slow, with a typical decay constant of 90ns [PERK79]. For particles with a large specific energy loss ($dE/dx \propto MZ^2/E$), such as protons, *quenching* of the scintillator occurs and the strength of the fast component relative to the slow component is reduced [BIRK64]. On the other hand, for electrons the effect of quenching is relatively small. Therefore, by examining the relative size of the fast and slow components it is possible to determine whether an event is due to an electron or a proton. One obvious method of examining the pulse shapes is to integrate the anode pulses from the photo-multiplier tube over two periods, say 25ns and 500ns, and then compare the sizes of the two integrated signals.

NE213 is a fast scintillator, hence the rise-time of the anode signals is effectively determined by the variation in transit-time of the electrons in the tube. It also has a high hydrogen density, so it is ideally suited to fast neutron counting.

2.7.2 Scintillator Cells

As described above, it was decided to use cylindrical scintillator cells with an inner diameter of 124mm and a depth of 50mm. These were constructed out of sections of aluminium tube. An aluminium plate was vacuum braised to one face of the cells and a glass window glued to the other face. The internal aluminium surfaces were coated with several layers of NE562 reflector-paint and an expansion/contraction chamber was added to the top of each cell. These chambers were filled with N_2 to allow for any thermal expansion or contraction of the liquid scintillator. The chambers also permitted the *bubbling* of the NE213 with nitrogen. The process of bubbling is necessary to remove dissolved oxygen from the scintillator. Oxygen acts as a powerful quenching agent; its presence reduces both the total light output and degrades the PSD properties of the scintillator.

2.7.3 Photo-multiplier Tubes

To gain the best possible timing resolution, it is essential to use fast focused linear photo-multiplier tubes. These are designed with complex focusing electrodes to ensure that the transit-time of the photo-electrons from the cathode to the first dynode does not depend on the point of emission of the electrons from the cathode. Normally, the cathodes of large diameter tubes are curved to help minimize the spread in the transit-time. This means that a plano-concave adaptor has to be used to couple the cathode to the scintillator cell.

A total of six photo-multiplier tubes were used in the present work. Three EMI-9823Bs and three RCA-8854s. The EMI-9823B and the RCA-8854 are both fast focused linear tubes. They have very similar specifications for timing, quantum efficiency, gain etc. A summary of their specifications is given below.

	spectral range (nm)	peak of spectral range (nm)	Q.E. at peak of spectral range (%)	Typical rise time (ns)	Typical gain
EMI-9823B	300-630	380	27	2.7	8.3×10^7
RCA-8854	225-600	375	30	4	5×10^7

N.B. the wavelength of maximum emission of NE213 is 425nm

One practical advantage of the EMI tubes, over the RCA tubes, was that they came with plano-concave adaptors already fitted. For the RCA tubes it was necessary to manufacture the adaptors.

2.7.4 Voltage-divider Design

The design of the voltage-divider determines the performance of the photo-multiplier tube. It limits the rate at which the detector can count, defines the linearity of amplification and effects the quality of the anode pulses.

Since the neutron energy was measured by the *time of flight* technique, linearity was not too important (in any case, NE213 is intrinsically non-linear). However, good timing and PSD properties were essential, hence clean anode pulses were required. It was also important that the gain of the tube was not

rate dependent, since any variation in the gain would cause the effective energy threshold to change.

The first step in designing a voltage-divider is to fix the divider chain current. Normally this is chosen such that it is very much larger than the average anode current. Assuming a maximum count-rate of 10kHz, the average anode current is less than or equal to $\sim$2μA. Therefore, a chain current of about 3mA is more than ample.

The voltage divider must also be designed so that the inter-dynode potentials do not vary significantly over the duration of the pulse. This is important since the gain of the tube depends critically on the dynode-dynode voltage. The most effective way of achieving the inter-dynode voltage stability is to capacitively de-couple the dynodes. The sizes of the capacitors are determined by ensuring that $\Delta V_{dy-dy}/V_{dy-dy} < 0.01\%$, where ΔV_{dy-dy} is the change in the inter-dynode voltage, V_{dy-dy}, during the pulse. For the voltage-divider discussed here, 10nF capacitors were selected, giving a voltage stability of better than 0.006%. Since the current flow from the dynodes is only significant at the bottom of the chain, it was only necessary to de-couple the last four dynodes. Further improvements to the voltage stability were made by employing Zener dynodes, instead of resisitors, in the last few stages of the chain. These help because they only require a small current (typically 30μA) to maintain a fairly stable reference voltage.

In most applications, photo-multiplier tubes are used with the cathode held at earth potential. This is certainly the safest way to operate them. However, it also means that the anode must be capacitively de-coupled from the external electronics. Unfortunately, the presence of a capacitor can cause over-shoot and ringing on the tail of the anode signal. These effects seriously degrade the PSD properties of the detector. To avoid this, it was decided to operate the tubes with their anodes held at earth and their cathodes at a high negative potential (typically -2300V). Consequently, great care had to be taken with the insulation of the photo-multiplier tubes.

The final voltage-divider design is shown in figure 2.17. This particular chain was the one that was used with the RCA tubes (the chain for the EMI tubes only differed in the number of dynodes). One feature, which is apparent from the diagram, but has not been mentioned so far, is the presence of a

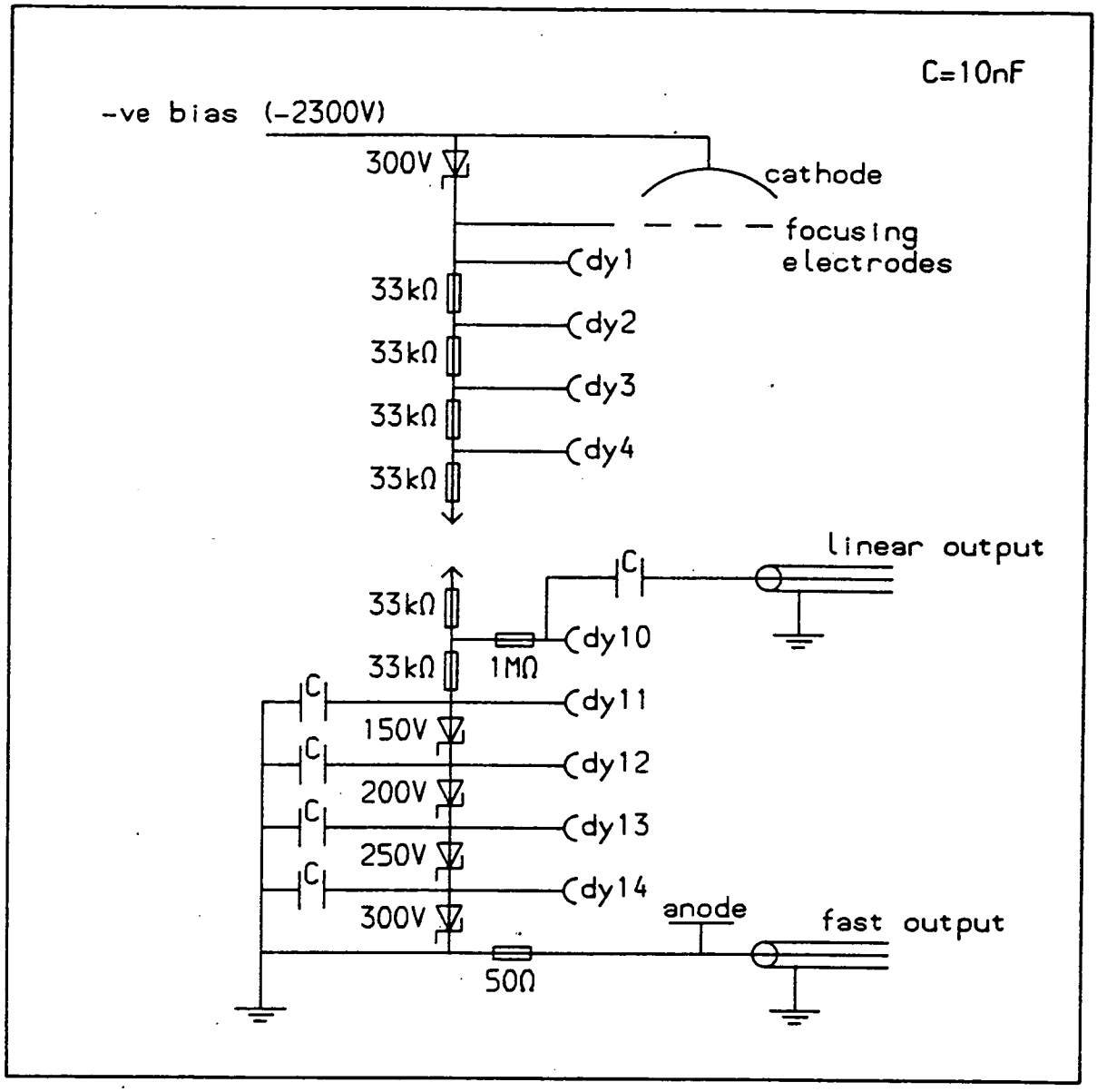

Figure 2.17: Voltage-divider design for RCA-8854 photo-multiplier tube.

linear output. This was mainly used to collect energy spectra of γ-ray calibration sources, so that the energy thresholds could be determined. The 1MΩ resistor provided matching with the Ortec 113 pre-amplifier that was used to boost the *linear* output signal.

2.7.5 Overall Assembly

The scintillator cell, photo-tube and dynode-chain were all mounted inside a cylindrical aluminium canister. A cut-away diagram of the detector is shown in figure 2.18, and a photograph of the detector in figure 2.19. The scintillator cell was coupled to the photo-multiplier tube with Dow Corning 7-Compound to ensure good optical bonding. To be sure of continuous coupling, the scintillator cell and photo-tube were held together under pressure. This pressure was provided by three strong springs.

The voltage-divider chain was soldered directly onto the base of the tube to minimize the length of the leads.

Finally, a photo-diode was positioned at the edge of the cathode. This was used to provide pulser signals to the neutron detector. By injecting a pulser in this way it was possible to check the performance of the entire electronic chain (tube + voltage-divider + PSD-unit + TAC) throughout the course of the experiment.

To gain flexibility and efficiency a total of 6 neutron detectors were constructed.

2.7.6 Measured Timing and PSD Properties

The anode pulses from the neutron detectors were very clean, with little noise and no evidence of ringing. The typical rise-time of the anode pulses was about 5ns (10%-90%).

The timing resolution of the detectors was measured by collecting *time of flight* spectra for particle+γ-ray and particle+neutron events produced by a ^{252}Cf fission-fragment source. The *start* signal was obtained by detecting the fission-fragments with a surface-barrier counter, mounted inside a vacuum chamber close to the ^{252}Cf source. A typical *time of flight* spectrum is shown in figure 2.20. The FWHM maximum of the prompt γ-ray peak is about 1.1ns. If allowance is made for the γ-ray *time of flight* across the cell, and for the

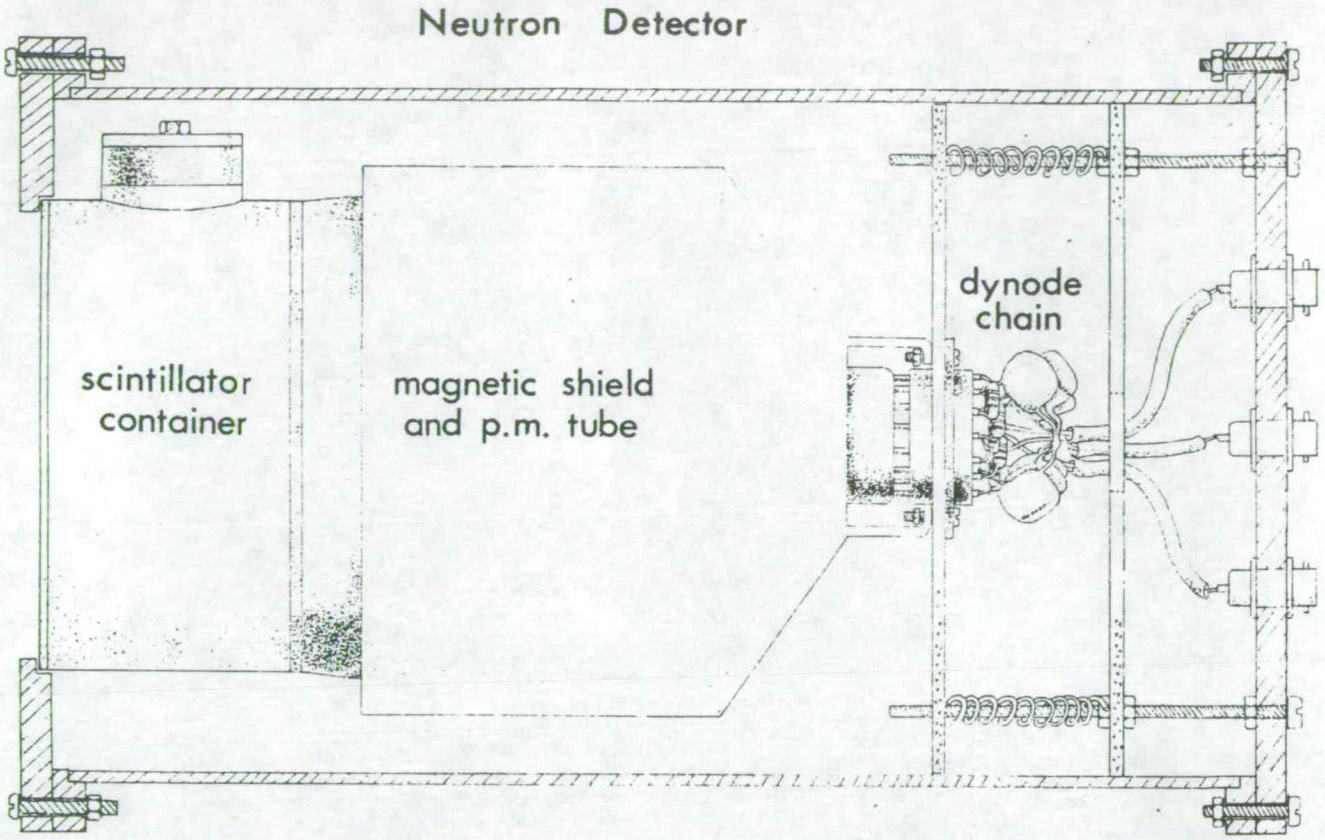

Figure 2.18: Cutaway diagram of the neutron detector.

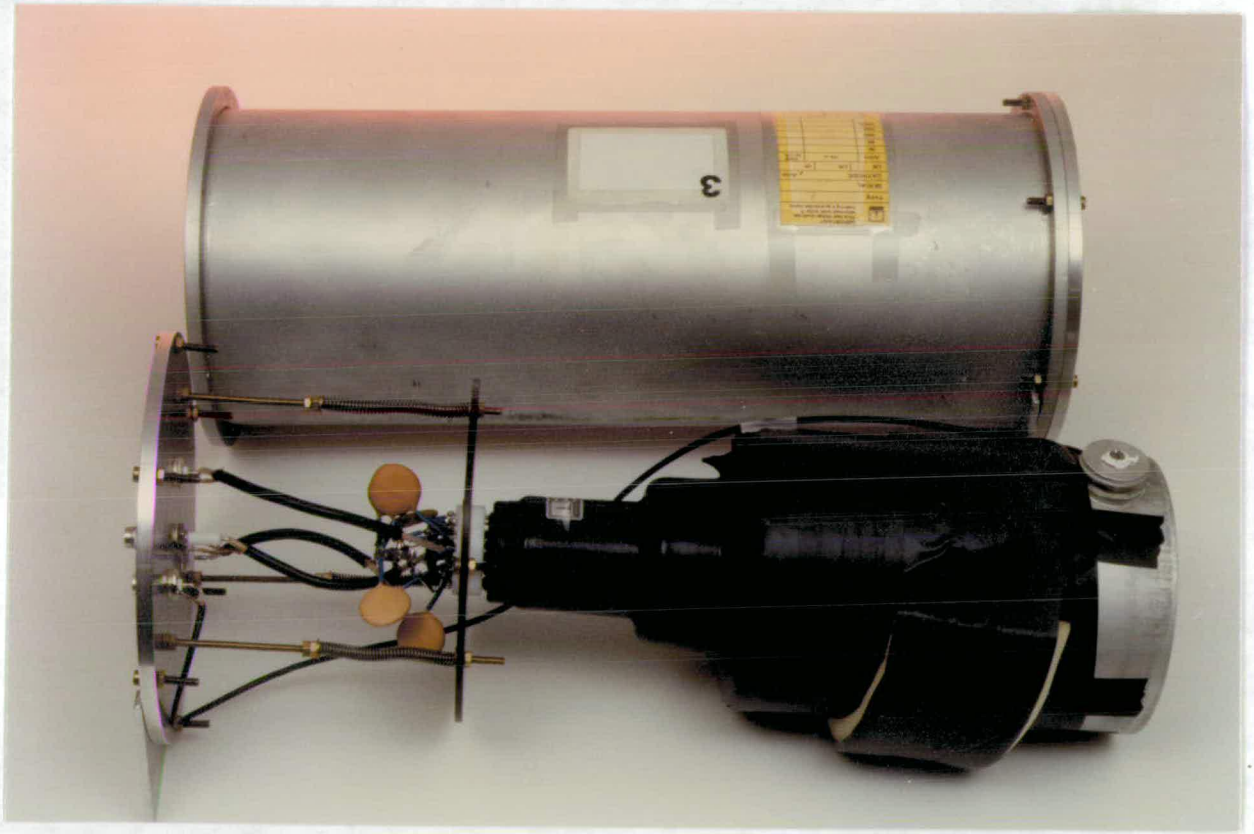

Figure 2.19: Photograph of one of the neutron detectors.

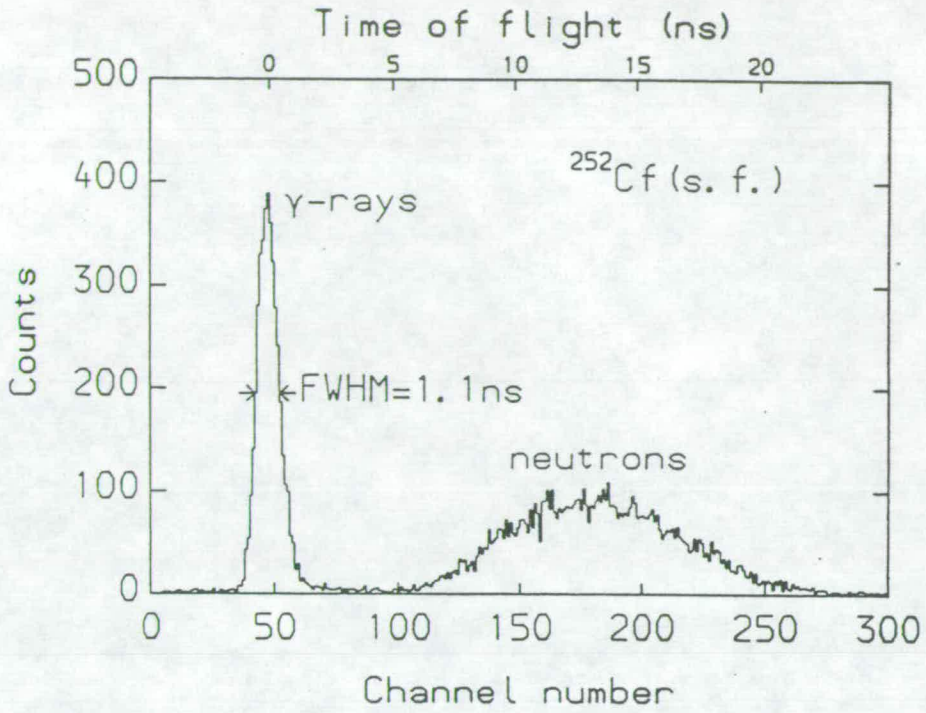

Figure 2.20: Typical neutron detector *time of flight* spectrum for fission-fragment+neutron and fission-fragment+γ-ray events produced by a ^{252}Cf fission-fragment source.

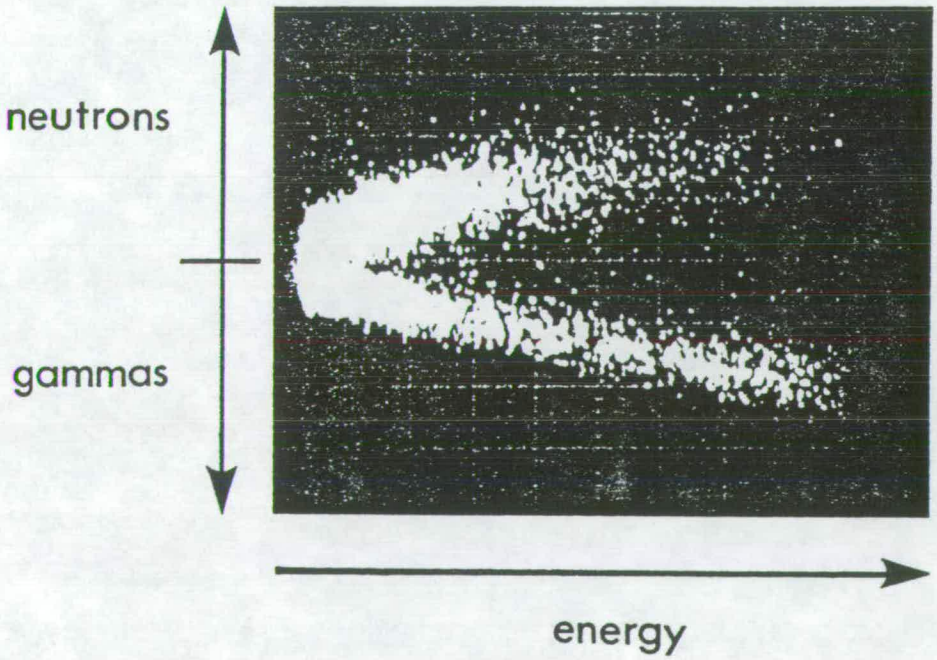

Figure 2.21: Oscilliscope display obtained with a 5010-PSD unit and an $^{241}Am+^{9}Be$ neutron/γ-ray source. This picture illustrates the pulse shape discrimination properties of the neutron detectors.

variation of the fission-fragment flight time, then this width implies an electronic timing resolution of about 0.9ns.

During the ^{9}Be breakup runs, a timing resolution of about 1.4ns was achieved. The t=0 of the *time of flight* spectra were obtained from the positions of the prompt γ-ray peaks. (Allowance was made for the flight time of the γ-rays from the target to the detectors). The *time of flight* spectra were calibrated using an ORTEC-462 Time-Calibrator. A typical *time of flight* spectrum is shown in figure 5.4 of Chapter 5. As is clear from the spectrum, the background due to random events is a very low. Among other factors, this is a consequence of the careful shielding of the detectors and the distance at which the beam was dumped from the target

The PSD properties of the detectors were tested using an ^{241}Am+^{9}Be mixed source. This source produces neutrons and γ-rays with energies in the range 0↶10MeV, via the reaction ^{9}Be+α→^{13}C*(nγ). The α-particles are produced by the radioactive decay of the ^{241}Am nuclei. The anode pulses from the neutron detectors were fed into LINK-SYSTEMS 5010 PSD units. These units employ the two-period integration technique. For each event, a NIM logic signal is furbished to either the γ-ray output or the neutron output, depending on the nature of the event. The 5010 unit also generates X, Y and Z oscilliscope signals, to enable the setting up of the input discriminator and the PSD threshold. These signals are defined as follows:

- X: total energy (equivalent to the long integrator output)
- Y: PSD signal (difference between the two integrator outputs)
- Z: brightness

A typical oscilliscope display for the ^{241}Am+^{9}Be source is shown in figure 2.21. The upper locus corresponds to neutron induced events, the lower to γ-ray events. A very clear separation between the two types of event has been achieved. Other useful features of the 5010 unit include:

- built in pile-up rejection circuit
- fast-logic timing output (via a constant fraction discrimination circuit)
- integrated total energy output

Six of the 5010 units were employed during the experimental runs to generate fast timing signals and PSD logic signals from the neutron detector anode pulses.

2.7.7 Efficiency

For 0–14MeV neutrons, p+n scattering is approximately isotropic in the centre of mass. Consequently, the proton energy spectrum produced by neutrons of energy E_n, is a rectangle extending from E_p=0 to E_p=E_n. Therefore, for an ideal (thin) detector, the efficiency (Eff_n) depends on the energy threshold in a simple manner, *viz.*

$$Eff_n=(1-E_{thresh}/E_n)\sigma^{tot}_{n+p}\, n_H\, d \qquad (2.3)$$

where:

σ^{tot}_{n+p} = the total n+p scattering cross-section

n_H = the hydrogen density of the scintillator

d = the depth of the scintillator cell

For a 5cm deep scintillator cell of NE213, operated with a proton energy threshold of 0.75MeV (which is approximately equal to a 0.25MeV electron energy threshold), this relation predicts a detection efficiency of 21% at E_n=10MeV.

To gain a more detailed picture of the dependence of the neutron detection efficiency on energy, the improved version of the Monte-Carlo simulation code of Stanton [CECI79] was employed (see Chapter 3). The efficiency spectra produced for neutron energy thresholds of E_{thresh}=0.25, 1.0 and 2.5MeV equivalent-electron energy, are shown in figure 2.22. As will be discussed in Chapter 3, the efficiency spectra generated by Stanton's code were used in determining the overall experimental efficiency of the detection system. Most of the neutron detectors were operated at thresholds of about 0.25MeV equivalent-electron energy. The energy thresholds were set by placing soft-ware gates, in the data collection program (see §2.10), on the neutron detector *linear* energy spectra. The gains of the *linear* signals were determined from the positions of the Compton edges of γ-ray spectra from several calibration sources e.g. ^{22}Na and ^{60}Co.

2.8 Overall Configuration and Efficiency of Detection System

The manner in which the ^{8}Be-telescope and the neutron detectors were positioned is shown in figure 2.23. The ^{8}Be-telescope was mounted on a manually rotatable table inside the scattering chamber. The neutron detectors

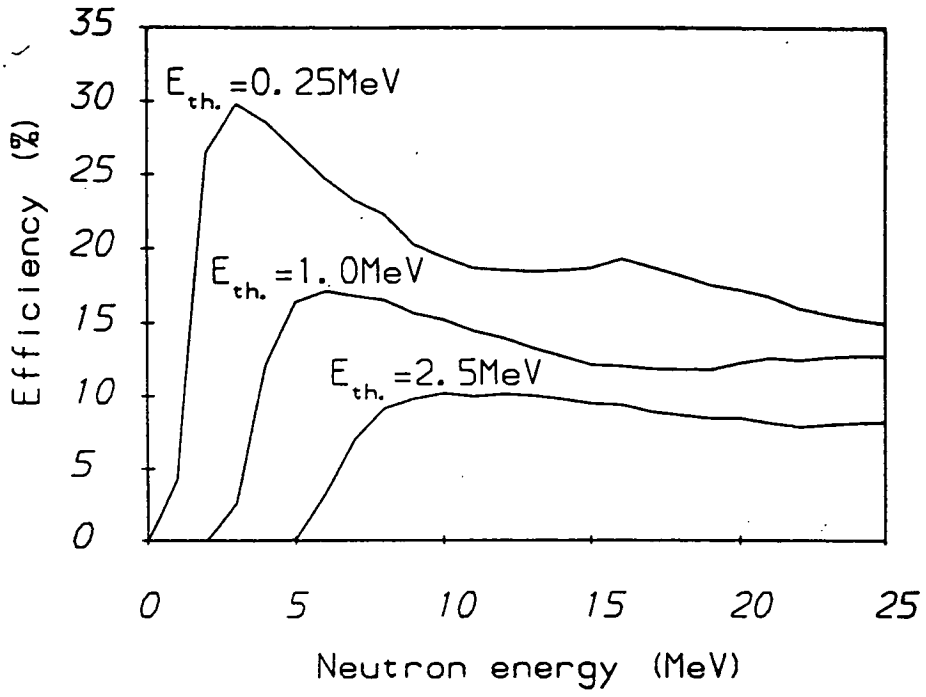

Figure 2.22: Efficiency of neutron detector as a function of neutron energy and detector threshold (the thresholds are in MeV equivalent-electron energy).

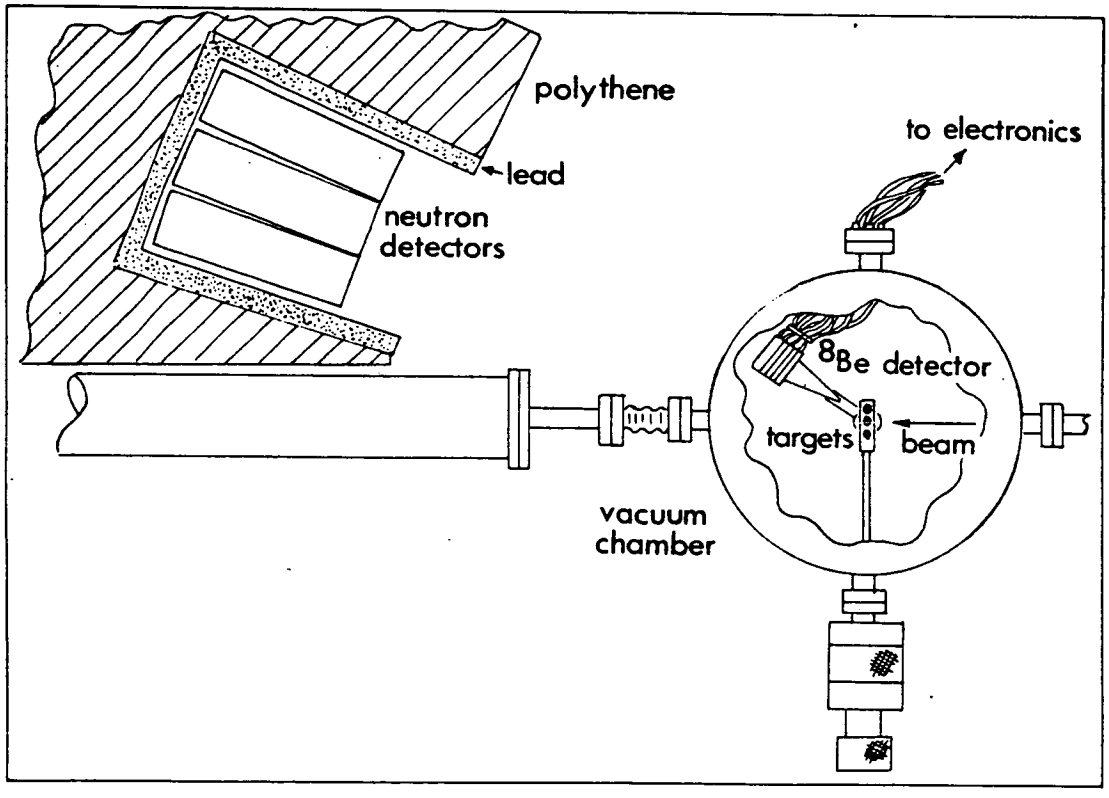

Figure 2.23: Arrangement of the ^{8}Be-telescope and neutron detectors.

were arranged in a tight cluster, three slightly above the reaction plane, and three slightly below, and were surrounded by a considerable amount of lead and polythene shielding. All of the neutron detectors and the shielding were placed on top of movable tables, so that the detectors could be easily positioned at any desired scattering angle. The distance from the target to the centre of the scintillation cells was 2m.

The total experimental efficiency of the ^{9}Be breakup detection system depended on:

- the efficiency of the ^{8}Be-telescope
- the intrinsic efficiencies of the neutron detectors
- the relative positions of the ^{8}Be-telescope and neutron detectors
- the details of the breakup process

For low relative-energies and 90MeV ^{9}Be, it can be shown that the average angular separation between the ^{8}Be and the neutron, θ^{av}, is given by:

$$\theta^{av} \backsim 14.2\varepsilon^{1/2}$$

Where ε is the ^{8}Be-n relative-energy in MeV and θ^{av} is in degrees. The highest efficiency for a particular relative-energy is achieved by positioning the ^{8}Be and neutron detectors with angular separations of θ^{av}.

Since most interest was in the low relative-energy region, the neutron detectors were arranged in a close cluster, which was positioned directly behind the ^{8}Be-telescope. This type of experimental setup is usually referred to as a close-geometry configuration. It is only in particle+neutron coincidence experiments that it is possible to position the counters with an angular separation of 0°. One of the advantages of a such a configuration is that it is possible to study very low relative-energy breakup reactions.

For a $\theta_{8Be-tel}=\theta_{n-cluster}$ configuration, the variation of the total effective solid-angle of the detection system (Ω_{eff}^{total}) with relative-energy is shown in figure 2.24. The effective solid-angle peaks at ε=0 and decreases dramatically with increasing ε. This behaviour illustrates a common feature of breakup detection systems, in that the experimental efficiency is strongly biased towards a particular relative-energy region.

Even at its peak value, the effective solid-angle of the ^{9}Be breakup detection system was very low, $\backsim$0.6msr. This was despite all the efforts that

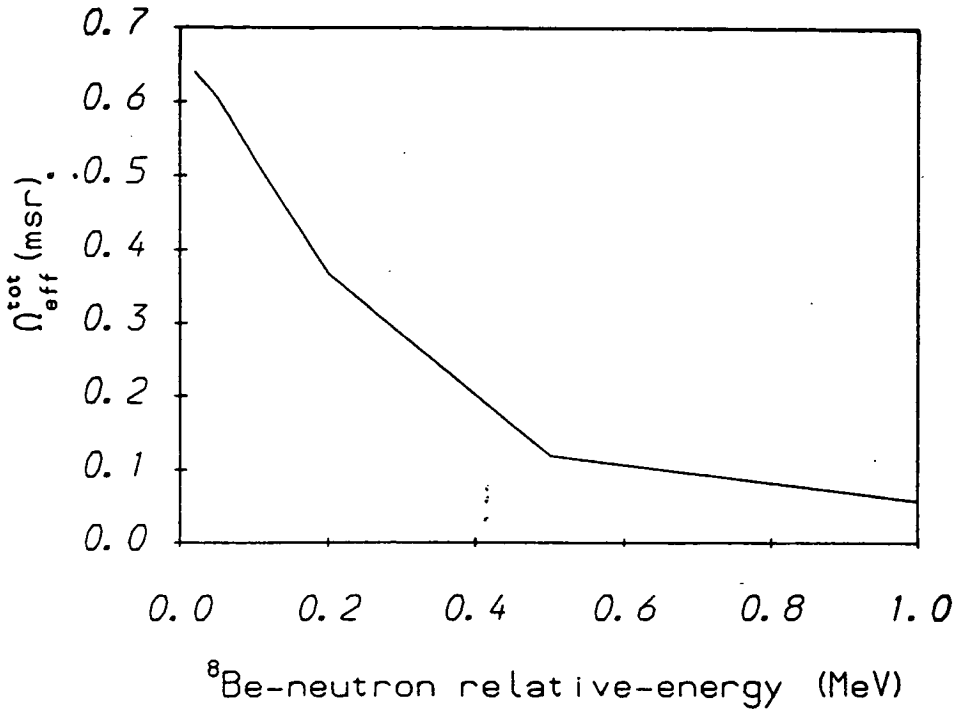

Figure 2.24: Variation of the total effective solid-angle of the detection system, for detecting $^8Be_{g.s.}$+n events, with the ^{8}Be-n relative energy.

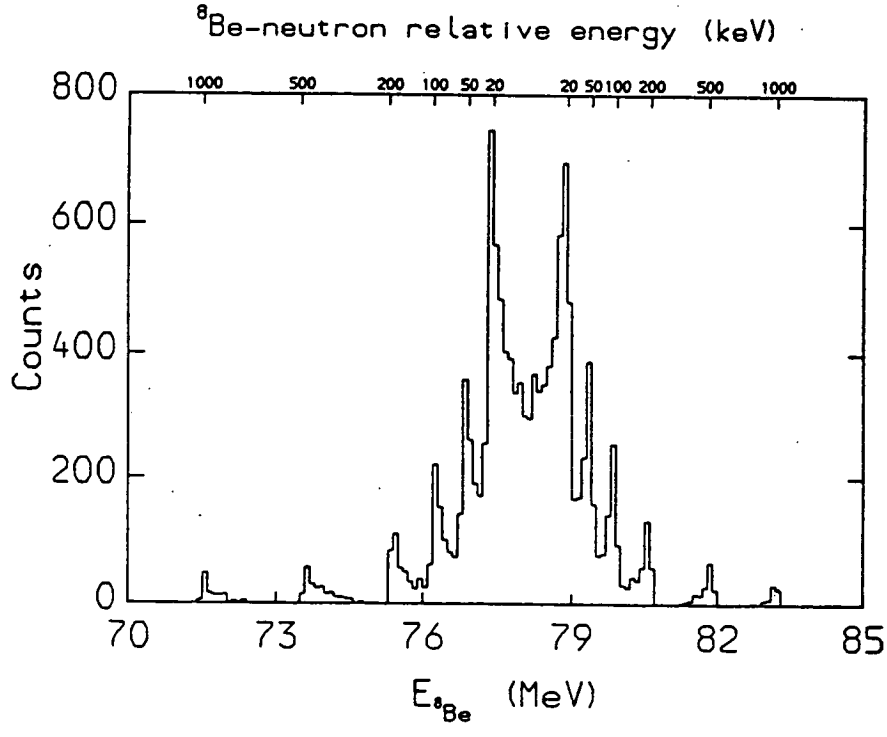

Figure 2.25: Monte-Carlo simulation of the ^{8}Be projected energy spectrum for ^{8}Be-n relative energies of 20, 50 , 100, 200, 500 and 1000keV.

had been made to improve the efficiency of the system, and indicated the intrinsic difficulty of performing the experiment.

The ability of the detection system to determine the ^{8}Be-n relative-energy is illustrated in figure 2.25. This figure is a Monte-Carlo simulation of the ^{8}Be energy spectrum that would be produced by ^{9}Be breakup reactions in which the ^{8}Be-n relative-energies were 20, 50, 100, 200, 500 and 1000keV. The same number of ^{9}Be breakup reactions were simulated for each value of the relative-energy. Corresponding to each value of ε there are two peaks in the spectrum. This is a consequence of there being two solutions to the reaction kinematics. The strength of the peaks falls off rapidly with increasing ε, which reflects the behaviour of the effective solid-angle curve of figure 2.24. The spectrum also demonstrates that the relationship between ε and the laboratory energy of the ^{8}Be is highly non-linear.

Sequential breakup of ^{9}Be from its 2.43 and 3.06MeV states will result in relative-energy values of 0.76 and 1.39MeV. Therefore, it should be possible to resolve these states from the E_{8Be} spectrum, even though the dispersion of the spectrum ($\Delta E_{8Be}/\Delta\varepsilon$) is low at these relative-energies.

Direct breakup processes will produce a continuous ε spectrum. Such an ε spectrum will result in a continuous E_{8Be} distribution. From the simulation of figure 2.25, it is apparent that the extraction of a continuous ε-spectrum from the E_{8Be} spectrum involves a considerable de-convolution of the data. Instead of attempting such a de-convolution, the ^{8}Be+n coincidence data will be analysed by using simulation programs to generate the E_{8Be} spectra for different ε distributions. The results of the simulations will then be compared with the experimental spectra.

The experimental version of figure 2.25 is created by placing a two dimensional window around the kinematic locus, on the E_n/E_{8Be} spectrum, that corresponds to the ground-state of the target. A ^{8}Be energy spectrum is then incremented for each event that falls within the window. Such spectra are commonly referred to as projected spectra, since the process of creating them is equivalent to *projecting* all the data within the window onto one of the axes of the two-dimensional spectrum.

2.9 Data Acquisition Hardware

The data-acquisition hardware employed in the ^{9}Be experiment consisted of:

- a signal processing circuit
- 24 analogue to digital converters (ADC)
- an interface between the ADCs and the computers (known as an event-manager)
- data collection and analysis computers

The roles of these systems are now discussed in turn.

2.9.1 Signal Processing Electronics

The signal processing electronics had to perform several functions. These included:

- amplifying and shaping the detector linear energy signals
- defining logic triggers for all of the events of interest
- keeping track of the number of triggers, piled up events and pulser events
- measuring the integrated beam current

A diagram of the circuit is shown in figure 2.26. There were three important sections of the circuit. The first section dealt with the ^{8}Be-telescope.

All of the signals from the strip-detectors were fed into charge-sensitive pre-amplifiers located close to the scattering chamber. The signals from the front strip-detector were also passed through fast-timing pre-amps. After the pre-amplification stage, the energy signals were then further amplified and shaped by shaping amplifiers. These amplifiers generated both bi-polar and uni-polar output pulses. The uni-polar pulses were fed into the ADCs, while the bi-polar pulses were used to define slow logic signals. The pre-amplified strip-detector energy signals were also used to derive fast timing pulses which were fed into pile-up rejection units. The timing signals from the fast pre-amplifiers were used to generate *start* and *stop* pulses for a charged-particle + charged-particle *timing to analogue* converter (TAC), and to provide the *start* pulses for the charged-particle + neutron TACs.

The second section of the circuit processed the signals from the neutron detectors. Since identical instrumentation was used for each detector, the details of only one detector are shown in the circuit diagram. The signals from

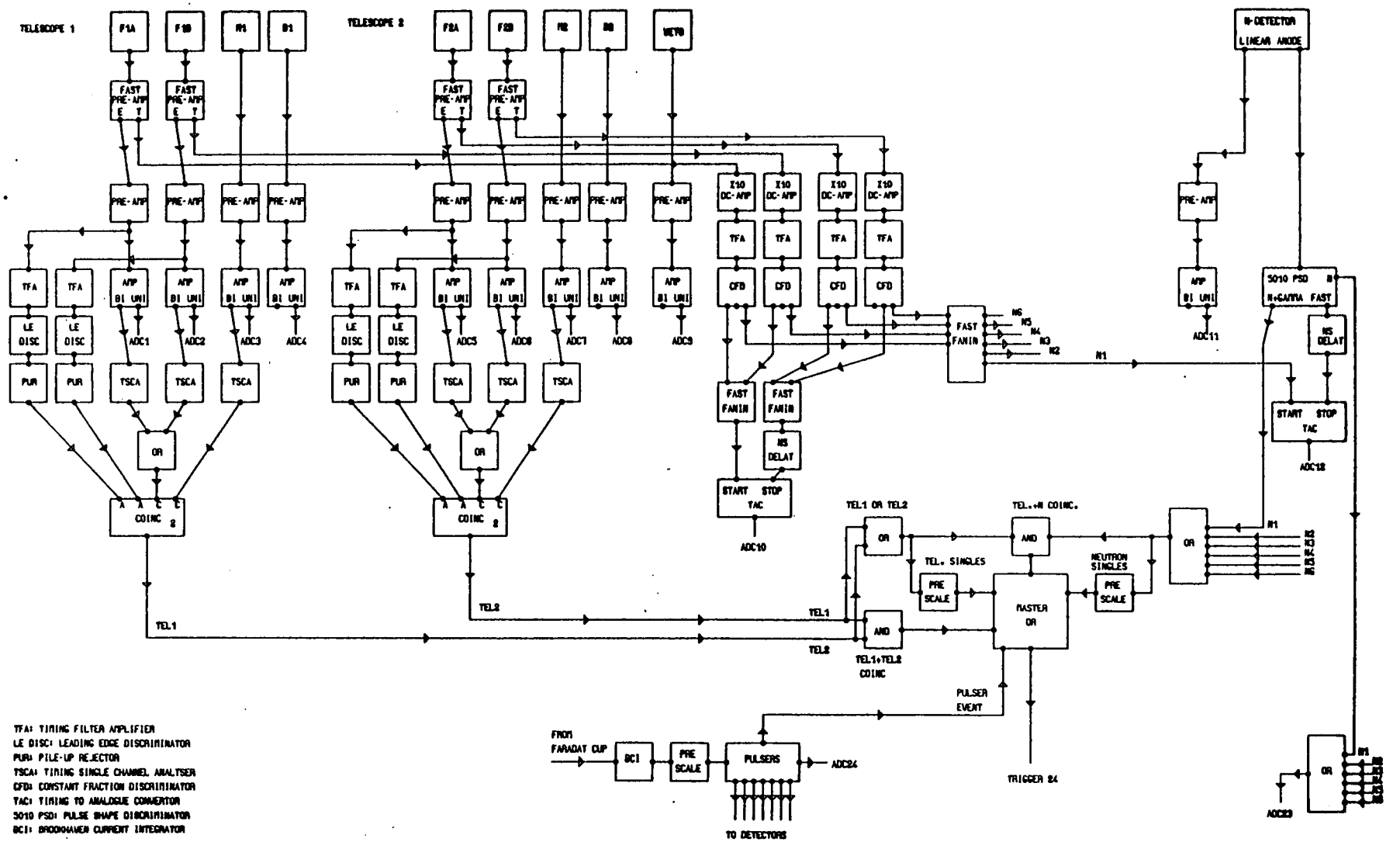

Figure 2.26: Diagram of signal processing circuit.

the linear outputs of the dynode chains were simply amplified and then read by ADCs. More complicated processing was performed on the anode pulses. These were fed into Link-Systems 5010-PSD units. The 5010 employs a pulse-shape discrimination technique, which was described in §2.7, to determine whether an event is due to a γ-ray or a neutron. For both types of event, a fast-timing signal is generated and a slow logic pulse is furbished to the neutron+γ-ray output. For neutron induced events a logic signal is also produced at the *neutron* output. The fast timing signals were used as the *stops* of the charged-particle+neutron TACs. In order to *tag* a neutron induced event, all of the neutron logic outputs were fanned together to generate a single logic pulse which was then fed into ADC number 23. The *OR* of all of the neutron+γ-ray outputs was used to define an event in which at least one of the neutron detectors had fired.

The final section of the circuit formed coincidences between the slow logic pulses, which were generated in the previous two sections, to determine the nature of the event. For each event of interest, a trigger signal was produced and sent to the event-manager. Pre-scaling was performed on the singles events to keep the total trigger rate down to about 200cps.

To be able to determine the pile-up rate, the rate of valid events and the number of pulser events, logic pulses were taken from the above circuitry and counted by NIM and CAMAC scalers.

The beam current from the Faraday cup was integrated using a Brookhaven Current Integrator (BCI). This device produces a stream of pulses whose rate is proportional to the current delivered to it. The pulses from the BCI were counted by a CAMAC scaler, and then pre-scaled. The pre-scaled BCI pulses were used to initiate pulser events. In these events, signals were injected by pulse-generators into all of the counters simultaneously. In addition, a pulse was sent to ADC number 24, which had been specially added to the circuit to enable the *tagging* of pulser events. Pulser events were fired into the system both to check-out the electronics and to permit the calculation of the deadtime of the detection system.

2.9.2 Event-manager

The inter-face between the electronics and the computers was a soft-ware programmable device known as the event-manager (EM). By means of a data collection program (DCP), the event-manager can be configured to respond in a variety of ways to the triggers fed into it from the logic circuit.

The only EM trigger input which was used in the work described here was the indirect trigger input (trigger 24). When a trigger pulse is received at this input, all of the ADCs which are in pre-conversion at the time of arrival of the trigger, and which are accompanied by pulses at the externally defined trigger pattern panel (ETP), are gated to convert. The ADC conversions are then stored in a buffer of multi-parameter events. The pattern of pulses sent to the ETP by the logic circuit determines which ADCs are to be read. It was by using the ETP that piled-up events were rejected.

2.9.3 Data Collection and Analysis Computers

Three linked computers are involved in the collection of data at the NSF. They are all members of the GEC4000 series, and are commonly referred to as the A, R and C machines since, respectively, they are responsible for Accumulation, Resources and Control. A block diagram of the NSF's data acquisition system is shown in figure 2.27. The functions of the A, R and C-machines are summarized below:

A-machine

The A-machine interacts with the event-manager and handles the flow of data from the EM to the rest of the data acquisition system. The user supplied data collection program, which resides in this computer, is used to set up the event-manager and to define the on-line experimental spectra. When the EM multi-parameter buffer is full, the A-machine reads-out the event-by-event data via an optically de-coupled data-way. The data is then sorted by the DCP and the relevant online spectra are incremented. Each event packet is also sent on to the R-machine.

R-machine

The function of the R-machine is to control the peripherals of the NSF data collection system. Its

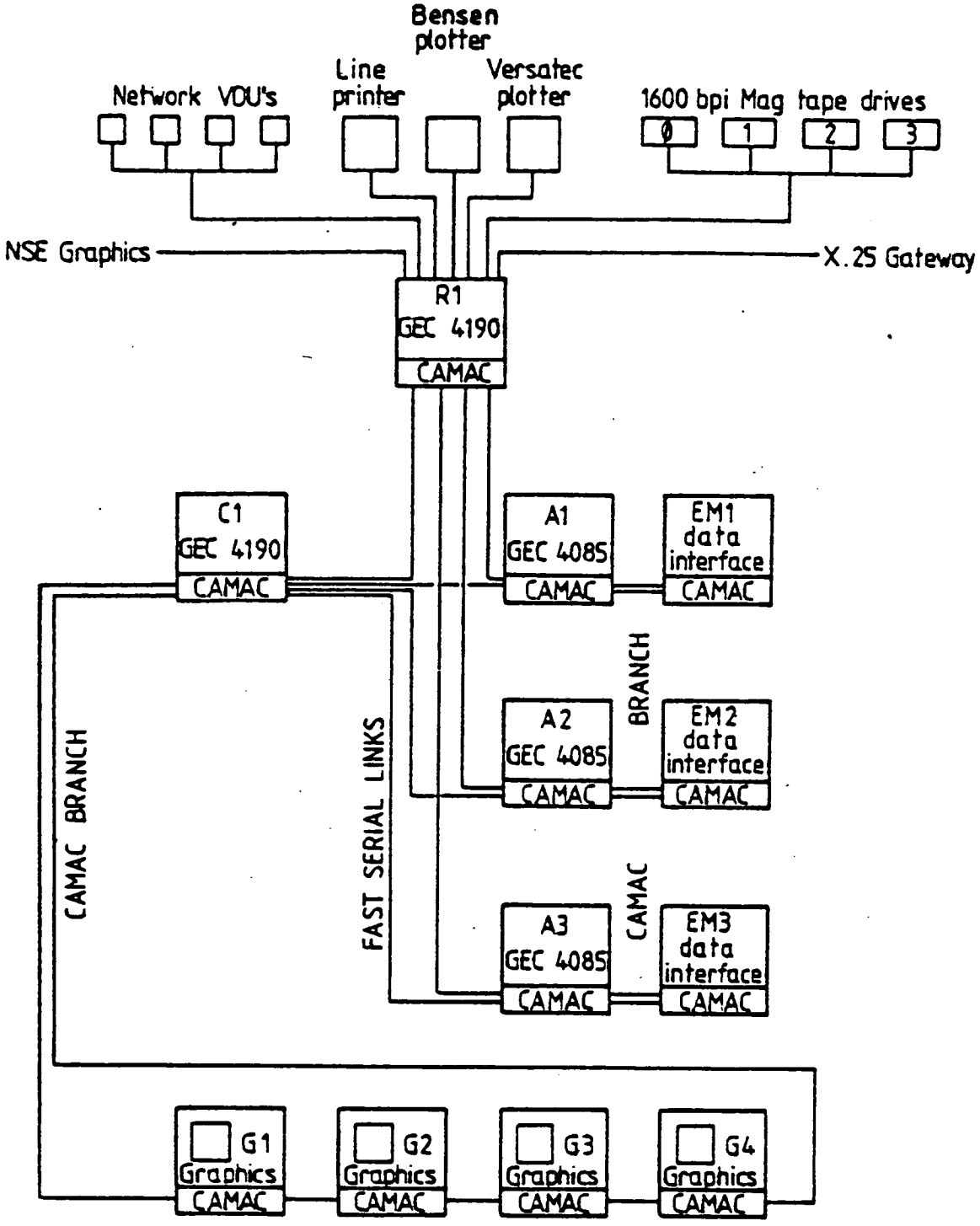

Figure 2.27: Block diagram of NSF data acquisition system.

most important task during the data collection process is to write the event-by-event data, transferred from the A-machine, to magnetic tape.

C-machine

The C-machine creates an interactive environment through which the data collection process is controlled. It is responsible for providing the graphics processing which enables the spectra accumulated by the A-machine to be inspected.

Due to this division of tasks, the NSF data acquisition system is capable of handling high event rates (>150kb/s) while simultaneously providing sophisticated online sorting.

2.10 Data Acquisition and Analysis Software

To provide on-line analysis of the data, and to perform the setting-up of the Event-Manager, a Data Collection Program (DCP) was necessary. This program was written in the GEC version of FORTRAN66 and was based around the library of data collection subroutines which is provided as part of the NSF data acquisition system. The structure of the DCP is outlined below.

SETTING-UP SECTION (entered only once)

- define Event Manager triggers
- specify the set of ADCs to be inspected for each trigger
- define and allocate space for the user-defined on-line spectra

EVENT PROCESSING SECTION (entered for every event)

- determine the nature of the event from the pattern of the ADCs which have converted, then jump to the relevant sorting section
- section for charged-particle singles events
    * check that the veto counter (ADC9) has not fired
    * calculate the energy deposited in each of the sections of the strip-detectors and increment a particle identification (PI) spectrum
    * place a window on the PI spectrum and increment the energy spectra
- section for charged-particle+charged-particle coincidence events
    * check that the veto counter (ADC9) has not fired
    * increment the charged-particle + charged-particle TAC spectrum

(ADC10) and place a window on the coincidence peak

* calculate the energy deposited in each of the sections of the strip-detectors and increment particle identification spectra
* place windows on the α-particle peaks of the PI spectra and increment the $E_{\alpha 1}/E_{\alpha 2}$ spectrum
* place a window around the $^{8}Be_{gs}$ kinematic loci and increment the E_{8Be} spectrum ($E_{8Be}=E_{\alpha 1}+E_{\alpha 2}-0.092MeV$)
* place a window on the $E_{\alpha 1}/E_{\alpha 2}$ spectrum and increment the $E_{\alpha 1}$ and $E_{\alpha 2}$ projected spectra

- section for neutron singles events

  * inspect ADC23 to see if the event was induced by a γ-ray or a neutron
  * increment energy spectra for the neutron linear outputs

- section for charged-particle + charged-particle+neutron triple coincidence events

  * check that the veto counter (ADC9) has not fired
  * increment the charged-particle + charged-particle TAC spectrum (ADC10) and place a window on the coincidence peak
  * calculate the energy deposited in each of the sections of the strip-detectors and increment particle identification spectra
  * place windows on the α-particle peaks of the PI spectra and increment the $E_{\alpha 1}/E_{\alpha 2}$ spectrum
  * place a window around the $^{8}Be_{gs}$ kinematic loci
  * inspect ADC23 to see if the event was induced by a γ-ray or a neutron
  * increment the neutron *time of flight* spectra and calculate the neutron energy
  * increment the $E_{8Be}+E_n$ spectra then place a window on the $E_{8Be}+E_n$ spectra and increment the E_{8Be} and E_n projected spectra.

- section for pulser-events

  * inspect the pattern of ADC conversions to see which ADCs were *live* during the pulser event
  * for each event-type of interest, determine whether the relevant set of ADCs were *live* during the pulser-event, and if so, increment the appropriate counter variable

DEADTIME SECTION (entered whenever the experimentalist wishes)

- calculate the deadtimes for each event-type from the pulser-event data which was processed and accumulated in the event processing section
- write out the deadtime values to the line-printer

The only non-standard part of the program was the deadtime section. One of the reasons for including this section in the on-line version of the code was that it permitted a rapid inspection of the status of the experimental equipment. On several occasions during the ^{9}Be data collecting runs, the output from the deadtime section indicated the existence of a problem with one of the NIM units or detectors.

Off-line sorting of the event-by-event data tapes was performed on the GEC4090 Edinburgh/DL work-station. An expanded version of the on-line DCP was employed in the off-line data analysis.

2.11 Determination of Absolute Cross-sections

Cross-sections were calculated using the following, standard, formula:

$$d\sigma/d\Omega(mb/sr) = 2.66\times10^{-7}NZA/(I\ \Omega_{eff}\ f\ T) \qquad (2.4)$$

where:

N = number of counts

Z = charge-state of the beam particles

A = target mass (amu)

I = integrated beam current (μC)

Ω_{eff} = effective solid-angle (sr)

f = fractional system livetime

T = target thickness (mg/cm^2)

For each individual run, the number of pulses generated by the Brookhaven Current Integrator gave the amount of charge collected in the Faraday cup. However, there was a beam current loss of $\sim$8% between the target and the Faraday cup. The uncertainty in the amount of beam lost lead to an error in the integrated beam current of $\sim$5%.

The target thicknesses were measured to about 10% (see §2.5).

The fractional livetime for each type of event followed directly from the deadtime calculations (see §2.10). An upper limit on the error of the livetime values was estimated to be about 6%.

The above three factors combine to give an uncertainty in the cross-section calculations of ↶13%.

For the α+α+neutron data the statistical quality varied from about 3% to 20%, depending on the angles of the detectors. In general, the statistics became poorer with increasing scattering angle. The statistics of the α+α data were on the whole better than 2%.

The final quantity, which is necessary in determining the differential cross-section, is the effective solid-angle (Ω_{eff}) of the detection system. The accuracy with which the effective solid-angle for a particular type of reaction can be calculated depends very much on the nature of the reaction. For example, the effective solid-angle for detection of sequential breakup from a particular state of ^{9}Be can be calculated with only one assumption, *viz.* that the breakup of the ejectile is isotropic relative to its centre of mass. However, in order to calculate Ω_{eff} for the direct breakup of ^{9}Be it is necessary to know the relative-energy distribution produced by the direct breakup process. As discussed in §2.8, information on the ε distribution can be gained by comparing simulated experimental spectra with the data. Of course, the ability to determine the shape of the ε distribution depends on the statistical quality of the data. A given shape of ε distribution defines a definite value of Ω_{eff}. Therefore, the range of shapes which produce an adequate fit to the data determines the error in Ω_{eff}.

CHAPTER 3
MONTE-CARLO SIMULATION PROGRAMS

3.1 Introduction

Throughout this work, considerable use has been made of the results of Monte-Carlo computer simulations. These simulations were undertaken to determine the properties of the detection system (e.g. effective solid-angle, angular resolution, identifying power) and to predict the shape of the spectral distributions that would be produced by particular reactions.

It was necessary to employ Monte-Carlo simulation techniques because of the complexity of the breakup reactions and detection system. The Monte-Carlo method also provided a very natural and flexible way of investigating the many processes that effected the data. This is due to the fact that in a Monte-Carlo simulation, each step of the reaction (i.e. projectile+target interaction, breakup of ejectile, breakup of ejectile fragments, interaction of fragments with the detectors) is simulated in the same order and manner as they are believed to occur. The Monte-Carlo technique is flexible because it is possible to introduce additional features (e.g. the simulation of the effect of energy loss in the target) to an existing program without changing the overall structure or philosophy of the code.

3.2 Description of the Breakup Simulation Program MONTEGEN

All of the breakup simulations were performed with the Monte-Carlo code MONTEGEN. This program was written in the GEC version of FORTRAN77 and was run on the NSF's GEC63/30. The GEC63/30 is a fast mini computer.

MONTEGEN is capable of simulating the response of a detection system comprising a strip-detector telescope and a cluster of six neutron detectors to a wide range of breakup reactions. Examples of the reactions which can be simulated are:

$^{120}Sn(^{7}Li,^{7}Li^{*})^{120}Sn^{*}$, $^{7}Li^{*}\rightarrow\alpha+t$

$^{12}C(^{9}Be,^{8}Be^{*}+n)^{12}C_{gs}$, $^{8}Be^{*}\rightarrow\alpha+\alpha$

$^{120}Sn(^{9}Be,^{8}Be_{gs})^{121}Sn_{gs}$, $^{8}Be_{gs}\rightarrow\alpha+\alpha$

From the above examples, it can be seen that the breakup reaction can be chosen quite generally. It is specified in the programs input card in the following manner:

1. target (projectile , ejectile) recoil
2. ejectile → fragment1 + fragment2
3. fragment1 → fragment1A + fragment1B (optional)

The energies and widths of the states of the nuclei can be freely chosen. The states are simulated by assuming that they have Lorenztian line shapes. For the breakup of the ejectile, it is possible to provide a relative energy distribution rather than specifying a state. In this manner, direct breakup reactions can be studied. An angular distribution for the ejectile breakup can also be supplied, otherwise the ejectile is assumed to breakup isotropically relative to its own centre of mass. By supplying an anisotropic distribution the decay of aligned ejectiles can be simulated.

The simulation of the breakup of one of the fragments of the ejectile can be performed, if wished. This breakup is always assumed to proceed isotropically.

The geometry and positions of all of the detectors can also be freely chosen. For example, the shape, number, orientation and connections of the strips of the strip-detectors can be selected, as can the angle and distance of the strip-detector telescope. Similarly, the angle, distance and dimensions of the neutron detectors can be chosen.

For the neutron detectors it is also necessary to provide an efficiency spectrum. The neutron efficiency spectra used in this work were calculated with the improved version of Stanton's efficiency code. This code will be discussed in §3.4.

A brief outline of the manner of operation of MONTEGEN is now given:

SETTING-UP SECTION

- read in the detector geometry and reaction parameters
- read in the neutron efficiency spectrum
- initialise arrays
- define constants

MAIN LOOP

- determine the excitation of the ejectile
- throw the ejectile into the solid-angle defined by the detection system
- perform the breakup of the ejectile
- perform the breakup of the ejectile fragments
- calculate the laboratory angles and energies of the fragments
- determine whether the fragments enter the detectors
- if fragments enter the ^{8}Be-telescope collimator, then follow their paths through the telescope and determine whether they enter any of the inter-strip regions
- if fragments enter the neutron detectors, then determine whether they are detected
- check that no two fragments pile-up in the same detector or have entered connected sections of the strip-detectors
- for good events, increment the relevant spectra
- go back to start of main loop

OUTPUT SECTION

- calculate the effective solid-angles from the number of good events
- write the spectra and solid-angle information to the output catalogue

3.3 Applications of MONTEGEN

The program MONTEGEN was used in the design of the ^{9}Be breakup detection system and in the interpretation of the experimental data. In particular, it played an important role in the design of the strip-detectors (§2.6.2). A considerable range of strip geometries were evaluated by calculating their effective solid-angles and angular resolutions. The merits of different strip connection schemes were also studied by using MONTEGEN.

Simulations of $^{9}Be \rightarrow {}^{8}Be_{gs}+n$ reactions were used to optimise the overall experimental efficiency for low relative energy ^{9}Be breakup reactions (§2.8). The spectra produced by the program were used to determine the analysing power of the detection system i.e. its ability to distinguish between different types of breakup events.

In Chapter 4, some anomalous features of the data are discussed. MONTEGEN was used extensively to try to understand these features.

Finally, the effective solid-angle data was used to determine the differential

cross-sections from the raw experimental data.

3.4 Neutron Efficiency Code

To determine the neutron detector efficiencies as a function of energy, the improved version [CECI79] of the Monte-Carlo computer simulation code of Stanton was employed. This code simulates the passage of a neutron through a scintillation cell and calculates the total light output produced by the interactions of the neutron with the scintillator. The neutron interactions which are taken into account are:

- $n+^{1}H \rightarrow n+^{1}H$, elastic scattering
- $n+^{12}C \rightarrow n+^{12}C$, elastic scattering
- $n+^{12}C \rightarrow n+^{12}C+\gamma$
- $n+^{12}C \rightarrow \alpha+^{9}Be$
- $n+^{12}C \rightarrow n+\alpha+\alpha+\alpha$
- $n+^{12}C \rightarrow n+^{1}H+^{11}B$ and $n+n+^{11}C$ and $^{1}H+^{12}B$
- $n+^{12}C \rightarrow n+^{12}C$, diffractive elastic scattering

For each of the neutron interactions, the kinetic energies and directions of all of the charged particles are computed. These particles are then propagated through the scintillator until they lose all their energy or they escape from the scintillator cell. From the energy deposited in the cell the light output is calculated using light-response functions. The path of the neutron is followed until it leaves the scintillator or is completely stopped. For each neutron, the total light output produced is compared to a threshold level to see if the neutron has been *detected*.

In the paper of R.A.Cecil et al [CECI79] this code has been compared with the existing neutron efficiency data. These data include efficiency curves for a variety of different scintillator types (PILOT-Y, NE102, NE102A, NE110, NE213, NE224, NE228) and detector geometries (5.08cm thick by 10.27cm diameter to 26.8cm thick by 30.0cm diameter). The range of neutron energies covered is from 1MeV to about 300MeV. The threshold settings vary from 0.1MeV to 16MeV equivalent-electron energy.

The improved version of Stanton's code is found in all cases to agree with the experimental efficiency data to better than 10%, in most cases to within a few percent. It is of particular interest to note that the code is shown to

reproduce the efficiency spectrum of a 5.6cm thick by 12cm diameter NE213 scintillator-cell to within a few percent for thresholds of 0.256, 1.02 and 2.56MeV equivalent-electron energy. The geometry of this cell is almost identical to that of the one used in the present work (5cm thick by 12.4cm diameter), and the type of scintillator used is the same. Also of importance is the fact that the code is shown to well reproduce the efficiency curves of the 5.6cm by 12cm diameter cell for thresholds as low as 0.256MeV. A threshold of ~0.25MeV was set on most of the neutron detectors used in the present work.

An example of the output of the code is shown in figure 2.22.

CHAPTER 4
ANOMALOUS FEATURES IN THE BREAKUP OF ^{9}BE

4.1 Introduction

During the course of the experimental work described here, anomalous features were observed in the ^{9}Be breakup data. A considerable amount of computational and experimental effort was expended in trying to understand these anomalies. The results and conclusions of this work are discussed in this chapter.

The anomalous features were present in both the α+α data and in the α+α+n triple coincidence data. Some of the α+α data that was collected with the strip-detector telescope is given in figure 4.1. This figure shows the experimental α+α coincidence yield as a function of the α-particle energies for the reaction ^{9}Be+^{12}C at $E_{^{9}Be}$=90MeV. The spectrum was obtained at a telescope angle of 16°. Kinematic loci have been plotted on the spectrum for α-α relative energy values of ε=0.092, 0.6 and 3.132MeV. The values 0.092MeV and 3.132MeV correspond to the relative energies produced by the decay of the ground and first excited states of ^{8}Be. As can be seen, the two central diagonal ridges can be attributed to the breakup of the ground state of ^{8}Be. There is also some evidence of breakup from the broad first excited state of ^{8}Be. Of particular interest are the two strong distributions located along the ε=0.6MeV curves. The symmetry of these distributions, about the central diagonal, suggests strongly that they are produced by the decay of a state of ^{8}Be. However, there is no known state of ^{8}Be at the appropriate excitation energy of ∿0.5MeV.

The anomalous features are not restricted to the data obtained with the ^{12}C target. They are also present in the $E_{\alpha 1}/E_{\alpha 2}$ spectra for the reaction ^{9}Be+^{120}Sn at 90MeV; for example see figure 4.2. A study of the α+α+n triple coincidence data reveals once again the same anomalous distributions. The triple coincidence data shows that the anomalous α+α+n events are produced in reactions in which the target is left in either its ground state or in one of its low lying excited states. This rules out transfer reactions as a possible explanation for the anomalous α+α+n events. It is, of course, possible that more than one mechanism is responsible for the anomalous data, and that the

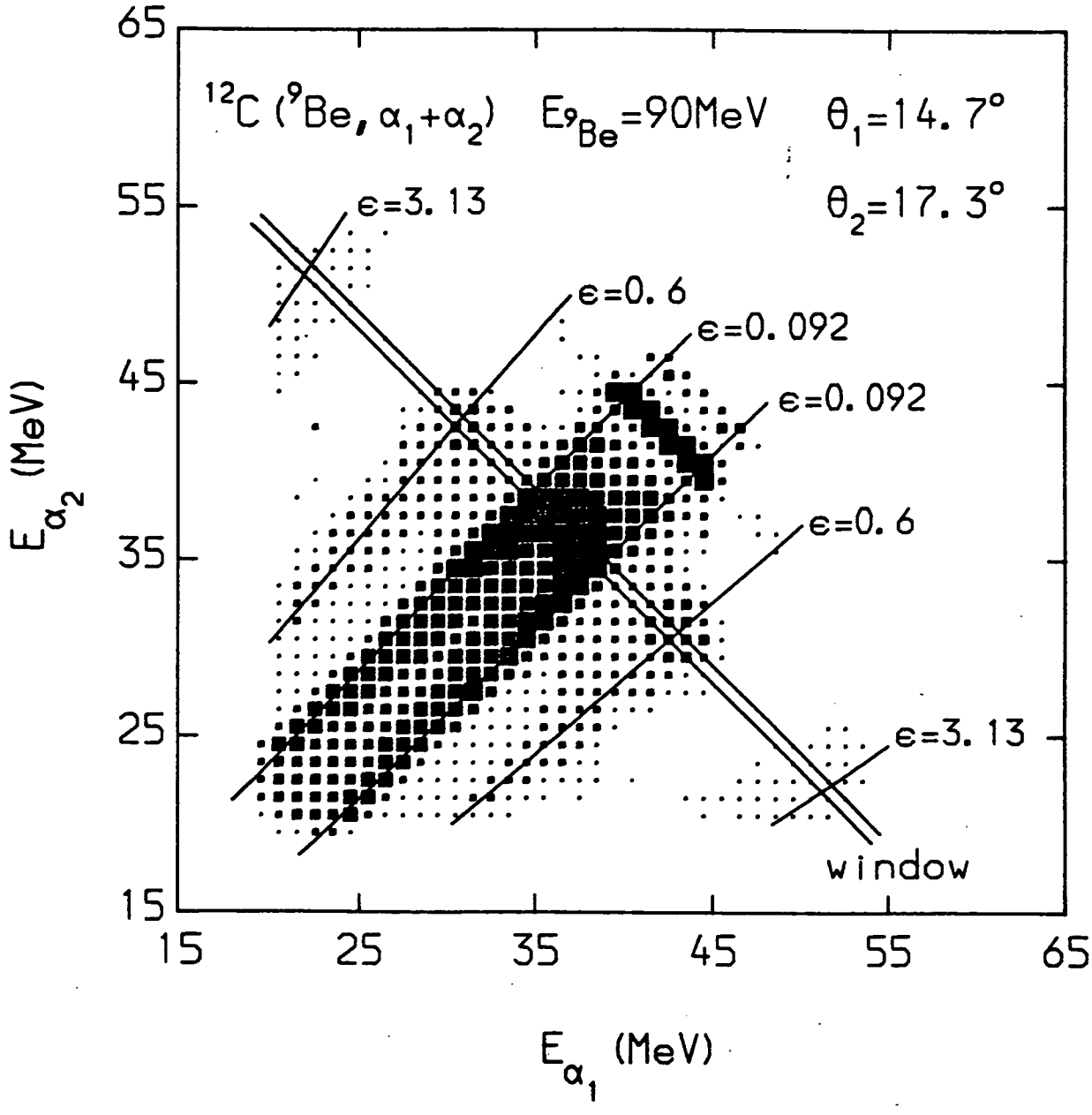

Figure 4.1: α+α coincidence data collected with the strip-detector telescope on the reaction $^{9}Be+^{12}C$ at $E_{^9Be}$=90MeV. The α+α coincidence yield is shown as a function of the α-particle energies. θ_1 and θ_2 are the scattering angles of the two sections of the strip-detectors in which α_1 and α_2 were detected. The window covers the energy range $73MeV<E_{\alpha1}+E_{\alpha2}<74MeV$.

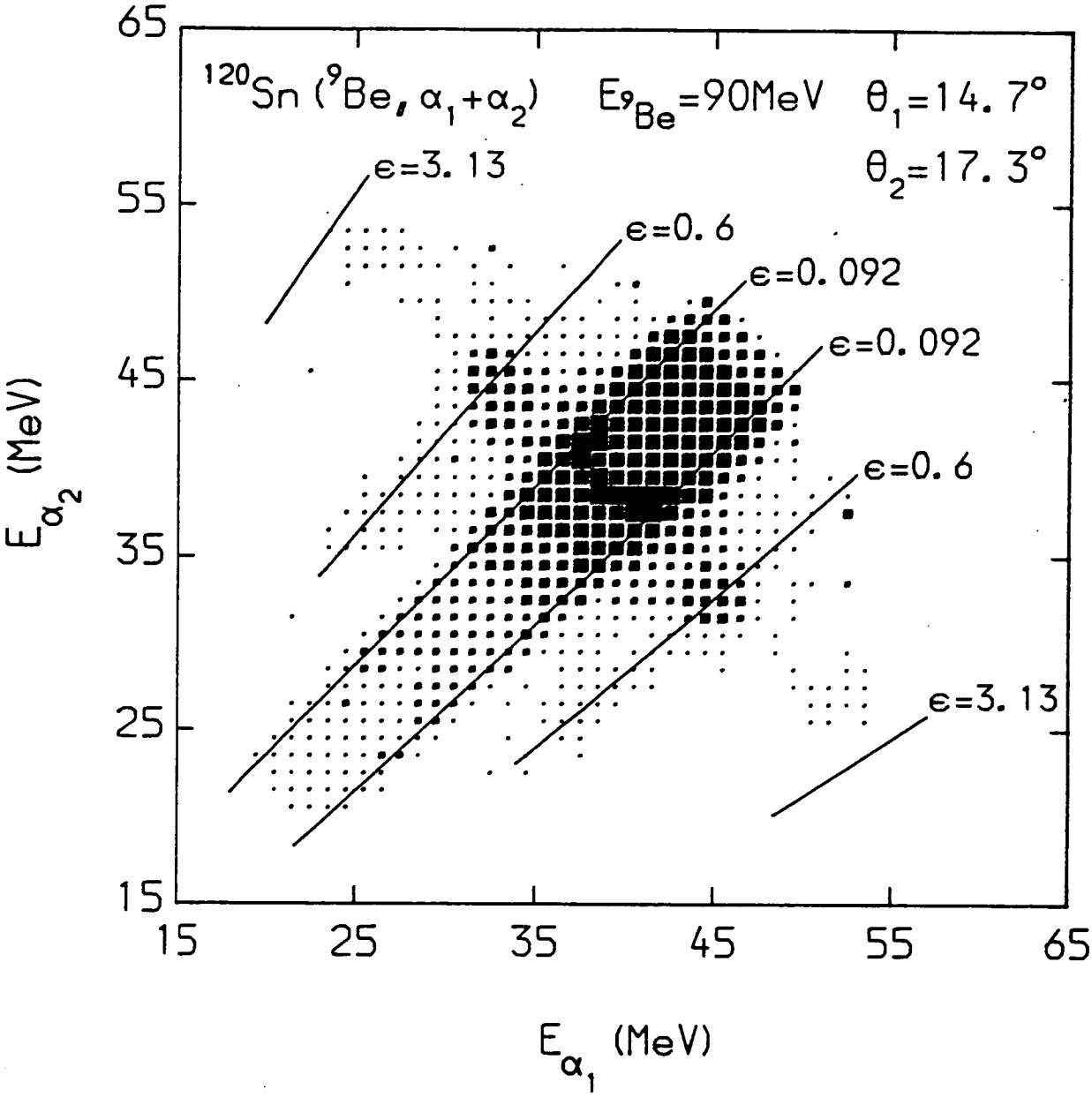

Figure 4.2: α+α coincidence data collected with the strip-detector telescope on the reaction ^{9}Be+^{120}Sn at $E_{^9Be}$=90MeV. The α+α coincidence yield is shown as a function of the α-particle energies. θ_1 and θ_2 are the scattering angles of the two sections of the strip-detectors in which α_1 and α_2 were detected.

anomalous distributions in the inclusive α+α data have a contribution from a mechanism which involves mass transfer. However, calculations suggest that the yield of the anomalous α+α+n reactions is sufficient to explain all of the strength of the α+α inclusive anomalous data.

The events within the anomalous distributions account for a substantial fraction of the experimental data. It was therefore of some importance to understand their origin, particularly since an instrumental origin might indicate a problem with the rest of the data.

Four possible explanations of the data were considered:

1. That the anomalous features resulted from an instrumental effect introduced by the use of strip-detectors.
2. That a state in ^{8}Be at E_x=0.5MeV actually exists (this is very unlikely).
3. That the anomalies are another manifestation of the *ghost* of the ground state of ^{8}Be, which has been reported by several authors.
4. That the α+α data can be explained in terms of the breakup of ^{9}Be into a channel other than the $^{8}Be_{gs}$+n channel

These possibilities are discussed in the following sections.

4.2 Possible Explanations of the Anomalous Data

4.2.1 Instrumental Effect

The ^{8}Be-telescope (§2.6) which was used to collect the data of figures 4.1 and 4.2 was a fairly complicated piece of apparatus. In total it contained four strip-detectors, 40 strips, 49 wires, 58 solder connections, 9 Conex connectors and 40 socket connectors, plus radioactive sources and magnets. In addition, strip-detectors have only recently become available, and their properties are not yet fully understood. Hence there were reasonable grounds to suspect an instrumental cause of the anomalous data. Nevertheless, it was hard to conceive of a detector effect that could produce peaks in the middle of an otherwise normal spectrum. Furthermore, the design of the ^{8}Be-telescope was tested by studying the reactions ^{12}C,^{120}Sn(^{7}Li,^{8}Be) at $E_{^{7}Li}$= 70MeV; these tests showed no sign of the anomalous features observed in the ^{9}Be induced reactions.

To determine whether an instrumental effect was responsible, $\alpha+\alpha$ coincidence data was collected on the reactions $^{9}Be+^{12}C$ and $^{9}Be+^{120}Sn$ at $E_{^{9}Be}$=90MeV with a conventional ^{8}Be-telescope.

The data was obtained at the Nuclear Structure Facility using the 1m scattering chamber on the 79° beam line (see §2.4). The detection system consisted of two conventional charged-particle telescopes. These were mounted in a close vertical geometry with one slightly above and one slightly below the reaction plane, such that there was a separation angle of 6° between the centres of the telescope collimators. The detection geometry employed was identical to that of figure 2.6.

The $\alpha+\alpha$ coincidence spectrum for the ^{12}C target is shown in figure 4.3. Although this spectrum is slightly different in detail to that of figure 4.1, the features of both spectra are the same. In particular the anomalous distributions are present in this data as well.

The apparatus used to collect this data was well trusted (since it had been used successfully on many prior occasions). Hence it was concluded that an instrumental cause for the anomalous distributions was very unlikely.

4.2.2 New State in ^{8}Be ?

The discovery of a new, low-lying state in a light nucleus is an extremely rare event. In fact, for a nucleus of such fundamental importance as ^{8}Be, which has been studied exhaustively both experimentally and theoretically, it is most unlikely that a state at E_x=0.5MeV could have been missed, even if such a state could only be excited by a small number of reactions. Nevertheless, it was of interest to see if a new state in ^{8}Be could, at least in principle, fit the data.

To pursue this objective, Monte-Carlo computer calculations were undertaken to simulate the $\alpha+\alpha$ coincidence data that would be obtained from the decay of a state in ^{8}Be at $E_x \backsim 0.5$MeV. It was found that if the state has a width of $\backsim$0.2MeV and is produced in the decay of the 2.43MeV state of ^{9}Be (i.e. via the reaction, $^{9}Be^{*}_{2.43} \rightarrow {}^{8}Be^{*}_{0.5}+n$), then the data is well reproduced.

Creation of $^{8}Be^{*}_{0.5}$ nuclei via the breakup of any state of ^{9}Be, other than it's 2.43MeV state, produces $E_{\alpha 1}/E_{\alpha 2}$ distributions which are either too extended or too smooth.

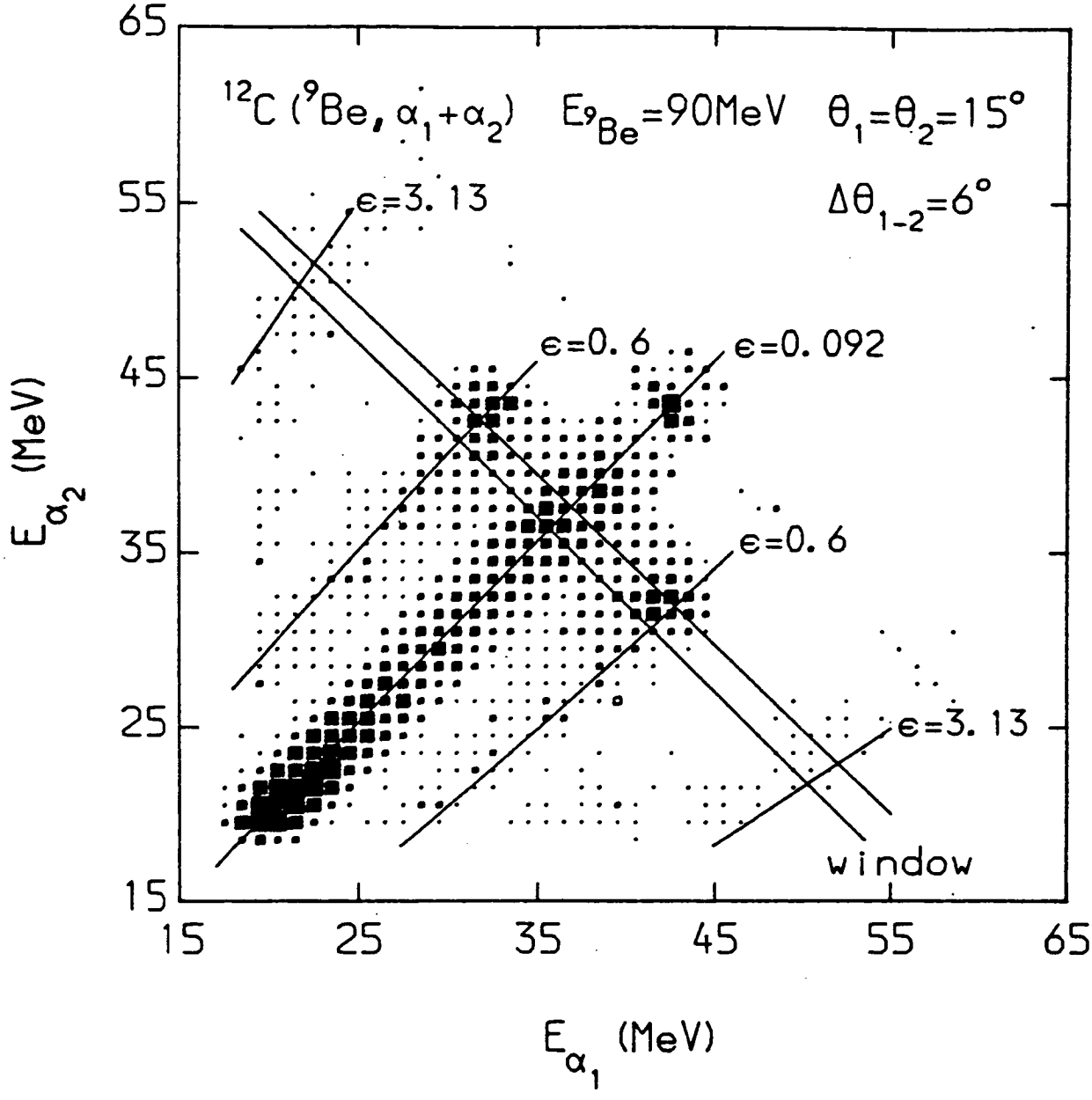

Figure 4.3: α+α coincidence data collected with the conventional ^{8}Be-telescope on the reaction ^{9}Be+^{12}C at $E_{^9Be}$=90MeV. The α+α coincidence yield is shown as a function of the α-particle energies. θ_1, θ_2 are the scattering angles of telescopes 1 and 2, $\Delta\theta_{1-2}$ is the angle between the centres of the telescope collimators. The window covers the energy range 72MeV<$E_{\alpha1}$+$E_{\alpha2}$<75MeV.

To compare the data with the simulation, it is convenient to work with the projected energy spectra. These can be created by placing a 2-dimensional window on the $E_{\alpha 1}/E_{\alpha 2}$ plane, and then producing α_1 and α_2 energy spectra for the events that fall within the window. Alternatively, the projected spectra can be created by putting a window on the summed α-energy spectrum (i.e. the $E_{\alpha 1}+E_{\alpha 2}$ spectrum). Figure 4.4 shows the summed α-energy spectrum for the reaction $^{9}Be+^{12}C$ at $E_{^{9}Be}$=90MeV. This spectrum was obtained using the strip-detector telescope at an angle of 16°. It displays the same data as was shown in figure 4.1, but in a different manner.

The peaks in figure 4.4 (at $E_{\alpha 1}+E_{\alpha 2}>75$MeV) are produced by neutron transfer reactions of the form:

$$^{12}C(^{9}Be,^{8}Be)^{13}C^{*}_{0.0,\ 3.7,\ 7.5,\ etc}$$

The broad *bump* centred about $E_{\alpha 1}+E_{\alpha 2}\sim 73$MeV includes ^{8}Be events that were produced by transfer and breakup reactions. It also includes the anomalous α+α events. The window over the *bump* covers the energy range $E_{\alpha 1}+E_{\alpha 2}$=73-74MeV. Figure 4.5 shows the projected α_1 energy spectrum for the events within the window; these events correspond to the events within the window on the $E_{\alpha 1}/E_{\alpha 2}$ spectrum of figure 4.1. On the upper axis of the α_1 projected energy spectrum, the α-α relative energies are plotted. This spectrum shows the structure of the data very clearly. The two central peaks correspond to the ground state of ^{8}Be (ε=0.092MeV). The two weak distributions at ε=3.13MeV are due to the decay of the first excited state of ^{8}Be. At ε=0.6MeV the two anomalous peaks can be seen.

Figure 4.6 shows a Monte-Carlo simulation of the α_1 energy spectrum which would be produced by the reaction:

$$^{12}C(^{9}Be^{*}_{2.43}\rightarrow ^{8}Be^{*}_{0.5}+n)^{12}C_{gs}$$

This simulation was performed for the detection geometry and sorting conditions that were used to collect the experimental α_1 spectrum of figure 4.5. A comparison of figures 4.5 and 4.6 shows that the anomalous features of the data can be explained by the existence of a state in ^{8}Be at E_x=0.5MeV. However, none of the existing experimental data on the states of ^{8}Be or the theoretical models for the structure of the ^{8}Be nucleus, provide any evidence for the existence of such a state. Therefore, other explanations were

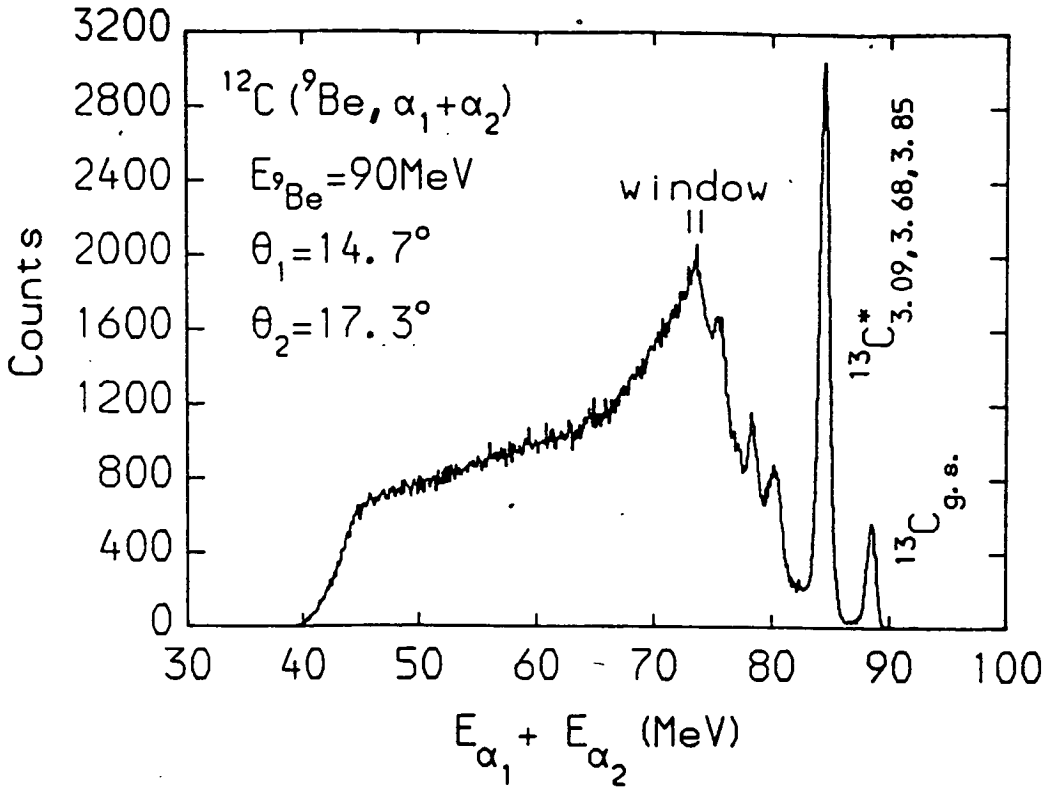

Figure 4.4: α+α coincidence data collected with the strip-detector telescope on the reaction $^{9}Be+^{12}C$ at $E_{^{9}Be}$=90MeV. The α+α coincidence yield is shown as a function of the summed α-particle energy. θ_1 and θ_2 are the scattering angles of the two sections of the strip-detectors in which α_1 and α_2 were detected. The window covers the energy range 73MeV<$E_{\alpha 1}$+$E_{\alpha 2}$<74MeV.

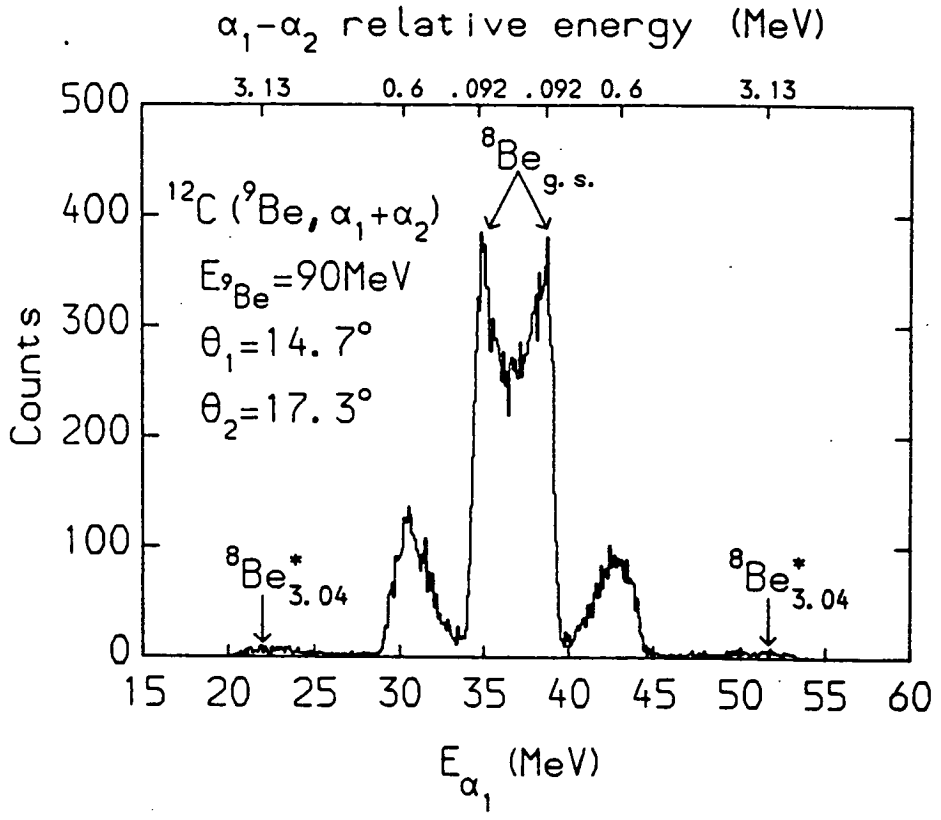

Figure 4.5: Projected α_1 energy spectrum for the events located within the window on the summed α energy spectrum of figure 4.4 (these events also lie within the window shown in figure 4.1).

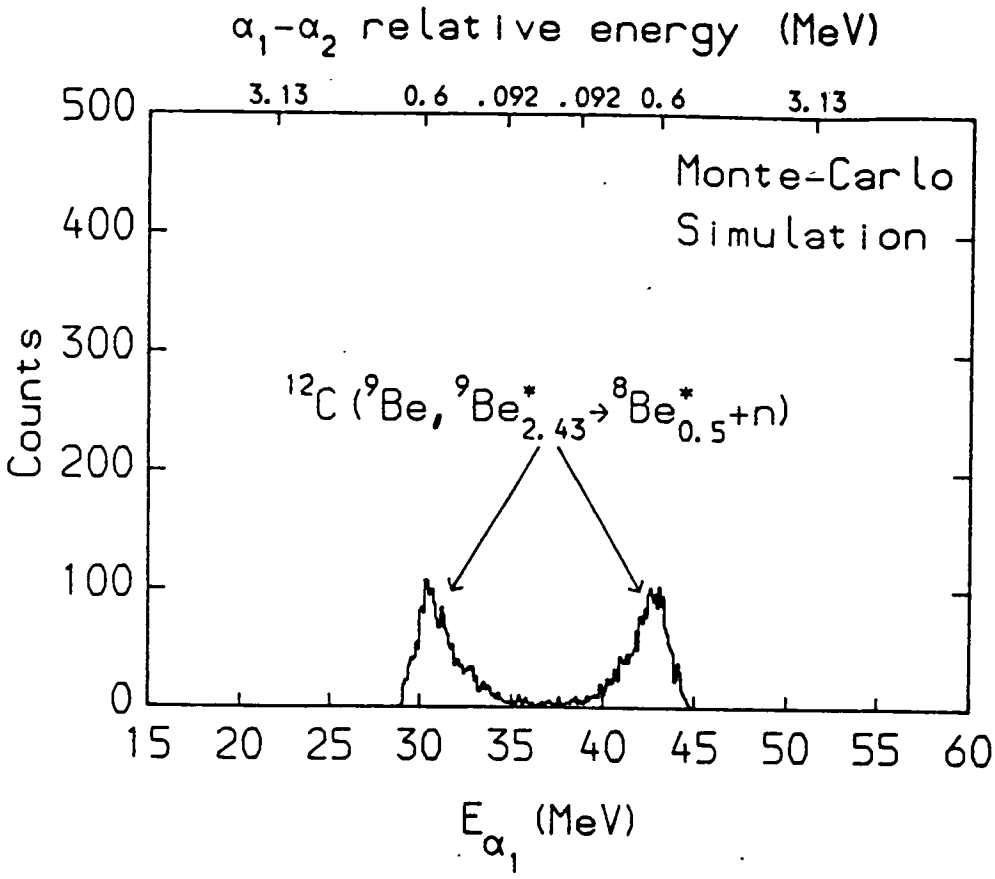

Figure 4.6: Monte-Carlo simulation of the projected α_1 energy spectrum of figure 4.5, for the reaction $^{12}C(^{9}Be,^{9}Be^{*}_{2.43}\rightarrow^{8}Be^{*}_{0.5}+n)^{12}C_{g.s.}$, $^{8}Be^{*}_{0.5}\rightarrow\alpha+\alpha$ at $E_{^{9}Be}$=90MeV.

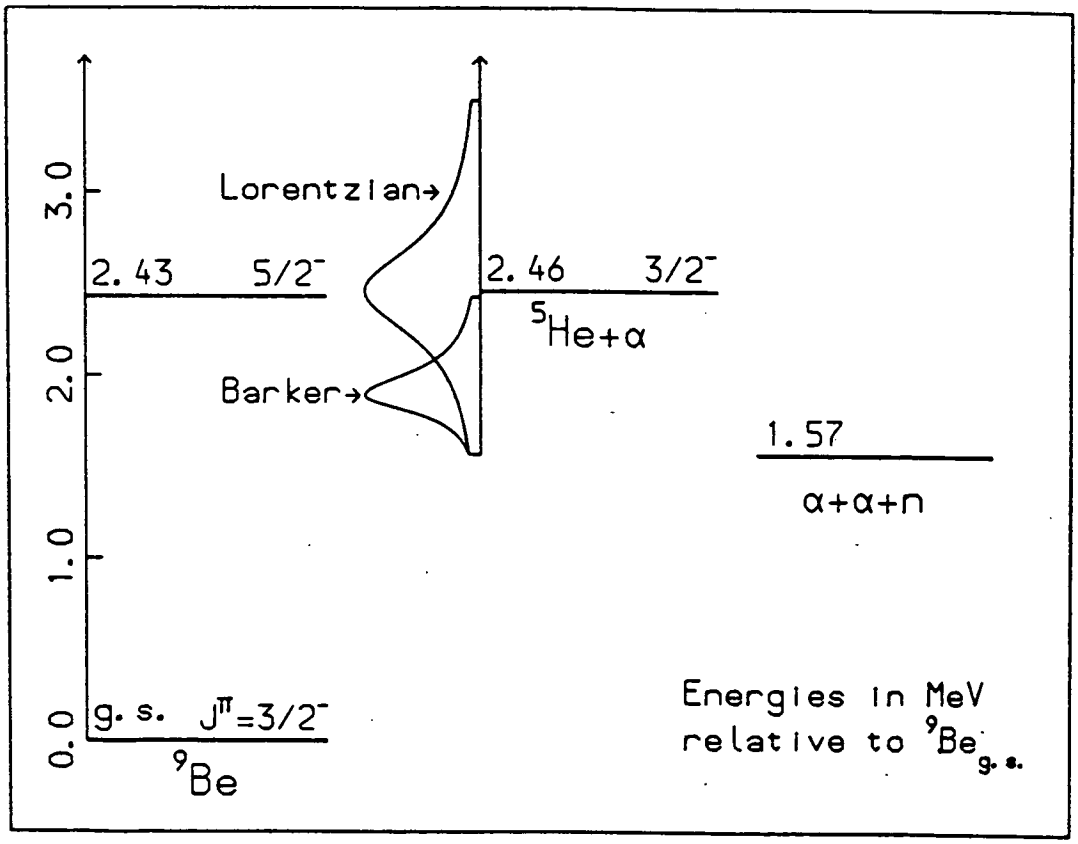

Figure 4.7: Energy level diagram for the reaction $^{9}Be^{*}_{2.43}\rightarrow^{5}He+\alpha$, $^{5}He\rightarrow\alpha+n$.

considered.

4.2.3 ^{8}Be Ghost State

In light-ion transfer reactions, an anomalous feature has sometimes been observed in those reaction channels where ^{8}Be is the residual nucleus [BARK76, OVER81, BECC81]. This feature consists of an unexpected peak in the ^{8}Be excitation spectrum at an energy of (0.6±0.1)MeV with a width of ∿1.5MeV. The anomaly has been interpreted as a *ghost* of the ground state of ^{8}Be. It has been shown by R-matrix theory [BARK62] that such a ghost-state can be produced if a narrow state is close to a decay threshold. In the case of ^{8}Be, the ground state is 92keV above the α-particle decay threshold, and a weak broad ghost-state at E_x∿0.6MeV is predicted [BARK76]. Although there has been some controversy over the interpretation of the anomalies, the higher quality data is consistent with the predictions of the ghost-state theory.

As mentioned previously, the present data can be fitted by assuming a state in ^{8}Be at E_x=0.5MeV. This excitation energy is very similar to that of the ghost state, therefore it is natural to ask if a ghost-state interpretation can explain the present data. For the following reasons though, such an explanation of the data is quite unsatisfactory:

1. The ghost-state predicted by the R-matrix theory [BARK76] has a width of ∿1.5MeV. To fit the present data, a width of 0.2MeV is required.
2. Calculations for a ghost-state give an intensity of about 10% relative to the ground state strength, whereas a value of ∿100% is necessary to explain the the ^{12}C+^{9}Be data in the region $E_{^{8}Be}$∿73MeV.
3. The calculations also predict that the relative intensity of the ghost-state to the ground state should be approximately independent of the mechanism of production of the ^{8}Be nuclei. However, to fit the present data a strength of ∿30% is required for the ^{120}Sn target and ∿100% for the ^{12}C target.
4. The relative intensity should also be approximately independent of the ^{8}Be kinetic energy. But as can be seen from figure 4.1, the ratio of the strength of the anomalous peaks to the strength of the ground state peaks varies dramatically with ^{8}Be kinetic energy. (The ^{8}Be kinetic energy is proportional to the distance along the kinematic loci).

These observations indicate that the anomalous distributions in the present data are unlikely to be explained in terms of a ghost of the ground

state of ^{8}Be.

4.2.4 Other Breakup Modes of ^{9}Be

To find a satisfactory explanation of the anomalous events, all of the likely ^{9}Be breakup reactions were investigated by calculating the expected experimental spectra using a Monte-Carlo simulation program. As a result of these simulations, the number of plausible reactions was narrowed to three:

1. $^{9}Be \rightarrow {}^{5}He_{gs} + \alpha$, $^{5}He_{gs} \rightarrow \alpha + n$
2. $^{9}Be \rightarrow {}^{9}Be^{*}_{2.43} \rightarrow {}^{5}He_{gs} + \alpha$, $^{5}He_{gs} \rightarrow \alpha + n$
3. $^{9}Be \rightarrow {}^{9}Be^{*}_{2.43} \rightarrow \alpha + \alpha + n$

Reaction 1 involves the direct 2-body breakup of the ^{9}Be projectile in the field of the target nucleus i.e. the breakup does not proceed via an intermediate state of ^{9}Be. As discussed in §1.3.2 such a direct breakup process has been observed for ^{7}Li projectiles fragmenting into the α+t channel [SHOT84]. At forward scattering angles, the Coulomb interaction between the projectile and the target dominates the breakup process. For ^{7}Li the main breakup reaction strength is through the E1 multipole interaction. For the direct breakup of ^{9}Be into the $^{5}He_{gs}+\alpha$ channel, the lowest possible Coulomb multipole is E2. This E2 character for the $^{9}Be \rightarrow {}^{5}He_{gs}+\alpha$ reaction will suppress the yield by $\curvearrowdown$1/200 compared to the ^{7}Li case. Such a yield is a factor of $\curvearrowdown$200 too low to explain the anomalous peaks in the ^{9}Be data. Even without this suppression, it is unlikely that this process, or any other direct breakup process (e.g. $^{9}Be \rightarrow \alpha+\alpha+n$ 3-body breakup), could reproduce the features of the present data. The reason for this is that the features of the anomalous peaks remain the same for scattering angles from 13.5° to 40°. This angular range corresponds to a wide range of impact parameters for the projectile on the target. In a direct breakup reaction the fragments are produced at or near the target surface. The final-state interactions of the fragments with the target will strongly depend on the projectile impact parameter. Therefore, the correlations between the fragments, and so the features of any anomalous peaks, will rapidly change with the observed scattering angles. This behaviour is not observed in the present data and indicates that the anomalous peaks cannot be explained by direct breakup processes.

The reason for considering reactions 2 and 3 is that the 2.43MeV $5/2^{-}$ state

of ^{9}Be has only a 7% decay branch to $^{8}Be_{gs}$+n [AJZE84]. The remaining decay strength is in the $^{5}He_{gs}$+α sequential breakup channel (reaction 2) with possibly a contribution from the direct 3-body α+α+n disintegration process (reaction 3). Because the Q-value for reactions 2 and 3 is -1.66MeV, the fragments are given relative energies which are consistent with the data.

Reaction 2 was numerically simulated using a ^{5}He-α relative energy distribution supplied by F.Barker [BARK87]. This distribution was calculated by combining a density of states function with a d-wave penetration factor for the $^{9}Be \rightarrow ^{5}He+\alpha$ breakup process. The energy level diagram for the $^{9}Be^{*}_{2.43} \rightarrow ^{5}He+\alpha$ reaction is shown in figure 4.7. On the diagram, a Lorentzian line-shape for the ground state of ^{5}He has been plotted. Also drawn on the diagram is the ^{5}He excitation distribution corresponding to Barker's ^{5}He-α relative energy distribution.

Figure 4.8 shows a Monte-Carlo simulation, using Barker's relative energy spectrum, of the α_1 projected energy spectrum that would be produced by the reaction $^{9}Be^{*}_{2.43} \rightarrow ^{5}He+\alpha$. The simulation was performed for the detection system and sorting conditions that were used to collect the data of figure 4.5 (i.e. the strip-detector telescope at 16° and $73MeV < E_{\alpha 1}+E_{\alpha 2} < 74MeV$). Also shown in figure 4.8 are simulations of the breakup of the ground and first excited states of ^{8}Be. The relative intensities of the three reactions contributing to the spectrum of figure 4.8 were adjusted to fit the projected spectrum of figure 4.5. As can be seen a good fit has been achieved.

It is of interest to see whether a simulation based on the $^{9}Be^{*}_{2.43} \rightarrow ^{5}He+\alpha$ reaction can also reproduce the data obtained with the conventional ^{8}Be-telescope. This is because the efficiency of each detection system varies with the α-α relative energy in a different manner. Therefore each system is sensitive to different parts of the α-α relative energy spectrum.

Figure 4.9 illustrates some of the data obtained with the conventional ^{8}Be-telescope. It shows the α_1 projected energy spectrum created from the events within the $72MeV < E_{\alpha 1}+E_{\alpha 2} < 75MeV$ window on the $E_{\alpha 1}/E_{\alpha 2}$ spectrum of figure 4.3. In this projected spectrum, the two kinematic solutions for breakup from the ground state of ^{8}Be are not resolved, unlike in figure 4.5, where the two solutions are visible. Furthermore, the number of anomalous events relative to the number of ground state events is substantially larger

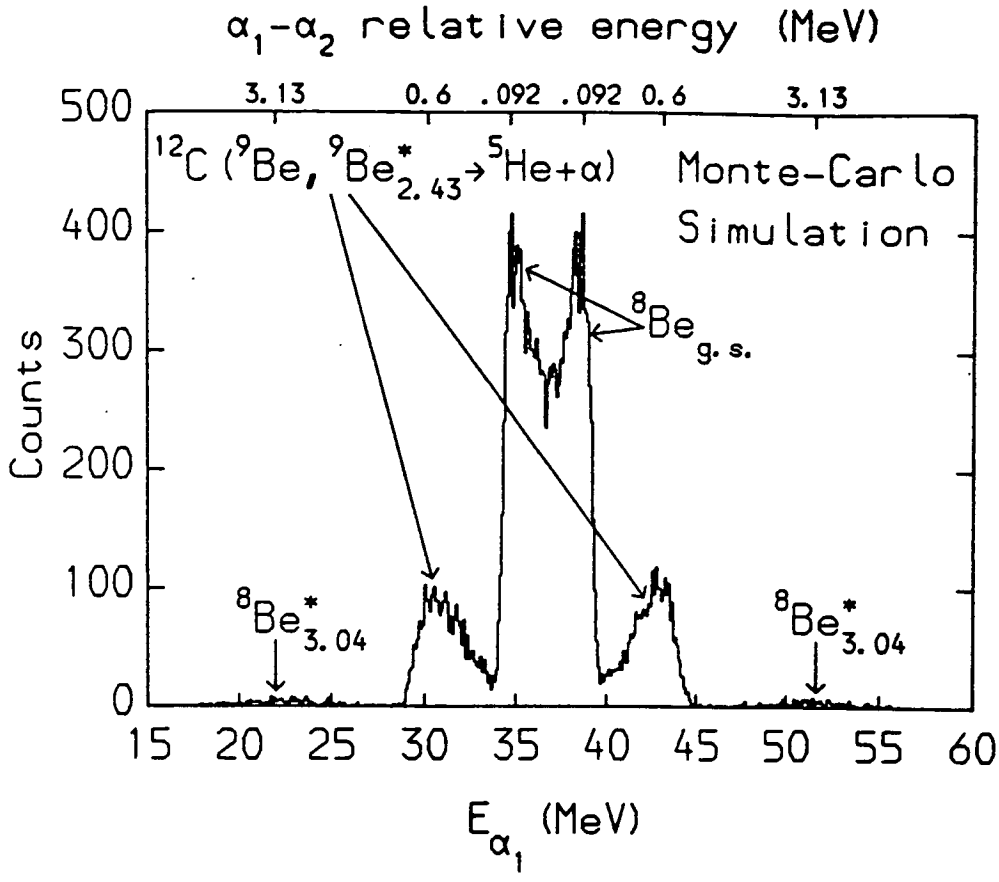

Figure 4.8: Monte-Carlo simulation of the projected α_1 energy spectrum of figure 4.5, for the reactions $^{12}C(^{9}Be,^{9}Be^{*}_{2.43}\rightarrow^{5}He+\alpha)^{12}C_{g.s.}$, $^{5}He\rightarrow\alpha+n$ and $^{8}Be^{*}_{g.s.,3.04}\rightarrow\alpha+\alpha$ at $E_{^{9}Be}$=90MeV.

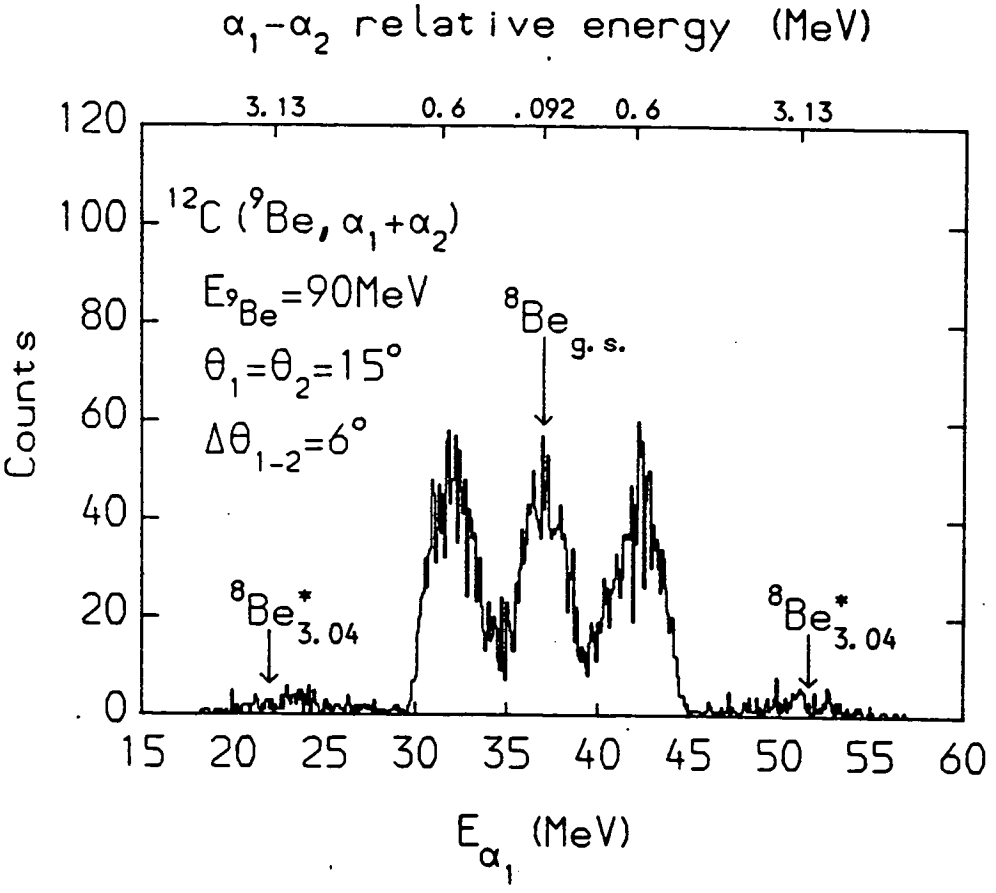

Figure 4.9: Projected α_1 energy spectrum for the events located within the window on the $E_{\alpha1}/E_{\alpha2}$ spectrum of figure 4.3.

than in figure 4.5. These points demonstrate the differences between the properties of the detection system.

A Monte-Carlo simulation of the projected spectrum of figure 4.9 is shown in figure 4.10. The same three reactions that were used to simulate the data obtained with the strip-detector telescope (figure 4.5) were used to produce this simulation i.e. $^{9}Be^{*}_{2.43}\rightarrow{}^{5}He+\alpha$, $^{8}Be_{gs}\rightarrow\alpha+\alpha$, $^{8}Be^{*}_{3.04}\rightarrow\alpha+\alpha$

The fit achieved between the simulation (figure 4.10) and the data (figure 4.9) is not as good as it was for the strip-detector telescope data. It was found that the fit could not be substantially improved by adjusting the $^{5}He+\alpha$ relative energy spectrum. However, if it is assumed that the $^{9}Be^{*}_{2.43}$ ejectiles are strongly aligned, then a good agreement is obtained between the simulation and the data. A simulation assuming complete alignment of the ejectile to the $m_{5/2}=5/2$ and $-5/2$ sub-states is shown in figure 4.11 (the quantization axis being perpendicular to the reaction plane). This simulation reproduces the data of figure 4.10 very well. In addition, it can be shown that the alignment of the $^{9}Be^{*}_{2.43}$ ejectile makes very little difference to the simulations of the strip-detector telescope data. Therefore it seems that the breakup of the 2.43MeV state of ^{9}Be into the $^{5}He+\alpha$ channel provides a good explanation for the anomalous peaks.

It is possible that a reaction of type 3 could also reproduce the data well. In this case, the shape of the projected α energy spectra would depend on the relative energy spectra of the three fragments. If these are dominated by the barrier penetration factor between the α-particles then one would achieve fits comparable to those shown in figures 4.8 and 4.11. Therefore, it is not possible to distinguish between reaction modes 2 and 3 from the present data.

If either reaction 2 or 3 is to provide a reasonable explanation of the data then the cross-section for excitation of the 2.43MeV state must be consistent with the strength of the anomalous peaks. Unfortunately, no inelastic scattering data has been published for the reaction $^{9}Be(^{12}C,^{12}C)^{9}Be^{*}_{2.43}$, so the actual excitation cross-section to the 2.43MeV state is not known. Experiments involving the inelastic scattering of a range of projectile nuclei ($^{1}H,\alpha,^{9}Be$) from ^{9}Be targets show that this state is strongly excited. For example, $\sigma(\theta_{cm.}=25^{o})\sim$20mb/sr for the reaction $^{9}Be(^{9}Be,^{9}Be)^{9}Be^{*}_{2.43}$ at 50MeV [OMAR84]. If the anomalous peaks of the present data are due to the decay of the 2.43MeV

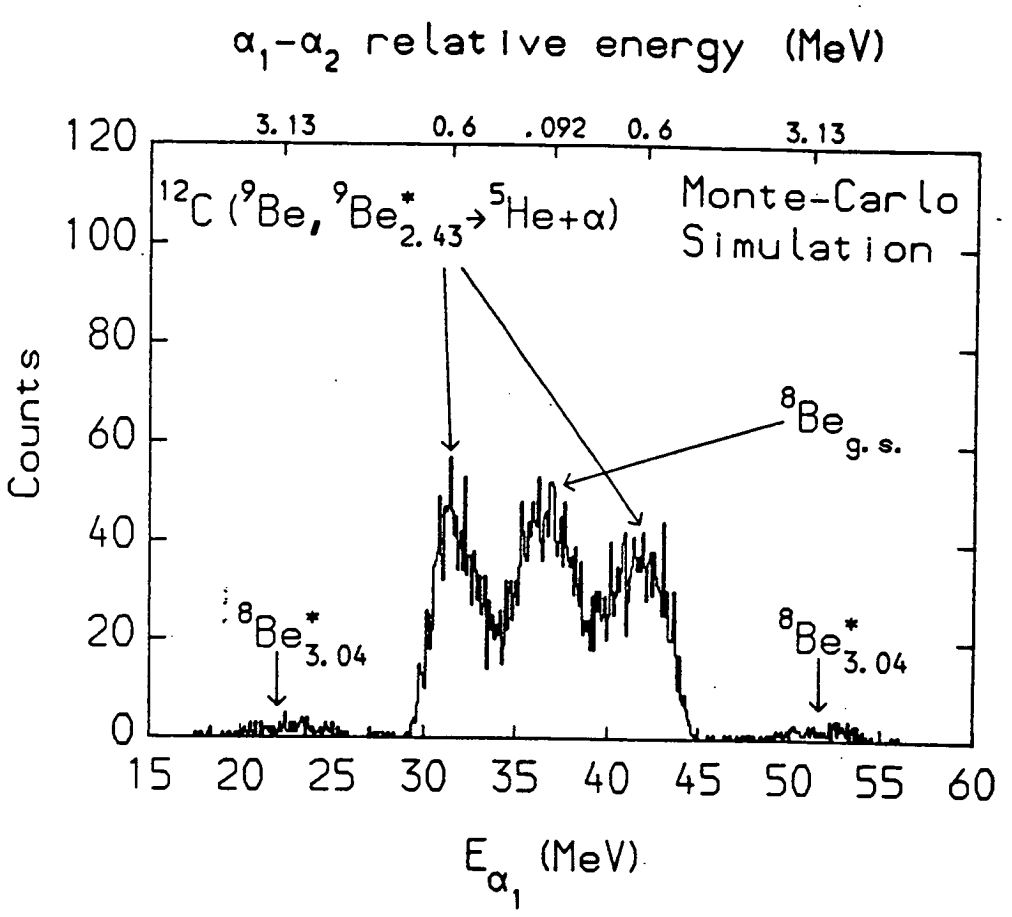

Figure 4.10: Monte-Carlo simulation of the projected α_1 energy spectrum of figure 4.9, for the reactions $^{12}C(^{9}Be,^{9}Be^{*}_{2.43}\rightarrow^{5}He+\alpha)^{12}C_{g.s.}$, $^{5}He\rightarrow\alpha+n$ and $^{8}Be^{*}_{g.s.,3.04}\rightarrow\alpha+\alpha$ at $E_{^{9}Be}$=90MeV.

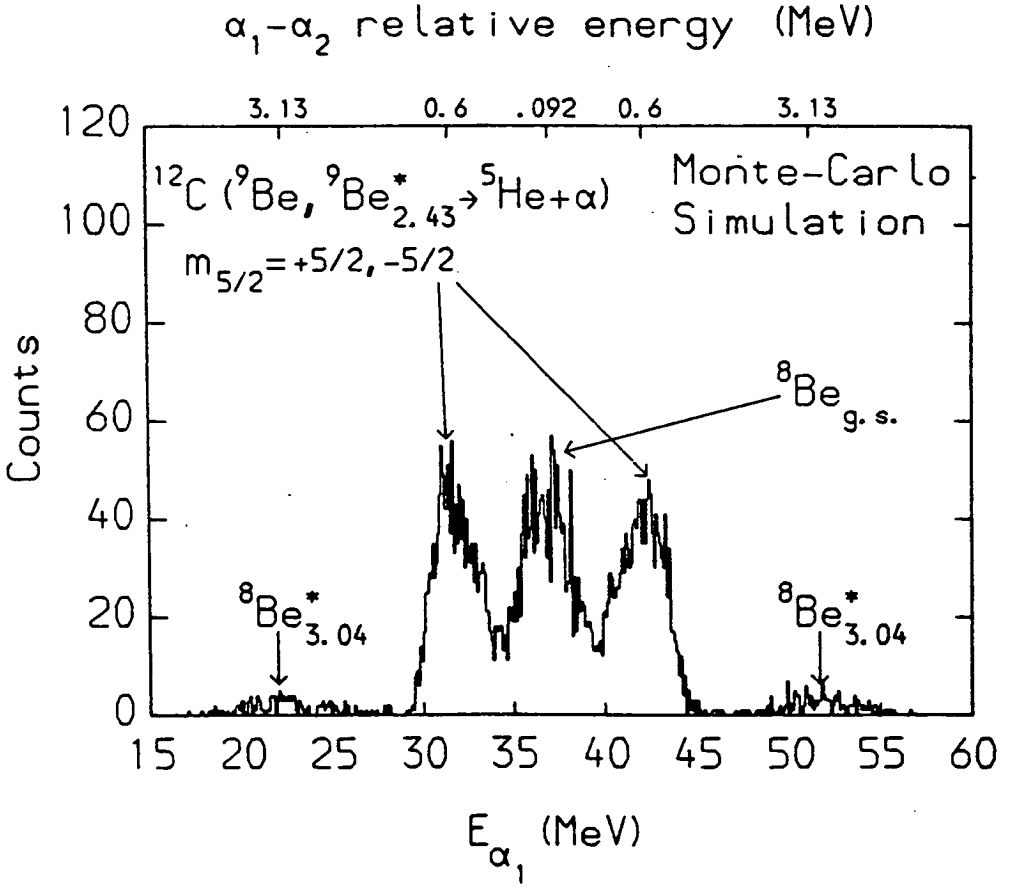

Figure 4.11: Same as figure 4.10 except that the simulation assumes complete alignment of the $^{9}Be^{*}_{2.43}$ ejectile to its $m_{5/2}$=+5/2 and -5/2 magnetic sub-states.

state, then, for the case of the ^{12}C target, the experimental yield of the anomalous events corresponds to a centre of mass differential cross-section for $^{9}Be^{*}_{2.43}$ ejectiles of (4.6±0.25)mb/sr at $\theta_{cm.}$=25.4°. Therefore it seems that the anomalous peaks have a strength consistent with their origin being associated with the decay of the 2.43MeV state of ^{9}Be.

4.3 Conclusions

Anomalous peaks have been observed in the 2α channel for the reactions $^{12}C,^{120}Sn(^{9}Be,\alpha+\alpha)$. Although these data suggest the presence of a state in ^{8}Be at ∿0.5MeV, it has been shown that they are not consistent with the ghost-state interpretation used to explain the previously observed anomaly in ^{8}Be at E_x∿0.6MeV. An explanation of the data in terms of the direct breakup of the ^{9}Be projectile has been considered, but rejected. Finally, the possibility that the anomalous peaks are due to the excitation and decay of the 2.43MeV $5/2^{-}$ state of ^{9}Be has been investigated. The results from a Monte-Carlo calculation, which simulated the breakup from the 2.43MeV state, agreed reasonably well with the experimental data, provided the ejectile was assumed to be strongly aligned. Therefore, it seems that the best available explanation of the anomalous peaks is that they are produced by the breakup of the 2.43MeV state of ^{9}Be into either the $^{5}He_{gs}+\alpha$ or α+α+n channels.

If the present interpretation of the anomalous peaks is correct, then it opens up the possibility of studying the $(^{9}Be,^{9}Be^{*}_{2.43})$ reaction without performing the experimentally difficult α+α+n triple coincidence experiment. This is due to the fact that it is possible from the α+α data alone to identify the excitation of the 2.43MeV state. Of course, it is not possible to know the state of the residual nucleus unless α+α+n data is obtained. For heavy targets however, e.g. ^{120}Sn, this is not a significant problem since most of the breakup yield is in the elastic breakup channel. Coulomb excitation to the 2.43MeV $5/2^{-}$ state is expected to be weak (E2 or M1), therefore an investigation of the $(^{9}Be,^{9}Be^{*}_{2.43})$ reaction may be an interesting way of studying nuclear breakup processes.

On the assumption that the anomalous peaks are produced by the decay of the 2.43MeV state into the $^{5}He_{gs}+\alpha$ channel and taking the branching ratio of the $^{9}Be^{*}_{2.43}\rightarrow^{5}He+\alpha$ decay as being 93% [AJZE84], angular distributions for the reactions $^{12}C(^{9}Be,^{9}Be^{*}_{2.43})^{12}C_{gs}$ and $^{120}Sn(^{9}Be,^{9}Be^{*}_{2.43})^{120}Sn_{gs}$ were calculated.

These are shown in figure 4.12. The α+α+n data was used to ensure that only elastic breakup events were selected.

The curve for the ^{120}Sn target shows Coulomb+nuclear interference inside the grazing angle. Outside the grazing angle the cross-section falls off steadily. (For 90MeV $^{9}Be+^{120}Sn$, the centre of mass grazing angle is 23.4°). By comparison with the ^{120}Sn curve, the curve for the ^{12}C target is featureless. This is not surprising since the $^{9}Be+^{12}C$ data was collected at angles considerably greater than the grazing angle. (For 90MeV $^{9}Be+^{12}C$, the centre of mass grazing angle is 5.8°).

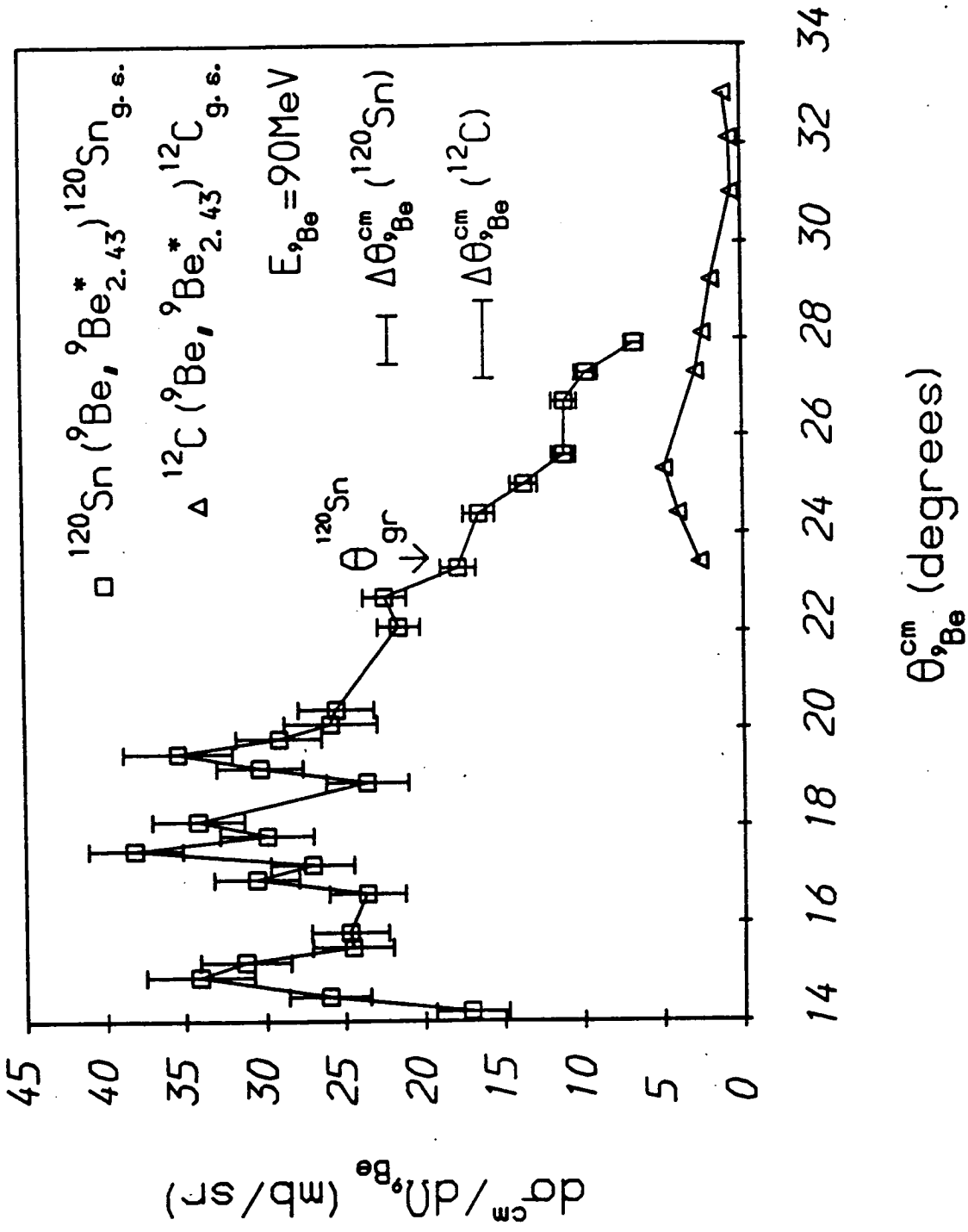

Figure 4.12: Angular distributions for the excitation of the 2.43MeV state of ^{9}Be. These distributions were calculated from the α+α+n data under the assumption that the anomalous peaks in the $E_{\alpha 1}/E_{\alpha 2}$ spectra are due to the reaction $^{9}Be^{*}_{2.43} \rightarrow ^{5}He+\alpha$.

CHAPTER 5
TRIPLE COINCIDENCE DATA

In this chapter the triple coincidence data is presented. This data was obtained with ^{120}Sn and ^{12}C targets at a beam energy of $E_{^9Be}$=90MeV. The ^{120}Sn data is discussed first.

5.1 $^{120}Sn(^9Be,\alpha+\alpha+n)$ Data

In section 2.6.6 it was described how the strip-detector based ^8Be-detector can be thought of as consisting of two separate detector telescopes. The particle-identification (PI) spectrum of telescope 1, for charged-particle + charged-particle + neutron events produced via the reaction $^9Be+^{120}Sn$ at $E_{^9Be}$=90MeV, is shown in figure 5.1a. (This spectrum was only incremented if the telescope 1 + telescope 2 TAC signal corresponded to that of a prompt coincidence event). Almost all of the yield of the telescope 1 PI spectrum is in the α-particle peak. The PI spectrum of telescope 2, for the events in which an α-particle was detected in telescope 1, is shown in figure 5.1b. Comparison of figures 5.1a and 5.1b shows that $\sim$95% of the experimental charged-particle + charged-particle + neutron yield is in the $\alpha+\alpha+n$ channel. This illustrates the loosely bound $\alpha+\alpha+n$ nature of the ^9Be nucleus.

The $E_{\alpha1}/E_{\alpha2}$ spectrum for the $\alpha+\alpha+n$ events is shown in figure 5.2. Kinematic loci have been plotted on this spectrum corresponding to breakup from the ground and first excited states of ^8Be (E_x=0.0 and 3.04MeV). There are two anomalous distributions located between the kinematic loci. The origin of these distributions was considered in Chapter 4. At present it is sufficient to note that the ^8Be ground-state events are well separated from the anomalous events. This separation can be clearly seen in figure 5.3. This figure is a spectrum of $(E_{\alpha1}-E_{\alpha2})/\sqrt{2}$; a quantity which is equal to the *perpendicular distance* (in MeV) of a point on the $E_{\alpha1}/E_{\alpha2}$ spectrum from the central diagonal of this spectrum i.e. the shortest distance from the point to the line given by $E_{\alpha1}=E_{\alpha2}$. The spectrum of figure 5.3 is equivalent to the spectrum which is obtained by compressing the data of the $E_{\alpha1}/E_{\alpha2}$ spectrum along the direction of the $E_{\alpha1}=E_{\alpha2}$ line.

Apart from the anomalous events, most of the detected $\alpha+\alpha+n$ events are associated with the ground-state of ^8Be. There is very little evidence of

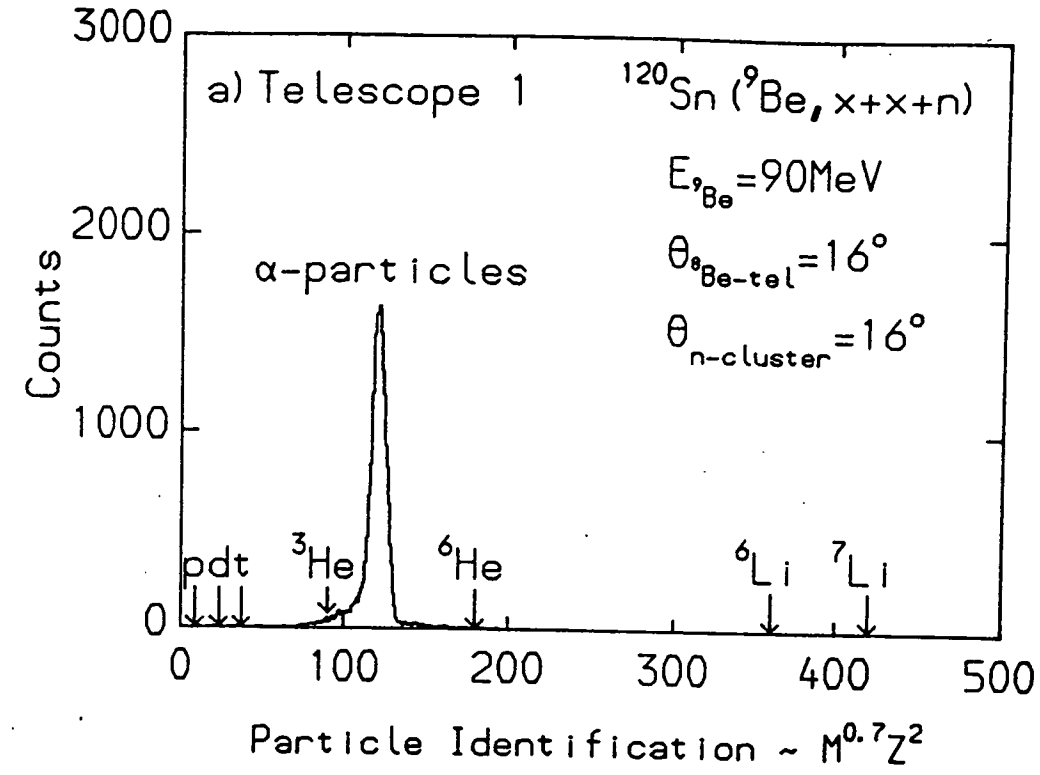

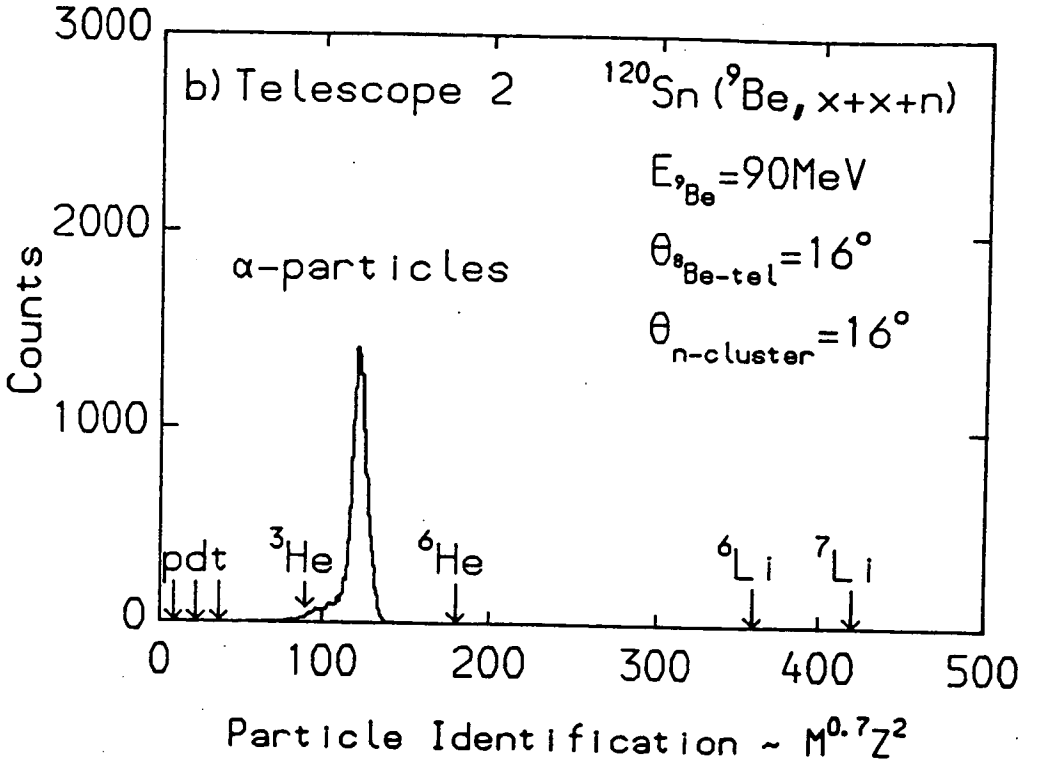

Figure 5.1: a) Particle identification spectrum of telescope 1 of the strip-detector based ^{8}Be-telescope for charged-particle + charged-particle + neutron coincidence events. b) Particle identification spectrum of telescope 2 for charged-particle + charged-particle + neutron events in which an α-particle is detected in telescope 1.

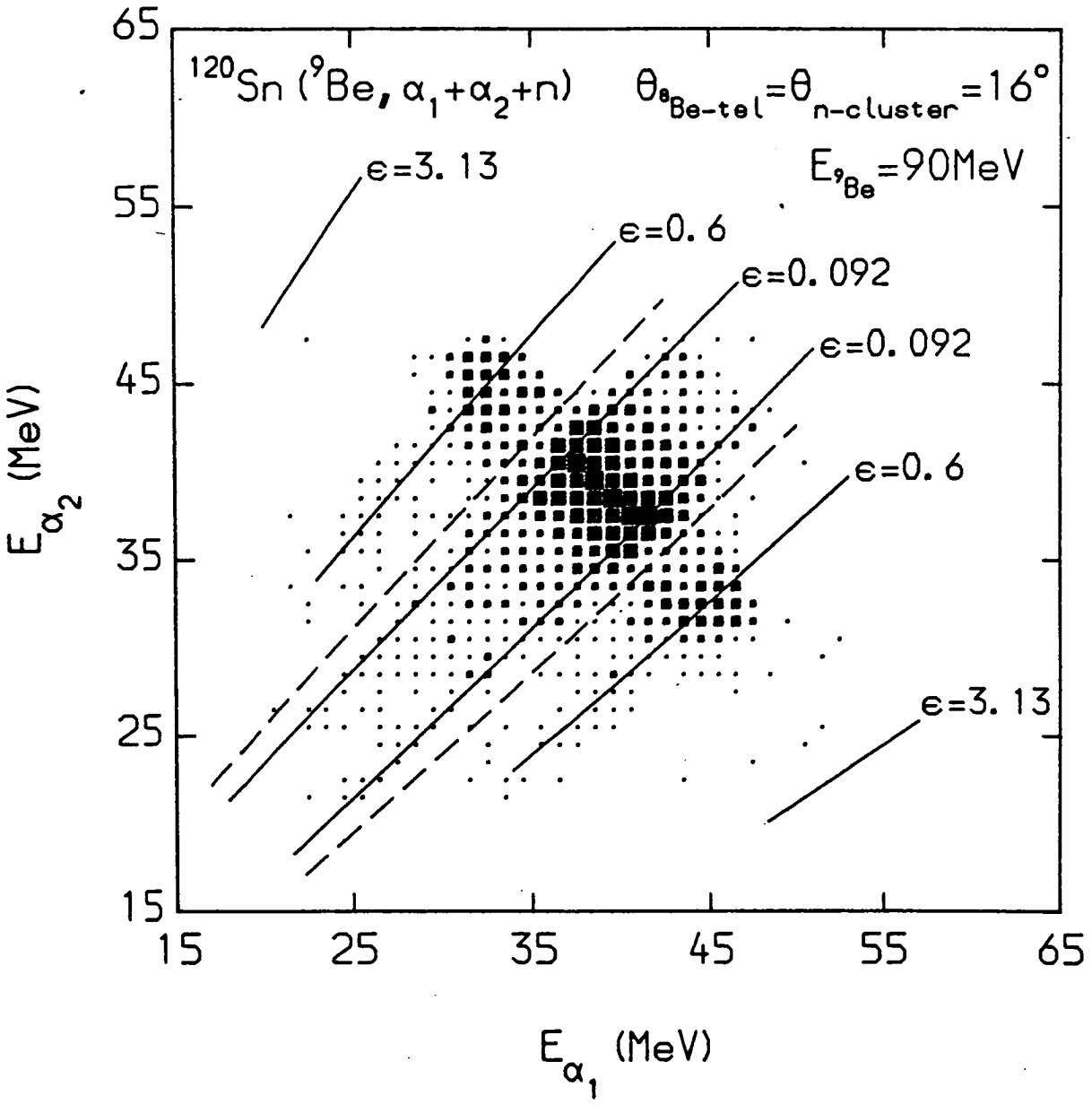

Figure 5.2: α+α+n coincidence yield for the reaction ^{9}Be+^{120}Sn as a function of the α-particle energies. The curves labelled ε=0.092 and 3.13MeV correspond to the reactions $^{8}Be_{g.s.}\rightarrow\alpha+\alpha$ and $^{8}Be^{*}_{3.04}\rightarrow\alpha+\alpha$ respectively. The dashed lines indicate the region used to define $^{8}Be_{g.s.}$ events.

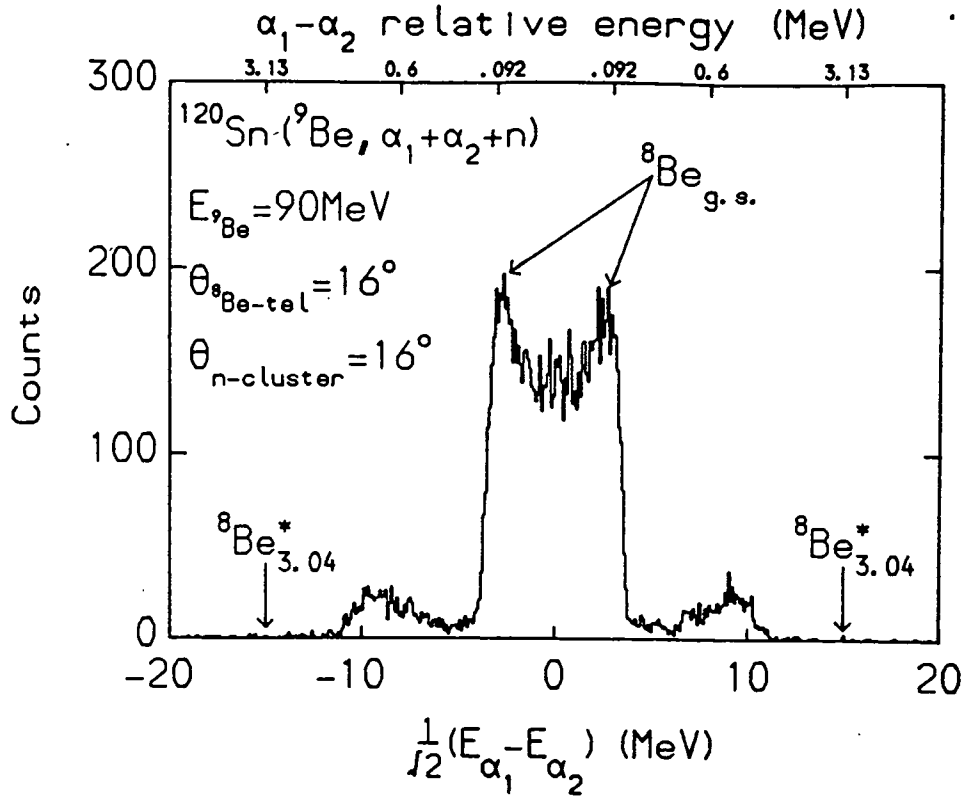

Figure 5.3: Projection of the $E_{\alpha 1}/E_{\alpha 2}$ spectrum of figure 5.2 along the line $E_{\alpha 1}=E_{\alpha 2}$. The quantity $(E_{\alpha 1}-E_{\alpha 2})/\sqrt{2}$ is equal to the *distance* from a point on the $E_{\alpha 1}/E_{\alpha 2}$ plane to the line given by $E_{\alpha 1}=E_{\alpha 2}$.

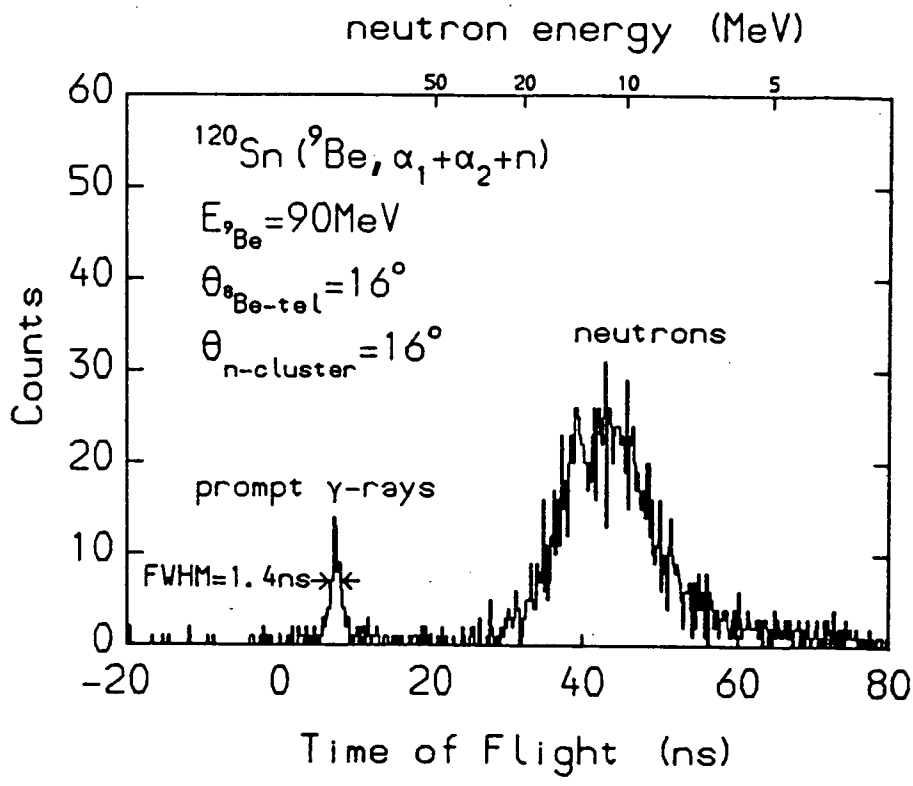

Figure 5.4: Neutron time of flight spectrum for the reaction $^{9}Be+^{120}Sn$. This spectrum includes charged-particle + γ-ray coincidences so that the prompt γ-ray peak can be seen.

breakup via the 3.04MeV first excited state of ^{8}Be. It should be noted that the detection efficiency of the ^{8}Be-telescope for $^{8}Be_{gs}$ nuclei is a factor of ∿19 larger than the efficiency for $^{8}Be^{*}_{3.04}$ nuclei (see figure 2.13). Due to the extremely poor statistics of the $^{8}Be^{*}_{3.04}$+n data and because the ^{8}Be-detector energy thresholds cut into the α-particle energy distributions produced by the decay of the 3.04MeV state, it is difficult to say anything conclusive about the reaction $^{9}Be \rightarrow {}^{8}Be^{*}_{3.04}+n$. Consequently, this reaction will not be discussed any further in this work.

On figure 5.2, dashed lines have been plotted to indicate the two-dimensional window that was used to define $^{8}Be_{gs}$ events.

5.1.1 $^{120}Sn(^{9}Be,^{8}Be_{gs}+n)$ Data

The neutron energy was determined from its *time of flight* . A typical neutron detector *time of flight* spectrum is shown in figure 5.4. This particular spectrum includes both charged-particle + neutron and charged-particle + γ-ray events. The FWHM of the prompt γ-ray peak is about 1.4ns, which would imply a neutron energy resolution of ∿1MeV.

The general features of the $^{8}Be_{g.s}$+n data are most easily seen from E_n/E_{8Be} two-dimensional spectra. A typical E_n/E_{8Be} spectrum is shown in figure 5.5. Kinematic loci for the reactions,

$$^{120}Sn(^{9}Be,^{8}Be_{gs}+n)^{120}Sn^{*}_{gs,\ 1.2,\ 2.3}$$

have been plotted on the spectrum. In addition, curves for ^{8}Be-neutron relative-energies of ε=0.024, 0.76 and 1.38MeV have been drawn. These values of ε correspond to breakup from the 1.69, 2.43 and 3.05MeV states of ^{9}Be respectively. Most of the events lie along the ^{120}Sn ground state locus i.e. they correspond to elastic breakup. There is very little evidence of target excitations of greater than ∿10MeV. The data peak at ε∿0 and then fall off rapidly with increasing ε, such that virtually all of the events are within the relative-energy range ε=0-1.5MeV. (This behaviour will be partly due to the fall off of the detection efficiency with increasing ε, see figure 2.24). There is no strong evidence of sequential breakup from the 2.43 and 3.05MeV states of ^{9}Be. Breakup from the 1.69MeV state of ^{9}Be may be contributing to the data, as may direct breakup reactions.

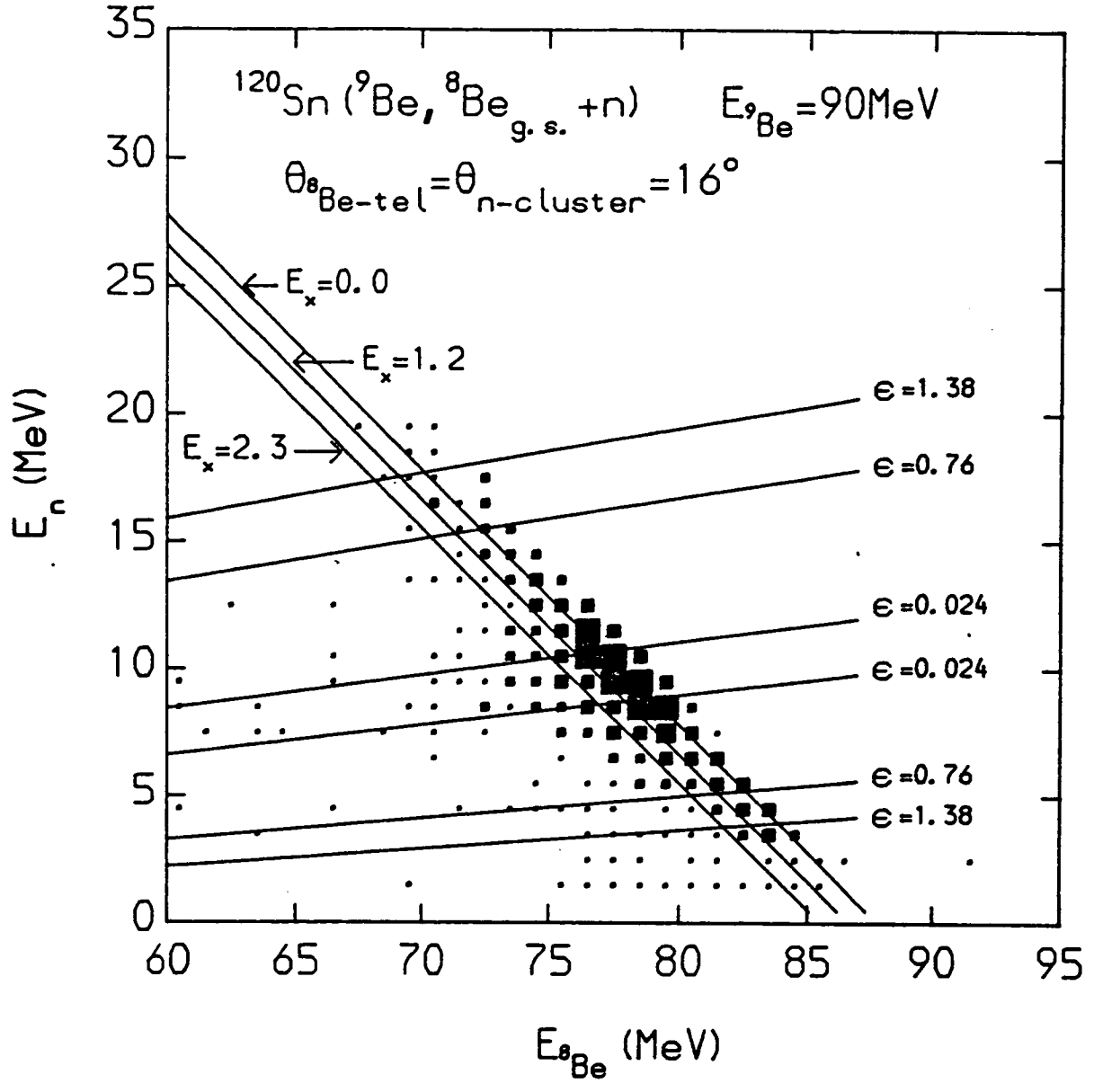

Figure 5.5: $^{8}Be_{g.s.}$+n coincidence yield for the reaction $^{9}Be+^{120}Sn$ as a function of the $^{8}Be_{g.s.}$ and neutron energies. The curves labelled ε=0.024, 0.76 and 1.38MeV correspond to the sequential break-up reactions $^{9}Be^{*}_{1.69}\rightarrow{}^{8}Be_{g.s.}$+n, $^{9}Be^{*}_{2.43}\rightarrow{}^{8}Be_{g.s.}$+n and $^{9}Be^{*}_{3.05}\rightarrow{}^{8}Be_{g.s.}$+n. Kinematic loci have also been plotted for target excitations of E_x=0.0, 1.2 and 2.3MeV.

In §2.2 it was demonstrated that a ^{8}Be+n summed energy spectrum reveals the states of the target which are excited in the breakup reactions. In figure 5.6, $E_{8Be}+E_n$ spectra are shown for several values of θ_{8Be} and θ_n. In considering these spectra, it is useful to refer to the scattering angle of the centre of mass of the ^{8}Be+n system, θ_{8Be+n}. The importance of θ_{8Be+n} is that it is related, in principle at least, to the impact parameter of the ^{9}Be projectile on the target. For the case of sequential breakup, θ_{8Be+n} is equal to the scattering angle of the excited ^{9}Be* ejectile. For given values of θ_{8Be} and θ_n the average value of θ_{8Be+n} is given by:

$$\theta_{8Be+n}=\theta_{8Be}+(\theta_n-\theta_{8Be})m_n/(m_n+m_{8Be})$$

The experimental θ_{8Be+n} resolution clearly depends on the angular resolutions of the ^{8}Be and neutron detectors. It also depends on the relative energy distribution of the breakup process. A typical value for the θ_{8Be+n} resolution, as determined by Monte-Carlo methods, is about 1°.

$E_{8Be}+E_n$ spectra are shown for θ_{8Be+n} values of 13.2°, 20.5° and 25.5° in figure 5.6. For all three spectra, the effective solid angles for ^{8}Be detection and neutron detection are the same, furthermore the difference between θ_{8Be} and θ_n is a constant, equal to 2.5°. Consequently, the effective solid-angle for ^{8}Be+n coincidence detection, for sequential processes at least, is the same for each spectrum.

It was necessary to subtract a background of random $^{8}Be_{gs}+\gamma$-ray events from figures 5.6b and 5.6c. These events could not be rejected in the analysis (by using the the PSD signal) since one of the electronic units had failed during the runs over which the data at large values of θ_{8Be+n} had been collected. To determine the shape of the background distributions, use was made of the $^{8}Be_{gs}$ inclusive data. A simulated random γ-ray was added on to each $^{8}Be_{gs}$ singles event. The resulting $^{8}Be_{gs}+\gamma$-ray *events* were then analysed in the same manner as the $^{8}Be_{gs}$+n events and $E_{8Be}+E_n$ spectra were generated and subtracted from the actual $E_{8Be}+E_n$ spectra. In general, the shape of the $E_{8Be}+E_n$ spectra for random events is not flat. It depends on the shape of the inclusive $^{8}Be_{gs}$ energy spectra and on the neutron TAC spectra. Even a flat TAC spectrum leads to a neutron energy spectrum with a $E^{-3/2}$ dependence.

In all three spectra of figure 5.6 the dominant feature is the elastic breakup peak. At forward scattering angles, i.e. $\theta_{8Be+n}<\theta_{gr}=21.8°$, the bulk of the data

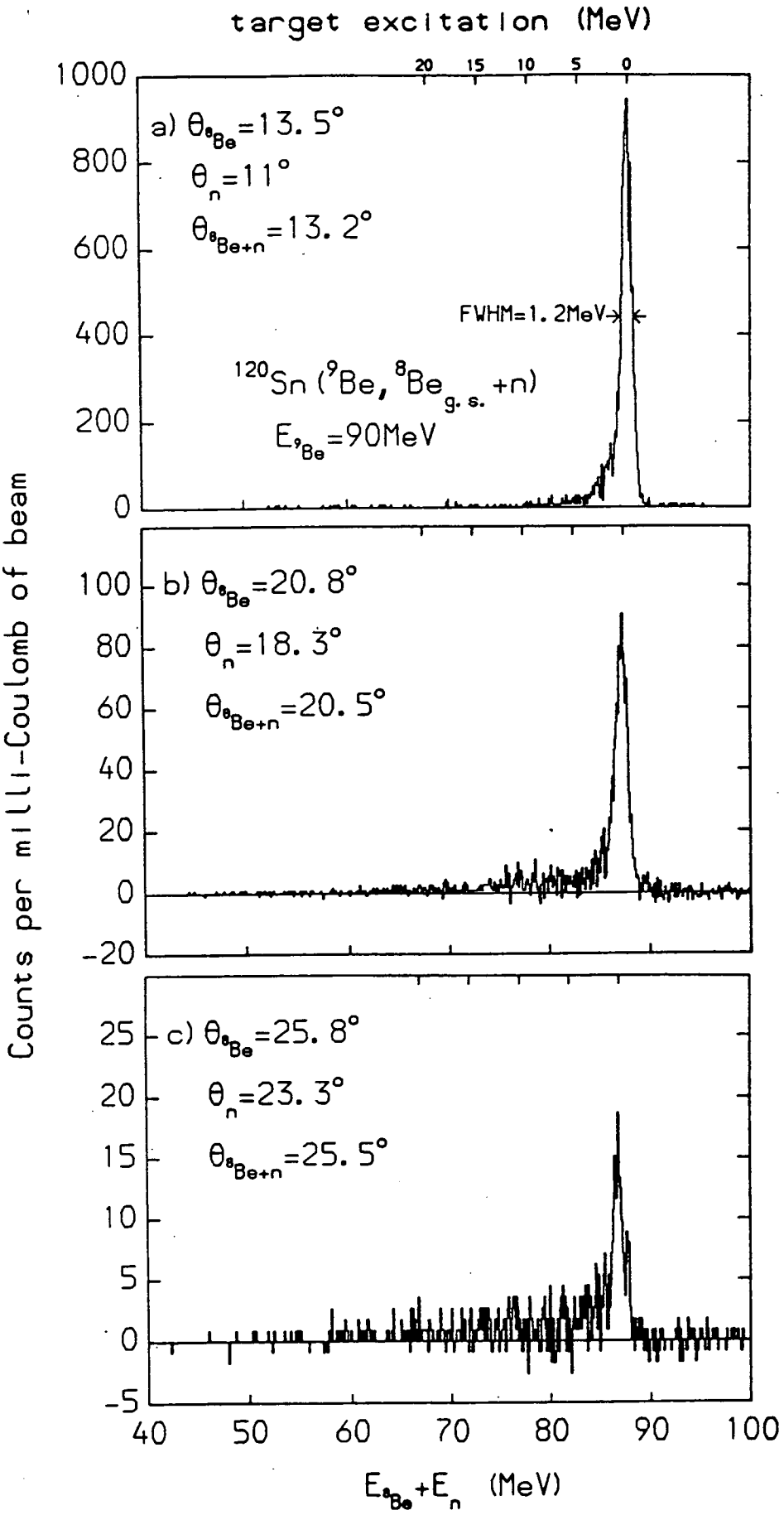

Figure 5.6: $^{8}Be_{g.s.}$+n coincidence yield for the reaction ^{9}Be+^{120}Sn as a function of the summed $^{8}Be_{g.s.}$+n energy.

is concentrated in this peak. As $\theta_{^8Be+n}$ increases, inelastic processes are seen to become relatively more important. These processes will include mutual-excitation and partial-fusion followed by neutron evaporation. Furthermore the measured breakup yield falls off dramatically with increasing $\theta_{^8Be+n}$. It is not surprising that the probability of inelastic processes increases as $\theta_{^8Be+n}$ increases since larger values of $\theta_{^8Be+n}$ correspond to smaller impact parameters and to harder collisions. Also for values of $\theta_{^8Be+n}$ beyond grazing, the projectile must have interacted with the nuclear field of the target.

There is no clear evidence from figure 5.6 of excitation of discrete states of ^{120}Sn. In part this will be due to the summed energy resolution ($\curvearrowright$1.2MeV) and the statistical quality of the data. Nevertheless, the broad inelastic distributions, which are seen in figures 5.6b and 5.6c, are perhaps more suggestive of partial fusion followed by neutron emission than of mutual excitation to discrete target states. One might imagine that the partial fusion of a neutron from a ^9Be projectile is quite likely, given that the neutron binding energy is low (1.66MeV) and that angular momentum considerations are not so critical for a low mass fragment like a neutron. Also, the probability of re-emmision of a neutron from the compound/pre-equilibrium system is high. Typically, the neutron will fuse with a kinetic energy of $\curvearrowright$10MeV. If it is re-emitted statistically, then target excitations of up to $\curvearrowright$10MeV will be inferred. The above comments are speculative. The statistics of the present data are not sufficient to permit a proper analysis of the inelastic processes. However, since absorptive processes are known to be responsible for a large fraction of the inclusive yields measured for other systems, it would be of considerable interest to investigate in detail ^9Be induced partial fusion reactions. For a ^9Be projectile, partial fusion might be unambiguously identified if experiments are performed to look for wide-angle coincidences between beam velocity $^8Be_{gs}$ nuclei and evaporative neutrons, or if $^8Be_{gs}$+γ-ray data is obtained in which the residual nucleus can be identified from the γ-ray energy. The investigation of ^9Be partial fusion reactions could be of particular interest, since it may be reasonable to assume that the $^8Be_{gs}$ ejectile follows a trajectory close to that of the Rutherford orbit of the ^9Be. If this is the case, then the variation of the partial-fusion yield with impact parameter can be extracted.

As previously noted, the bulk of the $^8Be_{gs}$+n data is associated with elastic breakup. To study this channel in more detail it is useful to look at the ^8Be projected energy spectra for the events within the elastic peaks of the summed

energy spectra of figure 5.6. These projected spectra are shown in figure 5.7. The $^{8}Be_{gs}$ kinetic energies which would result from the sequential decay of the 1.69, 2.43 and 3.05MeV states of ^{9}Be have been indicated on the upper axes of the projected spectra. It should be noted that both the 1.69 and 3.05MeV states are quite broad, $\curvearrowup$100 and 282keV respectively. So the $^{8}Be_{gs}$ kinetic energy distributions produced by their decay will also be broad, several MeV wide. The half-lives of these states are $\curvearrowup 66\times10^{-22}$s and 23×10^{-22}s respectively. These values are sufficiently larger than the transit time, of $\curvearrowup 8\times10^{-22}$s, to mean that final state interactions (FSIs) should not smear out the momentum correlations produced by the decay of the 1.69 and 3.05 MeV states. The position of the 2.78MeV state of ^{9}Be was not marked on figure 5.7; this was due to the fact that this state has a width of 1080keV, which means that it produces a very broad projected energy distribution. The half-life of the 2.78MeV state is 6×10^{-22}s which is comparable to the transit time. Consequently, the decay of this state will be influenced by FSIs. The 2.43MeV state has a width of only 0.77keV ($t_{1/2}\curvearrowup 8\times10^{-19}$s). Therefore, if excited, it should be clearly visible in the projected spectra. However, this state is known to have only a 7% decay branch to the $^{8}Be_{gs}$+n channel. The remaining decay strength is in the $^{5}He_{gs}$+α channel (see Chapter 4). This low decay branch will strongly suppress the contribution of the 2.43MeV state to the projected $^{8}Be_{gs}$ spectra.

Returning to the $^{8}Be_{gs}$ spectra, it is apparent that the vast majority of the events are concentrated within the region defined by E_x=0-3MeV. There is no clear evidence of decay via the 2.43 or 3.05MeV states of ^{9}Be. The 1.69MeV state is certainly contributing to the spectra. At forward scattering angles ($\theta_{^{8}Be+n}$=13.2°) the fall off of the data with increasing E_x (and therefore increasing ε) is dramatic. In part this will be due to the fall off of the detection efficiency with ε (see figure 2.24). Nevertheless, the projected spectrum still implies a rapidly decreasing ε-spectrum. This is suggestive of a Coulomb excitation process.

As $\theta_{^{8}Be+n}$ increases from 13.2° to 20.5°, the projected energy distributions become broader. However, for $\theta_{^{8}Be+n}$=25.5° (which is beyond the grazing angle of 21.8°) the central part of the projected spectrum appears to be narrower than for $\theta_{^{8}Be+n}$=20.5°. This behaviour can be explained if there is a considerable direct breakup component to the $^{8}Be_{gs}$+n coincidence yield. Firstly, the projected energy distribution for a direct breakup reaction will

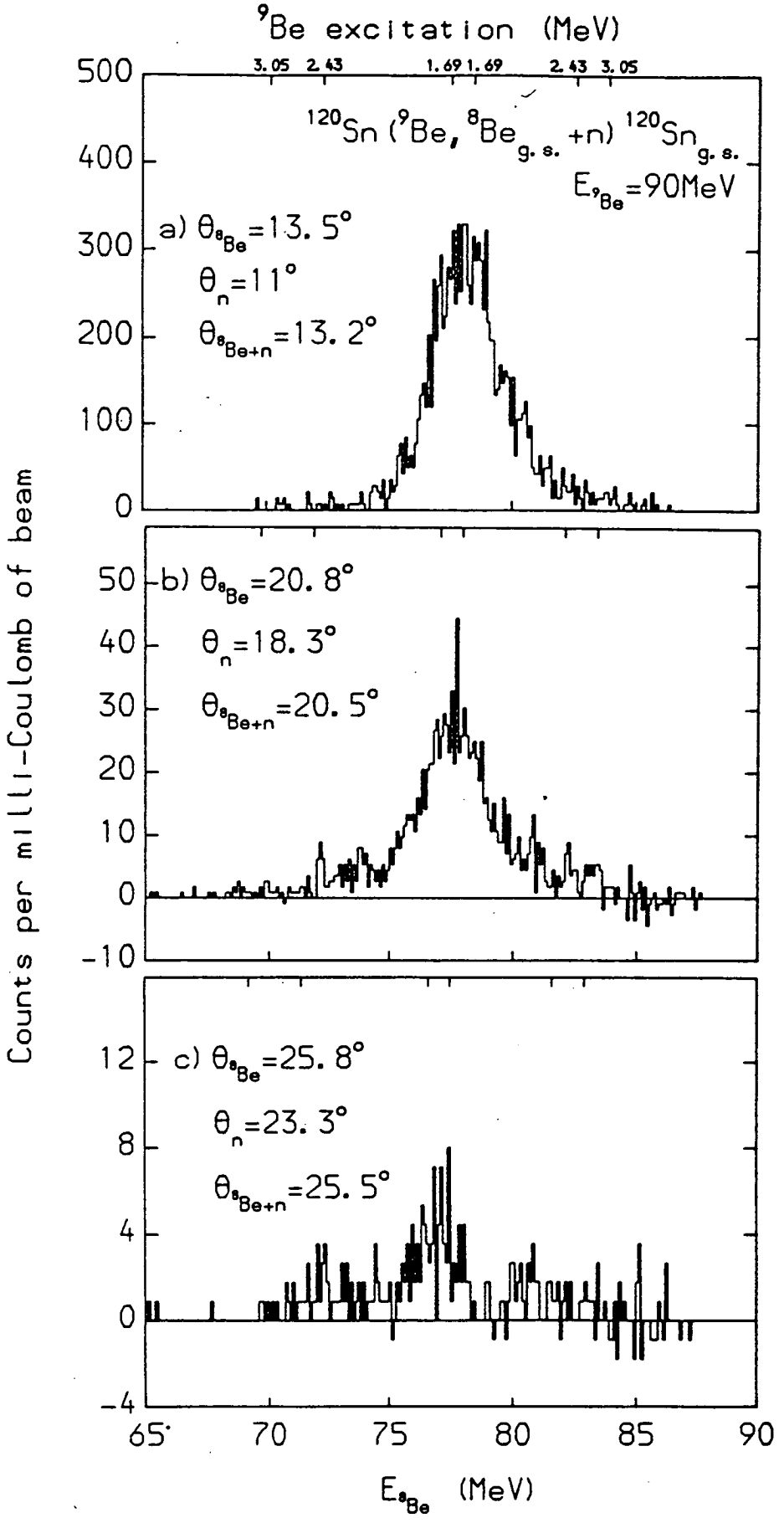

Figure 5.7: ^{8}Be projected energy spectra for the elastic break-up reaction ^{120}Sn(^{9}Be,^{8}Be$_{g.s.}$+n)^{120}Sn$_{g.s.}$.

become broader (due to the effect of FSIs) as the scattering angle increases. This would explain the behaviour of the data between 13.2° and 20.5°. For angles beyond the grazing angle however, nuclear FSIs will completely destroy the momentum correlation between breakup fragments which are produced in direct reactions. Therefore, at such angles, only sequential breakup processes will contribute to the projected spectra. This suggests that, the reason for the narrowing of the central region of the projected energy distributions, at angles beyond grazing, is that a strong direct breakup component has been completely smeared out and that what is seen is a residual sequential component due to the decay of the 1.69MeV state.

If this interpretation of the data is correct, then the angular behaviour of the breakup of ^{9}Be is similar to that of the breakup of ^{7}Li (see §1.3.2 and SHOT84). For the ^{120}Sn(^{7}Li,α+t)^{120}Sn$_{gs}$ reaction, the forward angle (close-geometry) yield is dominated by direct breakup. As the scattering angle increases, the projected energy distributions become broader, until at angles beyond grazing, only sequential breakup, via the 4.63MeV state of ^{7}Li, is seen in the spectra.

The statistics of the spectra of figure 5.7 limit the ability to identify sequential reactions. In an attempt to improve the statistics, spectra obtained at a range of θ_{8Be+n} angles were summed together, and are shown in figure 5.8. In performing the addition of the spectra, allowance was made for the different amounts of kinetic energy lost to the target at different values of θ_{8Be+n}. Since the shape of a projected spectrum depends on the value of $|\theta_{8Be}-\theta_{n}|$, the spectra were only summed together if they corresponded to the same value of $|\theta_{8Be}-\theta_{n}|$. Above each of the three spectra of figure 5.8, Monte-Carlo simulations of the sequential breakup reactions

$$^{120}\mathrm{Sn}(^{9}\mathrm{Be},^{9}\mathrm{Be}^{*}_{1.69,\ 2.43,\ 2.78,\ 3.05}\rightarrow^{8}\mathrm{Be}_{gs}+n)^{120}\mathrm{Sn}_{gs}$$

are shown. The same number of breakup events were simulated for each of the excited states, so the simulations illustrate the relative detection efficiencies for the sequential breakup reactions. In the case of the 1.69MeV state, the two kinematic solutions which are normally observed for sequential breakup, have merged to produce one distribution. This is caused by the width of the 1.69MeV state and its closeness to the ^{8}Be$_{gs}$+n decay threshold, which is at E_x=1.66MeV. In order to simplify the presentation of the simulations, the

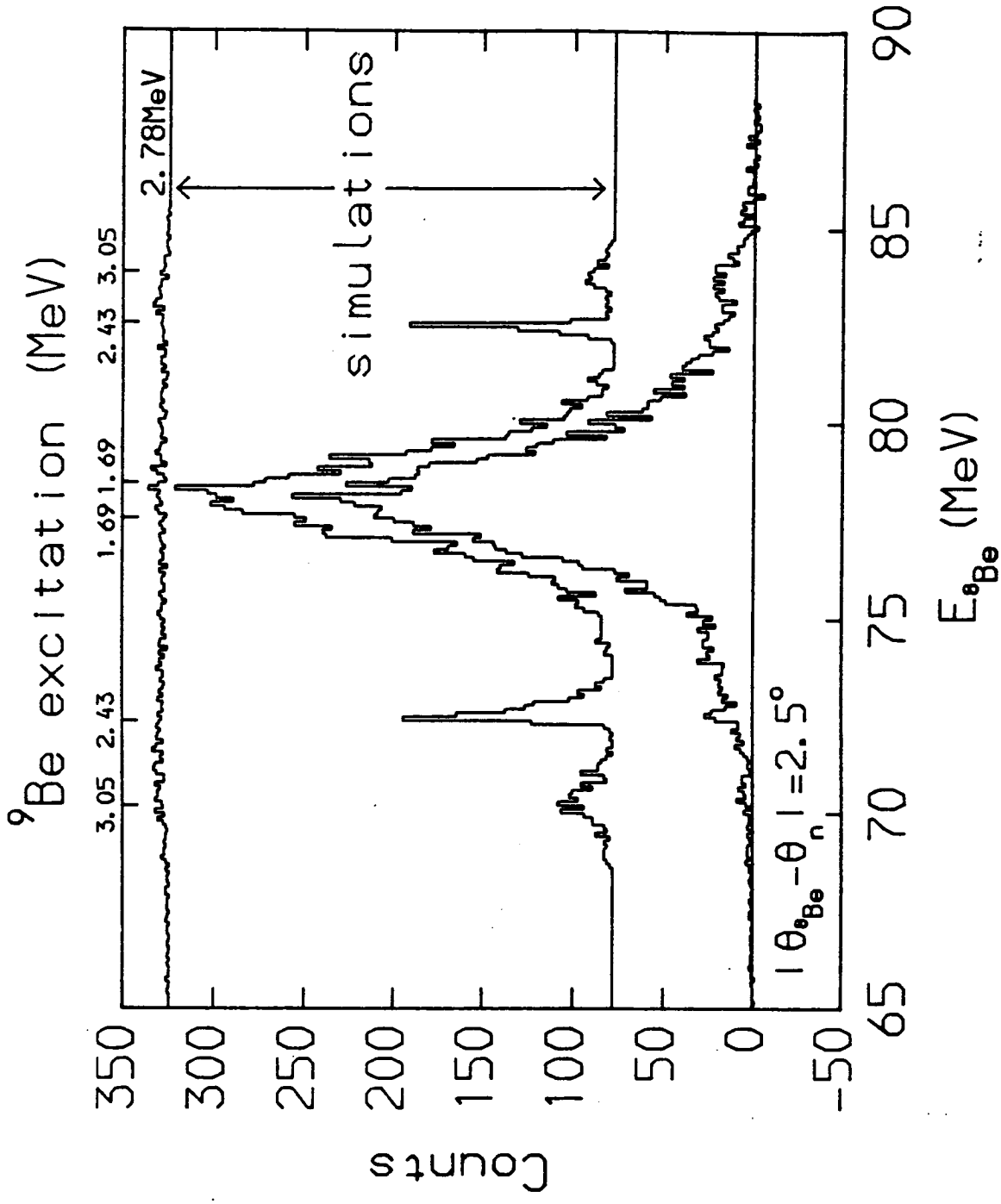

Figure 5.8a: Sum of all of the ^{8}Be projected energy spectra, for the elastic break-up reaction $^{120}Sn(^9Be,^8Be_{g.s.}+n)^{120}Sn_{g.s.}$, which were collected with $|\theta_{8Be}-\theta_n|=2.5°$. Monte-Carlo simulations of the sequential break-up reaction $^9Be^* \rightarrow ^8Be_{g.s.}+n$ are presented for the 1.69, 2.43, 2.78 and 3.05MeV states of ^{9}Be.

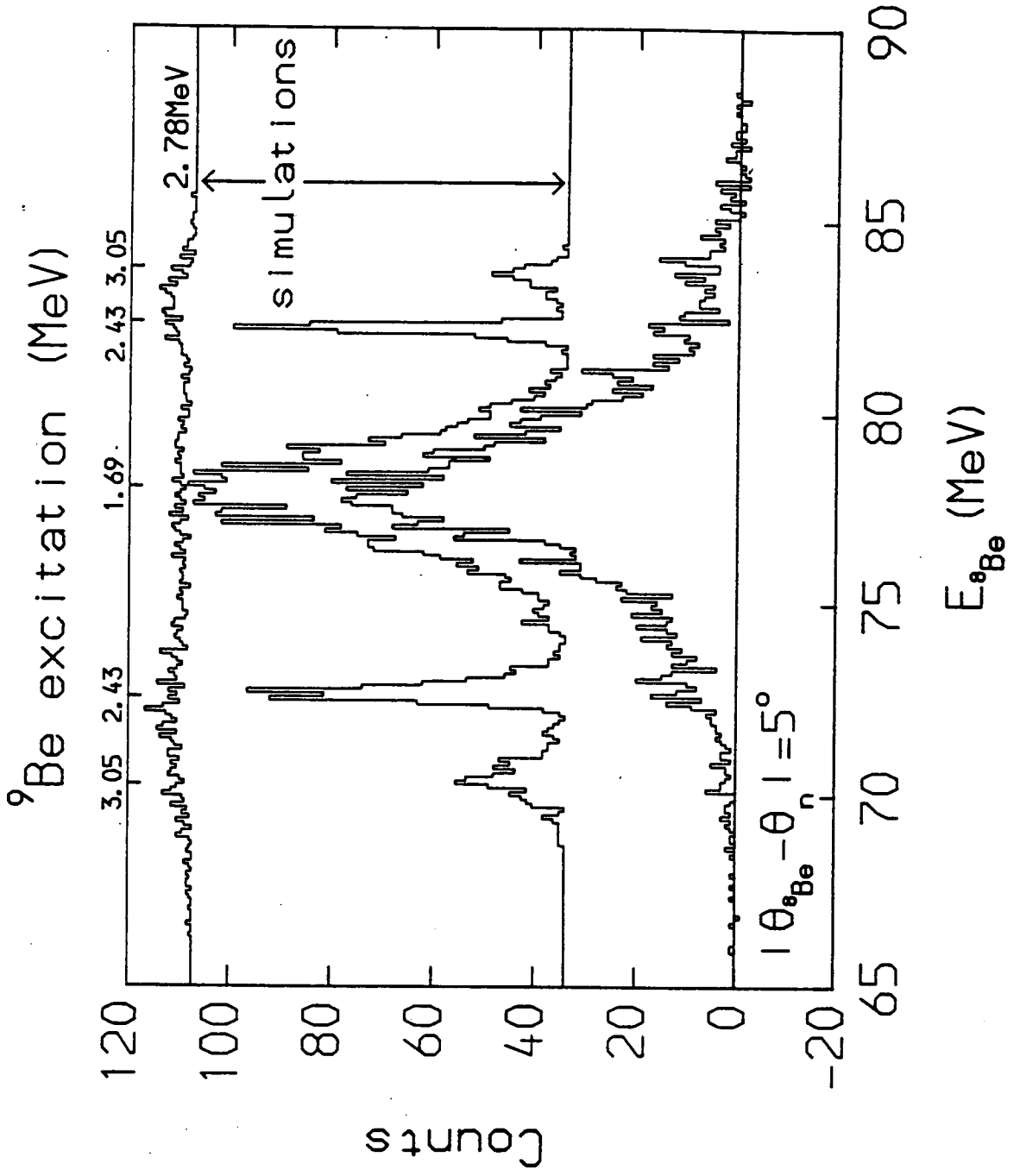

Figure 5.8b: Sum of all of the ^{8}Be projected energy spectra, for the elastic break-up reaction $^{120}Sn(^9Be,^8Be_{g.s.}+n)^{120}Sn_{g.s.}$, which were collected with $|\theta_{8Be}-\theta_n|=5°$. Monte-Carlo simulations of the sequential break-up reaction $^9Be^* \rightarrow ^8Be_{g.s.}+n$ are presented for the 1.69, 2.43, 2.78 and 3.05MeV states of ^{9}Be.

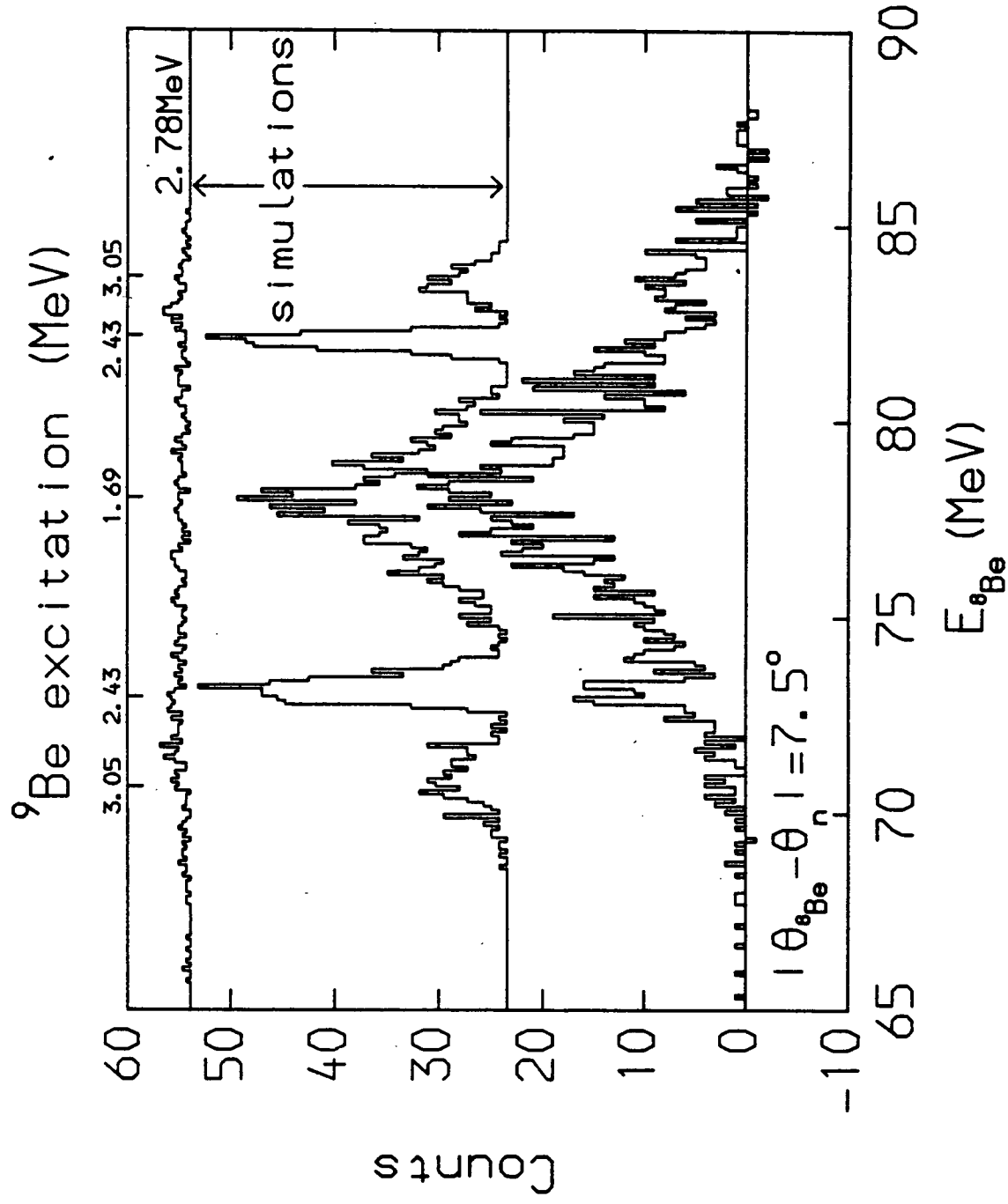

Figure 5.8c: Sum of all of the ^{8}Be projected energy spectra, for the elastic break-up reaction $^{120}Sn(^9Be,^8Be_{g.s.}+n)^{120}Sn_{g.s.}$, which were collected with $|\theta_{8Be}-\theta_n|=7.5°$. Monte-Carlo simulations of the sequential break-up reaction $^9Be^* \rightarrow ^8Be_{g.s.}+n$ are presented for the 1.69, 2.43, 2.78 and 3.05MeV states of ^{9}Be.

2.78MeV state of ^{9}Be was not included in the same spectra as the 1.69, 2.43 and 3.05MeV states. The shapes of the projected spectra for the 2.78MeV state are perhaps slightly puzzling at first, since these spectra have three *bumps*. The two outer *bumps* are the two usual kinematic solutions. The central *bump* is due to the width of the 2.78MeV state (1080keV) and the rapid increase of the detection efficiency as ε decreases. It is important to note that no account was taken of FSIs when performing the simulations and that each breakup step was assumed to proceed isotropically. The shape of the states was also assumed to be Lorentzian.

We consider first the 1.69MeV state. It is seen that the shape of the simulation for the 1.69MeV state is close to the shape of the data over the energy region 77MeV$<E_{^{8}Be}<$80MeV. Outside that region the fit is poor and there are certain areas of the experimental spectra, around 75 and 81MeV, that neither the 1.69, 2.43 or 3.05MeV states can explain. It is possible that the broad 2.78MeV state is contributing in these regions. Alternatively, the discrepancy between the simulated shape of the 1.69MeV state and the data indicates the presence of FSIs or of direct breakup.

There is some weak evidence of decay via the 2.43 and 3.05MeV states in figure 5.8. Unfortunately, the statistics are still such that it is impossible to say anything definite about sequential decay via these states.

As far as the 2.78MeV state is concerned, it would be very difficult, regardless of the statistics, to identify this state as it is so broad that the $^{8}Be_{gs}$ energy distribution produced by its decay underlies those of the 1.69, 2.43 and 3.05MeV states.

In summary. From the projected spectra, there is no unambiguous evidence of direct $^{9}Be \rightarrow ^{8}Be_{gs}+n$ breakup. It appears, on the basis of the shape of the projected $^{8}Be_{gs}$ spectra, that a large fraction of the breakup yield passes through the 1.69MeV resonance of ^{9}Be. However, the change of the shape of the projected spectra with scattering angle is suggestive of a considerable direct breakup component.

5.1.2 $^{120}Sn(^{9}Be,^{8}Be_{gs}+n)^{120}Sn_{gs}$ Angular Distributions

More information on the breakup processes of ^{9}Be can be gained by studying the angular distributions. In figures 5.9 and 5.10, double differential cross-sections for the reaction $^{120}Sn(^{9}Be,^{8}Be_{gs}+n)^{120}Sn_{gs}$ are shown. In these spectra the breakup yield is plotted as a function of θ_n, for several values of θ_{8Be}. These double differential cross-sections were calculated by integrating the projected spectra over energy. The error bars represent the 1σ level and only take into account the statistical errors. Any systematic errors, such as those involved in determining the neutron detector efficiency or the target thickness, have not been included (see §2.11).

For values of $\theta_{8Be} \leq 18.5^{\circ}$, the angular distributions are roughly symmetric about θ_{8Be}. This is indicative of sequential breakup. As θ_{8Be} increases, the distributions become smoother, which is a reflection of the fact that the relative energy spectra become flatter at more backward angles (larger values of ε will lead to greater values of $|\theta_{8Be}-\theta_n|$.

For values of θ_{8Be} greater than 18.5°, the angular distributions have only three data points each, so they are of limited use. However, it can probably be said that the curves continue to become flatter as θ_{8Be} increases. The flatness of the curves at backward angles indicates a reduction in the correlation between the $^{8}Be_{gs}$ and the neutron. Such a reduction in the $^{8}Be_{gs}$+n correlation could result from the onset of nuclear direct breakup and the effect of nuclear FSIs.

To show the behaviour of the breakup yield with increasing scattering angle, the double differential cross-section has been plotted versus θ_{8Be+n} in figure 5.11. A different curve has been drawn for each value of $|\theta_{8Be}-\theta_n|$ since the $^{8}Be_{gs}$+n detection efficiency depends on $|\theta_{8Be}-\theta_n|$.

Apart from one point, on the $|\theta_{8Be}-\theta_n|=2.5^{\circ}$ curve, the cross-section monotonically decreases with increasing θ_{8Be+n}. Beyond the grazing angle (21.8°) one would expect the cross-section to rapidly decrease. It is interesting to note that the present data falls off well inside grazing. The very strong forward focusing of the breakup yield indicates that it would be worthwhile to investigate the breakup of ^{9}Be at very forward angles ($\theta_{8Be+n}<13^{\circ}$). Unfortunately, making a measurement at these angles is extremely difficult due to the high yield of the elastically scattered ^{9}Be. Before such a measurement

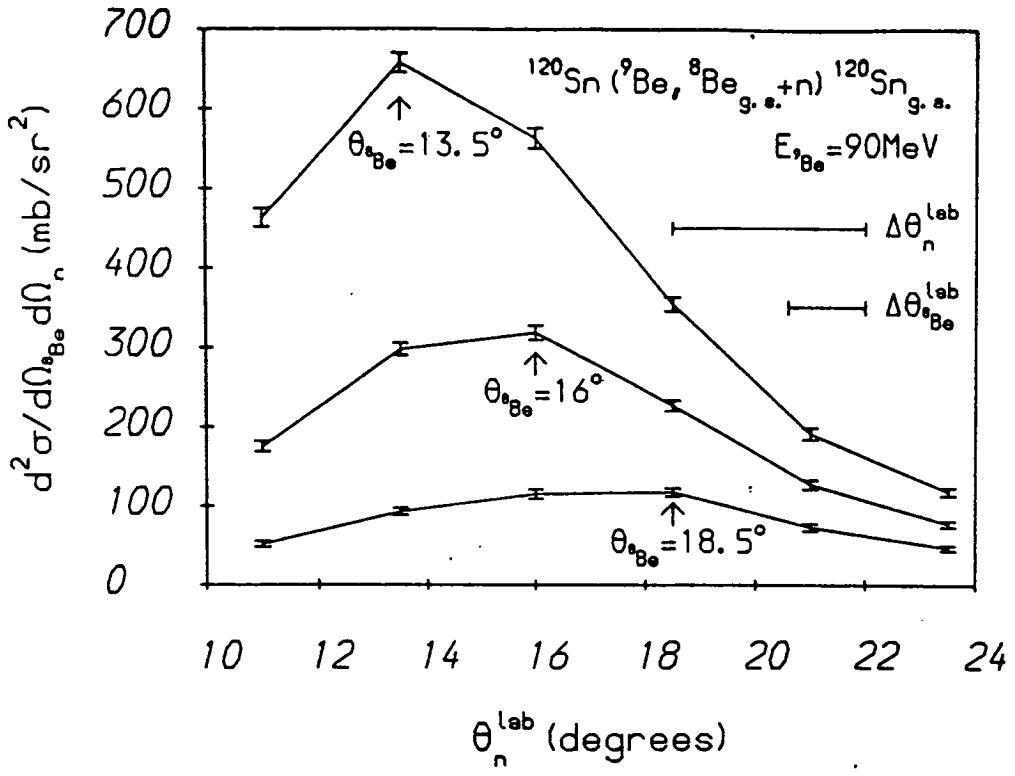

Figure 5.9: Double differential cross-sections for the elastic break-up reaction $^{120}Sn(^{9}Be,^{8}Be_{g.s.}+n)^{120}Sn_{g.s.}$ as a function of θ_n. The ^{8}Be and neutron angular resolutions ($\Delta\theta_n$ and $\Delta\theta_{8Be}$) are indicated by the two horizontal bars. The arrows indicate the value of θ_{8Be} for each curve.

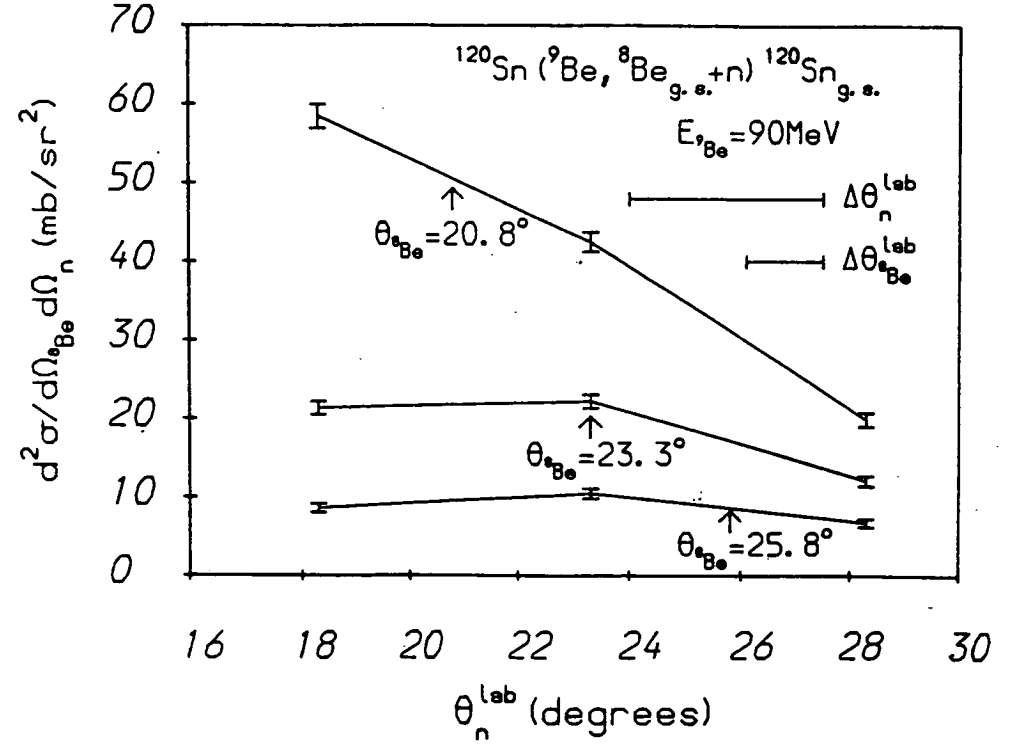

Figure 5.10: Double differential cross-sections for the elastic break-up reaction $^{120}Sn(^{9}Be,^{8}Be_{g.s.}+n)^{120}Sn_{g.s.}$ as a function of θ_n.

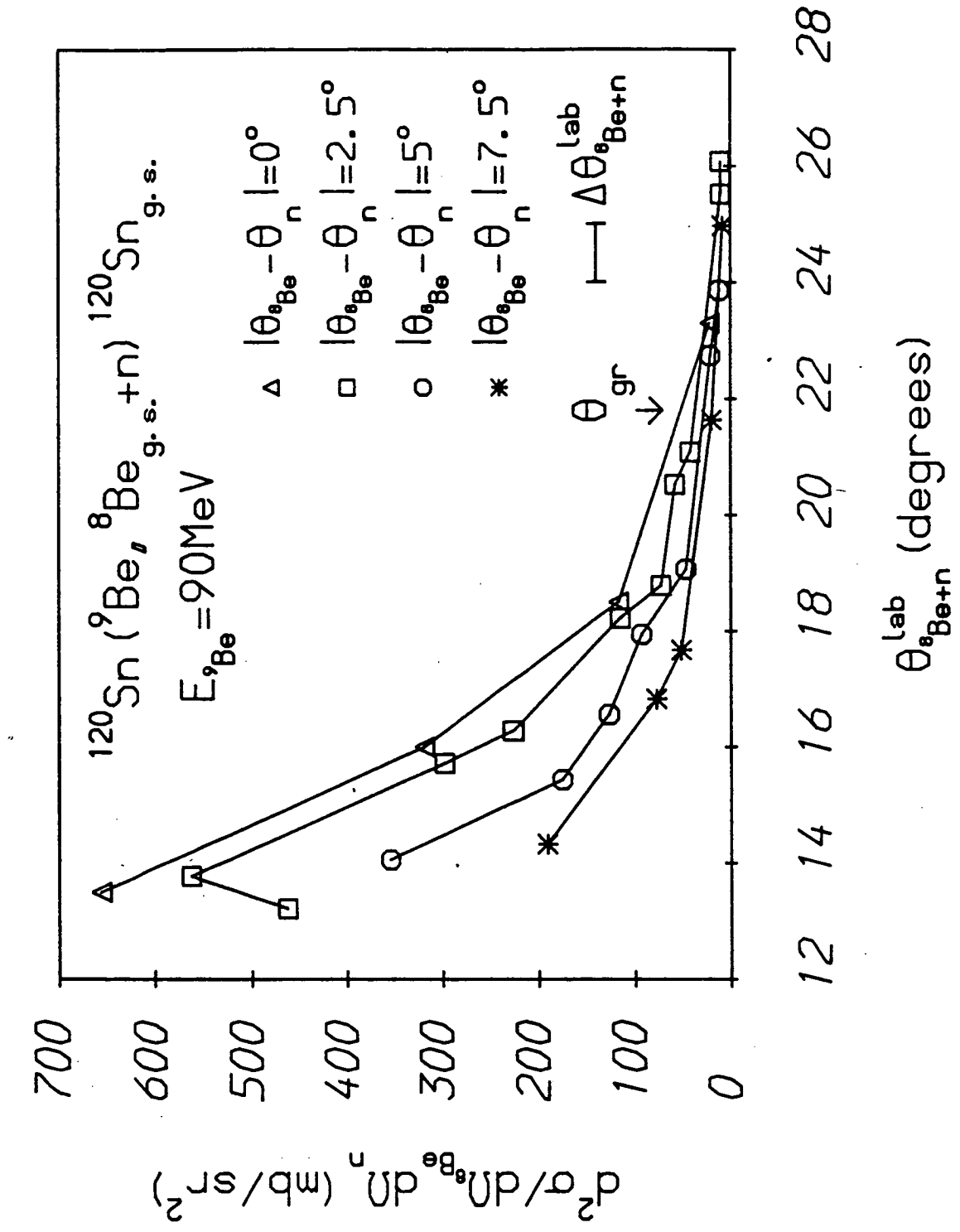

Figure 5.11: Double differential cross-sections for the elastic break-up reaction $^{120}Sn(^{9}Be,^{8}Be_{g.s.}+n)^{120}Sn_{g.s.}$ as a function of $\theta_{^{8}Be+n}$. The $\theta_{^{8}Be+n}$ angular resolution ($\Delta\theta_{^{8}Be+n}$) is indicated by the horizontal bar. The statistical errors in the cross-sections are comparable to, or smaller than, the size of the symbols used to indicate the data points.

could be made, it would be necessary to develop a multi-element detection system in which the solid-angles subtended by the individual detectors were small.

It is interesting to compare the angular distributions of figure 5.11 with the distribution for the sequential breakup reaction

$^{120}Sn(^{9}Be,^{9}Be^{*}_{2.43}\rightarrow^{5}He_{gs}+\alpha)^{120}Sn_{gs}$

which is shown in figure 4.12. (This distribution was calculated on the assumption that the anomalous peaks in the $\alpha+\alpha$ data (see Chapter 4) are due to the sequential decay of the 2.43MeV $5/2^{-}$ state of ^{9}Be into the $^{5}He_{gs}+\alpha$ channel). The angular distribution for the ($^{9}Be,^{9}Be^{*}_{2.43}$) reaction shows strong oscillations up to about 3° inside the grazing angle. Beyond this angle, the yield falls off sharply. This behaviour is in marked contrast to that seen in figure 5.11 for the $^{8}Be_{gs}+n$ yield. This yield steadily decreases over the entire angular range for which data was collected.

The contrast between the $^{9}Be^{*}_{2.43}$ and $^{9}Be\rightarrow^{8}Be_{gs}+n$ angular distributions is very similar to that which is observed between the angular distributions for the $^{120}Sn(^{7}Li,^{7}Li^{*}_{4.63}\rightarrow\alpha+t)^{120}Sn_{gs}$ sequential breakup reaction and the $^{120}Sn(^{7}Li,\alpha+t)^{120}Sn_{gs}$ direct breakup reaction [DAVI87, SHOT81, SHOT84]. The $^{7}Li^{*}_{4.63}$ sequential breakup yield shows some indications of oscillatory behaviour at forward angles. At $\sim$3° degrees inside the grazing angle, this yield begins to decrease rapidly. The direct breakup yield on the other hand decreases steadily over the entire angular range, in a manner which is very similar to the continuous fall off of the $^{9}Be\rightarrow^{8}Be_{gs}+n$ breakup yield. This similarity suggests that the $^{9}Be\rightarrow^{8}Be_{gs}+n$ yield has a large direct breakup component.

5.2 $^{12}C(^{9}Be,\alpha+\alpha+n)$ Data

Approximately 90% of the charged-particle + charged-particle + neutron data which was obtained with a ^{12}C target consists of $\alpha+\alpha+n$ events. Therefore the PI spectra for the ^{12}C target are almost identical to those for the ^{120}Sn target. The features of the $E_{\alpha1}/E_{\alpha2}$ spectra for $^{12}C(^{9}Be,\alpha+\alpha+n)$ reactions are also very similar to those for the $^{120}Sn(^{9}Be,\alpha+\alpha+n)$ reactions. Almost all of the $\alpha+\alpha+n$ yield produced by scattering off the ^{12}C target corresponds to either

^{9}Be breakup into the $^{8}Be_{gs}$+n channel or of excitation of the ^{9}Be projectile into its 2.43MeV state and the subsequent decay of this state into the ^{5}He+α channel. There is very little evidence of $^{8}Be^{*}_{3.04}$+n events. Since the (^{9}Be,$^{9}Be^{*}_{2.43}$) reaction is discussed in Chapter 4, we shall now concentrate on the $^{8}Be_{gs}$+n data.

In figure 5.12, $E_{8Be}+E_{n}$ summed energy spectra for the reaction $^{12}C(^{9}Be,^{8}Be_{gs}+n)$ are shown. The ground state 0^{+} and 4.4MeV 2^{+} states of ^{12}C are clearly visible. Elastic breakup is a strong reaction channel, but it is apparent that mutual excitation is much more important for ^{12}C than for scattering off a ^{120}Sn target.

Only a limited amount of data was collected with the ^{12}C target (this was principally due to the low small-angle breakup yield for the ^{9}Be+^{12}C system). Consequently, the statistics of the projected energy spectra are poor. To improve the statistics, all of the elastic breakup data collected with $|\theta_{8Be}-\theta_{n}|=2.5^{\circ}$ were summed together to produce one projected spectrum; this is shown in figure 5.13. Above this spectrum, simulations of the sequential breakup reactions

$$^{12}C(^{9}Be,^{9}Be^{*}_{1.69,\ 2.43,\ 3.05}\rightarrow^{8}Be_{gs}+n)^{12}C_{gs}$$

have been plotted. The 2.78MeV state of ^{9}Be has been omitted from the simulation since, for scattering angles beyond grazing ($\theta_{gr}=3.3^{\circ}$ for ^{12}C), this short-lived state disintegrates in the nuclear field of the target. The FSIs will therefore destroy the momentum correlation of the fragments.

There is no clear structure in the projected ^{8}Be energy spectrum of figure 5.13. The spectrum is much broader than that for the ^{120}Sn target. Since the $^{8}Be_{gs}$+n detection efficiency decreases rapidly with ε, this projected spectrum implies an ε-spectrum which increases as ε increases for low values of ε. It is not possible to say conclusively whether sequential breakup is present; all of the sequential processes included in the simulation may be contributing to the projected spectrum, as may direct reactions.

In figure 5.14, the double differential cross-sections for the reaction $^{12}C(^{9}Be,^{8}Be_{gs}+n)^{12}C_{gs}$ have been plotted. The yield is seen to decrease with scattering angle for all values of $|\theta_{8Be}-\theta_{n}|$. The curves for different values of $|\theta_{8Be}-\theta_{n}|$ are similar, reflecting the broad ε distribution (N.B. if the

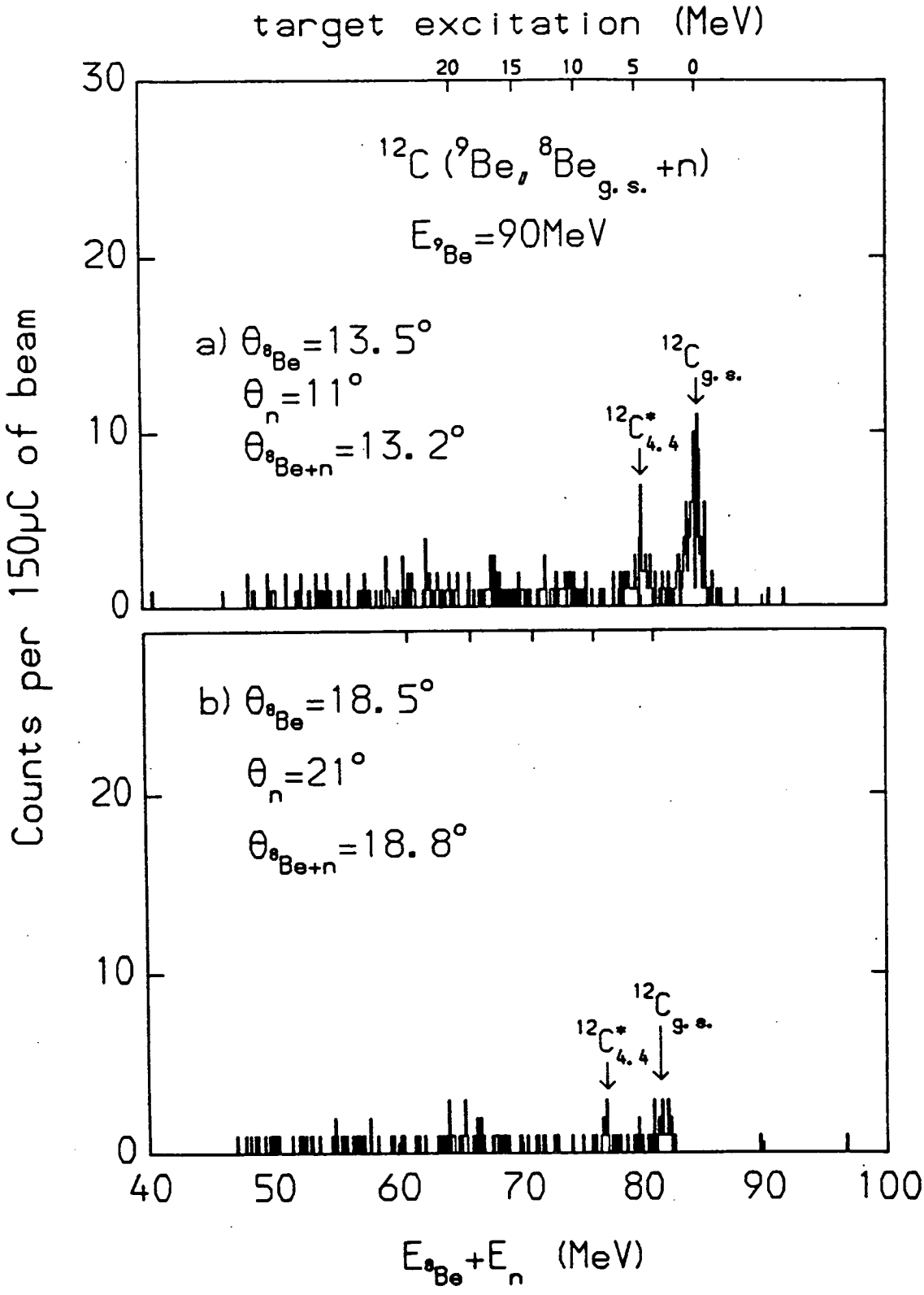

Figure 5.12: $^{8}Be_{g.s.}$+n coincidence yield for the reaction $^{9}Be+^{12}C$ as a function of the summed $^{8}Be_{g.s.}$+n energy.

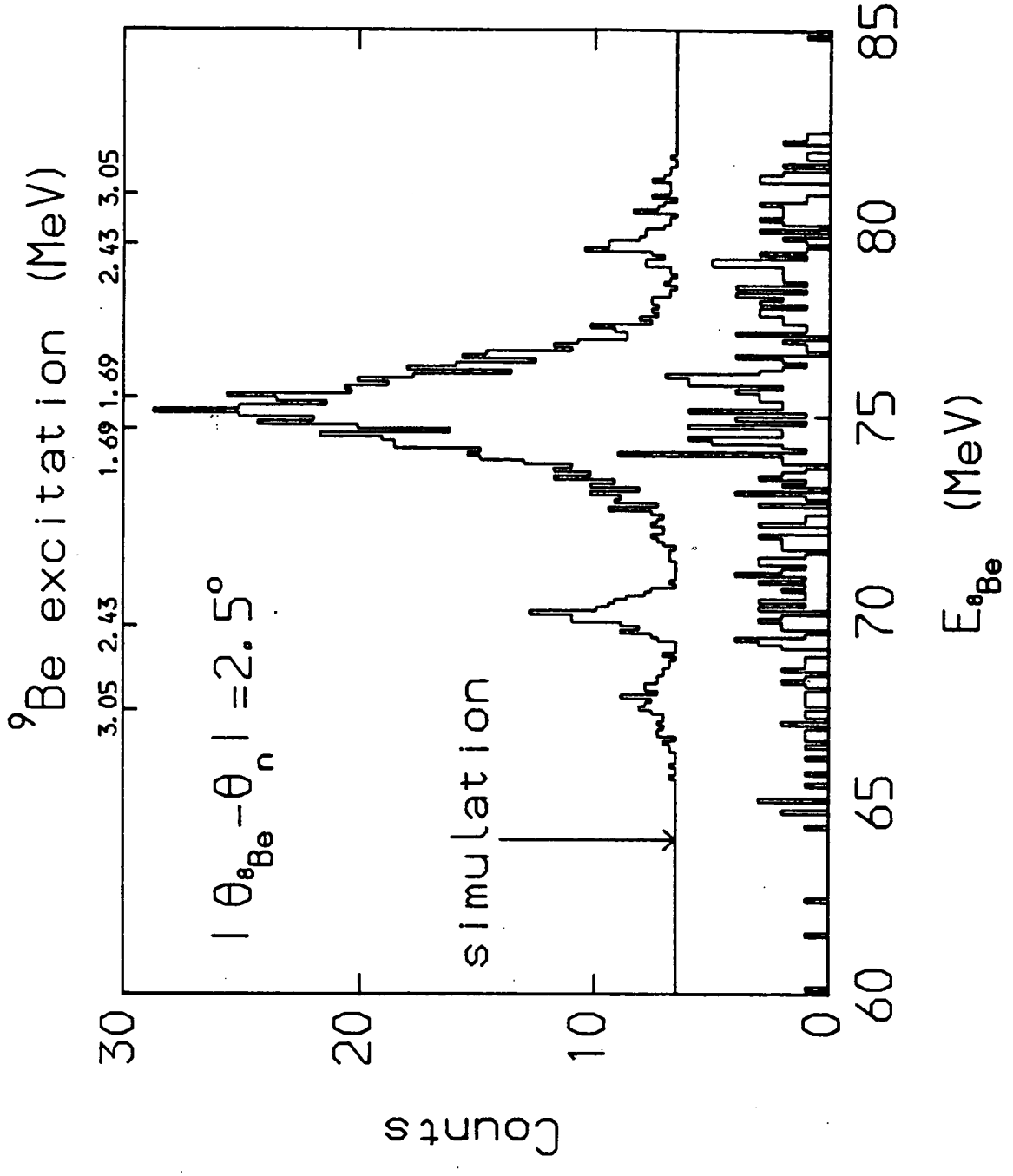

Figure 5.13: Sum of all of the ^{8}Be projected energy spectra, for the elastic break-up reaction $^{12}C(^9Be,^8Be_{g.s.}+n)^{12}C_{g.s.}$, which were collected with $|\theta_{8Be}-\theta_n|=2.5°$. Monte-Carlo simulations of the sequential break-up reaction $^9Be^* \rightarrow ^8Be_{g.s.}+n$ are presented for the 1.69, 2.43 and 3.05MeV states of ^{9}Be.

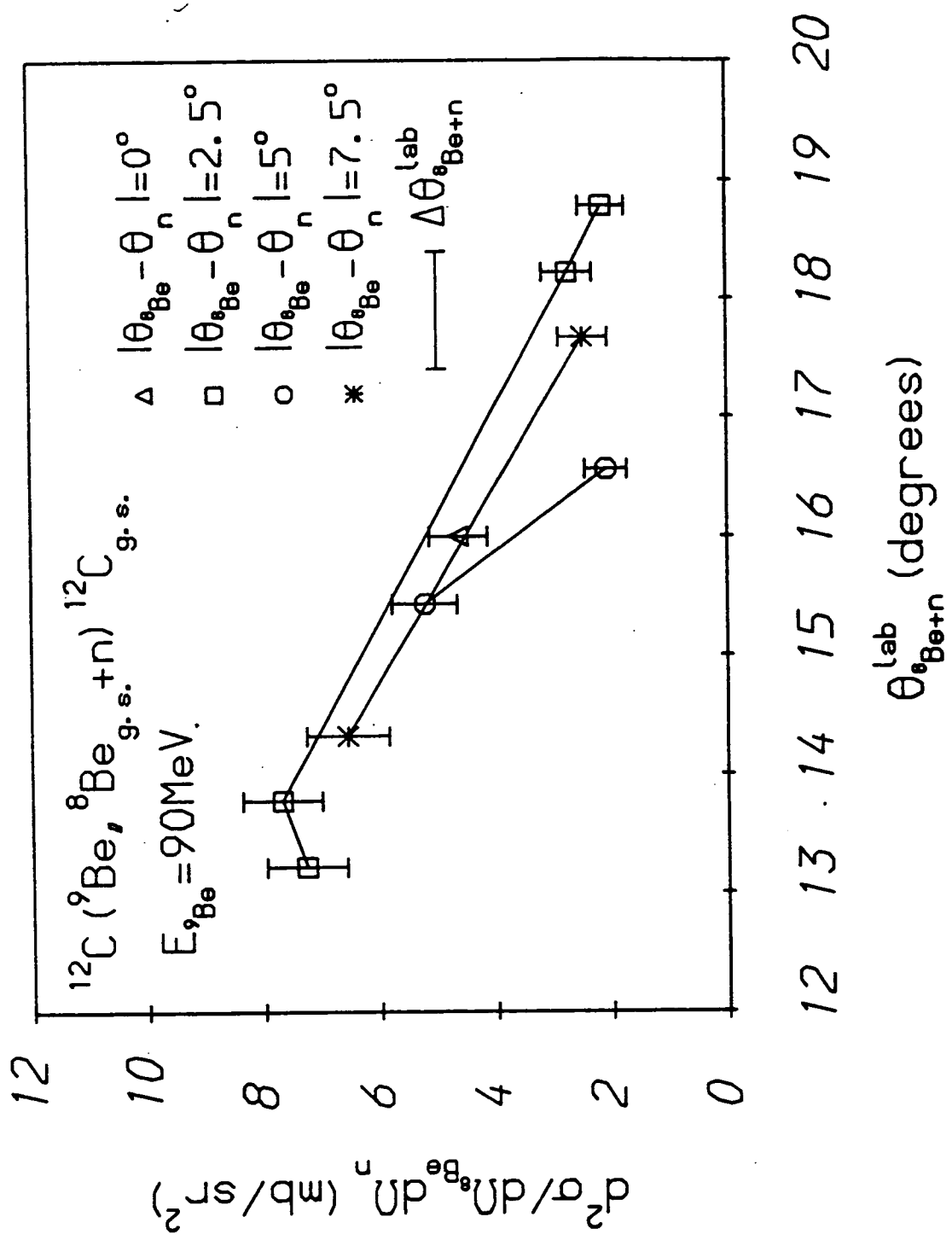

Figure 5.14: Double differential cross-sections for the elastic break-up reaction $^{12}C(^{9}Be,^{8}Be_{g.s.}+n)^{12}C_{g.s.}$ as a function of $\theta_{^{8}Be+n}$. The $\theta_{^{8}Be+n}$ angular resolution ($\Delta\theta_{^{8}Be+n}$) is indicated by the horizontal bar.

ε-spectrum is broad then the efficiencies for each value of $|\theta_{8Be}-\theta_n|$ are similar).

5.3 Comparison of the $^9Be+^{12}C$ and $^9Be+^{120}Sn$ Data

In some respects, the breakup of ^9Be on the ^{12}C and ^{120}Sn targets is similar. For both targets the bulk of the breakup yield is in the α+α+n channel and this channel is populated via the $^9Be \rightarrow ^8Be_{gs}+n$ and $^9Be \rightarrow ^9Be^*_{2.43}$ reactions. There are however differences between the two datasets. In summary these are:

1. At forward angles, the breakup of ^9Be on ^{120}Sn is dominated by the elastic breakup channel. For the case of ^{12}C, inelastic processes (notably mutual excitation) are comparable in strength to elastic breakup.
2. The ε distributions for breakup on the ^{120}Sn target are sharply peaked at low values of ε. For ^{12}C, the ε spectra are very much flatter.
3. The total elastic breakup yield for ^{120}Sn is ∽90 times greater than that for ^{12}C.

For scattering angles which are in the range $\theta_{gr}(^{12}C) < \theta_{8Be+n} < \theta_{gr}(^{120}Sn)$ the collision between the ^9Be and the target will be quite different for the two different targets. With the ^{120}Sn target a pure Coulomb trajectory is possible, whilst for the ^{12}C target the ^9Be must interact with the nuclear field of the ^{12}C. The $^9Be+^{120}Sn$ collision is therefore softer than the $^9Be+^{12}C$ interaction, so inelastic processes will be more likely with a ^{12}C target than with a ^{120}Sn target. Furthermore, nuclear breakup processes will in general produce a larger spread of ε values. These ideas go some way towards explaining the first two differences listed above.

The are several reasons for the difference between the magnitude of the $^9Be+^{12}C$ and $^9Be+^{120}Sn$ breakup cross-sections. The close-geometry detection arrangement means that final state interactions will reduce the observed coincidence yield for direct breakup reactions. The effect of FSIs will be greater for the ^{12}C target than for the ^{120}Sn target; this is because nuclear FSIs must be present for direct breakup on ^{12}C. Another factor is that the harder nature of the $^9Be+^{12}C$ collision makes excitation to high sequential states more probable than in $^9Be+^{120}Sn$ collisions. The strong excitation of the 4.4MeV state of ^{12}C, in the $^{12}C(^9Be,^8Be+n)$ reaction, is evidence for this statement (see figure 5.12). As is clear from the Monte-Carlo simulations shown in figures 5.8

and 5.13, the detection efficiency for sequential reactions falls off rapidly with increasing excitation e.g. $\Omega_{eff}(E_x=1.69) \backsim 14\ \Omega_{eff}(E_x=3.05)$. Therefore, there will only be a small contribution to the $^{8}Be_{gs}$+n coincidence yield from the sequential breakup of states of ^{9}Be at excitation energies higher than 3.05MeV. If a large fraction of the $^{9}Be+^{12}C$ breakup yield is through the breakup of such states then the observed yield will be reduced. Finally, since the ^{12}C breakup data was collected at angles greater than grazing and most of the ^{120}Sn data was obtained at angles inside grazing, absorptive and inelastic processes will be more probable for ^{12}C. These processes will take strength out of the elastic breakup channel.

Once again , it is interesting to compare the present data on ^{9}Be breakup with the close-geometry ^{7}Li breakup data collected by Shotter et al [SHOT81, SHOT84, DAVI87]. Both sequential and direct breakup of 70MeV ^{7}Li into the α+t channel were unambiguously identified. The sequential reaction, which proceeded via the 4.63MeV $7/2^-$ state of ^{7}Li, was observed for all of the targets studied; these were ^{12}C, ^{60}Ni, ^{96}Zr, ^{120}Sn and ^{208}Pb. The direct breakup reaction was observed for all of the targets apart from ^{12}C. It was conjectured that direct breakup was not identified with the ^{12}C target because of the strong FSIs that would be present for scattering angles greater than the $^{7}Li+^{12}C$ grazing angle. This lack of a 'non-sequential' distribution in the projected energy spectra for ^{12}C, was taken as further evidence that the 'non-sequential' component seen with the heavier targets was indeed due to a direct breakup process.

In the breakup of ^{9}Be it is seen that the projected energy spectra for the ^{12}C and ^{120}Sn targets are very different in shape. For the ^{120}Sn target, at forward angles (figure 5.7), there is a strong central distribution which peaks at low relative energies. This central distribution has almost completely disappeared with the ^{12}C target (figure 5.13). Bearing in mind the target dependence of ^{7}Li breakup, this behaviour is further evidence that there is a considerable direct breakup component to the $^{9}Be \rightarrow {}^{8}Be_{gs}$+n yield.

The total close-geometry $^{7}Li+^{12}C$ breakup yield was found to be a factor of $\backsim$13 lower than the $^{7}Li+^{120}Sn$ breakup yield [DAVI87]. This decrease in cross-section is at least qualitatively consistent with the behaviour of the present data. A possible explanation for the greater reduction in cross-section observed with the ^{9}Be projectile is that direct breakup processes may

constitute a greater fraction of the ^{9}Be breakup yield that they do the ^{7}Li breakup yield. Since direct reactions are subject to FSIs, the observed breakup yield would be more suppressed for ^{9}Be breakup on ^{12}C than for ^{7}Li breakup on ^{12}C.

For the ^{7}Li+^{120}Sn reaction, direct breakup was unambiguously identified. For the ^{9}Be+^{120}Sn reaction however, it is difficult to present unambiguous evidence for direct breakup. This is due to the presence of a low-lying resonance state in ^{9}Be at 1.69MeV. This excitation energy is just above the $^{8}Be_{gs}$+n breakup threshold. Since the 1.69MeV state has a spin-parity assignment of $J^{\pi}=1/2^{+}$, it will be strongly excited, at forward angles, by an E1 Coulomb transition. Nevertheless, the $^{9}Be \rightarrow {}^{8}Be_{gs}$+n data does indicate the presence of a strong direct component; for the following reasons.

- The shape of the projected spectra for the ^{120}Sn target changes rapidly with angle.
- The angular distributions for the $^{8}Be_{gs}$+n yield behave in the same manner as the $^{7}Li \rightarrow \alpha$+t direct breakup yield and in a very different manner to the (^{9}Be,$^{9}Be^{*}_{2.43}$) sequential breakup yield.
- The shape of the projected spectra for ^{12}C and ^{120}C are very different. In particular, there is a strong low relative energy component in the ^{120}Sn spectrum which is is not present in the ^{12}C spectrum.

All of these points suggest that there is a considerable direct breakup component in the $^{9}Be \rightarrow {}^{8}Be_{gs}$+n data. It is virtually impossible however, to separate out this direct component from the sequential distribution due to the decay of the 1.69MeV state if ^{9}Be. Therefore, an absolute magnitude for the direct breakup yield cannot be obtained.

CHAPTER 6
COULOMB BREAKUP CALCULATION

6.1 Motivation for Coulomb Breakup Calculation

In the scattering of ^{9}Be off a ^{120}Sn target it is observed that the $^{9}Be \rightarrow ^{8}Be_{gs}+n$ breakup yield is strongly forward focused (see figure 5.11) and dominated by the elastic breakup channel. The projected $^{8}Be_{gs}$ spectra (e.g. figure 5.7) demonstrate that the majority of the $^{8}Be_{gs}+n$ breakup events are associated with low projectile excitations, $E_x<3MeV$. As $\theta_{^{8}Be+n}$ decreases, the concentration of events at low values of E_x (and hence at low ε) increases.

This behaviour of the $^{9}Be+^{120}Sn$ breakup reaction, in the forward scattering region, is suggestive of a Coulomb breakup process. Indeed one might expect that the dominant interaction at forward angles would be the Coulomb interaction, especially since there is a low-lying resonance state in ^{9}Be at $\curvearrowleft$1.69MeV, which is just above the $^{8}Be_{gs}+n$ breakup threshold at 1.66MeV. This resonance has a spin-parity assignment of $J^{\pi}=1/2^{+}$, so it can be excited from the $3/2^{-}$ ground state of ^{9}Be via an E1 transition. The low excitation energy of the 1.69MeV state and the E1 nature of the transition implies that Coulomb excitation should be strong. Therefore it seems that a study of the Coulomb breakup of ^{9}Be would be worthwhile.

As discussed in §1.3.2 and §1.4.2, the forward angle direct breakup of 70MeV ^{7}Li into the α+t channel was well explained by Shotter et al [SHOT84], for the case of a ^{120}Sn target, in terms of a semi-classical Coulomb breakup calculation. The success of this approach provides motivation for applying the same technique to the case of ^{9}Be breakup.

A final reason for investigating the Coulomb breakup of ^{9}Be is that it is of interest to determine the extent to which Coulomb processes are responsible for projectile breakup. If it is demonstrated that the breakup reactions of a range of systems can be well understood in terms of the Coulomb interaction, it would give credibility to the technique of extracting fusion cross-sections from breakup data. For example it would be interesting to determine the $^{8}Be_{gs}+n \rightarrow ^{9}Be+\gamma$ yield from the $^{120}Sn(^{9}Be,^{8}Be_{gs}+n)^{120}Sn_{gs}$ data. Alternatively, if large discrepancies exist between the data and the Coulomb theory, then it should be possible to infer information about nuclear breakup reactions and

final states interactions.

6.2 Semi-Classical Breakup Calculation

The simplest manner of treating Coulomb breakup is by employing semi-classical excitation theory (this theory was discussed in §1.4.2). The basic assumptions of the theory are:

1. That the projectile orbit is well described by the Rutherford trajectory (i.e. that $E_x << E_{beam}$)
2. That the probability of excitation is low (this is necessary to ensure that 1st order perturbation theory is valid)

For the breakup of 90MeV ^{9}Be on ^{120}Sn, the first condition is easily met since the vast majority of the $^{8}Be_{gs}$+n coincidence events correspond to ^{9}Be excitations of less than 3MeV. The second condition is also met since, as will be shown later, a Coulomb calculation predicts an excitation yield of ↶100mb/sr at $\theta_{9Be}=10^{o}$ whilst the Rutherford cross-section at this angle is ↶96,000mb/sr.

The semi-classical theory is normally applied to reactions in which the beam energy is below the Coulomb barrier, so that, classically at least, the projectile trajectories are pure Coulomb. However, it is of interest to see if this method can be applied to beam energies above the Coulomb barrier for scattering angles inside the grazing angle. Of course, nuclear+Coulomb orbits are still possible in the forward scattering region, so nuclear+Coulomb interference may be important.

The E1 breakup yield, from equation 1.4, is given by,

$$d\sigma_{E1}=(Z_T e/hV_P)^2\ B(E1)df_{E1}(\theta,E_x)dE_x \qquad (6.1)$$

For the case of the ^{7}Li→α+t Coulomb breakup calculation, the values of the reduced transition probability, B(E1), were determined from α+t→^{7}Li+γ fusion data by use of the reciprocity theorem. Obviously, there is no $^{8}Be_{gs}$+n→^{9}Be+γ data available; since $^{8}Be_{gs}$ is α-particle unstable. However, the value of B(E1) as a function of E_x can be obtained from ^{9}Be(γ,n) photo-neutron data via the relation,

$$\sigma_{\gamma,n}(E_\gamma)=(16\pi^3/9)(E_\gamma/ch)B(E1) \qquad (6.2)$$

where $\sigma_{\gamma,n}(E_\gamma)$ is the $^9Be(\gamma,n)$ photo-neutron cross-section and E_γ is the gamma-ray energy (equal to E_x). We now consider the quality of the existing $^9Be(\gamma,n)$ data.

6.3 Survey of $^9Be(\gamma,n)$ Photo-neutron Data

The study of the $^9Be+\gamma \rightarrow {}^8Be+n$ reaction, in the threshold region, is problematic. To identify a photo-neutron event, it is necessary to detect one of the two residual fragments i.e. either the ^8Be or the neutron. Since the kinetic energy deposited in the ^8Be is low ($\curvearrowright$100keV) the ^8Be will not escape from the target, consequently the neutron must be detected. This leads to problems with the experimental efficiency and the absolute normalisation of the data. To kinematically define the event, it is necessary to either measure the energy of the detected fragment or to know the energy of the incident γ-ray. There are several approaches to studying the $^9Be(\gamma,n)$ reaction:

1. A pulsed electron beam is used to produce bremsstrahlung photons and the neutron energy is measured by the *time of flight* technique.
2. The bremsstrahlung difference method is used to determine the contribution to the photo-neutron cross-section from given γ-ray energies. The neutrons are detected but their energies are not measured.
3. Radio-isotopes are used to produce the γ-ray beam. Again, the neutrons are detected but their energies are not measured.

Each of the above approaches has its advantages and its disadvantages. The *time of flight* technique has a low efficiency since long flight paths are required to give a good neutron energy resolution. With the bremsstrahlung difference method, the γ-ray energy resolution is poor, and with the radio-isotope method the number of γ-ray energies which can be studied is limited. However, when using radio-isotopes, the γ-ray energy resolution is excellent, $\curvearrowright$2keV. For the second and third methods listed above, the efficiency can be improved by thermalising the neutrons before detecting them.

In figure 6.1, the available $^9Be(\gamma,n)$ radio-isotope data is shown. The solid line represents a least-squares fit to the data of Fujishiro et al [FUJI82]. The peak position and FWHM, as determined from the least-squares curve, are 1.695MeV and 100keV respectively. Fujishiro et al [FUJI83] have also

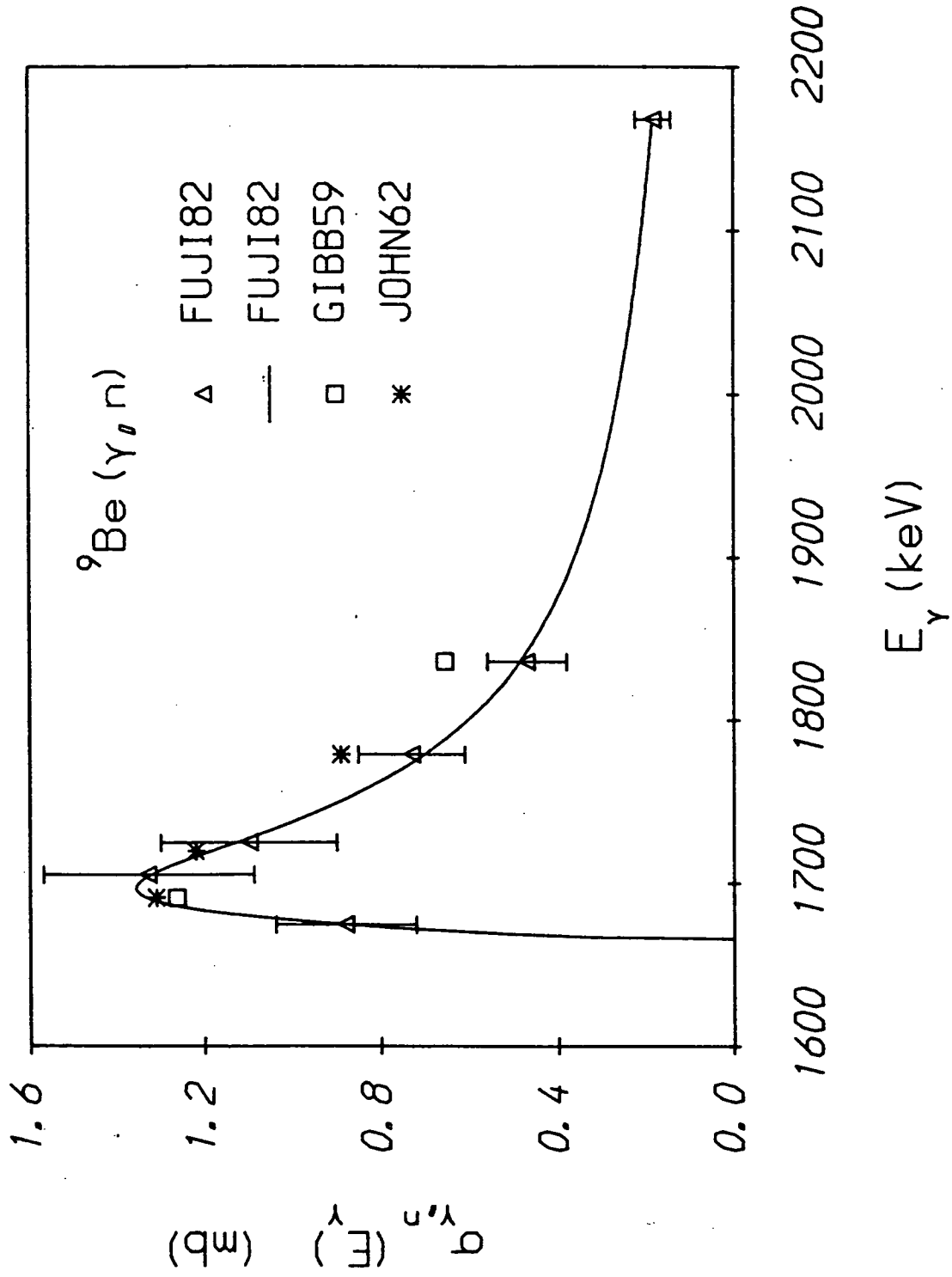

Figure 6.1: Photo-neutron cross-section for the reaction ^{9}Be(γ,n) as a function of E_γ. All data shown here were obtained in radio-isotope experiments.

investigated the effect of the $^{9}Be(\gamma,\alpha+\alpha+n)$ direct three-body reaction on the photo-neutron data. Using the 1576keV γ-rays from ^{142}Pr, the $^{9}Be(\gamma,\alpha+\alpha+n)$ photo-disintegration cross-section was measured to be $(0.4\pm0.18)\mu b$. This γ-ray energy was selected since it is greater than the $\alpha+\alpha+n$ threshold at 1570keV and less than the $^{8}Be_{gs}+n$ threshold at 1666keV. Since the $^{9}Be(\gamma,n)$ cross-section rises sharply to a peak of $\curvearrowright$1.4mb, just above the $^{8}Be_{gs}+n$ threshold, it was concluded that the effect of the $^{9}Be(\gamma,\alpha+\alpha+n)$ reaction on the $^{9}Be(\gamma,n)$ data was negligible. Incidentally, no evidence was found in the present data of $^{9}Be\rightarrow\alpha+\alpha+n$ direct reactions. If such reactions had been strong, then uncorrelated distributions would have been produced on the $E_{\alpha1}/E_{\alpha2}$ plane. The possibility that the anomalous peaks seen in the $\alpha+\alpha$ data were due to a direct reaction was discussed in Chapter 4, but was rejected due to the fact that the features of the anomalous peaks remain the same over a considerable range of scattering angles.

The bremsstrahlung difference data of Jakobson [JAKO61] also shows a peak in the $^{9}Be(\gamma,n)$ cross-section just above the $^{8}Be_{gs}+n$ threshold. The position of the peak is $\curvearrowright$1.7MeV and the width is $\curvearrowright$150keV. Not surprisingly, the width obtained by the bremsstrahlung difference method is considerably larger than that obtained with radio-isotopes. The cross-section given by Jakobson, at the peak maximum, is (1.15 ± 0.15)mb. This value compares favourably with the value of (1.36 ± 0.24) obtained by Fujishiro. Jakobson also measured the angular distribution of the photo-neutrons. Those corresponding to the peak at $\curvearrowright$1.7MeV had a spherically symmetric distribution. This indicated that the $\curvearrowright$1.7MeV peak was due to the decay of a $1/2^{+}$ resonance in ^{9}Be by s-wave neutron emission and/or the direct breakup of ^{9}Be into $\ell=0$ $^{8}Be_{gs}+n$ continuum states.

The neutron *time of flight* data of Berman et al [BERM67], again shows a similar photo-neutron spectrum. The position of the threshold peak is given as 1.672keV. The peak width cannot be extracted from this data since a γ-ray energy range of only 40keV is covered. Furthermore, no attempt was made to calculate absolute $^{9}Be(\gamma,n)$ cross-sections; instead, the data was normalised to the radio-isotope measurements.

It is apparent that the various datasets are in broad agreement. For the purposes of the present work, it was decided to make use of the radio-isotope data of Fujishiro et al. This data has very good E_{γ} resolution and there are

fewer problems with the normalisation of such data than with the normalisation of bremsstrahlung difference data. The neutron *time of flight* data is too limited to be of any use on its own.

In Chapter 5, it was shown that the $^{9}Be \rightarrow ^{8}Be_{gs}+n$ breakup data contains considerable evidence for a strong direct breakup component. There is nothing in the $^{9}Be(\gamma,n)$ data to suggest that such a component does not exist. The $\sigma_{\gamma,n}(E_\gamma)$ spectrum of figure 6.1 could easily be composed of a resonance plus a direct distribution.

The inverse of the $^{9}Be+\gamma \rightarrow ^{8}Be_{gs}+n$ direct breakup reaction is the radiative neutron capture reaction $^{8}Be_{gs}+n \rightarrow ^{9}Be+\gamma$. Simple arguments indicate that the radiative neutron capture cross-section has a $E_n^{-1/2}$ shape [BLAT79]. According to the reciprocity theorem, this would imply a direct $\sigma_{\gamma,n}(E_\gamma)$ yield which falls off as $E_\gamma^{-1/2}$. The $\sigma_{\gamma,n}(E_\gamma)$ spectrum of figure 6.1 could easily be fitted by a $E_\gamma^{-1/2}$ direct breakup component plus a Lorentzian shaped resonance.

The Coulomb excitation calculation only depends on the shape and magnitude of $\sigma_{\gamma,n}(E_\gamma)$ and not on whether the breakup reaction passes through a resonance or goes directly to a $^{8}Be_{gs}+n$ continuum state. So the predicted breakup yield will not depend on the magnitude of the direct component. The coincidence yield however, will depend on the magnitude of the direct component, since the direct component will be effected by final state interactions.

6.4 Comparison of Coulomb Breakup Calculation with Data

By using the least-squares curve of Fujishiro et al, in combination with equations 6.1 and 6.2, the values of $d^2\sigma_{E1}/d\Omega dE_x$ were calculated over the excitation range $1.666MeV<E_x<2.166MeV$. The resulting ^{9}Be excitation spectrum was fed into the Monte-Carlo simulation program MONTEGEN (see Chapter 3) and $^{8}Be_{gs}$ projected energy spectra were produced for the reaction $^{120}Sn(^{9}Be,^{8}Be_{gs}+n)^{120}Sn_{gs}$. Two, typical, simulated projected spectra are shown in figures 6.2 and 6.3, where they are compared with the corresponding experimental spectra. The spectra of these figures have been presented in such a manner that their shapes can be easily compared; their magnitudes cannot be compared. Isotropic angular distributions were used for the $^{9}Be^{*} \rightarrow ^{8}Be_{gs}+n$ and $^{8}Be_{gs} \rightarrow \alpha+\alpha$ breakup reactions. This is an exact procedure for

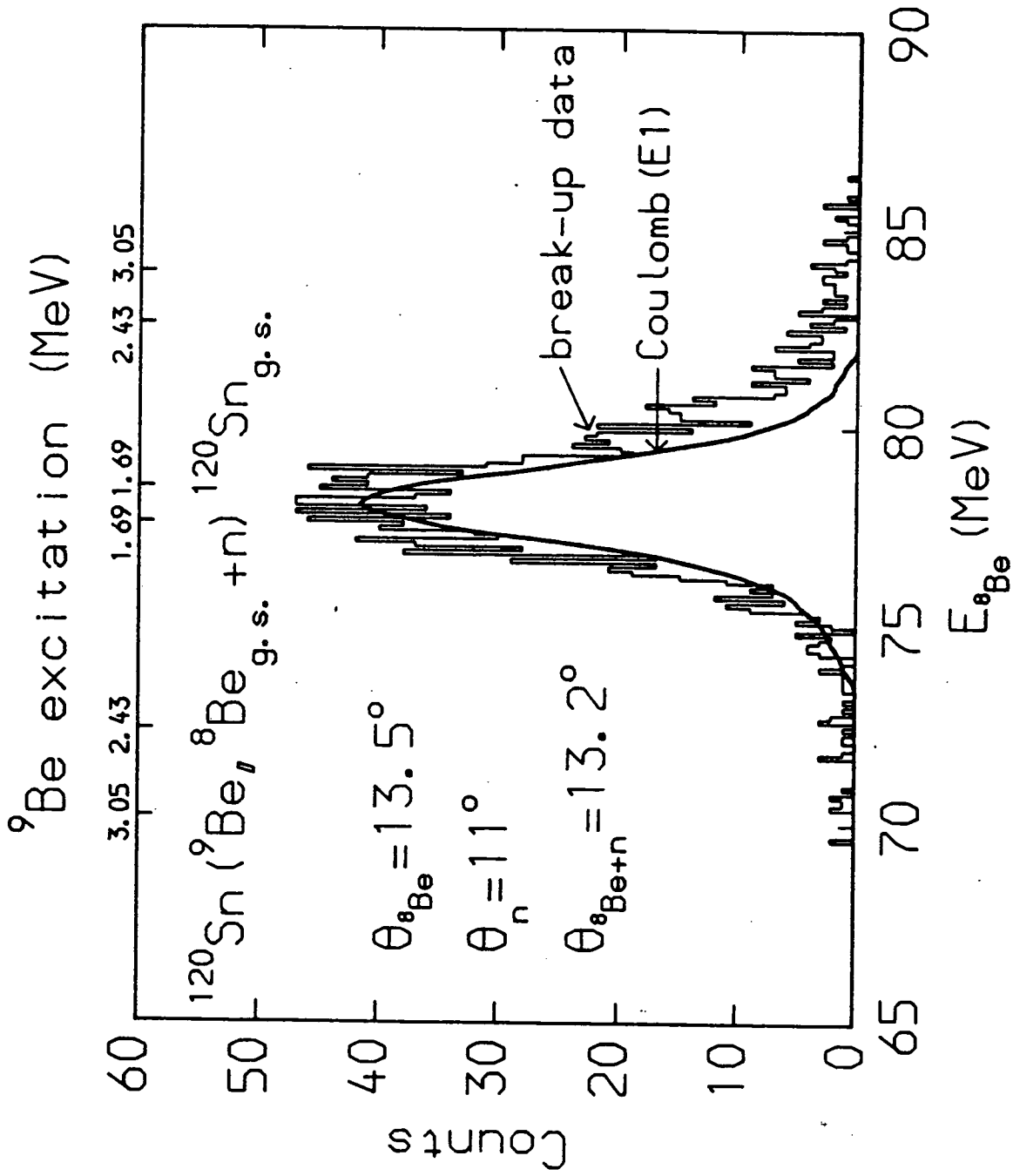

Figure 6.2: Comparison of an experimental $^8Be_{g.s.}$ projected spectrum with a Monte-Carlo simulation for the break-up reaction $^{120}Sn(^9Be,^8Be_{g.s.}+n)^{120}Sn_{g.s.}$. The simulation is based on a semi-classical Coulomb excitation calculation. The absolute magnitudes of the data and the simulation cannot be compared.

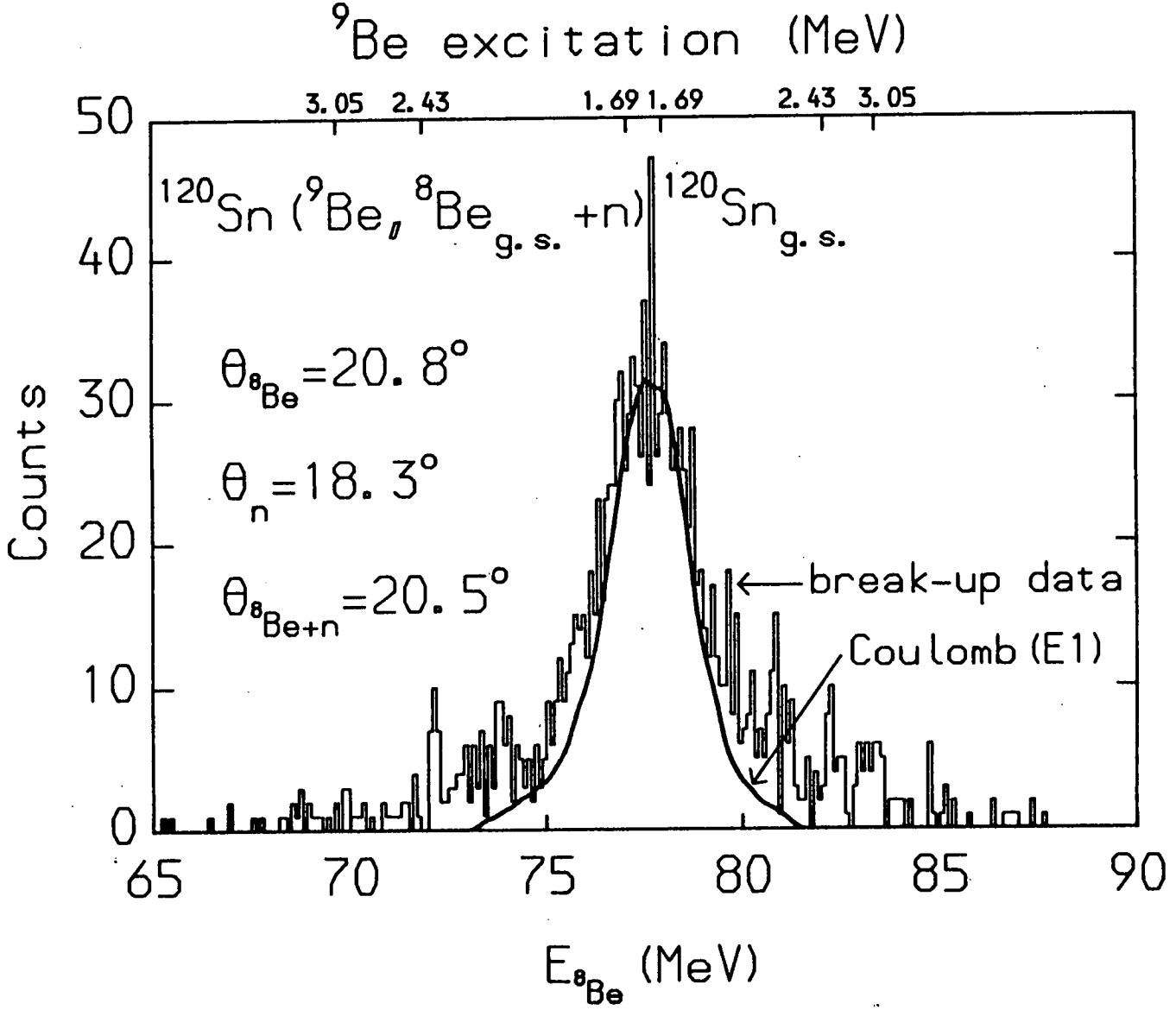

Figure 6.3: Same as for figure 6.2, except that a more backward scattering angle is considered in this figure.

the present case, since the ^{8}Be and neutron are in a relative ℓ=0 state and the 0^+ ground state of ^{8}Be decays by s-wave α-emission. Final state interactions were not included in the simulations. It should be noted that the simulations shown in figures 5.8 and 5.13 for the 1.69MeV state, employed a simple Lorentzian line-shape with a sharp cut-off at the $^8Be_{gs}$+n energy threshold.

The simulation of figure 6.2 reproduces the shape of the data reasonably well, apart from in the region of the upper tail of the $^8Be_{gs}$ energy distribution. The difference in this region may be due to Coulomb FSIs between the $^8Be_{gs}$ and the target. Such FSIs will tend to increase the energy of the $^8Be_{gs}$ nuclei. If a slightly flatter $\sigma_{\gamma,n}(E_\gamma)$ spectrum is chosen, such as one which passes through the data points of Gibbons [GIBB59] and John [JOHN62], then a moderately better fit is achieved.

The shape of $df_{E1}(\theta,E_x)$ as a function of E_x (1.666MeV<E_x<2.166MeV) does not depend greatly on the value of θ^{cm}_{8Be+n}; so long as this value is within the range of θ^{cm}_{8Be+n} values over which data was collected. Consequently, the shape of the simulated projected spectra does not change significantly with scattering angle. Since the shape of the experimental projected spectra does change with angle (see figure 5.7) the quality of fit of the simulation decreases as θ^{cm}_{8Be+n} increases; this is evident from a comparison of figures 6.2 and 6.3.

The overall similarity in shape of the simulations and the experimental spectra indicates that the breakup mechanism is via Coulomb excitation. To explore the Coulomb process further it is necessary to compare the cross-sections predicted by the Coulomb calculation with those extracted from the breakup data. In figure 6.4, the variation of the theoretical Coulomb cross-section with θ^{cm}_{8Be+n} is plotted. This curve was obtained by integrating the theoretical values of $d^2\sigma_{E1}/d\Omega dE_x$ over the excitation range 1.666MeV<E_x<2.166MeV. To calculate the experimental cross-section from the breakup data, it was necessary to know the $^8Be_{gs}$+n effective solid angles for the Coulomb-E1 breakup process. These were determined by means of the Monte-Carlo simulations described above. For each value of θ^{cm}_{8Be+n}, the total number of breakup events was obtained by integrating the appropriate experimental $^8Be_{gs}$ projected spectrum over the $^8Be_{gs}$ kinetic energy range corresponding to the E_x range 1.666MeV<E_x<2.166MeV. The experimental cross-section, as a function of θ^{cm}_{8Be+n}, has been plotted in figure 6.4. (The average values of θ^{cm}_{8Be+n} were also determined from the Monte-Carlo

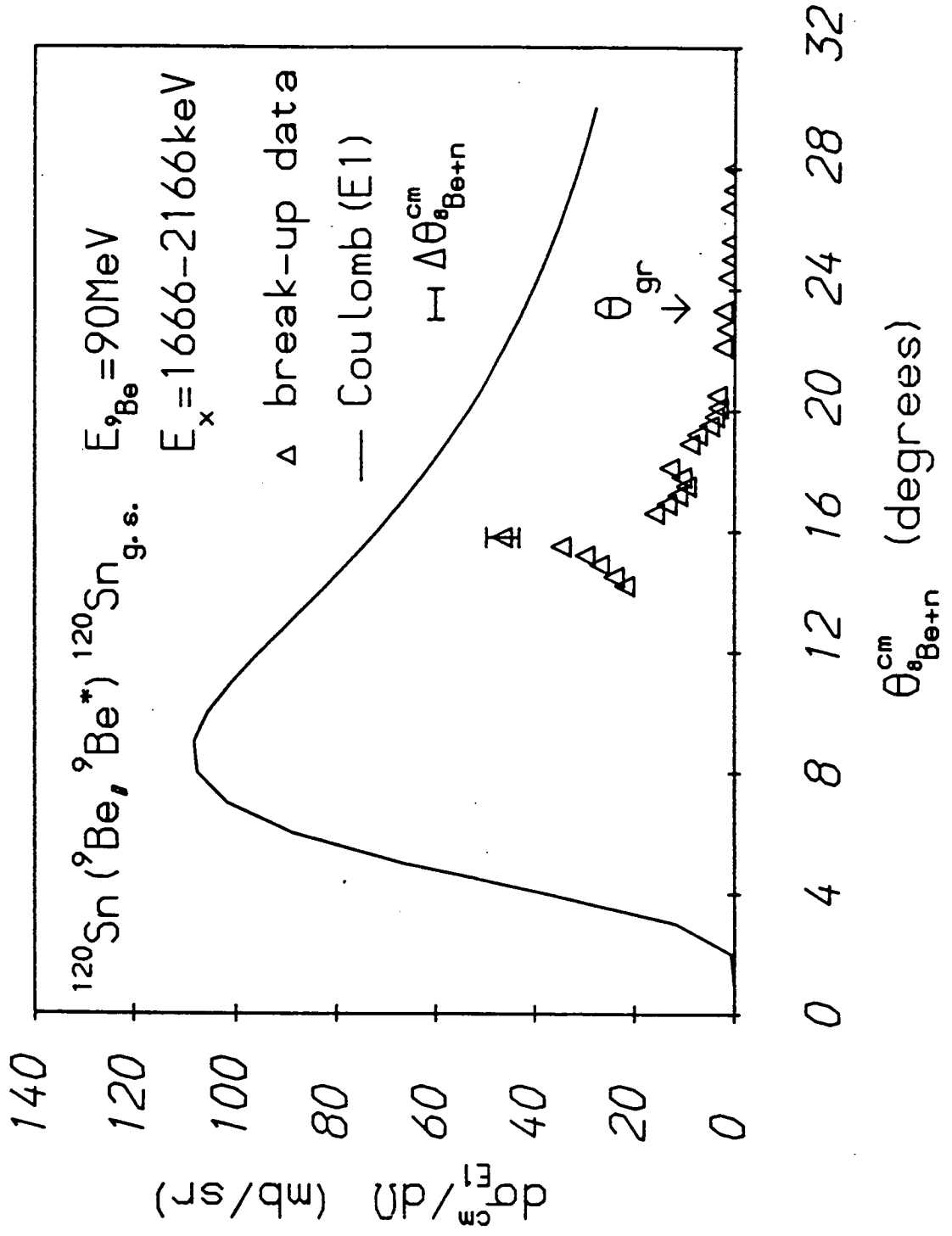

Figure 6.4: Theoretical and experimental angular distributions for the reaction $^{120}Sn(^{9}Be,^{8}Be_{g.s.}+n)^{120}Sn_{g.s.}$. The theoretical curve represents a semi-classical Coulomb excitation calculation. Unless shown, the statistical errors on the data-points are less than or equal to the size of the symbols used to indicate the data-points.

simulations).

The experimental cross-section peaks at $\curvearrowright 16^{\circ}$ with a value of $\curvearrowright 45$mb/sr. Beyond 16° the cross-section steadily decreases. At all scattering angles the Coulomb calculation considerably over predicts the experimental cross-section. Beyond the grazing angle, one would not expect the calculation to work, since in this region the projectile trajectory does not follow a Rutherford orbit. At angles well inside the grazing angle however one would expect that the Coulomb interaction would dominate and that a Coulomb calculation would at least reproduce the magnitude of the data. The fact that the calculation does not do so, may indicate that the breakup process has been incompletely simulated. For example, the omission of FSIs may lead to an over estimation of the effective solid-angles, and therefore to an under estimation of the cross-sections.

The turnover in the experimental cross-section at $\curvearrowright 16^{\circ}$ is surprising, given that the double differential cross-sections (plotted in figure 5.11) steadily decrease over all the angles for which data was collected. It is possible that the turnover is due to a systematic error in the calculation of the effective solid angles which increases as $|\theta_{8Be}-\theta_n|$ increases. It was previously noted that the Monte-Carlo simulations do not exactly reproduce the shape of the experimental projected spectra. In particular, it appears that a flatter $\sigma_{\gamma,n}(E_\gamma)$ spectrum will produce a better fit to the shape of the data. This being the case, the effective solid-angles will have been under estimated for small values of $|\theta_{8Be}-\theta_n|$ and over estimated for large values. Since the steady increase in the cross-section between 14° and 16° happens to correspond to a steady increase in $|\theta_{8Be}-\theta_n|$ and the decrease of the cross-section between 16° and 18° to a decrease in $|\theta_{8Be}-\theta_n|$, it is plausible that the turnover is, in part at least, the result of an incomplete simulation of the breakup process.

Of course the structure in the data may represent a genuine change in the breakup cross-section due to nuclear+Coulomb interference.

Another, more direct, method of comparing the magnitudes of the calculation and the data is to plot normalised versions of the simulated projected spectra with the experimental projected spectra. This has been done in figure 6.5. The normalisations of the simulated spectra were determined from the values of the integrated beam current, target thickness, livetime and

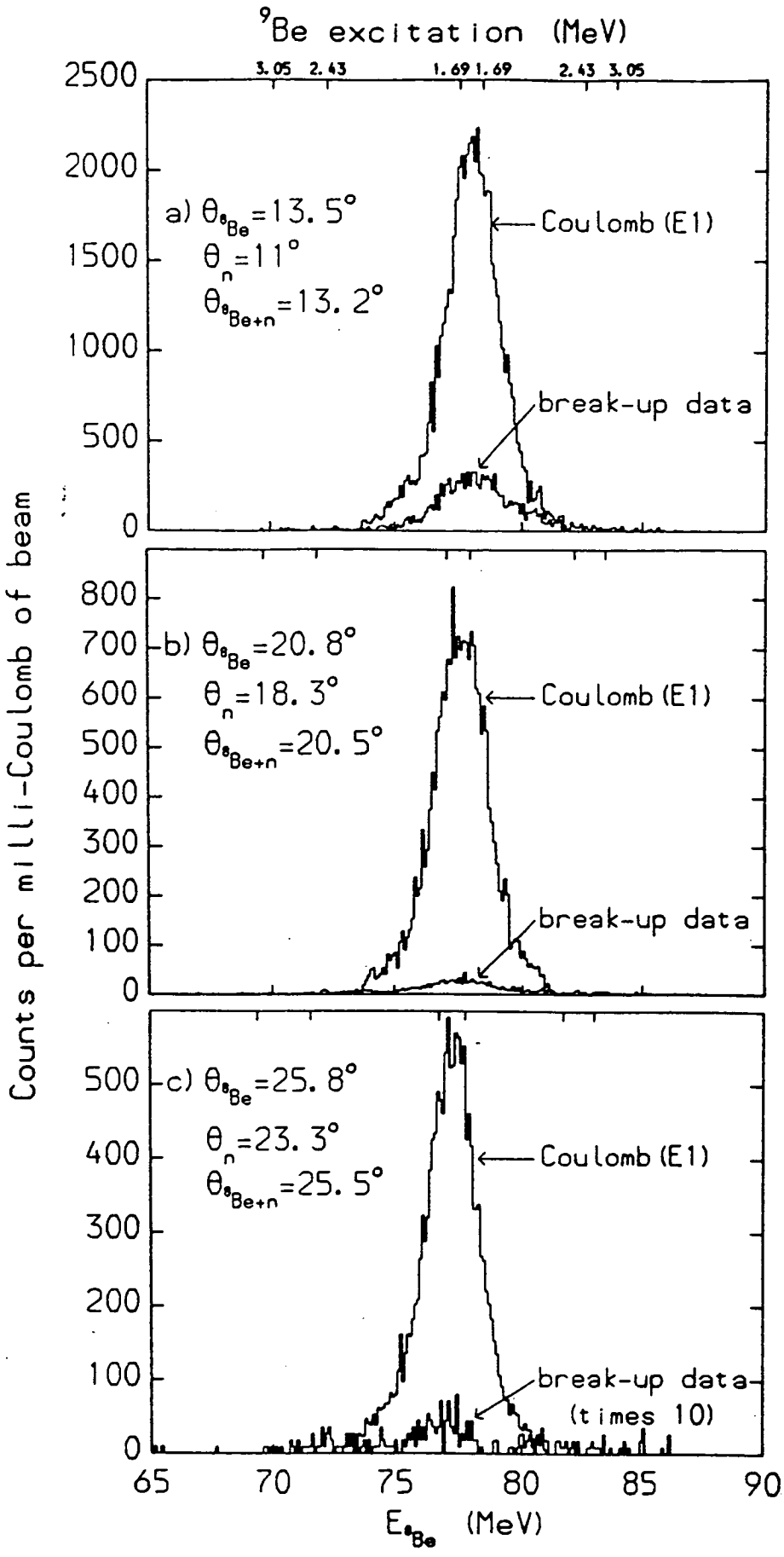

Figure 6.5: Comparison of the absolute magnitudes of the experimental $^8Be_{g.s.}$ projected spectra with Monte-Carlo simulations of the break-up reaction $^{120}Sn(^9Be,^8Be_{g.s.}+n)^{120}Sn_{g.s.}$. The simulation is based on a semi-classical Coulomb excitation calculation.

the magnitude of $d^2\sigma_{E1}/d\Omega dE_x$. The same picture emerges from figure 6.5 as from figure 6.4. The experimental cross-section is over-predicted at all angles. The magnitude of the over-prediction increases as the scattering angle increases.

It would be of interest to study the $^9Be \rightarrow ^8Be_{gs}+n$ reaction, at more forward angles than studied presently, to see if there is any region in which the Coulomb calculation fits the data. We now consider possible explanations for the difference between the Coulomb calculation and the breakup data.

If the ^9Be projectile breaks up in the Coulomb field of the target nucleus, then the breakup fragments will be subject to Coulomb final state interactions. If, at the point of breakup, the relative energy between the $^8Be_{gs}$ and the neutron is zero, then the neutron will travel along the tangent to the ^9Be orbit at the point of breakup, whilst the $^8Be_{gs}$ nucleus will be repelled by the Coulomb field of the target. For zero relative energy breakup, the Coulomb FSIs will always lead to an increase in the separation angle between the $^8Be_{gs}$ and the neutron. An extreme case of this effect is illustrated in figure 6.6, where $\varepsilon=0$ breakup at $r_{9Be}=R_{min}$ is considered. For this case, the separation angle between the $^8Be_{gs}$ and the neutron is approximately equal to half the Rutherford scattering angle. As the distance of the breakup point from the target increases, the separation angle decreases rapidly, such that, for breakup at $r_{9Be}=3R_{min}$ the separation angle is typically 0.5°.

The effect of Coulomb FSIs on the detection efficiency for the $^9Be \rightarrow ^8Be_{gs}+n$ reaction was investigated by means of Monte-Carlo simulations. It was found that, in general, the effective solid angles are reduced for values of $\theta_{8Be}<\theta_n$ and increased for values of $\theta_{8Be}>\theta_n$. The reductions in the effective solid angle vary from 100% at $r_{9Be}=R_{min}$ to 10% at $r_{9Be}=3R_{min}$. The increases vary from 400% at $r_{9Be}=R_{min}$ to 20% at $r_{9Be}=3R_{min}$. Beyond $r_{9Be}=4R_{min}$ the effect of the FSIs is negligible.

The fact that the efficiencies are increased as well as decreased, suggests that the Coulomb FSIs are not responsible for the difference between the experimental cross-section and the Coulomb calculation. This conclusion is strengthened when the life-time of the 1.69MeV resonance is considered. Taking the FWHM of the 1.69MeV state as being 100keV and applying $\Delta E\Delta t \backsim \hbar$, a half-life of 66×10^{-22}s is obtained. At a scattering angle of 16°, this half-life

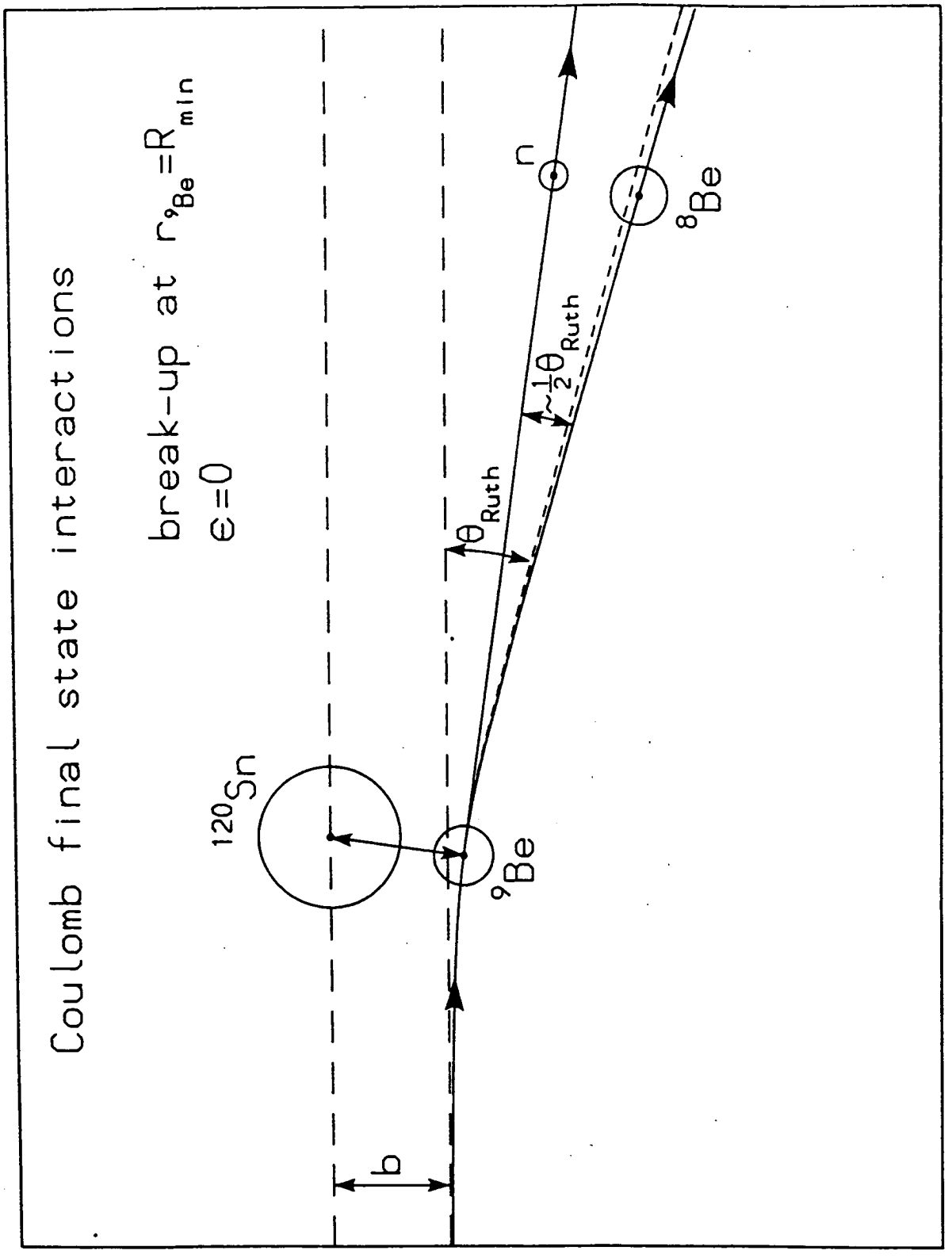

Figure 6.6: Schematic illustration of the effect of Coulomb final state interactions on the break-up of ^9Be into the $^8Be_{g.s.}$+n channel.

corresponds to a *half-distance* of $\backsim 16R_{min}$, so only $\backsim 8\%$ of the ^{9}Be breakup events, which pass through the 1.69MeV resonance, decay sufficiently close to the target (i.e. within a distance of $4R_{min}$) for FSIs to be significant.

The fall-off of the ^{9}Be breakup yield, at scattering angles well inside the grazing angle, is qualitatively similar to the behaviour of the ^{7}Li→α+t direct breakup yield in the reaction 70MeV ^{7}Li+^{120}Sn [SHOT84]. A Coulomb calculation for this reaction was shown to considerably over predict the data for scattering angles greater then $\theta_{gr}-10^{o}$. Recently, an explanation has been proposed for this behaviour [SHOT88c] which is based on the nature of the radial dependence of the breakup matrix-element. For the E1 Coulomb interaction, the breakup cross-section is proportional to $|<f|E1|i>|^{2}$ i.e.

$$d^{2}\sigma_{E1}/d\Omega dE_{x} \backsim |<f|E1|i>|^{2} \qquad (6.3)$$

where E1 has been used to denote the Coulomb operator. For the direct breakup of ^{7}Li, free-particle wave-functions are appropriate for the final channel, $|f>$. The wave-function of the initial channel, $|i>$, is that of the ground state of ^{7}Li. Since the free-particle wave-functions are slowly varying and the E1 operator is just 'r', it is found that the breakup matrix-element is concentrated at values of 'r' which are associated with the tail of the $^{7}Li_{gs}$ wave-function. Therefore, for breakup reactions, the effective radius of the ^{7}Li projectile is larger than the conventional strong absorption radius. Since a larger radius corresponds to a smaller grazing angle, the onset of strong nuclear processes will occur at angles which are smaller than those determined from the strong absorption radius. In general, nuclear processes will reduce the observed coincidence yield, either through the absorption of the breakup fragments or through the effect of nuclear FSIs on the fragment trajectories.

An estimate of the amount by which the observed breakup yield would be reduced, for the ^{7}Li→α+t reaction, is consistent with the difference between the Coulomb calculation and the ^{7}Li breakup data.

The application of these ideas, to the case of ^{9}Be→$^{8}Be_{gs}$+n breakup, is complicated by the fact that a certain fraction of the breakup yield passes through the 1.69MeV resonance of ^{9}Be. However, since this resonance is broad and the ground state of ^{9}Be has a slowly decaying exponential tail, the radial dependence of the matrix-element for ^{9}Be breakup is similar to that of the

matrix-element for ^{7}Li breakup and comparable reduction factors for the observed breakup yield are obtained. When the theoretical curve of figure 6.4 is multiplied by these factors, a new curve is produced whose magnitude and general shape are close to that of the experimental data-points [SHOT88c]. The peak in the experimental data is not reproduced but, as discussed earlier, this peak may not be due to structure in the $^{9}Be \rightarrow {}^{8}Be_{gs}+n$ cross-section.

6.5 Summary

A semi-classical Coulomb excitation calculation has been performed for the breakup reaction $^{120}Sn(^{9}Be,{}^{8}Be_{gs}+n)^{120}Sn_{gs}$. An E1 interaction was assumed and use was made of existing $^{9}Be(\gamma,n)$ photo-neutron data. In addition, experimental cross-sections for this ^{9}Be breakup reaction have been extracted from the $^{8}Be_{gs}+n$ coincidence data. Although it was found that Monte-Carlo simulations, based on the Coulomb calculation, could well reproduce the shape of the experimental projected spectra, the calculation considerably over-predicted the magnitude of the breakup cross-section.

It was found that Coulomb FSIs could not account for the discrepancy between the theory and the data. Instead, an explanation has been proposed which is based on the size of the effective radius of ^{9}Be for breakup reactions. This explanation results in a predicted yield which is consistent in magnitude with the experimental data.

CHAPTER 7
SUMMARY AND CONCLUSIONS

A summary of the work discussed in this thesis will now be presented. Four topics will be reviewed briefly.

- The development of new equipment and experimental techniques.
- The interpretation of the anomalous peaks in the $E_{\alpha 1}/E_{\alpha 2}$ spectra.
- The $^{9}Be \rightarrow {}^{8}Be_{gs}+n$ data.
- The coulomb excitation calculation for the $^{120}Sn(^{9}Be,{}^{8}Be_{gs})^{120}Sn_{gs}$ reaction.

Finally, some possible directions for future research will be considered.

7.1 Development of Experimental Equipment and Methods

One of the most novel aspects of this work has been the development of a ^{8}Be-telescope which has an efficiency that is an order of magnitude greater than that of any previous ^{8}Be identifier.

This new ^{8}Be-telescope was constructed from a stack of four, specially designed, silicon strip-detectors. The effective solid-angle of the telescope is $\sim$9msr for 80MeV $^{8}Be_{gs}$ nuclei. This solid-angle is a factor of $\sim$45 larger than that which can be achieved with conventional detectors.

In addition to the design of new detectors, one of the original features of this work has been the development of software which permits the online monitering of the deadtime of the experimental system. By means of this software it was possible to determine the deadtime of each type of event (i.e. of all of the 62 different combinations of detectors) at any time during the data collecting runs. This software facility was of considerable importance due to the great complexity of the experimental equipment. On several occasions, the deadtime monitering routine detected the failure of electronic units and detectors. Incidentally, the only occasion on which a unit failure went undetected was when one of the features of the deadtime inspection routine was *switched off*.

7.2 Anomalous α+α data

In both the 90MeV $^{9}Be+^{12}C$ data and the 90MeV $^{9}Be+^{120}Sn$ data, anomalous peaks were observed in the $E_{\alpha 1}/E_{\alpha 2}$ spectra. The anomalous peaks were present for both the α+α and α+α+n data. The symmetry of the anomalous distributions suggested that they originated from the decay of a state in ^{8}Be at 0.5MeV with a width of 0.2MeV. Since no known state of ^{8}Be exists at this energy, and ^{8}Be is a very well studied nucleus, is was concluded that the existence of a new, low-lying, state of ^{8}Be was a very unlikely explanation for the anomalous peaks. Several other explanations were considered.

An instrumental origin was rejected by collecting data on the reactions $^{12}C,^{120}Sn(^{9}Be,\alpha+\alpha)$ with a conventional detection system.

It was noted that, in some respects, the anomalous peaks in the present data suggest a state in ^{8}Be that is similar to the anomaly in the excitation spectrum of ^{8}Be at ∿0.6MeV which has often been observed before. This anomaly has been interpreted as a ghost of the ground state of ^{8}Be. It was concluded that the present data could not be described by a ghost-state theory. Furthermore, the anomalous features in the present data are sufficiently different from the previously observed anomaly to suggest that a different mechanism is responsible for their production. Therefore, the present data does not cast doubt on the ghost-state interpretation of the previous data.

A satisfactory explanation for the anomalous data was found in terms of the decay of the 2.43 $5/2^{-}$ state of ^{9}Be into the $^{5}He_{gs}+\alpha$ channel. Monte-Carlo simulations of the reactions

$$^{12}C,^{120}Sn(^{9}Be,^{9}Be^{*}_{2.43}\rightarrow^{5}He_{gs}+\alpha)$$

were found to fit the anomalous data well, if it was assumed that the $^{9}Be^{*}_{2.43}$ ejectile was strongly aligned.

This interpretation of the anomalous peaks was used to extract angular distributions for the reaction $(^{9}Be,^{9}Be^{*}_{2.43})$.

Subsequent to the analysis carried out for Chapter 4, it was discovered that the same anomalous feature had also been observed by Pochodzalla et al

[POCH87] in two-particle correlation data for ^{40}Ar induced reactions on ^{197}Au at a bombarding energy of 2,400MeV. In this work, a strong peak was seen in the α-α correlation spectra which corresponded to a ^{8}Be excitation of $\sim$0.5MeV. This peak was interpreted in exactly the same manner as the anomalous distributions in the present data i.e. that it was due to the decay of the 2.43MeV state of ^{9}Be into the $^{5}He_{gs}+\alpha$ channel. While it is perhaps disappointing that this reaction has been observed previously, the confirmation of its interpretation supports the manner in which the anomalous data was used to determine the (^{9}Be,$^{9}Be^{*}_{2.43}$) yield.

7.3 The $^{9}Be \rightarrow ^{8}Be_{gs}+n$ Data

Approximately 90% of the $\alpha+\alpha$ data was due to the breakup of ^{9}Be into either the $^{8}Be_{gs}+n$ or $^{5}He_{gs}+\alpha$ channels. The latter of these channels was discussed in the previous section. The $^{9}Be \rightarrow ^{8}Be_{gs}+n$ data will now be reviewed.

For the ^{120}Sn target, several general comments can be made about the $^{9}Be \rightarrow ^{8}Be_{gs}+n$ data.

- The breakup yield is strongly forward focused.
- Elastic breakup is the dominant reaction channel, particularly at forward scattering angles where it accounts for almost 100% of the breakup yield.
- The breakup yield is peaked at very low $^{8}Be_{gs}$-n relative energies. Virtually all of the $^{8}Be_{gs}+n$ events correspond to ^{9}Be excitations of less than 3MeV.

This behaviour of the $^{9}Be \rightarrow ^{8}Be_{gs}+n$ reaction suggests that Coulomb excitation is the dominant reaction mechanism at forward angles.

As regards the nature of the $^{9}Be \rightarrow ^{8}Be_{gs}+n$ breakup process, some aspects of the experimental data indicate the presence of a direct breakup component, while others suggest a contribution from the sequential decay of the 1.69MeV state of ^{9}Be. It is most likely that the $^{9}Be \rightarrow ^{8}Be_{gs}+n$ yield contains a contribution from both sequential and direct processes.

Apart from the fact that one would expect the (^{9}Be,$^{9}Be^{*}_{1.69}$) reaction to be strong (since it can be excited via an E1 transition), Monte-Carlo simulations of the decay of the 1.69MeV state produce a reasonable fit to the central region of the projected energy spectra.

The evidence for a direct component can be summarised as follows:

- The shape of the projected spectra for the ^{120}Sn target changes rapidly with angle, which is what one would expect for direct processes, since they are subject to FSIs.
- The angular distributions for the $^{8}Be_{gs}$+n yield behave in the same manner as the $^{7}Li \rightarrow \alpha+t$ direct breakup yield and in a very different manner to the (^{9}Be,$^{9}Be^{*}_{2.43}$) sequential breakup yield.
- The shape of the projected spectra for ^{12}C and ^{120}Sn are very different. In particular, there is a strong low relative energy component in the ^{120}Sn spectrum which is not present in the ^{12}C spectrum.

As noted earlier, it is not possible with the present data to separate the direct and sequential components.

7.4 Coulomb Excitation Calculation

In Chapter 6, a Coulomb excitation calculation was performed for the $^{120}Sn(^{9}Be,^{8}Be_{gs}+n)^{120}Sn_{gs}$ reaction. It was found that although Monte-Carlo simulations, based on this calculation, could well reproduce the shape of the experimental projected spectra, the calculation considerably over-predicted the magnitude of the breakup cross-section over all the scattering angles for which data was collected. This was particularly surprising at forward angles since in this region the assumptions involved in the calculation could be well justified.

The effect of Coulomb final state interactions on the data was investigated. It was shown that such interactions will only have a significant effect on the direct component of the breakup yield. Furthermore, their effect is complicated due to the fact that they increase the detection efficiency for some combinations of detectors and decrease the efficiency for other combinations. Therefore, it was concluded that Coulomb FSIs could not explain the difference between the calculation and the data.

It was noted that the behaviour of the $^{9}Be \rightarrow ^{8}Be_{gs}+n$ reaction was similar to that of the $^{7}Li \rightarrow \alpha+t$ direct breakup reaction. For the case of the ^{7}Li reaction a Coulomb excitation calculation was found to over-predict the experimental cross-section for angles greater than $\theta_{gr}-10^{\circ}$. A recent explanation [SHOT88c] for this behaviour is based on the idea that there is an effective radius for breakup reactions which is larger than the conventional strong absorption radius. Although the calculations are at an early stage, it looks as if the

behaviour of both the ^{7}Li and ^{9}Be breakup reactions can be explained in this manner.

7.5 Future Research and Development

7.5.1 Development of Detection Systems

The work on detector development, which was carried out to enable the ^{9}Be breakup experiment, has demonstrated the advantages that can be gained by making use of silicon strip detectors (SSDs). Order of magnitude improvements in solid-angle and efficiency can be achieved by the use of such detectors.

There are many areas in which SSDs are the ideal type of detector. For example:

- In the detection of high multiplicities of fragments.
- In the detection of breakup fragments with very low separation angles.
- To study reactions where very high position resolution is required.
- To study low cross-section reactions.

To make full use of SSDs however, advances have to made in two areas. Firstly, the range of detectors thickness has to be extended. The currently available range is 200-600μm. Experiments with heavy and light ions require detectors which are at least as as thin as 75μm and as thick as 5000μm. Since it will probably prove impossible to develop SSDs which are much thicker than 1000μm, it will be necessary to design thick (>5mm) stopping counters, which combined with SSDs will create a telescope with a sufficient dynamic range. Since SSDs can have areas of up to 50x50mm^2, the stopping detectors will also have to have large surface areas. One possibility is the use of thick CsI-crystals coupled to large area photo-diodes.

It is not difficult to conceive of applications for a strip-detector based telescope with several 100 individual elements. Indeed, such a telescope could easily be constructed, its instrumentation on the other hand would be an immense task with conventional electronics. It is clear that to fully utilise SSDs, a multi-channel signal processing system has to be developed. The unit cost of each pre-amplifier + amplifier + ADC chain in the system must be kept low due to the need for several hundred channels. Therefore, the system will almost certainly have to be based on hybrid micro-electronic technology.

7.5.2 Possible Areas of Future Research

As noted in Chapter 4, the separation on the $E_{\alpha 1}/E_{\alpha 2}$ plane of the distributions due to the decay of 2.43MeV state of ^{9}Be and the decay of the ground state of ^{8}Be, provides an experimentally simple method of identifying the (^{9}Be,$^{9}Be^{*}_{2.43}$) reaction. Furthermore, the cross-section for this reaction is high, typically 30mb/sr, so it would be possible to perform a survey of the reaction for a number of targets with only a moderate amount of accelerator time. Such a survey could provide interesting information on nuclear breakup processes, since the 2.43MeV state will only be weakly excited by the Coulomb field.

The $^{9}Be \rightarrow ^{8}Be_{gs}+n$ yield was observed to be very strongly forward focused. At forward angles the breakup yield is large, typically 40mb/sr. At all of the angles for which data was obtained, the Coulomb excitation calculation over-estimated the data. It would be interesting to study the $^{9}Be \rightarrow ^{8}Be_{gs}+n$ reaction at more forward angles than currently studied to see if there is any region in which the Coulomb calculation reproduces the breakup yield.

In the backward angle data, there was an indication of a partial-fusion component to the $^{8}Be_{gs}+n$ yield. The statistics of the present data do not permit a proper study of this reaction. Wide-angle $^{8}Be+n$ data or $^{8}Be+\gamma$-ray data would allow a careful study of ^{9}Be induced partial-fusion reactions. Such a study would be of interest, since partial-fusion reactions are known to contribute strongly to inclusive yields. Since ^{9}Be has a well defined $\alpha+\alpha+n$ cluster structure, one would expect a high yield for the ($^{9}Be,\alpha+\alpha$) and ($^{9}Be,\alpha$) partial fusion channels. A measurement of these channels would test the critical angular momentum theories.

The measurements presented here show that the total ^{9}Be breakup cross-section is high. They also indicate that there is a considerable direct component to this breakup yield. These results confirm the prediction made in §1.5 that ^{9}Be would have a large direct breakup yield due to its high E1 effective charge. It would be of interest to explore the breakup reactions of other nuclei with high predicted yields to gain further information on the direct breakup process. In particular, it would be worth studying the breakup reactions of neutron-rich projectiles, such as ^{13}C and ^{17}O, since these nuclei

have high E1 effective charges for breakup into the neutron channel. In fact, both the $^{13}C \rightarrow ^{12}C+n$ and $^{17}O \rightarrow ^{16}O+n$ reactions have the same E1 effective charge as the $^{9}Be \rightarrow ^{8}Be+n$ reaction.

References

AJZE84 F.Ajzenberg-Selove, *Nucl. Phys.* **A413** (1984) 1

ALDE56 K.Alder, A.Bohr, T.Huus, B.Mottelson and A.Winther *Rev. Mod. Phys.* **28** (1956) 432

BARK62 F.C.Barker and P.B.Treacy, *Nucl. Phys.* **38** (1962) 33-49

BARK76 F.C.Barker, G.M.Crawley, P.S.Miller and W.F.Steele, *Aust. J. Phys.* **29** (1976) 245-248

BARK87 F.C.Barker, Aust. Nat. University, private communication (1987)

BAUR72 G.Baur and D.Trautmann, *Nucl. Phys.* **A191** (1972) 321-331

BAUR76 G.Baur and D.Trautmann, *Phys. Lett.* **C25** (1976) 293-358

BAUR79 G.Baur et al, *Nucl. Phys.* **A315** (1979) 241

BAUR84 G.Baur et al, *Phys. Rep.* **111** (1984) 333

BECC81 F.D.Becchetti, C.A.Fields, R.S.Raymond, H.C.Bhang and D.Overway, *Phys. Rev.* **C24** (1981) 2401-2408

BERM67 B.L.Berman, R.L.Van Hemert and C.D.Bowman, *Phys. Rev.* **163** (1967) 958

BICE82 A.N.Bice, A.C.Shotter and J.Cerny, *Nucl. Phys.* **A390** (1982) 161

BINI80 M.Bini et al, *Phys. Rev.* **C22** (1980) 1945-1961

BIRK64 J.B.Birks, The Theory and Practice of Scintillation Counting, Permagon Oxford (1964) page 185

BHOW81 R.K.Bhowmik et al, *Nucl. Phys.* **A363** (1981) 516-532

BHOW82 R.K.Bhowmik et al, *Nucl. Phys.* **A390** (1982) 117-160

BLAT79 J.M.Blatt and V.F.Weisskopf, Theoretical Nuclear Physics, Springer-Verlag New York Inc. (1979)

CAST80 C.M.Castaneda et al, *Phys. Rev.* **C21** (1980) 179-197

CECI79 R.A.Cecil, B.D.Anderson and R.Madey, *N.I.M.* **161** (1979) 439-447

DAVI87 T.Davinson, Ph.D. Thesis , University of Edinburgh, 1987 (unpublished)

DRIE80 J. van Driel, Ph.D. Thesis, University of Groningen, 1980 (unpublished)

EDIN85 Annual Report of the Edinburgh University Nuclear Physics Group, (1985-1986), Section 19

FUJI82 M.Fujishiro, T.Tabata, K.Okamoto and T.Tsujimoto, *Can. J. Phys.* **60** (1982) 1672

FUJI83 M.Fujishiro, K.Okamoto and T.Tsujimoto, *Can. J. Phys.* **61** (1983) 1579

FULT86 B.R.Fulton et al, *Phys. Lett.* **B181** (1986) 233

GIBB59 J.H.Gibbons, R.L.Macklin, J.B.Marion and H.W.Schmitt, *Phys. Rev.* **114** (1959) 1319

HELM47 A.C.Helmholtz et al, *Phys. Rev.* **72** (1947) 1003

JARC73 L.Jarczyk, J.Lang et al, *Phys. Rev* **C8** (1973) 68-74

JOHN62 W.John and J.M.Prosser, *Phys. Rev.* **127** (1962) 231

JOHN70 R.C.Johnson and P.R.Soper, *Phys. Rev.* **C1** (1970) 976

LAWR35 E.O.Lawrence, E.M^{c}Millan and R.L.Thornton, *Phys. Rev.* **48** (1935) 493-499

MEIJ85 R.J. de Meijer and R.Kamermans, *Rev. Mod. Phys.* **57** (1985) 147

NAGA82 M.A.Nagarajan, I.J.Thompson and R.C.Johnson, *Nucl. Phys.* **A385** (1982) 525

OMAR84 A.R.Omar, J.S.Eck, J.R.Leigh and T.R.Ophel, *Phys. Rev.* **C30** (1984) 896-901

OPPE35a J.R.Oppenheimer, *Phys. Rev.* **47** (1935) 845

OPPE35b J.R.Oppenheimer and M.Phillips, *Phys. Rev.* **48** (1935) 500-502

OVER81 D.Overway, J.Janecke, F.D.Becchetti, C.E.Thorn and G.Kekelis, *Nucl. Phys.* **A366** (1981) 299-319

PERK79 L.J.Perkins and M.C.Scott, *N.I.M.* **166** (1979) 451-464

POCH87 J.Pochodzalla et al, *Phys. Rev.* **C35** (1987) 1695-1719

RAE81 W.D.Rae et al, *Phys. Lett.* **B105** (1981) 417-420

SAGU86 Y.Sakuragi, M.Yahiro and M.Kamimura, Institute for Nuclear Study, University of Tokyo, Japan, INS-Rep.600, Aug.1986

SATC78 G.R.Satchler and W.G.Love, *Phys. Lett.* **B76** (1978) 23

SATC79 G.R.Satchler, *Phys. Lett.* **B83** (1979) 284

SERB47 R.Serber, *Phys. Rev.* **72** (1947) 1008-1016

SIWE79 K.Siwek-Wilczynska et al, *Nucl. Phys.* **A330** (1979) 150

SHOT81 A.C.Shotter, A.N.Bice, J.M.Wouters, W.D.Rae and J.Cerny *Phys. Rev. Lett.* **46** (1981) 12–15

SHOT84 A.C.Shotter, V.Rapp, T.Davinson, D.Branford, N.E.Sanderson and M.A.Nagarajan, *Phys. Rev. Lett.* **53** (1984) 1539–1542

SHOT88a A.C.Shotter and M.A.Nagarajan, to be published

SHOT88b A.C.Shotter, to be published

SHOT88c A.C.Shotter, to be published

THOM81 I.J.Thompson and M.A.Nagarajan, *Phys. Lett.* **B106** (1981) 163

THOM83 I.J.Thompson and M.A.Nagarajan, *Phys. Lett.* **B123** (1983) 379–382

UTSU85 H.Utsunomiya, *Phys. Rev.* **C32** (1985) 849–853

WILC73 J.Wilczynski, *Nucl. Phys.* **A216** (1973) 386

WOZN74 G.J.Wozniak et al, *N.I.M.* **120** (1974) 29–40

WOZN76 G.J.Wozniak et al, *Phys. Rev* **C14** (1976) 815

YORK87 J.Yorkston, A.C.Shotter, D.B.Syme and G.Huxtable, *N.I.M.* **A262** (1987) 353–358

YORK88 J.Yorkston, Ph.D. Thesis, University of Edinburgh, 1988 (unpublished)